DOE Award # DE-FG02-12ER46843/ DE-SC0007908

Clemson University

FINAL REPORT

From Interfaces to Bulk: Experimental-Computational Studies Across Time and Length Scales of Multi-Functional Ionic Polymers

Dvora Perahia

Chemistry Department, Clemson University

Gary S. Grest

CINT, Sandia National Laboratories

Period Covered 05/01/2012- 12/30/2016

Report Date 30/12/2016

Award Period 2012-2016

STUDY GOALS AND RATIONAL

Using a **multi-faceted neutron** techniques and **computational** tools, we have set to resolve the factors that control the behavior of structured ionic polymers with segments tailored to enhance simultaneously transport and mechanical stability. The outstanding challenge lies in the fact that under the conditions where transport of electrons, ions and guest molecules is optimized, mechanical stability of the macromolecules is compromised. A potentially effective approach is tailoring multiple functionalities into one macromolecule, each with chemistries that pertains to a different role. To enable this approach, a highly controlled chemistry is required and the basic physics that underlines polymers that consist of highly incompatible segments has to be resolved. Linking the knowledge obtained from complimentary neutron and x-ray techniques with insight from atomistic and coarse grained molecular dynamics simulations provide a multi-scale approach to study these structured polymers and provide the basic physics understanding required for the design of materials for energy generation, capture, and storage.

*Here **neutron** experiments coupled with **computational** components have resulted in unprecedented understanding of the factors that impact the behavior of ionic structured*

polymers. Additionally, computational tools including technical developments for confinement of large molecules, surface compositional analysis and paths for probing interfacial strength as well as conceptual tools to coarse grain polymers while retaining as much as possible of the chemical nature, were developed. The funding resulted in 16 publications (15 published and one in review) and numerous presentations. In parallel, this DOE funding have enabled the education of the next generation of material researchers who are able to take the advantage neutron tools offer to the understanding and design of advanced materials.

Our research has provided unprecedented insight into one of the major factors that limits the use of ionizable polymers, combining the macroscopic view obtained from the experimental techniques with molecular insight extracted from computational studies leading to transformative knowledge that will impact the design of nano-structured, materials. With the focus on model systems, of broad interest to the scientific community and to industry, the research addressed challenges that cut across a large number of polymers, independent of the specific chemical structure or the transported species.

Specifically, this initiative has aimed to: a-resolve structure, b-local dynamics and macroscopic dynamics in a structured polymer and c-derive predictive models to correlate the molecular architecture with transport and mechanical stability. It encompasses multiple efforts including neutron based research directly coupled with invaluable computational insights.

A model tailored co-polymer with one block to enhance transport, one to enhance mechanical stability and one to allow sufficient mobility, for the polymer to rearrange into an optimal structure has been investigated. Its chemical structure is shown in Figure 1. *This polymer consists of tailored multiple functions into one macromolecule* ***enabling*** *actual transformation into usable materials. The role of this polymer is further demonstrated in recent work published by competing groups on either the same polymer (Weiny, Runt, Stein, Freeman) or on co-polymers that constitute part of this pentablock (Weiny, Balsasa, Hickner, Elbad).*

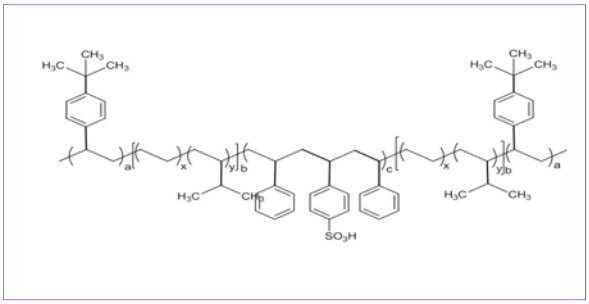

Figure 1 The chemical formula of the pentablock model polymer. The blocks are t-butyl styrene, bound to randomly sulfonated polystyrene by polyethylene propylene (7% random).

The research incorporated studies of single molecules in dilute solutions, micellar solutions, membranes and interfaces. Small angle neutron scattering, neutron reflectometry and inelastic techniques have been used. Computationally the study employs available atomistic and bead-spring models while developing coarse graining methods that transpose the atomistic nature into a coarse grained scale, while retaining the essential atomistic insight.

While focusing on the pentablock, isolating specific effects, we also probed individual blocks in comparison with the entire structured molecule. With the need to schedule neutron experiments over four different instruments, several segments of the research were carried out as the facilities became available and were later seamlessly tailored together.

ACHEVEVMENTS

Outline of activities

Activities included direct measurements on the pentablock itself; measurements on polymers that enable tailoring the rigidity of the ionic block and individual blocks. Intertwined with the science advancements, we have developed new computational tools and embarked on our quest to coarse grain the pentablock to allow correlation with macroscopic structure and transport studies.

From a Molecule to a Micelle: Solution structure is a key to controlling film formation as they serve as the media from which ionic polymers are cast. Using small angle neutron scattering and atomistic molecular dynamics simulations we probed the structure of the pentablock copolymer from a single molecule to clusters. The study have shown that in dilute solutions unimolecular micelles are formed which assemble into soft nano particles with a nano-ionic network dominating the structures. While the overall structure changes with changing of solvent environment, the nano-networks remain stable. Unprecedented detailed structure was captured by neutron scattering (J. Chem. Phys. 2016) and the assembly process was captured directly for the first time by commutations and neutron dynamics are shown in Figure 2.

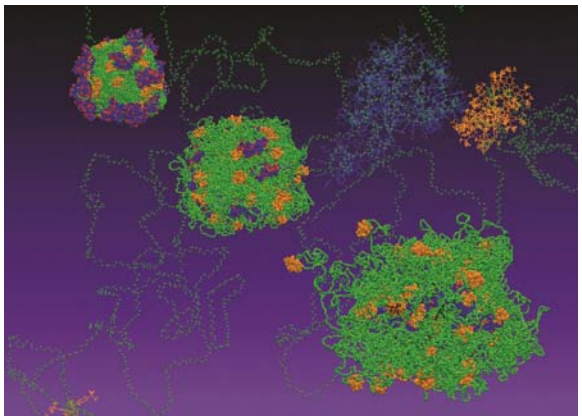

Figure 2 Cover (Nanoscale, Feb 2017) Soft nano particles that consist of ionizable co-polymers where the ionic segments denoted by blue spontaneously assemble to form long-lived nano networks. Depending on the nature of the solvent, the hydrophobic blocks, marked by green and orange, reside either within the network or at the interface forming a switchable responsive soft nanoparticle.

Mechanical and Interfacial Stability: Neutron reflectometry studies were carried out to probe the time evolution of the interfaces: a) between the pentablock and its constituting homopolymers and b) between polystyrene sulfonate that constitutes the center block of the pentablock and polystyrene, which is the major component of the end block. In parallel, the interfacial regions within the pentablock were probed by neutron reflectometry.

To obtain molecular insight into the role of the different blocks in enhancing stability methods to correlate interfacial structure with mechanical stability using coarse grained computational models were derived. We have shown that the interfacial strength is controlled by entanglements. *These observations are of immense importance and* ***open the way*** *to correlate with our neutron reflectometry results.*

Membranes and Macroscopic Solvent Dynamics: Transport in structured polymeric membranes was studied by *Freeman and Weiny* providing qualitative data that attempts to correlate structure with transport. The molecular mechanism that underlines the motion of ions, solvents and electrons and their impact on the polymer phase structure and mechanical stability remains unresolved. Here we were able to computationally form membranes and have extracted the basic path of transport. We find that with increasing ionizable group concentrations, isolated clusters form percolating networks. In presence of water vapor re-arrangements of the ionic domains take place. The study has resolved for the first time a-the time constants associated with initial delay to allow re-arrangements, b-identified the environments of the water molecules; c-understand the effects of connectivity of the ionizable block to segments with different mechanical properties.

Local dynamics: The dynamics at and around the ionic styrene block is a complex sum of polymer re-arrangements and solvent dynamics. We quickly learned that the dynamics of the pentablock is rather complex and there is a need to separate the behavior of the blocks. Experimentally we began with resolving dynamics of the ionic blocks both highly rigid ones and polystyrene. We were able to resolve the multiple environments around the ionic blocks and extract their effects on macroscopic dynamics. Computationally we were able to show for the first time a direct correlation of ionic clustering with backbone dynamics in polystyrene.

Methodology development: In order to carry out molecular dynamics simulations of large systems that will provide insight into the structure and transport of a structured polymer, as outlined in the proposal, we have developed several computational methodologies. The first one has been to cage a large molecule and compress it into dimensions that will allow it to interact. The second has been to develop quantitative pathways to model interfaces. Both were carried out on model polymers.

II-PUBLICATIONS RESULTING FROM DOE DE-FG02-12ER46843/DE-SC007908 SUPPORT UP TO DATE

Both neutron studies and the computational work required sample preparation and synthesis, measurement, analysis and theory contributions. The Clemson team has worked in collaboration with several groups to supplement expertise when required. The work of the Clemson team has been funded through this DOE award. As samples preparation for computational studies and specific code development take an enormous amount of computation time, available samples and codes prepared/developed under support of other resources were used and acknowledged accordingly. Dvora Perahia has

led all neutron studies. Dvora Perahia and Gary Grest have worked jointly to develop the computational approach to complex systems. The jointly advised students and postdoctoral fellows. As the project numbering have changed during the cores of the grant, the publication list includes both numbers.

II-A Published and in Print

1-Ting Ge, Flint Pierce, Dvora Perahia, Gary S. Grest, and Mark O. Robbins, ***"Molecular Dynamics Simulations of Welding: Strength from Interfacial Entanglements",*** *Physical Review Letters* **110**, 098301 (2013) – Editor's Choice.

Highlights: This paper presented for the first time a mesoscopic insight into the strength of the interfaces between polymer films. *Results of neutron reflectometry experiments for related systems are in review.*

Clarification of Contributions: "This work was supported in part by the National Science Foundation under Grants No. DMR-1006805, No. CMMI-0923018, No. OCI-0963185, and No. DMR-0907390. *D. P. and G. S. G. acknowledge support from the U.S. Department of Energy Award No. DE-FG02-12ER46843.* M. O. R. acknowledges support from the Simons Foundation. This research used resources at the National Energy Research Scientific Computing Center, which is supported by the Office of Science of the United States Department of Energy under Contract No. DE-AC02-05CH11231. Research was carried out in part at the Center for Integrated Nanotechnologies, a U.S. Department of Energy, Office of Basic Energy Sciences, user facility. Sandia National Laboratories is a multiprogram laboratory managed and operated by Sandia Corporation, a wholly owned subsidiary of Lockheed Martin Corporation, for the U.S. Department of Energy's National Nuclear Security Administration under Contract No. DE-AC04-94AL85000."

The work in this paper is a full-fledged collaboration between Perahia, Grest and Robbins, supported by multiple agencies. D. P. and G. S. G. (non-paid co-PI) kindly acknowledged BES support. The support enabled the generalization of concepts obtained by *Pierce, Perahia and Grest* (EPL, 2011) of dynamics across polymeric interface, to the realization of failure mechanism at interfaces, presented in this paper. F. Pierce had worked under the supervision of D. P. and G. S. G. to study interfacial healing while T. Ge has carried out the studies of shear under the supervision of M. O. R. in collaboration with D. P. and G. S. G. Peirce was a postdoctoral fellow of D. P. D. P. also acknowledged NFS support for experimental work on semifluorinated polymers (not presented in the paper) that inspired the computational work in this paper.

2-Sabina Maskey, Naresh C. Osti, Dvora Perahia, and Gary S. Grest, "**Internal Correlations and Stability of Polydots, Soft Conjugated Polymeric Nanoparticles",** ACS Macro Letters 2, 700–704 (2013).

Highlight: This paper presents the development of the computational methodology to collapse large molecules into compact objects that can assemble in a realistic time frame for computational studies without losing the physics that underline their behavior.

Clarification of Contributions: *"*The authors gratefully acknowledge financial support from DOE Grant No. DE-FG02-12ER46843. This work was made possible by advanced computational resources deployed and maintained by Clemson Computing and Information Technology. This work was performed, in part, at the Center for Integrated Nanotechnology, a U.S. Department of Energy and Office of Basic Energy Sciences user facility. Sandia National Laboratories is a multi-program laboratory managed and operated by Sandia Corporation, a wholly owned subsidiary of Lockheed Martin Corporation, for the U.S. Department of Energy's National Nuclear Security Administration under Contract No. DE-AC04-94AL85000. "

Here Maskey and co-workers have developed a method to confine macromolecules such as the center-block of the polymer, in collaboration with Naresh Osti who has carried out dynamic studies in ionic polymers. The method developed by Maskey et al has been instrumental to our ability to confine the pentablock in solvents

3-Anupriya Agrawal, Dipak Aryal, Gary S. Grest and Dvora Perahia, "**Interfacial Response of Semifluorinated Multi-block Co-Polymers",** Handbook of Fluropolymer Science & Technology, edited by Dennis W. Smith, Jr., Scott T. Iacono, and Suresh Iyer (Wiley, Hoboken, NJ, 2014) Chapter 3, 2014.

Highlight: This work developed the computational methodology to explore surface properties such as surface tension where the surface consists of incompatible nano-domains.

Clarification of Contributions: "We thank NSF 206-2007419 and DOE DE-FG02-12ER46843 for partial support of this work. This work was performed, in part, at the Center for Integrated Nanotechnologies, a U.S. Department of Energy, and Office of Basic Energy Sciences user facility. Sandia National Laboratories is a multi-program laboratory managed and operated by Sandia Corporation, a wholly owned subsidiary of Lockheed Martin Corporation, for the U.S. Department of Energy's National Nuclear Security Administration under Contract No. DE-AC04-94AL85000. "

The current work, using DOE funding, developed computation pathways to analyze structured interfaces. Sample preparation is a lengthy process of equilibrating polymeric melts. The semifluorinated polymer films that **were made** under the NSF grant (therefore acknowledged). Using samples that were previously prepared allowed us to focus on deriving computational methods quantifying the interfacial composition and surface energies.

4- Lilin He, Chris J. Cornelius, and Dvora Perahia**. "Water dynamics within a highly rigid sulfonated polyphenylene,"** *European Polymer Journal* 56, 168-173 (2014).

Highlights: Based on our previous SANS data, this study identified different aqueous environments within ionic polymer using NMR and established time constants to set the conditions for inelastic neutron scattering (J. Chem. Phys. 2016). The study is carried out on a polyphenylele polymer since it is sufficiently rigid to suppress the polymer NMR signal and focus on the Polar Regions.

Clarification of Contributions: "The authors gratefully acknowledge financial support from DOE Grant No. DE-FG02-12ER46843." Chris J. Cornelius provided the materials.

5- Anupriya Agrawal, Dipak Aryal, Dvora Perahia,* Ting Ge, and Gary S. Grest, **"Coarse-graining atactic polystyrene and its analogues."** *Macromolecules* 47, 3210-3218 (2014).

Highlights: This paper present a first of its kind coarse grained model of polystyrene that is transferrable to its analogues and captures the stero chemistry of polystyrene.

Clarification of Contributions: "We gratefully acknowledge financial support from DOE Grant No. *DE-FG02-12ER46843* and NSF Grant No. DMR-1006805. This research was supported in part by the National Science Foundation under Grant No. NSF PHY11-25915. This research used resources at the National Energy Research Scientific Computing Center, which is supported by the Office of Science of the United States Department of Energy under Contract No. DE-AC02-05CH11231. This work was made possible by advanced computational resources deployed and maintained by Clemson Computing and Information Technology. This work was performed, in part, at the Center for Integrated Nanotechnology, a U.S. Department of Energy and Office of Basic Energy Sciences user facility. Sandia National Laboratories is a multi-program laboratory managed and operated by Sandia Corporation, a wholly owned subsidiary of Lockheed Martin Corporation, for the U.S. Department of Energy's National Nuclear Security Administration under Contract No. DE-AC04-94AL85000."

The Clemson team was supported under the current DOE funding. Ting Ge was funded by NSF through John Hopkins University and Gary S. Grest was funded through Sandia.

6- Ting Ge, Mark O. Robbins, Dvora Perahia, and Gary S. Grest **"Healing of polymer interfaces: Interfacial dynamics, entanglements, and strength,"** *Physical Review E* 90, 012602 (2014).

Highlights: Here we probed the strength of damaged interfaces and answered the challenge of how much do polymer chains have to cross the interface for the system to regain its bulk strength.

Clarification of Contributions: "This work was supported by the National Science Foundation under grants DMR-1006805, CMMI-0923018, and OCI-0963185. MOR acknowledges support from the Simons Foundation**.** D.P. and G.S.G. acknowledge support from Department of Energy Award No. DE-FG02-12ER46843. This research used resources at the National Energy Research Scientific Computing Center (NERSC), which is supported by the Office of Science of the United States Department of Energy under Contract No. DE-AC02-05CH11231. Research was carried out in part, at the Center for Integrated Nanotechnologies, a U.S. Department of Energy, Office of Basic Energy Sciences user facility. Sandia National Laboratories is a multi-program laboratory managed and operated by Sandia Corporation, a wholly owned subsidiary of Lockheed Martin Corporation, for the U.S. Department of Energy's National Nuclear Security Administration under contract DE-AC04-94AL85000.
The student, Ting Ge, was supported by M.O.R.'s NSF grant."

7- Aryal, Dipak, Thusitha Etampawala, Dvora Perahia,* and Gary S. Grest, **"Phase Behavior of a Single Structured Ionomer Chain in Solution,"** *Macromolecular Theory and Simulations* 23, 543-549 (2014).

Highlights: This study showed for the first time that the blocks of a single pentablock chain locally phase separate into distinct regions depending on the solvent. By varying the solvent and temperature, the local morphology of membranes formed from by solvent processing of these pentablocks can be varied depending on how readily the different blocks can associate

Clarification of Contributions: "The authors gratefully acknowledge financial support from DOE Grant No. DE-FG02-12ER46843. This research used resources at the National Energy Research Scientific Computing Center, which is supported by the Office of Science of the United States Department of Energy under Contract No. DE-AC02-05CH11231. This work was made possible by advanced computational resources deployed and maintained by Clemson Computing and Information Technology. This work was performed, in part, at the Center for

Integrated Nanotechnologies, a U.S. Department of Energy and Office of Basic Energy Sciences user facility. Sandia National Laboratories is a multi-program laboratory managed and operated by Sandia Corporation, a wholly owned subsidiary of Lockheed Martin Corporation, for the U.S. Department of Energy's National Nuclear Security Administration under Contract No. DE-AC04-94AL85000."

8- Thusitha N. Etampawala, Dipak Aryal, Naresh. C. Osti, Lilin He, William T. Heller, Carl L. Willis, Gary S. Grest and Dvora Perahia, "**Association of a multifunctional ionic block copolymer in a selective solvent,**" Journal of Chemical Physics 145, 184903 (2016).

Highlights: The structure of micelles formed by the pentablock was resolved by neutron scattering and further supported by molecular dynamics simulations. Details critical to the effects of ionic groups have been resolved for the first time.

Clarification of Contributions: "This work was supported by the US Department of Energy under the contract DE-FG02-12ER46843. The SANS measurements conducted using the EQ-SANS at ORNL's Spallation Neutron Source and GP-SANS at ORNL's High Flux Isotope Reactor was sponsored by the Scientific User Facilities Division, Office of Basic Energy Sciences, US Department of Energy. Travel to Oak Ridge National Laboratory to carry out this work was supported by a Travel Fellowship from the DOE-EPSCoR Grant to the University of Tennessee, DE-FG02-08ER46528. This work was performed, in part, at the Center for Integrated Nanotechnologies, a U.S. Department of Energy and Office of Basic Energy Sciences user facility. Sandia National Laboratories is a multi-program laboratory managed and operated by Sandia Corporation, a wholly owned subsidiary of Lockheed Martin Corporation, for the U.S. Department of Energy's National Nuclear Security Administration under Contract No. DE-AC04-94AL85000. Authors would also like to thank Dr. Karen Winey for helpful discussions."

9-Naresh C. Osti, Thusitha N. Etampawala, Umesh M. Shrestha, Madhusudan Tyagi, Souleymane O. Diallo, Eugene Mamontov, Christopher J. Cornelius, and Dvora Perahia, **"Water dynamics in rigid ionomer networks,"** *Journal of Chemical Physics* 145, 224901 (2016).

Highlights: Dynamics of water in a rigid ionomer was studied by neutron backscattering. We found that as expected the water molecules occupy two sites, bound and free. Surprisingly however a slow mode where water molecules reside in the hydrophobic region was observed.

Clarification of Contributions: "We gratefully acknowledge the support of U.S. Department of Energy under contract DE-FG02-12ER46843. Work at Oak Ridge National Laboratory is supported by the U.S. Department of Energy, Office of Basic Energy Sciences. Travel to Oak Ridge National Laboratory to carry out this

work was supported by a Travel Fellowship from the DOE-EPSCoR Grant to the University of Tennessee, DE-FG02-08ER46528. This work also utilized facilities supported in part by the National Science Foundation under Agreement No. DMR-0944772. We acknowledge the support of the National Institute of Standards and Technology, U.S. Department of Commerce, in providing the neutron research facilities used in this work." Beamline scientists involved are co-authors as customary in all of the PI work. Chris J. Cornelius provided the polymer.

10- Anupriya Agrawal, Dvora Perahia, and Gary S. Grest, **"Clustering effects in ionic polymers: Molecular dynamics simulations,"** *Physical Review E* 92, 022601 (2015).

Highlights: This study was able to resolve the molecular origin for the first time the effects of ionic clusters on the structure and dynamics of ionic polymers.

Clarification of contributions: "We gratefully acknowledge financial support from Grant No. DE-SC0007908. We acknowledge computational resources at the National Energy Research Scientific Computing Center, which is supported by the Office of Science of the United States Department of Energy, under Contract No. DE-AC02- 05CH11231 and Clemson Computing and Information Technology. This work was performed, in part, at the Center for Integrated Nanotechnology, a U.S. Department of Energy and Office of Basic Energy Sciences user facility. Sandia National Laboratories is a multiprogram laboratory managed and operated by Sandia Corporation, a wholly owned subsidiary of Lockheed Martin Corporation, for the U.S. Department of Energy's National Nuclear Security Administration under Contract No. DE-AC04-94AL85000"

11-Aryal, Dipak, Dvora Perahia, and Gary S. Grest, **"Solvent controlled ion association in structured copolymers: Molecular dynamics simulations in dilute solutions,"** *Journal of Chemical Physics* 143, 124905 (2015).

Highlights: This work demonstrate the ability of hydrophilic and hydrophobic solvents to control association of ionic co-polymers though controlling clustering.

This work is directly correlated with our neutron studies (Etampawala et al, J. Chem. Phys. 2016).

Clarification of Contributions: The authors gratefully acknowledge financial support from DOE under Grant No. DE-SC007908. This research used resources at the National Energy Research Scientific Computing Center, which is supported by the Office of Science of the United States Department of Energy under Contract No. DE-AC02-05CH11231. This work was made possible by advanced computational resources deployed and maintained by Clemson Computing and Information Technology. This work was performed, in part, at the Center for Integrated Nanotechnology, a U.S. Department of Energy and Office of Basic Energy Sciences user facility. Sandia National Laboratories is a multi-program laboratory managed and operated by Sandia Corporation, a wholly owned

subsidiary of Lockheed Martin Corporation, for the U.S. Department of Energy's National Nuclear Security

12-Agrawal, Anupriya, Dvora Perahia, and Gary S. Grest, "**Cluster Morphology-Polymer Dynamics Correlations in Sulfonated Polystyrene Melts**: **Computational Study.**" *Physical Review Letters* 116, 158001 (2016).

Highlights: The study attained a fundamental molecular understanding of the correlation of ionomer clusters structure and multiscale dynamics, resolving one standing challenge in ionic polymer physics.

Clarification of contributions: "We gratefully acknowledge financial support from DOE Grant No. DE-SC007908 at Clemson University. We acknowledge computational resources at the National Energy Research Scientific Computing Center, which is supported by the Office of Science of the U.S. Department of Energy, under Contract No. DE-AC02-05CH11231 and Clemson Computing and Information Technology. This work was performed, in part, at the Center for Integrated Nanotechnologies, a U.S. Department of Energy and Office of Basic Energy Sciences user facility. Sandia National Laboratories is a multiprogram laboratory managed and operated by Sandia Corporation, a wholly owned subsidiary of Lockheed Martin Corporation, for the U.S. Department of Energy's National Nuclear Security Administration under Contract No. DE-AC04-94AL85000."

13-K. Michael Salerno, Anupriya Agrawal, Dvora Perahia, and Gary S. Grest, **"Resolving Dynamic Properties of Polymers through Coarse-Grained Computational Studies."** *Physical Review Letters* 116, 058302 (2016).

Highlights: This work resolves the effects of the degree of coarse graining on the ability to capture the dynamics of polymers through computational studies.

Clarification of contributions: A full flagged collaboration between DP and GSG. "A. A. and D. P. acknowledge financial support from Grant No. DE-SC007908 and an allotment of time on the Clemson University Palmetto cluster. This research used resources at the National Energy Research Scientific Computing Center, which is supported by the Office of Science of the U.S. Department of Energy under Contract No. DE-AC02-05CH11231. This work was supported by the Sandia Laboratory Directed Research and Development Program. Research was carried out in part, at the Center for Integrated Nanotechnologies, a U.S. Department of Energy, Office of Basic Energy Sciences user facility. Sandia National Laboratories is a multiprogram laboratory managed and operated by Sandia Corporation, a wholly owned subsidiary of Lockheed Martin Corporation, for the U.S. Department of Energy's National Nuclear Security Administration under Contract No. DE-AC04-94AL85000."

14- K. Michael Salerno, Anupriya Agrawal, Brandon L. Peters, Dvora Perahia, and Gary S. Grest, **"Dynamics in entangled polyethylene melts,"** European Physics Journal: Special Topics 225, 1707–1722 (2016).

Highlights: This work resolves the effects of the degree of coarse graining on the ability to capture the structure and dynamics of polymers through computational studies.

Clarification of contributions: A full flagged collaboration between DP and GSG. "DP acknowledge financial support from Grant No. DE-SC007908 and an allotment of time on the Clemson University Palmetto cluster. This research used resources at the National Energy Research Scientific Computing Center, which is supported by the Office of Science of the U.S. Department of Energy under Contract DE-AC02-05CH11231. This work was supported by the Sandia Laboratory Directed Research and Development Program. Research was carried out in part, at the Center for Integrated Nanotechnologies, a U.S. Department of Energy, Office of Basic Energy Sciences user facility. Sandia National Laboratories is a multi-program laboratory managed and operated by Sandia Corporation, a wholly owned subsidiary of Lockheed Martin Corporation, for the U.S. Department of Energy's National Nuclear Security Administration under contract DE-AC04-94AL85000."

15-Dipak Aryal, Gary S. Grest, and Dvora Perahia, "**Soft Nanoparticles: Nano Ionic Networks of Associated Ionic Polymers,"** *Nanoscale* (2017) Published online, ***Back Cover*** Image.

Highlights: Detailed atomistic structure of a pentablock co-polymer micelle that consists of ionic block was attained. The study has used the methodology developed by Maskey et al. (publication 2) to enable the assembly of the pentablocks. These studies are complimentary to those recently published by our group using small angle Neutron scattering (J. Chem. Phys 2016)

Clarification of contributions: "The authors gratefully acknowledge financial support from DOE Grant No. DE-FG02-12ER46843. This research used resources at the National Energy Research Scientific Computing Center, which is supported by the Office of Science of the United States Department of Energy under Contract No. DE-AC02-05CH11231. This work was made possible by advanced computational resources deployed and maintained by Clemson Computing and Information Technology. This work was performed, in part, at the Center for Integrated Nanotechnologies, a U.S. Department of Energy and Office of Basic Energy Sciences user facility. Sandia National Laboratories is a multi-program laboratory managed and operated by Sandia Corporation, a wholly owned subsidiary of Lockheed Martin Corporation, for the U.S. Department of Energy's National Nuclear Security Administration under Contract No. DE-AC04-94AL85000."

II B-In Review

1-Thusitha Etampawala, Lilin He, Naresh C. Osti, Umesh Shrestha, Dilru Ratnaweera, Jaroslaw Majewski, Christopher J. Cornelius, and Dvora Perahia, "**In Situ Neutron Reflectivity Study of Alcohols at the Interface with Thin Ionomer Films,"** Journal of *Chemical Physics. (awaiting neutron beam time to clarify questions)*

Highlights: The diffusion of alcohols into structured ionomer depends is strongly impacted by the nature of the interface and the length of the alcohol length. Surprisingly though, the dependence is not linear.

Clarification of Contributions: "This work was supported by the U.S. Department of Energy under contract DE-SC007908. This work has benefited from the use of SPEAR at the Lujan Center at Los Alamos Neutron Science Center, funded by the DOE Office of Basic Energy Sciences. Los Alamos National Laboratory is operated by Los Alamos National Security LLC under DOE Contract DE-AC52-06NA25396."

III PRESENTATIONS (*With Published Abstracts*)

Aryal, Dipak; Perahia, Dvora; Grest, Gary S., "Molecular Dynamics Simulations of a Single Chain Pentablock Ionomer in Dilute Solutions." American Physical Society, APS March Meeting 2013, March 18-22, 2013, abstract #A31.009

Etampawala, Thusitha; Pangpaiboon, Nampueng; Perahia, Dvora; Halbert, Candice; Bro wning, Jim; Traiphol, Nisanart; Traiphol, Rakchart, "Insight into Polymer De-wetting: A Neutron Reflectivity Study of Three-Arm Polystyrene Stars in Polystyrene Thin films," American Physical Society, APS March Meeting 2013, March 18-22, 2013, abstract #B34.010

Perahia, Dvora, "Where Scattering and Computations Meet: Structure and Dynamics of Ionic Co-Polymers**,"** APS March Meeting 2014, abstract #L14.002

Aryal, Dipak; Perahia, Dvora; Etampawala, Thusitha; Grest, Gary, "Association of Multi-Chain Pentablock Ionomers in Solutions: A Molecular Dynamics Simulation Study," APS March Meeting 2014, abstract #A21.011

Agrawal, Anupriya; Perahia, Dvora; Grest, Gary S., "Coarse graining of atactic polystyrene and its derivatives," APS March Meeting 2014, abstract #B19.003

Etampawala, Thusitha; Senanayake, Manjula; Osti, Naresh; He, Lilin; Heller, William; P erahia, Dvora, "Self-assembled Structures of a Multifunctional, Structured Block Copolymer in Solution; A SANS Study." APS March Meeting 2014, abstract #B21.010

Senenayake, Manjula; Etampawala, Thusitha; Wijesinghe, Sidath; Osti, Naresh; He,Lilin; Perahia, Dvora "Solvents effect on the structure of pentablock ionic polymers: A SANS study." APS March Meeting 2015, abstract #D43.005

Perahia, Dvora; Agrawal, Anupriya; Grest, Gary S., "Coarse graining of polystyrene sulfonate." APS March Meeting 2015, abstract #W42.001

Agrawal, Anupriya, Dvora Perahia, and Gary S. Grest. "Cluster Morphology in Lightly Sulfonated Polystyrene." APS March Meeting 2015, abstract # T45.00007

Grest, Gary; Salerno, K. Michael; Agrawal, Anupriya; Perahia, Dvora "Properties of Coarse-Grained Polymer Models: Statics, Dynamics, and Crystallinity." APS March Meeting 2015, abstract #W42.003

Wickramasinghe, Anuradhi; Perahia, Dvora "Surface Structure of Thin Films of Multifunctional Ionizable Copolymers." APS March Meeting 2016, abstract #S33.005

Senanayake, Manjula; Aryal, Dipak; Perahia, Dvora; Grest, Gary "Computational Insight into Solvent Effects on Conformation and Assembly of Structured Ionic Polymer," APS March Meeting 2016, abstract #F42.006

Aryal, Dipak; Perahia, Dvora; Grest, Gary S., " Effects of Structured Ionomer Interfaces on Water Diffusion: Molecular Dynamics Simulation Insight," APS March Meeting 2016, abstract #H33.002

PERSONNEL

Dr. Dvora Perahia (One month summer salary)

Dr. Gary S. Grest; Sandia National Laboratories (No support)

Dr. Anupriya Agrawal (full support postdoctoral research associate)

Dr. Thusitha Etampawala (Partial student support)

Dr. Naresh Osti (Partial student support)

Dr. Sabina Maskey (Partial student support)

Mr. Dipak Aryl (Partial student support)

Mr. Manjula Senanayake (Partial Student support)

Ms. Anuradhi Wickramasinge (Partial Student Support)

Mr. Kamkanam Mohott Supun (Partial Student support)

EXPENDITURES

Funds were spent on student salaries, postdoctoral fellow, one month PI salary, laboratory supplies and travel as outlined by the financial report provided by the institution.

APPENDIX

Molecular Dynamics Simulations of Polymer Welding: Strength from Interfacial Entanglements

Ting Ge,[1] Flint Pierce,[2,3] Dvora Perahia,[3] Gary S. Grest,[2] and Mark O. Robbins[1]

[1]*Department of Physics and Astronomy, Johns Hopkins University, Baltimore, Maryland 21218, USA*
[2]*Sandia National Laboratories, Albuquerque, New Mexico 87185, USA*
[3]*Department of Chemistry, Clemson University, Clemson, South Carolina 29634, USA*

(Received 20 November 2012; published 28 February 2013; corrected 6 March 2013)

Large-scale simulations of thermal welding of polymers are performed to investigate the rise of mechanical strength at the polymer-polymer interface with the welding time t_w. The welding process is at the core of integrating polymeric elements into devices as well as in the thermal induced healing of polymers, processes that require the development of interfacial strength equal to that of the bulk. Our simulations show that the interfacial strength saturates at the bulk shear strength long before polymers diffuse by their radius of gyration. Along with the strength increase, the dominant failure mode changes from chain pullout at the interface to chain scission as in the bulk. The formation of sufficient entanglements across the interface, which we track using a primitive path analysis, is required to arrest catastrophic chain pullout at the interface. The bulk response is not fully recovered until the density of entanglements at the interface reaches the bulk value. Moreover, the increase of interfacial strength before saturation is proportional to the number of interfacial entanglements between chains from opposite sides.

DOI: 10.1103/PhysRevLett.110.098301 PACS numbers: 82.35.Gh, 68.35.Fx, 81.20.Vj, 83.10.Mj

Thermal welding is a common means of joining polymeric elements [1,2]. Two polymer surfaces are brought into close contact above their glass transition temperature T_g and are allowed to interdiffuse for a welding time t_w. Polymer melt dynamics suggests that for homopolymer melts the properties of the weld should be indistinguishable from those of the bulk once the chains have diffused by about their radius of gyration R_g. In practice, however, welds reach the bulk strength at much shorter times [2]. A key question is what determines the rapid rise in interfacial strength and how it is related to mass uptake across the surface and polymer entanglement. Entanglements are topological constraints of polymers by other chains [3] that control their bulk viscoelastic and plastic responses.

Experiments have quantified the strength of welds by measuring the interfacial fracture toughness in tensile fracture and the peak shear strength of lap joints [4–6]. Both quantities grow as $t_w^{1/4}$ at short times and then saturate at their bulk values. Several different molecular mechanisms have been proposed to explain the scaling of strength with t_w. Some assume the strength is simply related to interpenetration depth [7–9] or the areal density of chain segments bridging the interface [10] or the contour length of bridging segments [11]. In many cases, these models are motivated by physical pictures of the development of entanglements at the interface, but chain friction may also be important [12].

It is difficult to distinguish between the proposed strengthening mechanisms with experiments. Entanglements are not directly observable, and experiments are usually restricted to the postanalysis of fracture surfaces [13] or bulk scattering [8], which does not isolate the response of the failing region. In contrast, computer simulations provide full spatial resolution throughout the failure process, allowing macroscopic stresses to be directly related to molecular structure and dynamics. Recently developed methods also enable the tracking of entanglements on a microscopic level [14–16].

In this Letter, we present results from large-scale molecular dynamics simulations of welding between surfaces of highly entangled homopolymers. The interfacial strength after a welding time t_w is determined by a simple shear test that mimics experiments [4–6]. As in the experiments, the interfacial strength rises linearly with $t_w^{1/4}$ before saturating at the bulk value well before the time t_d for the chains to diffuse a distance R_g. The dominant failure mechanism changes from chain pullout at small t_w to chain scission at large t_w and in the bulk. Evolution of entanglements during welding is tracked using a primitive path analysis algorithm [14,17]. The crossover to bulk response coincides with a rise in the entanglement density at the interface to the bulk density. Moreover, the areal density of entanglements between chains from opposing surfaces is linearly related to the interfacial strength at small t_w.

Our simulations employ a canonical bead-spring model [18] that captures the properties of linear homopolymers. Each polymer chain contains N spherical beads of mass m. All beads interact via the truncated, shifted Lennard-Jones (LJ) potential

$$U_{\mathrm{LJ}}(r) = 4u_0[(a/r)^{12} - (a/r)^6 - (a/r_c)^{12} + (a/r_c)^6], \quad (1)$$

where r_c is the cutoff radius and $U_{\mathrm{LJ}}(r) = 0$ for $r > r_c$. All quantities are expressed in terms of the molecular diameter a, the binding energy u_0, and the characteristic time $\tau = a(m/u_0)^{1/2}$.

For equilibration, beads along the chain were connected by an additional, unbreakable finitely extensible nonlinear elastic (FENE) potential

$$U_{\mathrm{FENE}}(r) = -\frac{1}{2}kR_0^2 \ln[1 - (r/R_0)^2], \quad (2)$$

with $R_0 = 1.5a$ and $k = 30u_0a^{-2}$. For mechanical tests, chain scission plays an essential role, and a simple quartic potential was used,

$$U_Q(r) = K(r - R_c)^2(r - R_c)(r - R_c - B) + U_0, \quad (3)$$

with $K = 2351u_0/k_B$, $B = -0.7425a$, $R_c = 1.5a$, and $U_0 = 92.74467u_0$. This potential gives the same equilibrium bond length as U_{FENE} and prevents chains from crossing each other so that entanglements can be studied. The bonds break at a force that is 100 times higher than that for breaking interchain bonds, consistent with experiments and previous simulations [19,20]. Previous work has shown that the entanglement length for this model is $N_e = 85 \pm 7$ and that the mechanical response for $N = 500$ is characteristic of highly entangled (large N) polymers [19,21–24].

The equations of motion were integrated using a velocity-Verlet algorithm with a time step $\delta t \leq 0.01\tau$. The temperature was held constant by a Langevin thermostat with a damping constant Γ [18]. A million τ will be abbreviated as $1M\tau$. All simulations were carried out using the LAMMPS parallel molecular dynamics code [25].

Two thin films were constructed following the standard methodology discussed by Auhl *et al.* [26]. Each film contains $M = 4800$ chains of length $N = 500$ beads or a total of 2.4 million beads. Periodic boundary conditions were applied along the x and y directions with dimensions $L_x = 700a$ and $L_y = 40a$. The thickness in the z direction was maintained at $L_z = 100a$ using two repulsive confining walls. Each film was well equilibrated at a temperature $T = 1.0u_0/k_B$ with $r_c = 2.5a$, $\Gamma = 0.1\tau^{-1}$, and pressure $P = 0$ maintained by expansion or contraction along the x direction. To form the welding interface at $z = 0$, the films were placed as close to contact as possible without overlap. The interdiffusion was along the z direction. During interdiffusion, volume was held fixed by repulsive walls perpendicular to the z direction.

After welding for a time t_w, the system was quenched rapidly below the glass temperature $T_g \approx 0.35u_0/k_B$. First, the cutoff radius was reduced to $r_c = 1.5a$ to decrease computational cost, reduce density changes, and facilitate comparison with past mechanical studies [19,21–24]. Then, the temperature was quenched at constant volume with a rate $\dot{T} = -10^{-3}u_0/(k_B\tau)$ to $T = 0.5u_0/k_B$, where $P = 0$. Subsequent quenching to $T = 0.2u_0/k_B$ was done at $\dot{T} = -2 \times 10^{-4}u_0/(k_B\tau)$ and $P = 0$. A Nose-Hoover barostat with time constant 50τ was applied to P_{xx} and P_{yy}. The repulsive walls were maintained at $z = \pm L_z$. We verified that our conclusions are not sensitive to the details of the quench protocol or geometry.

Shear was applied to the interface in a manner similar to a shear test of a lap joint [2]. Beads within $5a$ of the top and bottom were held rigid and displaced at constant velocity in opposite directions along the y axis. The average strain rate in the film $d\gamma/dt = 2 \times 10^{-4}\tau^{-1}$ was low enough that it did not affect the mode of failure, and stress had time to equilibrate across the system [27]. The shear stress σ was determined from the mean lateral force per unit area applied by the top and bottom walls. The temperature was maintained at $T = 0.2u_0/k_B$ with a Langevin thermostat ($\Gamma = 1\tau^{-1}$) acting only on the x component to avoid biasing the flow.

Stress-strain curves for polymer welds at different t_w are compared to the bulk response in Fig. 1(a). The bulk curve is typical of amorphous polymers. A narrow elastic region

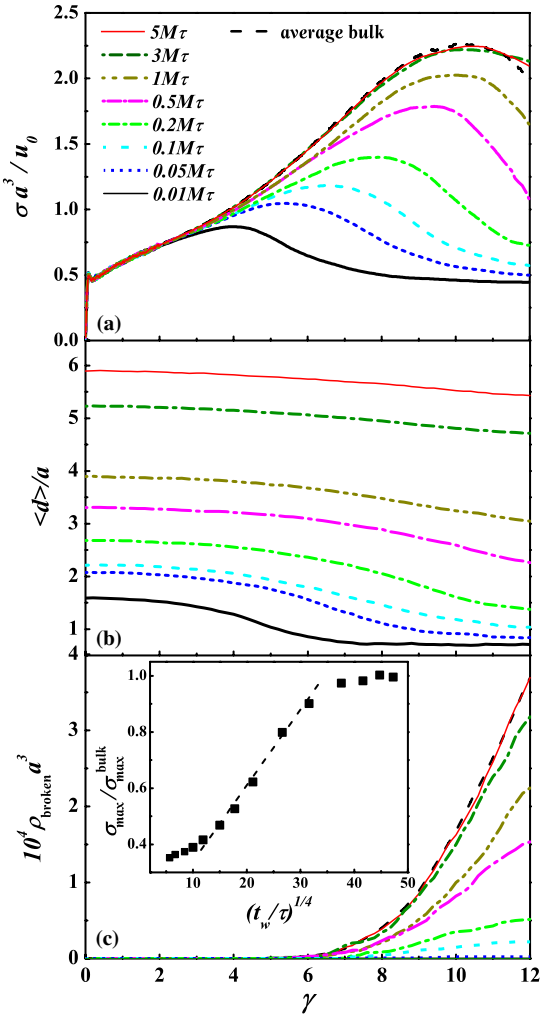

FIG. 1 (color online). (a) Shear stress σ versus shear strain γ for the indicated t_w. (b) Average interpenetration depth $\langle d \rangle$ versus strain. (c) Number density ρ_{broken} of broken bonds versus γ. The inset shows the maximum shear stress σ_{max} normalized by its average bulk value $\sigma_{\mathrm{max}}^{\mathrm{bulk}}$ versus $t_w^{1/4}$.

is followed by yield and strain hardening—a gradual increase in stress with strain. At sufficiently large strain, the material begins to fail. The shear stress reaches a maximum value $\sigma_{\max}^{\text{bulk}}$ and then drops.

Even for the shortest t_w, the stress-strain curve follows the bulk response up to $\gamma \sim 4$. As t_w increases, the stress follows the bulk curve to larger γ. For $t_w \geq 2M\tau$, the response is nearly indistinguishable from the bulk. In experiments, the strength of the weld is characterized by the maximum shear stress $\sigma_{\max}$ before failure and plotted against $t_w^{1/4}$ to test scaling predictions [2]. Our results, shown in the inset of Fig. 1(c), are very similar to experiments [2]. There is a constant strength from van der Waals (LJ) interactions at times too short for appreciable interdiffusion. The strength saturates to the bulk value as t_w increases past $1M\tau$ and is statistically indistinguishable from bulk behavior by about $3M\tau$. This is much shorter than the time for polymers to diffuse by their radius of gyration $t_d \gg 10M\tau$ [28]. At intermediate times, there is a linear rise in strength [dashed line, inset of Fig. 1(c)] that is consistent with $\sigma_{\max} \sim t_w^{1/4}$. Both simulations and experiments are limited to a factor of $\sim$3 change in stress that prevents a precise test of power law scaling. However, $t_w^{1/4}$ scaling is motivated by an assumption that strength is proportional to the interdiffusion distance. This is directly tested as described below.

Simulations allow the change in maximum stress to be correlated with changes in failure mechanism and molecular conformation. Strain leads to stretching and orientation of polymer chains that is directly related to strain hardening [23,29,30]. Starting near $\gamma \sim 4$, we see a noticeable tension along polymer backbones that grows rapidly with γ. This tension acts to pull back any chain segments that have diffused across the interface. One way to quantify chain pullout is to measure the evolution of the average interpenetration depth $\langle d \rangle$ of beads that have crossed the initial interface ($z = 0$) as a function of strain [Fig. 1(b)]. For $t_w < 0.1M\tau$, $\langle d \rangle$ begins to drop at the strain where the stress deviates from the bulk response and decreases most rapidly near $\sigma_{\max}$. The final interfacial width $\langle d \rangle$ is less than the size of a single bead and corresponds to complete chain pullout. At this point, the stress reaches a constant value that represents the friction between two separated films.

At larger t_w, chains cannot be pulled out from the opposing surface and the small ($\sim 0.5a$) decrease in $\langle d \rangle$ is consistent with conformational changes near chain ends in the bulk. The chains have diffused far enough that the tension required for chain pullout is high enough to break bonds along the backbone. Figure 1(c) shows the strain dependence of the number density ρ_{broken} of broken bonds averaged over the entire volume between moving layers. The curves for $t_w > 2M\tau$ are similar to the bulk. Bonds begin to break above $\gamma = 6$, and the highest rate of bond breaking is reached near $\gamma = 10$. This point coincides with the peak in shear stress that indicates mechanical failure. For $0.1M\tau < t_w < 2M\tau$, there is a crossover where the number of broken bonds rises rapidly and the amount of chain pullout measured by the drop in $\langle d \rangle$ decreases. At smaller t_w, bond breaking is localized near the initial interface. For $t_w > 2M\tau$, bonds break uniformly throughout the system, confirming that the interface has become as strong as the bulk. It is interesting to note that a similar transition from chain pullout to scission occurs with increasing chain length in previous simulations of craze formation [19,21,22]. Chain scission only occurs when chains are long enough to form entanglements (typically, $N > 2N_e$) that prevent chain pullout. By analogy, it is natural to expect that the transition to scission and bulk response occurs when chains have interdiffused enough to form entanglements at the interface.

Entanglements have proved elusive in experimental studies. However, the representation of entanglements as binary contacts between the primitive paths of polymer chains has provided many insights into the properties of polymer melts [14–16]. The primitive paths are obtained by fixing the chain ends and minimizing the chain length without allowing chain crossing. To limit excluded volume effects, the chain diameter is then decreased by a factor of 4 [17]. Contacts between the resulting primitive paths are counted to determine the number of topological constraints (TCs). We found that the ratio of the density of TCs, ρ_{TC}, to the bulk density, $\rho_{\text{TC}}^{\text{bulk}}$, was insensitive to the precise details of the procedure used to identify TCs. Past bulk studies show that ρ_{TC} is proportional to the entanglement density [14–17], and we refer to TCs and entanglements interchangeably below.

Figure 2(a) shows the normalized density of TCs as a function of height relative to the initial interface. At small t_w, the chains have not interdiffused enough to produce any entanglements at the interface, but there are two peaks near $z = \pm 10a$. These peaks reflect the fact that polymers near free surfaces are compressed perpendicular to the surface [31,32]. Chains in this pancakelike anisotropic conformation are subject to more TCs. As welding proceeds, diffusion increases the density of entanglements at the interface and reduces the peaks on either side. By $2.5M\tau$, the density has become nearly uniform across the system.

To correlate between $\sigma_{\max}$ and entanglements more quantitatively, we focus on the number of TCs between chains that are on opposite sides of the interface at $t_w = 0$. All of these are formed by interdiffusion, and it is natural that these interfacial entanglements should be most important in strengthening the interface by preventing chain pullout. Figure 2(b) shows the profiles of the normalized interfacial TC density ρ_{TC}^I. As the polymers diffuse, interfacial TCs spread outward from the interface and grow in number. The inset in Fig. 2(b) shows the correlation between the normalized weld strength $\sigma_{\max}/\sigma_{\max}^{\text{bulk}}$ and the areal density of interfacial TCs, N_{TC}^I/A. There is a linear

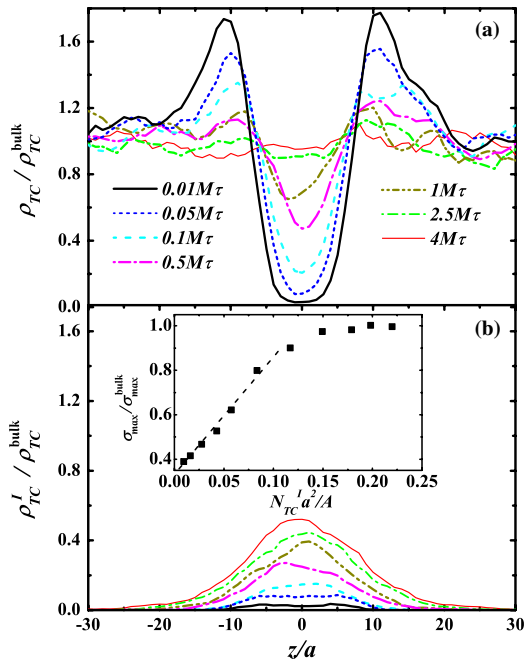

FIG. 2 (color online). Density profiles for (a) total and (b) interfacial TCs at the indicated t_w. The inset shows the reduced maximum shear stress versus the areal density of interfacial TCs N_{TC}^{I}/A. The error bars are comparable to the symbol size.

correlation between strength and interfacial entanglements at short times. At long times, the interfacial strength saturates while the number of interfacial entanglements continues to grow.

From the chain-packing model of entanglements [33–35], the number of interfacial entanglements N_{TC}^{I} scales with the volume spanned by chains that have diffused across the interface. This can be estimated as $2A\langle d\rangle$. Figure 3 confirms that there is a linear relation between N_{TC}^{I}/A and $\langle d\rangle$ over the entire range studied [36]. As noted above, welding models have generally assumed that $\sigma_{\max}$ rose linearly with $\langle d\rangle$ and then used reptation theory to argue that both scale as $t_w^{1/4}$. Subsequent work has shown

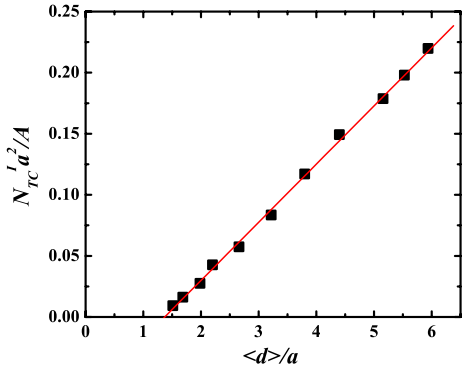

FIG. 3 (color online). The interfacial density of TCs N_{TC}^{I}/A versus the average interpenetration depth $\langle d\rangle$ and a linear fit.

that interfacial diffusion is more complicated because of the anisotropy that produces the peaks in entanglement density noted above and the prevalence of chain ends at the interface [2,28]. Indeed, recent simulations show that there is not a single simple scaling exponent over the range of times studied here [28]. Figures 2 and 3 show that, whatever the time dependence is, the fundamental factor determining strength is the entanglement density. One of the main differences between welding models is that some have assumed a simple proportionality between N_{TC}^{I}/A and $\langle d\rangle$ [2,7,10,12], while others assume a minimum interpenetration distance is needed for entanglements [9,37,38]. Figure 3 supports the latter interpretation, with a minimum distance $\sim 1.5a$ that is about one-third of the distance needed for saturation.

To summarize, we have demonstrated that the development of interfacial strength during welding is closely related to the formation of entanglements across the interface. The interface becomes mechanically indistinguishable from surrounding regions when the bulk entanglement density is recovered at the interface. There are then sufficient entanglements to prevent chain pullout at the interface, and the joint fails through the bulk mechanism of chain scission. Before the bulk strength is recovered, the interfacial strength rises linearly with the areal density of interfacial entanglements. This quantity is not accessible to experiments but is linearly related to the interdiffusion distance which has been measured.

These findings should help further development of theoretical descriptions of entanglement evolution across a polymer-polymer interface and constitutive molecular modeling of fracture in polymers. Of particular fundamental interest will be studies that vary the entanglement density by changing the entanglement length or making systems immiscible. An improved description of real experimental systems will require inclusion of chain polydispersity and the detailed process of crack propagation through lap shear joints [1,2]. Finally, studies at elevated temperatures could address the fracture of polymer melts where diffusion by the radius of gyration may be required to achieve bulk strength [39,40].

This work was supported in part by the National Science Foundation under Grants No. DMR-1006805, No. CMMI-0923018, No. OCI-0963185, and No. DMR-0907390. D. P. and G. S. G. acknowledge support from the U.S. Department of Energy Award No. DE-FG02-12ER46843. M. O. R. acknowledges support from the Simons Foundation. This research used resources at the National Energy Research Scientific Computing Center, which is supported by the Office of Science of the United States Department of Energy under Contract No. DE-AC02-05CH11231. Research was carried out in part at the Center for Integrated Nanotechnologies, a U.S. Department of Energy, Office of Basic Energy Sciences,

user facility. Sandia National Laboratories is a multiprogram laboratory managed and operated by Sandia Corporation, a wholly owned subsidiary of Lockheed Martin Corporation, for the U.S. Department of Energy's National Nuclear Security Administration under Contract No. DE-AC04-94AL85000.

[1] R. A. L. Jones and R. W. Richards, *Polymers at Surfaces and Interfaces* (Cambridge University Press, New York, 1999).
[2] R. P. Wool, *Polymer Interfaces: Structure and Strength* (Hanser, Munich, 1995).
[3] P. G. de Gennes, J. Chem. Phys. **55**, 572 (1971).
[4] K. Jud, H. H. Kausch, and J. G. Williams, J. Mater. Sci. **16**, 204 (1981).
[5] D. B. Kline and R. P. Wool, Polym. Eng. Sci. **28**, 52 (1988).
[6] R. Schnell, M. Stamm, and C. Creton, Macromolecules **31**, 2284 (1998).
[7] R. P. Wool and K. M. O'Connor, J. Appl. Phys. **52**, 5953 (1981).
[8] R. Schnell, M. Stamm, and C. Creton, Macromolecules **32**, 3420 (1999).
[9] H. R. Brown, Macromolecules **34**, 3720 (2001).
[10] S. Prager and M. Tirrell, J. Chem. Phys. **75**, 5194 (1981).
[11] P. G. de Gennes, C.R. Acad. Sci., Ser. 2 **308**, 1401 (1989).
[12] J. J. Benkoski, G. H. Fredrickson, and E. J. Kramer, J. Polym. Sci. B **40**, 2377 (2002).
[13] T. R. Russell, V. R. Deline, W. D. Dozier, G. P. Felcher, G. Agrawal, R. P. Wool, and J. W. Mays, Nature (London) **365**, 235 (1993).
[14] R. Everaers, S. K. Sukumaran, G. S. Grest, C. Svaneborg, A. Sivasubramanian, and K. Kremer, Science **303**, 823 (2004).
[15] M. Kröger, Comput. Phys. Commun. **168**, 209 (2005).
[16] C. Tzoumanekas and D. N. Theodorou, Macromolecules **39**, 4592 (2006).
[17] R. S. Hoy and G. S. Grest, Macromolecules **40**, 8389 (2007).
[18] K. Kremer and G. S. Grest, J. Chem. Phys. **92**, 5057 (1990).
[19] J. Rottler, S. Barsky, and M. O. Robbins, Phys. Rev. Lett. **89**, 148304 (2002).
[20] M. J. Stevens, Macromolecules **34**, 2710 (2001).
[21] J. Rottler and M. O. Robbins, Phys. Rev. Lett. **89**, 195501 (2002).
[22] J. Rottler and M. O. Robbins, Phys. Rev. E **68**, 011801 (2003).
[23] R. S. Hoy and M. O. Robbins, Phys. Rev. Lett. **99**, 117801 (2007).
[24] R. S. Hoy and M. O. Robbins, Phys. Rev. E **77**, 031801 (2008).
[25] S. Plimpton, J. Comp. Phys. **117**, 1 (1995).
[26] R. Auhl, R. Everaers, G. S. Grest, K. Kremer, and S. J. Plimpton, J. Chem. Phys. **119**, 12 718 (2003).
[27] J. Rottler and M. O. Robbins, Phys. Rev. E **68**, 011507 (2003).
[28] F. Pierce, D. Perahia, and G. S. Grest, Europhys. Lett. **95**, 46 001 (2011).
[29] T. Ge and M. O. Robbins, J. Polym. Sci. B **48**, 1473 (2010).
[30] K. Chen and K. S. Schweizer, Phys. Rev. Lett. **102**, 038301 (2009).
[31] D. N. Theodorou, Macromolecules **21**, 1400 (1988).
[32] A. Silberberg, J. Colloid Interface Sci. **125**, 14 (1988).
[33] Y.-H. Lin, Macromolecules **20**, 3080 (1987).
[34] L. J. Fetters, D. J. Lohse, D. Richter, T. A. Witten, and A. Zirkel, Macromolecules **27**, 4639 (1994).
[35] H. R. Brown and T. P. Russell, Macromolecules **29**, 798 (1996).
[36] To reduce the effects due to capillary waves at the interface, the width was measured from the local midplane, where the densities for beads from opposite sides are equal, rather than simply from $z = 0$.
[37] D. Adolf, M. Tirrell, and S. Prager, J. Polym. Sci., Polym. Phys. Ed. **23**, 413 (1985).
[38] A. G. Mikos and N. A. Peppas, J. Chem. Phys. **88**, 1337 (1988).
[39] R. Schach, Y. Tran, A. Menelle, and C. Creton, Macromolecules **40**, 6325 (2007).
[40] R. Schach and C. Creton, J. Rheol. **52**, 749 (2008).

ACS Macro Letters

Letter

pubs.acs.org/macroletters

Internal Correlations and Stability of Polydots, Soft Conjugated Polymeric Nanoparticles

Sabina Maskey,[†] Naresh C. Osti,[†] Dvora Perahia,*[,†] and Gary S. Grest[‡]

[†]Department of Chemistry, Clemson University, Clemson, South Carolina 29634, United States

[‡]Sandia National Laboratories, Albuquerque, New Mexico 87185, United States

Supporting Information

ABSTRACT: Conjugated polymers collapsed into long-lived highly luminescent nanoparticles, or polydots, have opened a new paradigm of tunable organic particles with an immense potential enhancing intracellular imaging and drug delivery. Albeit the chains are not in their equilibrium conformation and are not confined by cross-links, they remain stable over astounding long times. Using fully atomistic molecular dynamics simulations with an innovative method to controllably collapse an inherently rigid polymer, we determined for the first time the internal structure and stability of polydots made of dialkyl-*para*-phenylene ethynylene, immersed in water, a biological relevant medium. In contrast to natural aggregates, the aromatic rings within the polydots are uncorrelated, with little to no water in its interior. This lack of correlation explains the differences of luminescence characteristics between spontaneously aggregated conjugated polymers and polydots. Resolving the conformation and stability of these particles will enable transforming an idea to a new effective tool.

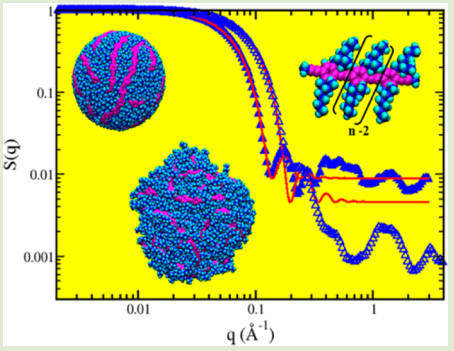

Conjugated polymers collapsed into long-lived, nanometer-size, globular conformations form a new class of light-emitting and absorbing soft particles. Their luminescence characteristics differ significantly from those of spontaneously aggregated conjugated polymers, pointing to a new conformation of the rigid polymers in confined geometry.[1] The chemistry and the softness of these nanoparticles (NPs) present a new tunable manifold that will augment the use of organic NPs at interfaces with biological membranes, as sensors, as imaging markers, and as targeted-drug delivery tools.[1−5] These particles consist of a multitude of chromophores confined into small dimensions, often on the same order of magnitude as the size of biological membranes. They are luminescent, and their surface can be modified to either tether them to an interface or graft functionalities that allow their insertion into living organisms. Packing a large number of chromophores into a small particle while retaining the ability of the molecule to absorb and emit light results in a unique hybrid that combines the advantages of organic dyes and the high brilliance characteristics of inorganic NPs and quantum dots. Therefore, the polydots open a new paradigm, where a single molecule-particle can be detected. Here we probe the internal conformation and the stability of one model polydot which is a critical first step to design soft organic NPs with defined properties, using newly designed computational tools. Beyond the insight into the structure and stability of polydots, the study provides new insight into the behavior of confined polymers.

The majority of conjugated polymers are relatively rigid, and their collapsed state is far from the equilibrium conformation.[6,7] These macromolecules are often forced into the nano-dimension by imposing constraints on the polymer backbone, either cross-linking or physically trapping the chains into a confined space. The most common approach to achieve long-lasting nanoconfigurations is to cross-link the polymers, where the resulting dimensions depend on the molecular weight of the polymer, its smallest rigid segment, and the number of cross-links.[8,9] A new fascinating pathway to form highly luminescent NPs is to confine polymers to a NP without cross-linking.[10] These particles are of particular interest since rearrangements of the chromophores can take place. The conformational freedom of the polymer chains leads to a new class of tunable particles. Their unique photophysics[3,11] is often determined by the conformation of the polymer backbone.

Here we probe the interactions that underlie the formation and internal structure of these long-lived soft NPs formed by physical confinement of the macromolecules using atomistic molecular dynamics (MD) simulations. Computational studies are among the very few methodologies that can directly probe the conformation of the polymer chains and derive the internal correlations *within* a soft NP. The highly congruent experimental and computational structure factors of the shape of the polydot serves as a bridge between macroscopically measured properties and internal structure and correlations within the polydot obtained from computational studies.

Experimentally, these soft NPs are formed by dissolving an aliquot of polymer in a good solvent, below the critical micellar

Received: May 6, 2013
Accepted: July 12, 2013
Published: July 23, 2013

   dx.doi.org/10.1021/mz400225d | *ACS Macro Lett.* 2013, 2, 700−704

concentration.[3,12] The solutions are then dripped into a poor solvent such as water, while vigorously mixed via sonication, forming polymer-containing nanometer size droplets dispersed in the poor solvent.[3,10,12] As the good solvent evaporates, the polymers collapse into NPs that remain suspended in the poor solvent.

The process results in long-lived, luminescent NPs that consist of polymers collapsed into dimensions that are smaller than their inherent rigid segment.[3,10,12] These polymeric NPs, often referred to as polydots, not only remain fluorescent but can be inserted into living organisms.[13−15] The fluorescence characteristics of polydots indicate that the structure of the confined polymer molecules differs from that in melts or in spontaneously formed aggregates. The soft nature of the polydots and their inherently organic exterior enhance the ability to tailor specific chemistries at the polymer interface needed for different functions. Resolving the internal structure and dynamics of these confined polymers is fundamental to the design of polydots with well-defined photophysics.

The current study uses MD simulations to probe directly for the first time the internal structure of long-lived NPs formed by dialkyl-*para*-phenylene ethynylene (PPE). PPEs are hardly soluble in water and assume extended conformation even in good solvents such as toluene and tetrahydrfurane. Experimentally, PPE polydots remain in aqueous solutions without cross-linking for extended periods of time. PPEs are uniquely tunable polymers since the degree of coplanarization of the backbone aromatic rings determines the degree of conjugation and therefore the absorption and emission characteristics. The backbone becomes fully conjugated when all aromatic rings lie in the same plane. The side chains grafted on the backbone impact the solubility and assembly of the PPEs and, indirectly, the electronic structure of the polymer. Overall, the light-emitting and absorption characteristics of PPEs strongly depend on the chemical structure of the backbone and the side chains that together determine the conformation of the polymer.[7,16]

Using a process close to the experimental preparation method, we were successful in computationally forming polydots that consist of PPEs. The NPs were formed by compressing an isolated chain in an implicit poor solvent. The molecules were enclosed in a large spherical cavity, the radius of which was slowly reduced over 1 ns. The cavity wall interacted with the PPE chain via a harmonic potential.[17] The encapsulation within a spherical cavity provides a parallel to the experimental process in which the polymers are trapped in droplets of good solvents that are immersed in a poor solvent. As the good solvent evaporates experimentally the polymer cage becomes smaller, mimicked here by decreasing the size of the confining cavity. PPE with a polymerization number of 240 with disubstituted by ethyl hexyl side chains, as prepared and in its early stages of compression, is shown in Figure 1a and b. The polymer molecules were initially compressed to dimensions that result in internal density comparable to that of the polymer melt. This criterion resulted in a final diameter of 5.0 nm for a diethyl-hexyl PPE and 2.0 nm for a PPE without side chains. Once the melt density reached bulk value, the spherical cavity was removed, equivalent to the experimental stage where all of the good solvent evaporated, and the polydots were placed in implicit solvents to equilibrate.

A snapshot of the diethyl-hexyl PPE polydot as prepared is shown in Figure 1c. Following the release of the cavity, the polydot assumed a fully spherical shape with a smooth interface

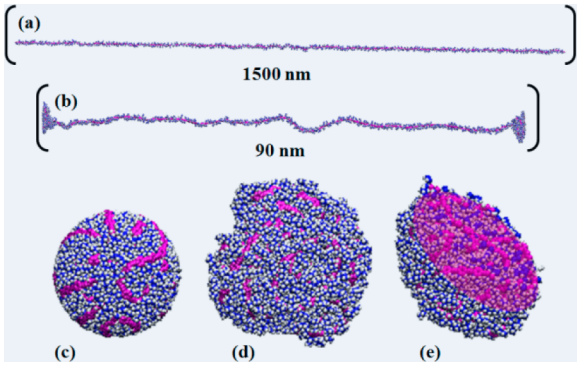

Figure 1. Snapshots of diethylhexyl PPE of polymerization number 240, for (a) t = 0 ns, (b) t = 0.5 ns, and (c) t = 1 ns in an implicit poor solvent. The final diameter of the indenter is 5.0 nm. (d) Polydot in water after 25 ns and (e) a slice through the center of the polydot presented in d. For clarity, dark blue corresponds to carbon atoms on side chains; hydrogen atoms on side chains are white, and the backbone is represented by magenta. Separate visualizations of the backbone and the side chains in water and implicit solvents are given in the Supporting Information, Figure S1.

dominated by the side chains. Following a short equilibration in an implicit poor solvent the collapsed polydots were relaxed in solvents of varying quality, including water and toluene, as well as in good and poor implicit solvents.

The stability of the polydot strongly depends on the solvent quality, as one would expect for a collapsed polymer that is not cross-linked. When placed in water, the polydots slightly changed their conformation, as shown in Figure 1d, but remained in their nanoconfiguration for up to 25 ns in water and 100 ns in explicit a poor solvent. Water is a poor solvent for PPEs; however, the small number of molecules that do dissolve remain extended or aggregated, rather than collapsed. This stability over extended periods is consistent with experimental observations where the polydots remain stable over months in their collapsed state, dispersed in water. In comparison with neutron spin echo results, these computational intervals are sufficient for most local dynamics to take place. A first insight into the structure of the polydot can be obtained by slicing it through its center, as shown in Figure 1e. The center of the polydot is dense, and no obvious spatial correlations were observed and no water molecules.

In contrast to the conformation of the polydot in water, in toluene, the chain rapidly unfolded. Snapshots of diethyl hexyl PPE polydots in toluene at times ranging from 5 to 100 ns after the indenter was removed are presented in Figure 2. To probe a longer time scale, implicit poor and good solvents are used.[6] We found that the results for an implicit poor solvent are

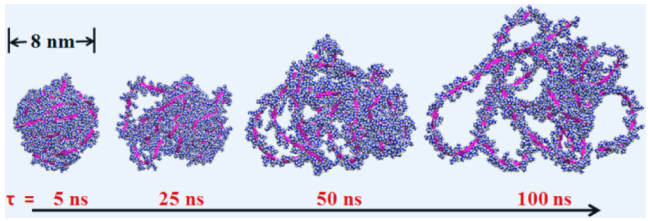

Figure 2. Time sequence for polydots that consist of diethyl ethyl PPE in toluene. Carbon atoms on side chain are marked in dark blue, hydrogen on side chain in white, and backbone is represented by magenta.

dx.doi.org/10.1021/mz400225d | *ACS Macro Lett.* 2013, 2, 700−704

similar to those obtained for water. The results for polydots in an implicit good solvent are similar to those obtained for toluene, while reflecting the fact that the backbone and the side chains interacted equally with the solvent, whereas toluene is a better solvent for the backbone than for the side chains of the PPE. The implicit solvents will be referred in the rest of the paper as poor and good.

The dimensions of the polymers in toluene are smaller than the dimensions of those in a good implicit solvent for the same unraveling time. These differences present a remarkable demonstration of the significance of specific interactions of the segments of polymers with solvents. In an implicit good solvent, the interactions of the backbone and the side chains with the solvent are equally good, whereas the interactions of toluene with the backbone and side chains are different. In contrast, the dimensions of the polydots in both water, which is a poor solvent for both the backbone and the side chains, and in an implicit poor solvent, are similar.

The radius of gyration of the polymer was measured as a function of time after the polydots were immersed in the four solvents. Figure 3 presents R_g as a function of time for PPE

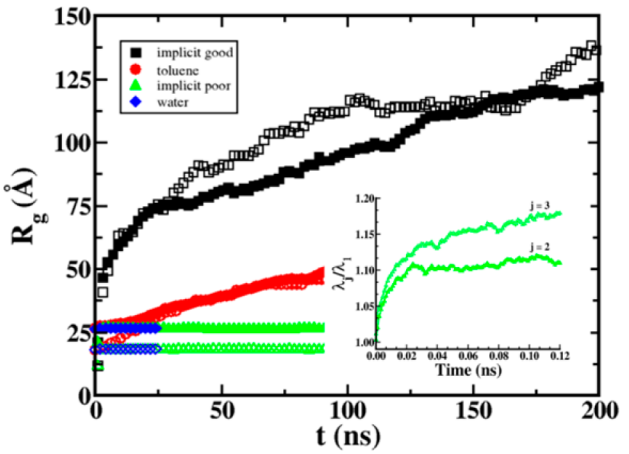

Figure 3. Radius of gyration R_g of the PPE molecule as a function of time in water and toluene, poor and good solvents for substituted PPE (solid symbols) and without side chains (open symbols). The inset presents the ratios for the moment of inertia for an implicit poor solvent for first 0.12 ns.

polydots with and without side chains. After a very small expansion of the polydot in the first few picoseconds after the indenter was removed, the polydots remained collapsed for the length of the simulation in both water and the implicit poor solvent.

Surprisingly, the presence of alkyl side chains did not enhance the stability of the polydot in poor solvents. This observation suggests that the stability is achieved through arrest of the backbone motion at temperatures below the glass transition of the polymer rather than interdigitation of the side chains. In the two good solvents, however, R_g of the polydot continued to increase over the course of the simulation as the chain unraveled. After an initial faster increase in R_g in the good solvent compared to toluene, the rate of increase in R_g was comparable for the two solvents for late times. From these results, it is clear that the conformational stability of the polydot depends strongly on the solvent−polymer interactions.

In contrast to having little or no effect on the stability of the NPs in poor solvents, the lack of side chains enhanced the rate of unraveling of the polymer in good solvent, as shown in Figure 3. Though the polydots were locked into place by the backbone in the poor solvents, their packing was impacted by the side chains. As the backbone becomes dynamic, the side chains affected the conformational dynamics of the polymer.

The evolution of the shape of the polydots was probed by calculating the three eigenvalues of the moment of inertia tensor λ_1, λ_2, and λ_3. The ratios of the two largest eigenvalues to the smallest one, immediately following the release of the constraints for implicit poor solvent, are shown in the inset of Figure 3. The ratio of the eigenvalues which is one at the onset as expected for a fully spherical particle[18] increases with time for the first 20 ns and then fluctuates around $\lambda_3/\lambda_1 = 1.2$ and $\lambda_3/\lambda = 1.1$. For PPEs with no side chains, $\lambda_3/\lambda_1 = 1.6$ and $\lambda_2/\lambda_1 = 1.2$. These eigenvalues show that the PPEs with side chains are significantly more spherical than those made of bare PPEs. This is the first observation that the side chains impact the packing of the backbone. The ability of the polymer to rearrange following the removal of the constraint shows that the preparation method does not lock the polymer conformation.

The radial density of the polydots from their center of mass is shown in Figure 4 in water and in a poor solvent. The density

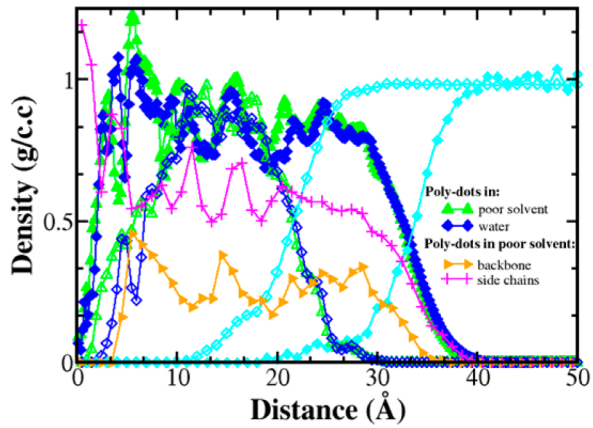

Figure 4. Radial mass density of the polymer and water within polydots. Zero corresponds to the center of the particle. The solid symbols correspond to substituted PPEs and open symbols to PPEs without side chains. The PPE in water is represented by diamonds and in poor solvent by circles. The density profiles of water are marked by triangles.

of the polydot with side chains is uniform, within the noise of the measurement, while the density for the polydot without side chains is lower near the center. Little or no water molecules are found inside the polydot in both cases; however at the boundary between the outer surfaces of the polydots a higher density of water is observed over a range of approximately 1 nm. The access is in part due to the fact that the polydots are not perfectly spherical, and their external interface is rough, particularly those without side chains. Comparing the density of the side chains and the backbone separately, the side chains dominate the surface of the polydots. Undulations observed may correspond to the dimensions of a tube that encapsulate the backbone and side chains.

An important aspect of the functionality of polydots for light absorption and emission is the correlation between the aromatic rings. One measure of the correlation of the aromatic rings within the PPE backbone was obtained using a first-order

dx.doi.org/10.1021/mz400225d | ACS Macro Lett. 2013, 2, 700−704

orientation order parameter, given by $P_\theta = 1/2\ \langle 3(\cos^2\theta) - 1\rangle$, where P_θ corresponds to the average alignment of aromatic rings with a particular spatial direction, and θ is the measure of deviation perpendicular to the interface for two aromatic rings which are separated along the backbone by a degree of polymerization Δn. P_θ has a range of $[-1/2, 1]$.[19] Results for P_θ for polydots with and without side chains in water are shown in Figure 5. In agreement with our previous results for extended

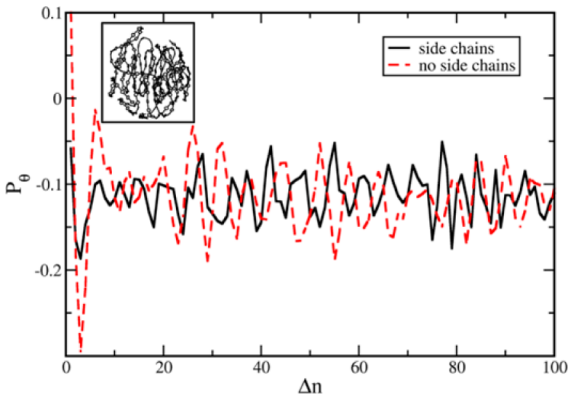

Figure 5. Order parameter P_θ as a function of the separation of phenyl rings Δn in the aromatic plane for polydots substituted (solid black line) and without (dashed red line) side chains in water. Insert shows the snapshot of the polydot with side chains in which only the backbone carbon atoms are shown and side chains and hydrogen atoms are removed for clarity. Data are averaged over 200 configurations.

PPE chains, no correlations were observed between the orientations of the aromatic rings beyond the error in the estimate of P_θ, except for the nearest neighbor ring, which have a tendency to align perpendicularly. This lack of correlation between the aromatic rings accounts for their light emission and absorption characteristics.

The calculations of the correlations within the polydots have provided the first insight into their luminescence behavior. In order to bridge between structural experimental studies and computational ones we calculated the structure factor $S(q)$, where q is the momentum transfer vector. $S(q)$ is the most accurate experimental measure of the structure of polydots. The analysis of the experimental scattering data is often model-dependent and requires further support. The scattering factor of the polydots was calculated using: $S(q) = |\sum_i b_i e^{iqr_i}|^2$ where b_i and r_i are the scattering length and position vector of atom i, respectively.[20] The results for the calculated $S(q)$ of the polydots in water are shown in Figure 6. These simulation results capture the shape of the NPs in the low q region together with internal structural features at high q.

The calculated $S(q)$ was modeled with a typical sphere scattering convoluted with a Gaussian to describe a gradual drop-off in the scattering length density.[21] The results are shown in Figure 6. This fitting resulted in a radius of gyration of 25.1 Å for the PPE with side chains and 17.6 Å without side chains. These compare to the values of $\langle R_g^2\rangle^{1/2}$ = 26.8 Å for PPE with side chains and 18.2 Å without side chains determined directly. The results obtained by simulations are similar to those obtained separately (not shown) by neuron scattering. This multiple length scale insight into the structure of the polydot is unique to computational studies and cannot be captured experimentally.

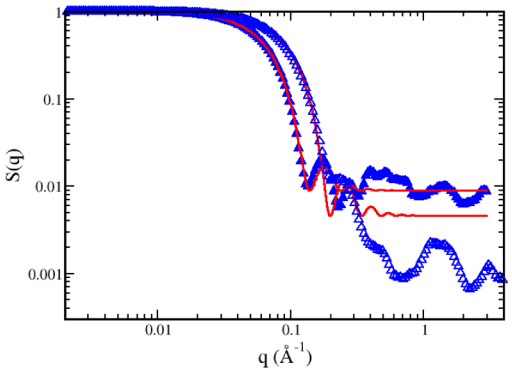

Figure 6. $S(q)$ as the function of q for polydots substituted (solid triangles) and without (open triangles) side chains in water. The best fit to a fuzzy spherical form factor[21] is shown by solid lines.

In conclusion, this study introduces the first insight into the structure of a new type of luminescent particles that consist of conjugated polymers collapsed into the nanodimension, as obtained from MD simulations. The simulations conceptually mimic the experimental caging of the polymer within boundaries of a droplet to force a collapsed geometry. A spherical smooth NP with the alkyl chain dominating the surface of their interface was formed. The NPs were placed in four different solvents, and their structure was followed as a function of time. In water and poor solvent, the polydots remained predominantly spherical and compact, while their interface became significantly rough. In toluene as well as in a good solvent, the polymer unraveled as a function of time. The alkyl side chains affected the symmetry of the NP in water, where the alkyl-substituted polymer forms a more spherical NP, but no effect was observed for the stability of the polydot. This suggests that the frozen conformation of the polymer below the glass transition temperature is the prime factor that retains the stability of the polydots in poor solvents. No internal correlations were observed between the aromatic rings on the polymer within the polydot, consistent with the experimental luminescence of PPEs. This study has opened the way to explore internal structures of soft nanoparticles that in turn will impact the design of new NPs with well-defined luminescent characteristics.

■ ASSOCIATED CONTENT

Ⓢ Supporting Information

Model and methodology details. This material is available free of charge via the Internet at http://pubs.acs.org.

■ AUTHOR INFORMATION

Corresponding Author

*E-mail: dperahi@clemson.edu.

Notes

The authors declare no competing financial interest.

■ ACKNOWLEDGMENTS

The authors gratefully acknowledge financial support from DOE Grant No. DE-FG02-12ER46843. This work was made possible by advanced computational resources deployed and maintained by Clemson Computing and Information Technology. This work was performed, in part, at the Center for Integrated Nanotechnology, a U.S. Department of Energy and Office of Basic Energy Sciences user facility. Sandia National

Laboratories is a multi-program laboratory managed and operated by Sandia Corporation, a wholly owned subsidiary of Lockheed Martin Corporation, for the U.S. Department of Energy's National Nuclear Security Administration under Contract No. DE-AC04-94AL85000. We thank S. J. Plimpton, F. Pierce, and J. McNeill for helpful discussions.

REFERENCES

(1) Tuncel, D.; Demir, H. V. *Nanoscale* **2010**, *2*, 484−494.
(2) Pecher, S.; Mecking, S. *Chem. Rev.* **2010**, *110*, 6260−6279.
(3) Wu, C.; Chiu, D. T. *Angew. Chem., Int. Ed.* **2013**, *52*, 3086−3109.
(4) Dorresteijn, R.; Haschick, R.; Klapper, M.; Müllen, K. *Macromol. Chem. Phys.* **2012**, *213*, 1996−2002.
(5) Cordovilla, C.; Swager, T. M. *J. Am. Chem. Soc.* **2012**, *134*, 6932−6935.
(6) Maskey, S.; Pierce, F.; Perahia, D.; Grest, G. S. *J. Chem. Phys.* **2011**, *134*, 244906.
(7) Perahia, D.; Traiphol, R.; Bunz, U. H. F. *Macromolecules* **2001**, *34*, 151−155.
(8) Beck, J. B.; Killops, K. L.; Kang, T.; Sivanandan, K.; Bayles, A.; Mackay, M. E.; Wooley, K. L.; Hawker, C. J. *Macromolecules* **2009**, *42*, 5629−5635.
(9) Liu, J. W.; Mackay, M. E.; Duxbury, P. M. *Europhys. Lett.* **2008**, *84*, 46001.
(10) Szymanski, C.; Wu, C. F.; Hooper, J.; Salazar, M. A.; Perdomo, A.; Dukes, A.; McNeill, J. *J. Chem. Phys. B* **2005**, *109*, 8543−8546.
(11) Yu, J.; Wu, C.; Tian, Z.; McNeill, J. *Nano Lett.* **2012**, *12*, 1300−1306.
(12) Wu, C.; Szymanski, C.; McNeill, J. *Langmuir* **2006**, *22*, 2956−2960.
(13) Wu, C. F.; Bull, B.; Szymanski, C.; Christensen, K.; McNeill, J. *ACS Nano* **2008**, *2*, 2415−2423.
(14) Li, K.; Liu, B. *J. Mater. Chem.* **2012**, *22*, 1257−1264.
(15) Howes, P.; Green, M.; Levitt, J.; Suhling, K.; Hughes, M. *J. Am. Chem. Soc.* **2010**, *132*, 3989−3996.
(16) Halkyard, C. E.; Rampey, M. E.; Kloppenburg, L.; Studer-Martinez, S. L.; Bunz, U. H. F. *Macromolecules* **1998**, *31*, 8655−8659.
(17) Plimpton, S. *J. Comp. Phys.* **1995**, *117*, 1−19.
(18) Theodorou, D.; Suter, U. W. *Macromolecules* **1985**, *18*, 1206−1214.
(19) Hariharan, A.; Harris, H. J. *J. Chem. Phys.* **1994**, *101*, 4156−4165.
(20) Sorensen, C. M. *Aerosol Sci. Technol.* **2001**, *35*, 648−687.
(21) Stieger, M.; Richtering, W.; Pedersen, J. S.; Lindner, P. *J. Chem. Phys.* **2004**, *120*, 6197.

Anupriya Agrawal, Dipak Aryal, Gary S. Grest and Dvora Perahia, "**Interfacial Response of Semifluorinated Multi-block Co-Polymers",** Handbook of Fluropolymer Science & Technology, edited by Dennis W. Smith, Jr., Scott T. Iacono, and Suresh Iyer (Wiley, Hoboken, NJ, 2014) Chapter 3, 2014.

DOI: 10.1002/9781118850220.ch3

Summary

This chapter presents a new insight into the interfacial behavior of semifluorinated polymers and its origin as derived from molecular dynamics simulations of a model polymer that consists of semifluorinated multi-blocks of alternating protonated and fluorinated linear carbon chains of varying segment length while the total number of monomers remains constant. It revealed for the first time the effects of topology of the polymers and rigidity of the blocks on the interfacial characteristics of semifluorinated polymers. Examples of films formed by polymers with an identical number of carbons, whose topology is varied by varying the dimension of fluorinated and protonated segments, are shown in the chapter. The chapter probes a model system using atomistic molecular dynamics simulations. The interfacial characteristics of semifluorinated polymers are impacted not only by the degree of fluorination but also by the distribution of the fluorine along the polymer backbone.

Keywords:

- fluorination;
- interfacial response;
- multi-block copolymers;
- semifluorinated multi-block copolymers;
- simulation model

European Polymer Journal 56 (2014) 168–173

Contents lists available at ScienceDirect

European Polymer Journal

journal homepage: www.elsevier.com/locate/europolj

Water dynamics within a highly rigid sulfonated polyphenylene

Lliin He [a,c], Chris J. Cornelius [b,1], Dvora Perahia [c,*]

[a] Biology and Soft Matter Division, Neutron Scattering Directorate, Oak Ridge National Laboratory, Oak Ridge, TN 37831, United States
[b] Department of Chemical and Biomolecular Engineering, University of Nebraska, Lincoln, NE 68588, United States
[c] Department of Chemistry, Clemson University, Clemson, SC 29634, United States

ARTICLE INFO

Article history:
Received 4 December 2013
Received in revised form 27 March 2014
Accepted 31 March 2014
Available online 21 April 2014

Keywords:
Water molecules
Polyphenylene ionomers
Pulse field gradient (PFG) NMR
FTIR

ABSTRACT

Complex water molecule interactions within the confined environments of a sulfonated polyphenylene (sPP) ionomer were studied using ^{1}H nuclear magnetic resonance (NMR), and Fourier transform infrared (FTIR) spectroscopy. Multiple water environments were observed due to variations in hydrophilicity created by its structure, and chemical composition. Confined water properties are strongly dependent upon water content, degree of ionization, and temperature. Increasing the degree of sulfonation (DS) results in the creation of more water states and sites. The chemical shifts of water depend upon its environment with a smaller dependence on temperature. Confined water relaxation time T_1 is than significantly lower bulk water and increases with temperature. Pulse field gradient (PFG) NMR studies reveals that water self-diffusion coefficients increase with. Water molecules diffuse faster in sPP than Nafion, which implies that diffusion is facilitated by bundled hydrophilic pathways. Time-dependent FTIR reveals that bound water evaporates slower than unbound water during drying, which illustrates the difference of bulk and confined water within sPP ionomers. Hindered water evaporation is due to a reduction in the degrees of freedom for ion containing domains and mass transfer limitations at interfacial boundaries between hydrophobic and hydrophilic domains.

1. Introduction

Water dynamics within an ionomer is important to many current and future applications ranging from fuel cells to separation membranes [1–4]. Water is often a critical operational parameter in these applications with excess water hindering function. For example, hydration of an ionomer facilitates proton transport within a hydrogen fuel cell. However, excess water floods electrodes and impacts performance [1,5–7]. Consequently, a delicate water balance must be maintained in order to guarantee optimal electrochemical performance.

The need to control water transport within ionomers and its impact on applications has led to a significant effort discerning the mechanisms of transport [8–10]. Nafion™ developed by DuPont is still the most prevelant polymer electrolyte membrane (PEM) for fuel cells [1,8–10]. This ionomer has a semiflexible tetrafluoroethylene backbone that is substituted with sulfonated perfluorovinyl ethers. Upon hydration, it forms a bicontinuous nanometer-sized hydrophilic and hydrophobic domains [11]. Water resides predominantly in the hydrophilic regions, where specific sites depend on the hydrated ionomer structure. Interfacial boundaries arising from the microstructure of the ionomer physically constrains the mobility of water molecules through electrostatics, hydrogen bonding, and other intermolecular forces [12–17]. While water molecules preferentially partition at hydrophilic sites, three states of water have been proposed to include bulk water, loosely bound

* Corresponding author. Tel.: +1 864 656 7703; fax: +1 864 656 6613.
E-mail addresses: ccornelius2@unl.edu (C.J. Cornelius), dperahi@clemson.edu (D. Perahia).
[1] Co-corresponding author. Tel.: +1 402 472 4344; fax: +1 402 472 6989.

http://dx.doi.org/10.1016/j.eurpolymj.2014.03.035
0014-3057/

water, and non-freezable water [18–20]. Bulk water molecules interact weakly with ionomer groups exhibiting bulk-water diffusion dynamics. Loosely-bound water includes solvent molecules located at the polymer/water internal interfaces. Slow water molecule dynamics are associated with loosely-bound and bound water. Non-freezable water is bound strongly to ionic groups.

This study focuses on water dynamics in hydrated polyphenylene ionomers, which represents a class of fluorine-free rigid polymers with high thermal and chemical stability. The chemical formula of SPP is shown in Fig. 1. Water relaxation times and diffusivity studies using ^{1}H NMR was used to identify water binding sites and quantify mobility in the hydrated ionomers [17,21–24]. Both NMR resonance frequencies and line shape distinguish between water molecules residing in different environments, reflecting provide information about the bonding sites and the nature of interactions between the ionomer network and absorbed water. The magnetic spin lattice relaxation time (T_1), is sensitive to the degree of water molecule confinement. PFG NMR studies were used to determine the water self-diffusion coefficients in these ionomers. These studies together with FTIR probe the water dynamics in hydrated rigid ionomers for the first time.

2. Experimental

2.1. Materials

Polyphenylenes were synthesized using a Diels–Alder polymerization reaction of 1,4-bis(2,4,5-triphenylcyclopentadienone)benzene and 1,4-diethynylbenzene as described elsewhere [25]. A post-sulfonation reaction was done with a stoichiometric amount of chlorosulfonic acid to create sPP ionomers. Membranes with different ion exchange capacities (IEC) were obtained by controlling the concentration of chlorosulfonic acid. Dissolving sPP into *N*-methyl-2-pyrrolidone (NMP) was done to create 5 wt% solutions [25]. Solutions were cast upon glass plates, and the solvent was evaporated at 60 °C in a vacuum oven for 24 h to form membranes. sPP were washed with deionized water to remove excess N-methyl-2-pyrrolidone [25].

Table 1
IEC, water uptake, and DS of sPP.

	IEC[a] (mmol/g)	Water uptake 100% RH (wt%)	DS (wt%)
sPP1	0.98	13	13.5
sPP2	1.60	49	20.0
sPP3	2.20	137	33.3

[a] IEC = Ion Exchange Capacity.

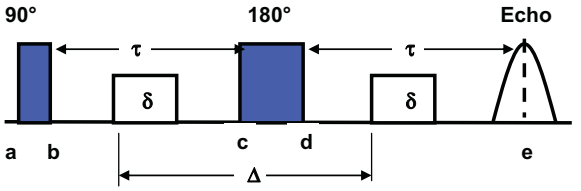

Scheme 1. Stejskal–Tanner pulse sequence [26–28].

The relative concentration of the sulfonic acid groups is characterized IEC or degree of sulfonation (DS). In this study, three IECs corresponding to 13.5 wt%, 20.0 wt%, and 33.3 wt% were studied. The IEC, water uptake, and DS of sPP are summarized in Table 1.

2.2. NMR and T_1 relaxation time measurement

^{1}H NMR measurements and T_1 relaxation times were carried out on a JEOL 500 MHz Fourier Transform NMR liquid spectrometer. This instrument is equipped with a variable temperature unit that controls temperature to ±0.5 °C. Ionomer films were cut into strips and placed into a standard 5-mm NMR tube with d-chloroform used as an internal reference. Inversion Recovery Pulse Sequence p-τ-p/2-$t_1$where p corresponds to a 180 ° pulse, τ is the delay between the 180 ° and the 90 ° pulses and t_1 is the time between the 90 ° pulse and detection was used to measure the relaxation times. T_1 is obtained by fitting the signal intensity at different times τ where $M_{z,eq}$ is the magnetization at equilibrium with a measurement duration of π/2 equal to 13.8 μs. The details of each experiment are given in each figure. The equilibrium magnetization is given by:

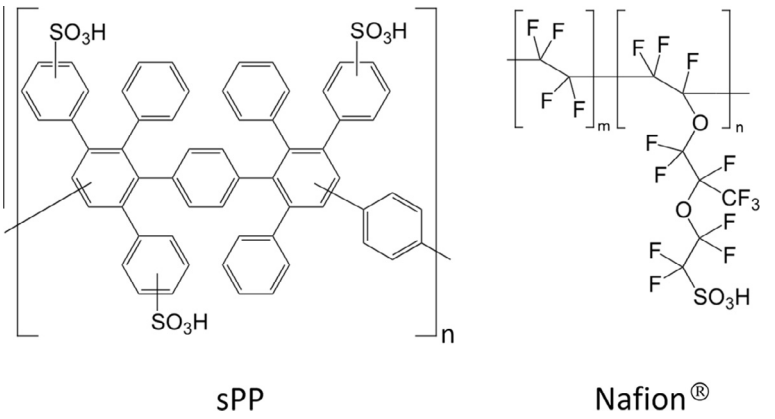

Fig. 1. Chemical structures of sPP and Nafion. N and m are the number of repeating units.

$$M_z(\tau) = M_{z,eq}(1 - 2e^{\tau/T_1}) \quad (1)$$

2.3. Pulse filed gradient NMR

Diffusion experiments were performed on a Bruker 300 NMR spectrometer with a gradient probe. Self-diffusion coefficients of water were measured with a Stejskal Tanner pulse sequence $\pi/2$-$G(\delta)$-π-$G(\delta)$-(echo) is shown in Scheme 1. The strength of the magnetic field gradients is varied from 0 to 35 Gauss/cm. The length of the gradient δ is 3 ms and the time between gradient pulses Δ is 100 ms. The pulse duration of $\pi/2$ is 9.9 μs.

2.4. Time-dependent FTIR measurements

A Nicolet Magna 550 FTIR using a dry nitrogen purge was used to collect time dependent spectra. The dehydration process was followed by recording changes in IR as a function of evaporation time. 2 × 2 cm samples were fully hydrated with deionized water overnight and excess water was wiped off prior to a measurement. All spectra were incoprotae eight scans with a wavenumber resolution of 0.125 cm^{-1} recorded from 4000 to 400 cm^{-1} at 25 °C.

3. Results and discussion

3.1. ^1H NMR

The ^1H NMR spectra of protonated sPP in the H^+ form is shown in Fig. 2 at room temperature as a function of IEC. The spectrum consists of broad lines centered at ~3.8 ppm with no aromatic protons. Line broadening is attributed to dipolar interactions and chemical shift anisotropy. Bulk water was measured independent of sPP and is characterized by a sharp peak at δ = 4.8 ppm. Because this signal is not present it confirms that no free water resides within these ionomers. The 1 ppm shift from 4.8 ppm is due to internal environmental changes for the water molecules. Numerous factors may cause these shifts such as the proximity to SO_3^- groups, water confinement in hydrophobic areas, and the strength of hydrogen bonding. At ambient humidity at 33.3 wt% sulfonation, the spectrum consists of three distinct lines corresponding to water molecules within well-defined sites as shown in the top curve in Fig. 2-a. With decreasing sulfonation levels, the lines further broadened. Upfield chemical shifts are due to shielding increases within a confined geometry as compared to bulk water. Surprisingly, it appears that the water resides

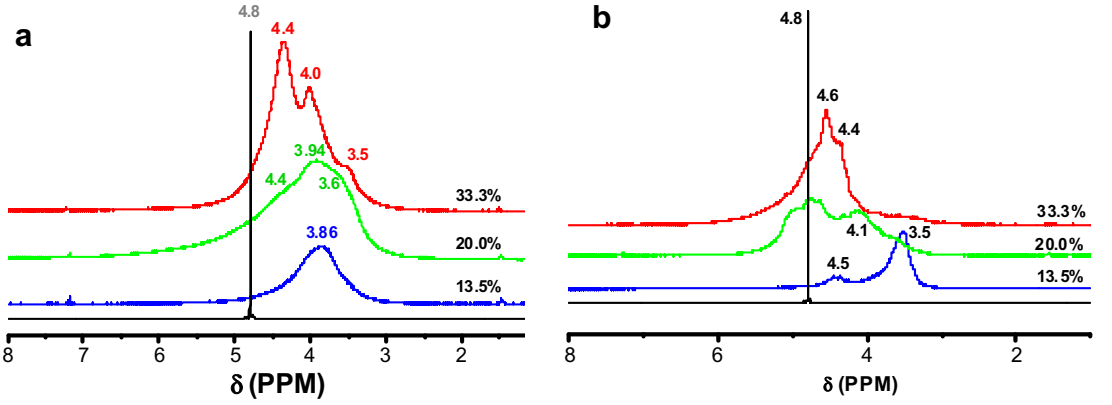

Fig. 2. ^1H NMR spectra of sPP membranes at room temperature (a) atmospheric moisture and (b) fully hydrated. As inner reference NMR tube with d-chloroform was used. The line at 4.8 ppm corresponds to bulk H_2O measured separately. Line broadening used is 1.0 Hz. The curves are shifted vertically for clarity.

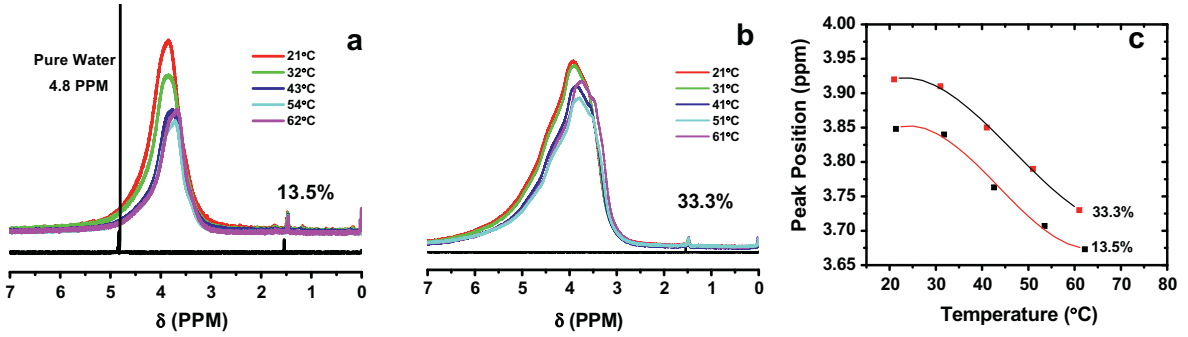

Fig. 3. ^1H NMR spectra of sPP membranes at different temperatures at ambient humidity. (a) sPP1 (sulfonation degree: 13.5%), (b) sPP4 (sulfonation degree: 33.3%), and (c) peak position as a function of temperature. The continuous lines through the data represent polynomial fitting.

in both hydrophilic and hydrophobic regions. In the hydrated state, multiple chemical shifts and line broadening indicates that several types of water environments are present. While the lines are broad compare to liquid water, they are sufficiently narrow to suggest that the water molecules exchange sties within the time scale of the spin lattice relaxation times.

The impact of temperature on the solvent distribution is shown in Fig. 3. Fig. 3a is a ^{1}H NMR spectrum of sPP1 at ambient humidity as a function of temperature. Upfield water shifts with increasing temperature are observed and shown in Fig. 3c. These shifts are consistent with water diffusion into a region that is more hydrophobic. Heating samples between 15 °C and 52 °C corresponds to 2.4–2.7 kJ/mol of thermal energy, which is sufficient for water molecules to overcome diffusional barriers into hydrophobic regions. Line width decreases with increasing temperature indicate that water is in a freer environment for diffusion. This temperature dependent behavior was observed for sPP3 as well, though in contrast to lower sulfonation level membranes distinctive sites are observed. Temperature independent redistribution of water regions suggests the existence of a fast water exchange environment (Fig. 3b).

3.2. Spin lattice (T_1) relaxation time studies

Time dependent water interactions within sPP were evaluated by measuring T_1 at I_{max}. Fig. 4 is the relaxation times of sPP at three sulfonated levels using ambient humidity versus fully hydrated or swollen ionomers. The relaxation times of all samples are less than 0.4 s, which is significantly lower than that of bulk water (3.4 s) [29]. This result provides evidence that the motion of water is inhibited and confined within these materials. The change in T_1 with temperature of fully hydrated sPP films increased in the following order: sPP3 > sPP2 ~ sP1 with sPP1 and sPP2 having very small changes. The slight increase in T_1 is indicative of penetration of water to different environment and enhanced exchange between sites. In higher sulfonation levels, the water in the swollen sample are significantly more free in comparison with lower sulfonation levels [30].

The sPP temperature dependence of T_1 is shown in Fig. 4. At low sulfonation levels, only small changes in T_1 are observed for both ambient and fully hydrated states. At higher sulfonation levels, T_1 increases with temperature, which is expected for a material with enhanced water mobility. The most significant effect of temperature upon T_1 is observed for hydrated sPP3 films versus their ambient state. Overall, water content in hydrated sPP films affects the T_1 relaxation times which are temperature dependent.

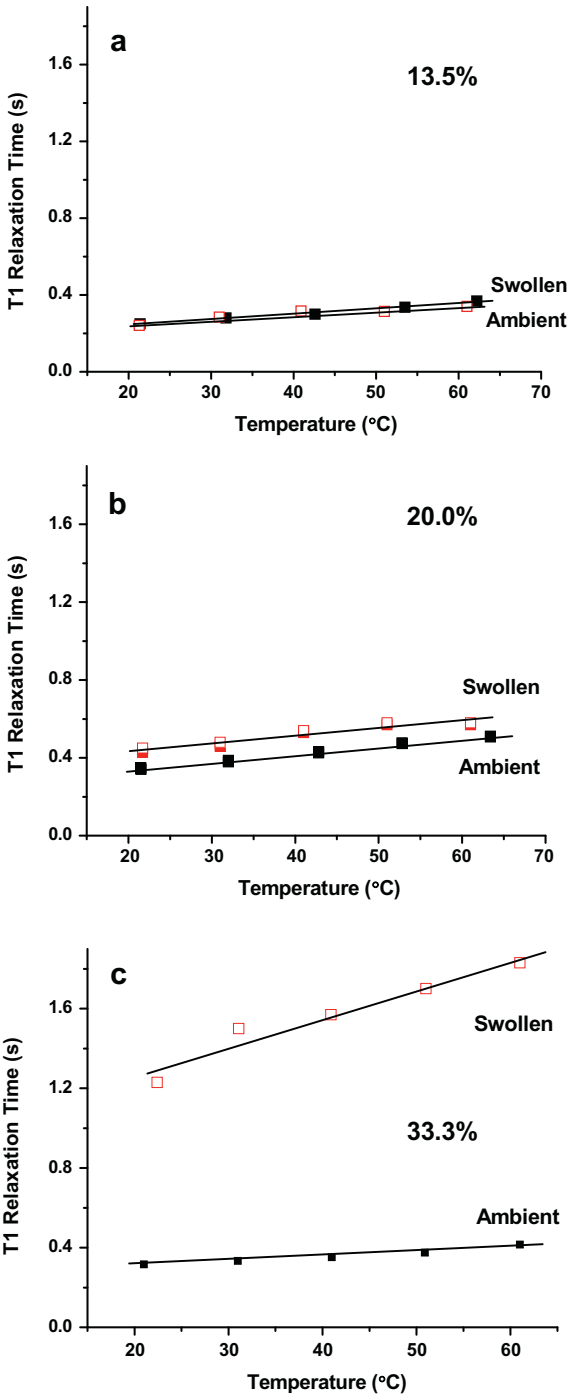

Fig. 4. T_1 relaxation times of water in sPP membranes at ambient (solid squares) and swollen states (open squares): (a) sPP1 13.5 wt%, (b) sPP2 20.0 wt%, and (c) sPP3 33.3 wt%. Lines through data are guide lines.

3.3. Pulse field gradient NMR

The bulk water self-diffusion coefficients were measured using the Stejskal–Tanner pulse sequence [26–28]. Proton spin-echo intensities were measured as a function of the field gradient intensity G. The self-diffusion coefficient D is extracted from

$$\ln(I_g/I_0) = -(\gamma G\delta)^2 D\left(\Delta - \frac{\delta}{3}\right) \quad (2)$$

In this equation, the signal intensity with an applied gradient is I_g and I_0 is the signal with an applied gradient. The diffusion time is Δ, τ is the time between two magnetic

field gradients, G is the gradient amplitude (G/cm), γ is the gyromagnetic ratio, and D is the self-diffusion coefficient.

Fig. 5a shows the normalized intensity of NMR signals versus the square of gradient strength (G^2). Straight lines result from fitting this data using Eq. (2). The slopes of these lines are proportional to the apparent water diffusion coefficients corresponding to 1.8×10^{-10} m^2/s (sPP2), 4.2×10^{-10} m^2/s (sPP3), and 6.9×10^{-10} m^2/s (sPP4). Diffusion rates are strongly dependent on IEC as shown in Fig. 5b. These results are comparable with other material systems using this technique [23,31]. The water diffusion of sPP1 was not measurable using these gradient strength, suggesting extremely slow water transport. The diffusion of bulk water is 2.13×10^{-9} m^2/s, which is considerably faster than sPP [29]. At ambient conditions; sPP has 1–3 water molecules per sulfonic group, which is the same as Nafion. The apparent diffusion coefficient of Nafion is 1.2×10^{-10} m^2/s, which is much lower than sPP ionomers [31,23]. This result shows that water transports is faster in sPP than in Nafion at humidity levels. The internal structure and morphology of sPP are strongly affected by its rigidity, which forms larger hydrophilic channels in comparison to Nafion. NMR measurements reveal that water molecules occupy different sites in these sPP ionomers with varying degrees of confinement. However, the effective diffusion coefficients are an average of all water transport. Consequently, both fast and slow water exchange within these sites is convoluted into this single constant. Future experiments will be done to separate each diffusive contribution within these ionomers.

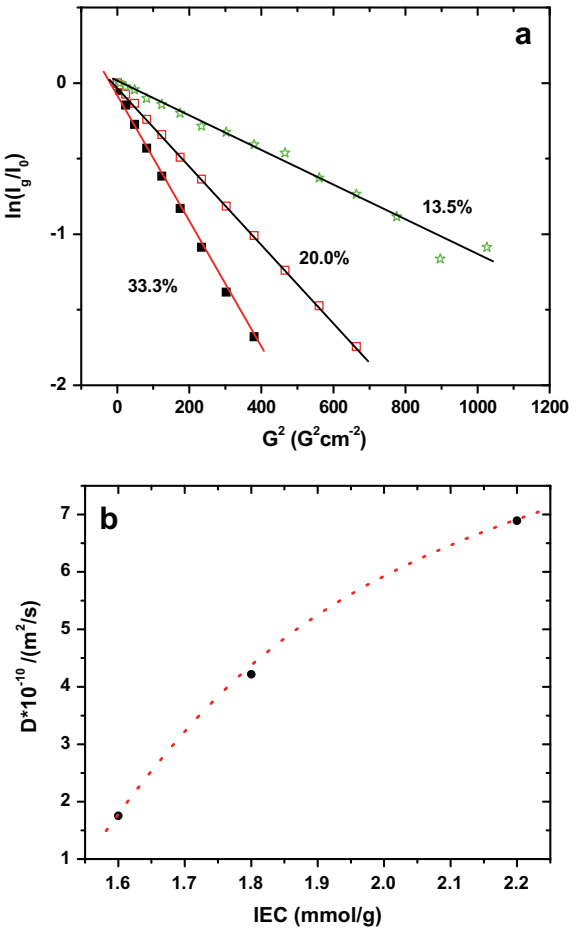

Fig. 5. (a) Echo amplitude as a function of gradient intensity for sPP1, SPP2, and sPP3 at ambient conditions and (b) effective diffusion coefficients as a function of IEC of fully water swollen films.

3.4. FTIR results

FTIR spectroscopy probed the dynamics of water as it diffused out of sPP. This study was done by fully hydrating a sPP film and monitoring changes in water concentration versus time at room temperature within a dry N_2 environment. The change in wavenumber and intensity associated with water was followed as a function of time for sPP1 shown in Fig. 6a. Two distinct water absorptions are observed at 3640 cm^{-1} and 3460 cm^{-1}. The former is assigned to a stretching band associated with interfacial water that is bound to the internal interfaces between

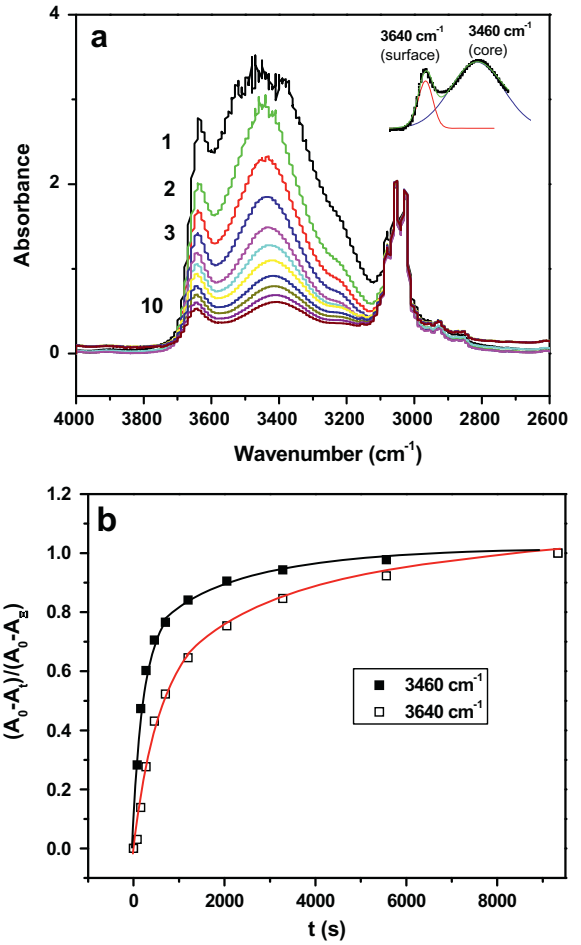

Fig. 6. (a) 4000–2600 cm^{-1} of infrared spectra of sPP at different dehydration times. Time dependent spectra in minutes from top to bottom: 0, 1.4, 2.7, 4.6, 7.7, 11.7, 20.0, 34.3, 54.8, 93.8, and 155.6 and (b) normalized integrated intensities of surface and core water at 3640 and 2460 cm^{-1} as a function of dehydration time.

hydrophilic and hydrophobic domains. The latter is a water molecule within the continuum of the material [32,33]. The wavenumbers of free water are distinctive and centered about 3400 cm^{-1}. The water peak stretch of sPP is much broader than free water illustrating its confinement at multiple states and energies.

In order to quantify the dehydration process, overlapping signals were deconvoluted using PeakFit v4.12. The integrated peak area A of the observed intensity is proportional to the water concentration within sPP. The change in water concentration was normalized based upon a change in the integrated intensity A. In this normalization procedure the maximum water concentration at equilibrium is A_o, the lowest water concentration A_{inf}, and the observed water concentration at any given time is A_t (Fig. 6b). The result reveals that bound water evaporates slower than free water.

An estimate of the interaction energy at both water sites is Arrhenius and it can be modeled with $k = k_o[-E_a/(RT)]$. In this analysis, the pre-exponential factor k_o was set to one, R is the ideal gas constant 8.314 J/(K mol), T is absolute temperature, and E_a is the activation energy. The water interaction energies for free and loosely bound water sites are 15.2 kJ/mol, and 17.0 kJ/mol. These values are less than water hydrogen-bonding to itself at 23.3 kJ/mol [34]. These activation energies define the hydrogen bonding energy limits of unbound and loosely bound water in this ionomer. Bound water has higher interaction energies than loosely bound water with a difference of 1.8 kJ/mol. This is obviously only a first insight and does not take into account the pre-exponential factor. More accurate interaction energies can be obtained by measuring at different temperatures, humidity, and IEC.

4. Conclusions

NMR and FTIR studies reveal distinctly different water environments associated with hydrophilic and hydrophobic regimes. The distribution between these sites strongly depends on the degree of sulfonic acid group ionization, DS, spatial arrangement of groups, temperature, and water concentration. Water chemical shifts moved upfield with increasing temperature. T_1 relaxation time of confined water is much lower than bulk water and increases with temperature. The water self-diffusion coefficients of sPP are on the order of 10–10 m^2/s as measured by PFG NMR. The water diffusivity increases with DS and then Nafion that is attributed enhanced diffusion pathways at the interfaces hydrophilic bundles. Free, loosely, and bound water changes in sPP are measurable using FTIR. During water dehydration, bound water evaporates slower than unbounded water, which illustrates the effect of confined water. This study provides strong evidence that interfacial boundary size reduces the degrees of freedom for water molecule mass transfer within this rigid ionomer.

Acknowledgements

The authors gratefully acknowledge financial support from DOE Grant No. DE-FG02-12ER46843, and support from Sharp Corporation.

References

[1] Mauritz KA, Moore RB. Chem Rev 2004;104:4535.
[2] Ugo P, Moretto LM, Vezzà F. ChemPhysChem 2002;3:917.
[3] Whiteley DL, Martin C. Anal Chem 1987;59:1746.
[4] Marrink SJ, Berkowitz M, Berendsen HJC. Langmuir 1993:3122.
[5] EG&G Services, Parsons Inc., and Science Applications International Corporation. Fuel cell handbook, 5th ed. Morgantown (WV): U.S. Department of Energy; 2000.
[6] Hickner MA, Fujimoto CH, Cornelius CJ. Polymer 2006;47:4238.
[7] Eikerling M, Kornyshev AA, Kucernak AR. Phys Today 2006;59:38.
[8] Weber AZ, Newman J. J Electrochem Soc 2003;150:A1008.
[9] Saito M, Armura N, Hayamizu K, Okada T. J Phys Chem B 2004;108:16064.
[10] Saito M, Armura N, Hayamizu K, Okada T. J Phys Chem B 2005;109:3112.
[11] Gebel G. Polymer 2000;41:5829.
[12] Gieke TD, Munn GE, Wilson FCJ. JETP Lett 1981;19:1687.
[13] Hsu WY, Gierke TD. J Membr Sci 1983;13:307.
[14] Falk M. Can J Chem 1980;58:1495.
[15] Kreuer KD. J Membr Sci 2001;185:29.
[16] Rubata L, Rollet AL, Gebel G, Diat O. Macromolecules 2002;35:4050.
[17] MacMillan B, Sharp AR, Armstrong RL. Polymer 1999;40:2471.
[18] Paddison SJ. Annu Rev Mater Res 2003;33:289.
[19] Kreuer KD, Paddison SJ, Spohr E, Schuster M. Chem Rev 2004;104:4637.
[20] Elliott JA, Paddison SJ. Phys Chem Chem Phys 2007;9:2602.
[21] Siyashiinsky N, Tanny GB. J Appl Polym Sci 1981;26:2625.
[22] Starkweather Jr HW, Chang JJ. Macromolecules 1982;15:752.
[23] Zawodzinski TA, Neeman M, Sillerud LO, Gottesfeld S. J Phys Chem 1991;95:6040.
[24] Motupally S, Becker AJ, Weidner JW. J Electrochem Soc 2000;147:3171.
[25] Fujimoto CH, Hickner MA, Cornelius CJ, Loy DA. Macromolecules 2005;38:5010.
[26] Stejskal EO, Tanner JE. J Chem Phys 1965;42:288.
[27] Price WS. Concepts Magn Reson 1997;9:299.
[28] Price WS. Concepts Magn Reson 1998;10:197.
[29] Simpson HJ, Carr YH. Phys Rev 1958;111:1201.
[30] He L, Fujimoto HC, Cornelius JC, Perahia D. From solutions to membranes: structure studies of rigid sulfonated ionomers, 42. Washington, DC, United States: Macromolecules; 2009. p. 7084.
[31] Jayakody JRP, Stallworth PE, Mananga ES, Farrington-zapata J, Greenbaum SG. J Phys Chem B 2004;108:4260.
[32] Wang Y, Kawano Y, Aubuchon RS, Palmer AR. Macromolecules 2003;36:1138.
[33] Falk M. ACS Symp Ser 1982;180:139.
[34] Suresh SJ, Naik VM. J Chem Phys 2000;113:9727.

Macromolecules

Article

pubs.acs.org/Macromolecules

Coarse-Graining Atactic Polystyrene and Its Analogues

Anupriya Agrawal,[†] Dipak Aryal,[†] Dvora Perahia,*[,†] Ting Ge,[‡] and Gary S. Grest[§]

[†]Department of Chemistry, Clemson University, Clemson, South Carolina 29634, United States

[‡]Department of Physics and Astronomy, Johns Hopkins University, Baltimore, Maryland 21218, United States

[§]Sandia National Laboratories, Albuquerque, New Mexico 87185, United States

Supporting Information

ABSTRACT: Capturing large length scales in polymers and soft matter while retaining atomistic properties is imperative to computational studies of dynamic systems. Here we present the results for a coarse-grained model based on atomistic simulation of atactic polystyrene (PS). Similar to previous work by Harmandaris et al. and Fritz et al., each monomer is described by two coarse-grained beads. In contrast to these early studies in which intramolecular potentials were based on Monte Carlo simulations of isotactic and syndiotactic single PS molecules to capture stereochemistry, we obtained intramolecular interactions from a single molecular dynamics simulation of an all-atom atactic PS melt. The nonbonded interactions are obtained using the iterative Boltzmann inversion (IBI) scheme. This methodology has been extended to coarse graining of poly(4-*tert*-butylstyrene) (PtBS) in which an additional type of coarse-grained bead is used to describe the *tert*-butyl group. Similar to the process for PS, the intramolecular interactions are obtained from a single all-atom melt simulation for atactic PtBS.

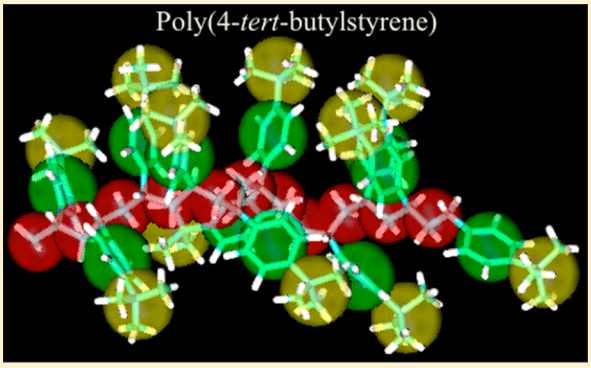

1. INTRODUCTION

Polymer properties are often determined by structure and dynamics on multiple length and time scales. The presence of a wide range of spatial and temporal scales that are often correlated remains a challenge for both experimental and computational studies of polymers.[1−5] Computationally, a fully atomistic description of polymers that would capture the electronic behavior and assembly of the macromolecules does not allow reaching large enough dimensions where mechanical properties are manifested, whereas generic coarse-grained bead−spring models which capture mesoscopic length scale often miss atomic level details. Developing models that capture atomistic details and expand to mesoscopic length scales is imperative to the understanding of polymer dynamics driving a large effort to coarse-grained polymers while retaining some of the atomistic characteristics. A significant number of these studies depict polystyrene (PS) as a model polymer to develop coarse-grained potentials. Because of its low glass transition temperature and narrow polydispersity, PS has been intensively studied both experimentally and computationally, providing a vast amount of data for comparison and validation of new models. Significant strides have been made in coarse graining of polymers.[6−21] Different pathways were developed to determine the coarse-grained potentials, some of which were obtained from melts and some from single molecules. All these studies have clearly demonstrated the need for systematically coarse-graining polymers with transferability while capturing their stereochemistry. Transferability could relate to different temperatures, chemical analogues, and a coarse-graining scheme that allows formation of structured polymers. Building on the state of the art, we present here the results of a coarse-grained methodology that captures the chain stereochemistry from a single molecular dynamics simulation of a fully atomistic PS melt.

Early computational studies using bead−spring models have captured the universal physics of chemically diverse polymers. Kremer and Grest[6] for example resolved dynamics of linear polymers in melts using the bead−spring model at temperatures above glass transition temperature. These studies have realized the power of this simple model. Nevertheless, detailed chemical information is essential for a full realization of the behavior of polymers on multiple length scales. To accelerate simulations of specific polymers, coarse-grained techniques that reduce the degrees of freedom in a simulation have been developed. Coarse graining in this case signifies bundling of several atoms into one "coarse-grained bead" (CG) and treating these CG beads as the building blocks of polymers.[7−9,22] Depending on the properties that need to be explored, these CG beads can be defined and their interaction potential can be obtained from atomistic simulations of either a single polymer chain or a melt of short chains. Most commonly used methods to obtain these interaction potentials are iterative Boltzmann

Received: February 11, 2014
Revised: March 19, 2014
Published: April 17, 2014

inversion (IBI),[10−16] inverse Monte Carlo (IMC),[17−19] force matching (FM),[4,5,20,21,23,24] and relative entropy.[25,26]

Depending on number of beads used to define a monomer of PS, a coarse-grained model of PS can be categorized as 1:1,[13,14] 2:1,[27−31] and 4:1[32] models where *n*:1 represent *n* beads to define a monomer of polystyrene. Each of these models captures a different aspect of the polymer properties. For a detailed comparison of these different models for PS see recent reviews by Karimi-Varzaneh et al.,[2] Li et al.,[4] and Brini et al.[5] The first coarse-grained model for PS was suggested by Milano and Müller-Plathe,[13] who described a PS monomer using 1 bead (1:1 model) such that the bead center was at CH_2 group and mass of phenyl group was equally distributed between two consecutive beads. They used two types of beads depending on the relative configuration of two consecutive phenyl groups. When two consecutive phenyl rings are on the same side of the chain, this configuration is called meso while when they are on opposite side of backbone, it is called racemic. For isotactic PS, all the monomers are in the meso configuration where two consecutive phenyl rings are on the same side of the backbone, while for syndiotactic PS, all the monomers are in the racemic configuration; i.e., the phenyl groups are on the opposite side. Atactic PS consists of monomers in the two configurations randomly. Milano and Müller-Plathe[13] used an atactic PS all-atom melt simulation of 56 chains of 10 monomers at 500 K to obtain the intramolecular bond, angle, and dihedral distributions which were used to develop the interaction potentials for coarse-grained simulations. The nonbonded interactions were developed using the IBI method. Spyriouni et al.[33] improved these CG potential functions for PS melts from previous works done by Müller-Plathe and co-workers and showed that they can capture the correct entanglement length of PS melts. The packing length and tube diameter were found to be in agreement with experiments. However, the obtained isothermal compressibility is far from the experimental value, which indicates poor transferability of the potential. Qian et al.[34] chose another mapping scheme with two types of beads defined according to the absolute configuration of the monomer in a 1:1 model and found that the newly obtained potentials could reproduce the thermal expansion and structure properties of the PS melts from 400 to 500 K.[2] These potentials provided insight into the interphase structure in silica−nanoparticle nanocomposites.[35]

Sun and Faller[14,36] also used one bead to describe the PS monomer (1:1 model), however, without any stereochemical detail. Starting from all-atom melt simulation of 48 chains of 15 monomers of atactic PS at 450 K temperature, they obtained the interaction parameters. The nonbonded potential were developed using the IBI method. Using their 1:1 coarse-grained model of polystyrene, Sun et al.[36] showed that new set of potential is needed to be developed to study polystyrene in different environment such as dilute solution and dense melt; however, the same set of potentials can be used to study the effect of chain length. They further used their model to study the shift from unentangled to entangled dynamics of polystyrene melt and reported the entanglement length to be about 85 monomers from their 1:1 model.[37] Bayramoglu and Faller[38] extended their previous work to study polystyrene in four different environments including melt, dilute solution, unconfined, and confined concentrated solutions and showed that coarse-graining is most effective for polymer melts and least effective for dilute solutions due to stronger slowdown of diffusive dynamics in atomistic simulations with concentration. To explore the transferability of the potentials developed through IBI methodology, Bayramoglu and Faller[39] studied the effect of confinement on the concentrated solution of polystyrene in toluene. They show that the interaction potential between confinement wall and polystyrene monomer/toluene molecules, developed from a parent system, could not be transferred to the other systems.

Further complexity has been introduced to CG by Hermandaris et al.,[27] who described PS using two bead models for the first time and demonstrated that the choice of the beads are crucial for obtaining the correct structure of the melt. When the two beads described a CH_2 group and the second bead consists of C_6H_5−CH group, the melt structure of polystyrene could not be well replicated. They[27] suggested another 2:1 scheme (Figure 1a), which had a phenyl group constituting one bead and a second bead involved the CH−CH_2−CH group along the backbone. In this scheme, however, the mass of the two CH groups was equally distributed between two consecutive beads. This scheme was more successful in replicating the atomistic melt structure of polystyrene. They used a united atom model of atactic PS melts at 463 K to obtain the interaction potential for coarse-grained beads. The nonbonded interactions between the beads were assumed to be the form of the purely Lennard-Jones 6−12 potential with modified coefficients. Using this model, they studied the dynamics of polystyrene melts in molecular weight range 1 and 50 kDa and showed that time scaling between coarse-grained and atomistic simulations is dependent on molecular weight of the constituting chains.[28,40] These coarse-grained simulations are in excellent comparison to experiment, without any parameter fit to experiment. The only quantity used is the density.

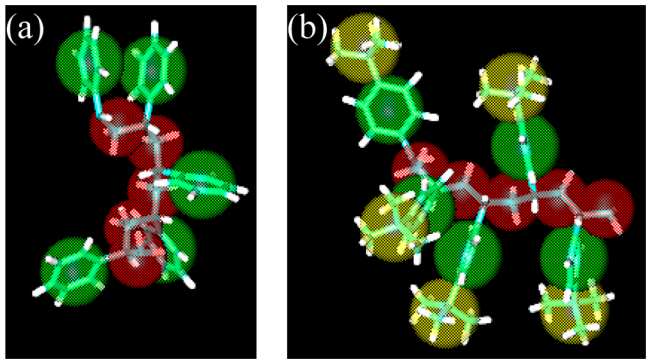

Figure 1. Coarse-grained model for (a) polystyrene and (b) poly(4-*tert*-butylstyrene). A (red), B (green) and C (yellow) represent the beads for their corresponding monomers.

To incorporate stereochemistry, Fritz et al.[30] used the two comparable bead-mapping scheme proposed by Hermandaris et al.[28,29] and obtained the bond lengths, angle, and dihedrals distributions from a single isotactic and a single syndiotactic PS chain simulation. In contrast to previous work,[28] they[30] used the potential of mean force between the beads to develop the nonbonded potentials. Although the atomistic simulations were carried out at 503 K temperature, these potentials were transferable to temperature range 400−500 K. Using this coarse-grained potential, they studied the dynamics of the PS melts with different tacticities and mapped the results to atomistic simulations.

dx.doi.org/10.1021/ma500319v | *Macromolecules* 2014, 47, 3210−3218

In this paper, building on the two-bead CG model previously discussed, we show that one can capture the stereochemistry of PS and extract all the relevant potentials from a single atomistic MD simulation of atactic melts. From the single atactic PS melt simulation, all the intramolecular interactions were determined as well as intermolecular RDF, which is used as a target for the IBI to iterate the nonbonded interaction. We also include a separate pressure correction term to obtain the accurate density of the melt at ambient pressure. Densities of PS melts with varying chain lengths formed by our coarse-grained model were in good agreement with the experimental values. This methodology is ideally suited for extending the coarse-graining methodology to PS derivatives such as atactic poly(4-*tert*-butylstyrene) (PtBS) by introducing a third type of CG bead, shown in Figure 1b. A similar approach of introducing an additional bead has been used to coarse grain a diblock copolymer poly(styrene-*b*-butadiene) melt[41] as well as polystyrene/polyisoprene blends.[42]

In the next section we present the details of the atomistic and coarse-grained simulations followed by the details of coarse-grained modeling methodolgy for polystyrene in section 3. The extension of the methodology to PtBS is discussed in section 4 followed by conclusions.

2. MODEL AND SIMULATION METHODS

The All Atom Optimized Potential for Liquid Simulations (OPLS-AA) force field by Jorgensen et al.[43,44] was used for the fully atomistic simulations. The attractive (r^{-6}) dispersion term in the Lennard-Jones interaction and the electrostatic interactions were calculated using particle−particle particle-mesh algorithm.[45] As a result, the Lennard-Jones interaction becomes a fully long-range potential. Interactions closer than 1.2 nm are calculated in real space; those outside this range are calculated in reciprocal Fourier space with precision of 10^{-4}. The repulsive (r^{-12}) Lennard-Jones interaction is truncated at 1.2 nm. All simulations in this paper were performed using the parallel molecular dynamics code Large Atomic Molecular Massive Parallel Simulator (LAMMPS).[46]

Atactic PS and PtBS chains were created using Accelrys Materials Studio.[47] Simulation cells with periodic boundary conditions with 20 unique chains of atactic PS and PtBS with 20 monomers (2.0 and 3.2 kDa, respectively) each were equilibrated using NPT ensemble with temperature 500 K and 1 atm pressure where temperature and pressure were controlled using a Nosé−Hoover thermostat and barostat, respectively. Once polymer melts were equilibrated, production runs of 35 ns with a time step δt = 1 fs were performed at constant volume for the two polymer systems. For these constant volume runs each monomer was coupled weakly to a Langevin thermostat with a damping constant of 100 fs to maintain a constant temperature. The atomistic density of this short chain melt is 0.90 g/cm^3 for PS and 0.85 g/cm^3 for PtBS. This result is in agreement with the experimental density of 0.90 g/cm^3 at 500 K temperature and 1 atm pressure for short chain PS (0.9 kDa).[48] Cutting off the dispersion (r^{-6}) term in the Lennard-Jones interaction at 1.2 nm, as is often done, leads to a slightly lower melt density of 0.87 g/cm^3.

Bond length, angle, and dihedral distributions used to extract the intramolecular interactions were obtained from these fully atomistic melt simulations. The intermolecular RDF $g(r)$, which is used as the target for iteration of nonbonded potential, was also extracted from the same atactic melt simulations. RDF was extracted from a simulation of 35 ns in which snapshots were saved every 10 ps.

For the fitting of nonbonded CG potential for polystyrene, a system of 160 chains of 40 CG beads (20 PS monomers) was used. Constant volume simulations at the equilibrium density obtained from the atomistic simulation with a time step δt = 1 fs were run for 3 ns for which RDF was obtained from last 2 ns of simulation. RDF was averaged over 200 snapshots for each iteration. Potential forces were obtained by taking the derivative of the interaction energy. These values were used in the tabulated form for the simulations. Following the work of Fritz et al.,[30] we also include a special 1−5 interaction, which were treated as bonded potential. The nonbonded potential between CG beads within four beads along the backbone is not included. All CG pairs beyond the 1−5 pairs along the backbone were treated as nonbonded pairs.

Using the set of bonded and nonbonded potential, we studied larger PS systems (Table 1), which were created in Materials Studio and then converted to coarse-grained beads. For 5, 12, and 20 and 52 kDa molecular weight, we make samples with six chains with different, random tacticity, which were subsequently replicated to increase number of chains to that shown in Table 1. Polymers with six chains with different, random tacticity, which were subsequently replicated. Each was equilibrated with both our new potential. The systems are presented in Table 1.

Table 1. Coarse-Grained PS Systems Studied at T = 500 K and P = 1 atm

M_w (kDa)	no. beads/chain	no. of chains	t (ns)	density (g/cm^3)
2.0	40	1280	24	0.896
5.2	100	384	35	0.928
12.4	240	384	22	0.936
20.8	400	162	26	0.941
52.0	1000	162	23	0.942

3. POLYSTRYENE

Polystyrene consists of aliphatic backbone and phenyl ring as side group on alternative carbon along the backbone. In this coarse-graining model of PS, we have used the 2:1 (2 beads to represent 1 monomer) mapping scheme of Harmandaris et al.[28] as shown in Figure 1a. Here, bead A encompasses the −CH−CH_2−CH− group such that CH groups contribute half of their mass to the consecutive bead and the phenyl group constitutes B bead. The advantage of this 2:1 model over 1:1 mapping scheme is that it captures the effect of tacticity as well as the steric effects of phenyl ring. A minimum of five beads are required to capture the stereochemistry of atactic PS as shown by Fritz et al.[30] In the five-bead configuration when started from A (A-B-A-B-A), both B's can be in meso configuration or racemic configuration. In those two cases, first A is assigned two different types of beads. For five-bead configurations that start at B (B-A-B-A-B), three B can be in meso, racemic, or mixed configuration for which three B types of beads are assigned. These configurations are shown in Figure S1 of the Supporting Information. Thus, to include the stereochemistry of atactic PS in CG model, we have defined five types of beads: two types of A beads and three types of B beads.

The energy U of this CG model consist bonded (B) and nonbonded (NB) potential

dx.doi.org/10.1021/ma500319v | Macromolecules 2014, 47, 3210−3218

$$U^{CG} = \sum U_B^{CG} + \sum U_{NB}^{CG} \quad (1)$$

Intramolecular interactions are generally obtained from intramolecular distributions of bond lengths, angles, and dihedrals and are assumed to be decoupled from the CG nonbonded interactions. The most common strategy is to use Boltzmann inversion to convert distributions to potential energies. The underlying principle to obtain potential from these distributions is that these distributions are not correlated such that

$$P^{CG}(r, \theta, \phi, T) = P^{CG}(r, T)P^{CG}(\theta, T)P^{CG}(\phi, T) \quad (2)$$

where P are probability distributions, r is bond length, θ is bond angle, ϕ is dihedral angle, and T is temperature. Thus, the mapping scheme must be chosen so that the above equation holds true.

We have compared the distribution obtained from atactic PS melt with the distribution obtained by Fritz et al.[30] from single chain isotactic (meso) and syndiotactic (racemic) PS atomistic simulations. Distribution of bond lengths between beads A and B is shown in Figure 2a. These bonds can be of two types

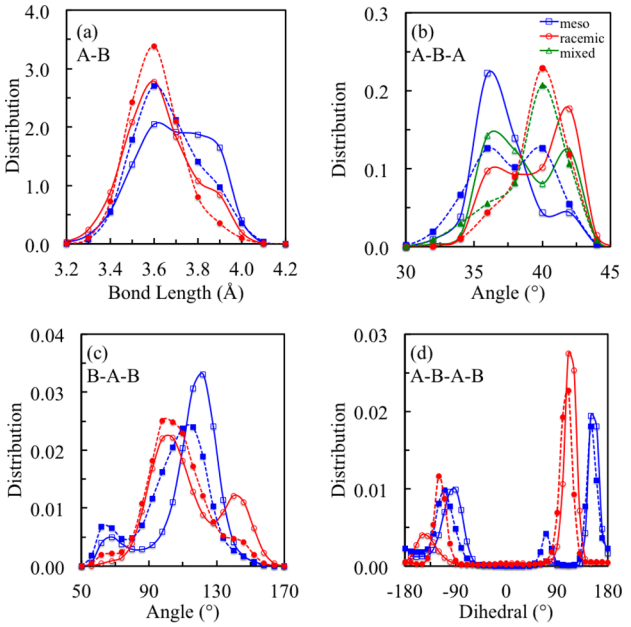

Figure 2. (a) AB bond length distribution, (b) ABA angle distribution, (c) BAB angle distribution, and (d) ABAB dihedral distribution. Open symbols are the data obtained from Fritz et al.,[30] and filled symbols are obtained from a single atomistic atactic polystyrene melt simulation.

depending on whether A is meso type or racemic type. As can be seen, our racemic distribution matches well with the single chain simulation of Fritz et al. However, our meso AB bond distribution shows a peak at 3.6 Å and a slight second peak at 3.9 Å, and Fritz et al.[30] show double peak at 3.6 and 3.8 Å. The second peak in our distribution has lower intensity as the result of presence of racemic configuration along the chain thus having a smearing effect at longer distances.

The ABA angle distributions obtained from the melt simulation are somewhat different than that found by Fritz et al. There are three angle distributions depending on type of B bead. For meso type of B bead, the ABA angle shows two peaks at ~36° and ~40° compared to results of Fritz et al.,[30] who found two peaks at 36° and 42°. Our racemic and mixed distributions are very similar to a peak at ~40°; however, the Fritz et al.[30] mixed distribution is the average of racemic and meso distributions. For the BAB angle distributions there are only two types, meso and racemic, and they match well with those of Fritz et al.,[30] except their racemic distribution shows an additional peak at 145°. The ABAB dihedral distributions obtained from two methods match very well as shown in Figure 2d.

As discussed by Fritz et al.,[30] the distance between CG beads separated by three intermediate beads, the 1−5 distance, is important to maintain the rigidity of the backbone. These distributions were obtained for five types of beads and are shown in Figures 3a and 3b for A and B beads, respectively.

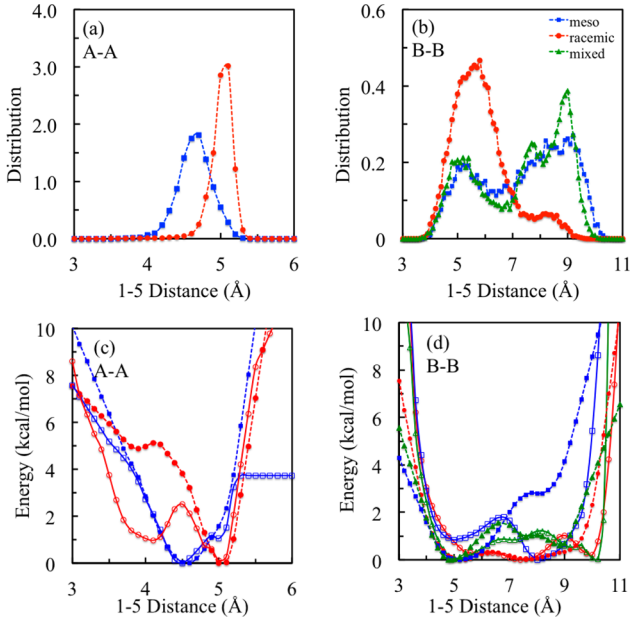

Figure 3. Distribution of 1−5 distances obtained from all-atom atactic polystyrene melt simulations for (a) A beads and (b) B beads. The corresponding energy is shown in (c) A beads and (d) B beads. Filled symbols are from this work, and open symbols are from Fritz et al.[30]

The distributions of bond lengths between the 1−5 CG beads show a single peak at 4.9 and 5.1 Å for meso and racemic A beads, respectively. Meso B beads exhibit a broad double peak, which could be explained by steric effects of phenyl ring. Racemic B beads exhibits a peak at ~6 Å and a smaller peak at ~8 Å.

The distributions were then converted to the corresponding potential energy using the inverse Boltzmann scheme

$$U^{CG}(r, T) = -k_B T \ln(P^{CG}(r, T)/r^2) \quad (3)$$

$$U^{CG}(\theta, T) = -k_B T \ln(P^{CG}(\theta, T)/\sin(\theta)) \quad (4)$$

$$U^{CG}(\phi, T) = -k_B T \ln(P^{CG}(\phi, T)) \quad (5)$$

Bonded energies corresponding to the bond, angles, and dihedrals show minima at the maxima in the distributions curves. These energy curves are given in Figure S2 of the Supporting Information. The 1−5 distributions were inverted using eq 3 to obtain the respective potentials, which are plotted in Figure 3c,d. Results are compared with the potential obtained by Fritz et al.[30] The 1−5 interactions for the meso A beads obtained from the melt simulation match very well with those obtained by Fritz et al. However, for racemic A

dx.doi.org/10.1021/ma500319v | Macromolecules 2014, 47, 3210−3218

beads, Fritz et al. have a local broad minima around 4 Å. Similarly, Fritz et al.[30] found that the racemic B beads show a global minima at ∼8 Å; however, our global minima lies at 5 Å. Mixed type of B beads from both methods show mixed character of meso and racemic type of B beads.

In this work, we have used the IBI method to get the nonbonded potential between CG beads, which are on different chains or separated by more than four beads along the backbone. An initial guess for the nonbonded interactions is taken from a Boltzmann inversion of intermolecular RDF, determined from the fully atomistic simulations, for the AA, AB, and BB CG monomers as

$$U^{\mathrm{CG}}_{\mathrm{NB},0} = -k_{\mathrm{B}}T\,\ln(g(r)) \tag{6}$$

These RDFs, obtained from the atomistic simulations, are the target functions for determining the various nonbonded potentials from the IBI method.

In order to take the potential and corresponding force smoothly to zero at cutoff distance, the Mei−Davenport−Fernando taper function[49] was applied

$$U^{\mathrm{CG}}_{\mathrm{NB,cutoff}} = \begin{cases} 1, & r < r_{\mathrm{m}} \\ (1-x)^3(1+3x+6x^2), & r_{\mathrm{m}} \le r < r_{\mathrm{c}}, \\ 0, & r \ge r_{\mathrm{c}} \end{cases} \tag{7}$$

where $x = (r - r_{\mathrm{m}})/(r_{\mathrm{c}} - r_{\mathrm{m}})$, r_{m} is the start of the taper range, and r_{c} is the cutoff distance. Here we used r_{m} as 0.94 nm and r_{c} as 1.0 nm.

The nonbonded potentials were iterated using the IBI scheme[10] as follows

$$U^{\mathrm{CG}}_{\mathrm{NB},i+1} = U^{\mathrm{CG}}_{\mathrm{NB},i} + \lambda_1 k_{\mathrm{B}}T\,\ln\left(\frac{g_i(r)}{g(r)}\right) \tag{8}$$

where $g_i(r)$ is the RDF after the ith iterations and λ_1 is a constant to control the rate of change in the energy in each iteration. We set $\lambda_1 = 0.1$ since the rate of convergence is very poor for $\lambda_1 = 1$. Using this scheme, starting from the initial guess of the nonbonded potential eq 6, the CG simulation was simulated for 3 ns, $g_i(r)$ was calculated from last 2 ns of simulation, and a new estimate of the nonbonded potential was determined using eq 8. After 167 iterations $g_i(r)$ and $g(r)$ converged as shown below. It is important to note that the IBI scheme is iterated only on RDF and there is no term to control the pressure of the system. The average pressure for the constant volume CG simulation was 200 atm for the 167th iteration. In order to obtain density consistent with an ambient pressure, in addition to the IBI term in eq 8, we applied a pressure correction term[13,14,50]

$$\Delta U^{\mathrm{pc}}_{i+1} = -(P_i - P)V_{\mathrm{atom}}\lambda_2\left(1 - \frac{r}{r_{\mathrm{c}}}\right) \tag{9}$$

where P_i is the average pressure obtained from ith iteration, P is the target pressure, V_{atom} is the volume per atom, and λ_2 is a constant to control the rate of change of energy between the iterations. Here we take $\lambda_2 = 0.1$. For larger values of λ_2, the pressure fluctuations are large and the iterative procedure does not converge. For $\lambda_2 = 0.1$, the pressure converges quickly after a few iterations. The pair correlation functions $g(r)$ and the corresponding nonbonded potential are shown in Figure 4 after the pressure correction. The nonbonded A−A interaction is not affected by the pressure correction while the A−B and B−B interactions have slightly lower minima after the pressure correction is applied. For separations less than 4 Å, the pressure correction does not have significant effect on the potential since $g(r)$ is zero in this region. Fritz et al.[30] found a single attractive minimum for all the components of nonbonded potential. The location of their attractive minima for all the components is ∼0.25 Å lower than our potential using the IBI method, which could explain the higher density of ∼0.98 g/cm^3 at P = 1 atm obtained using the Fritz et al. potential for the same 20 PS monomer system. When we use the Fritz et al.[30] CG potential at 0.89 g/cm^3, the system phase separated into a denser melt and vacuum.

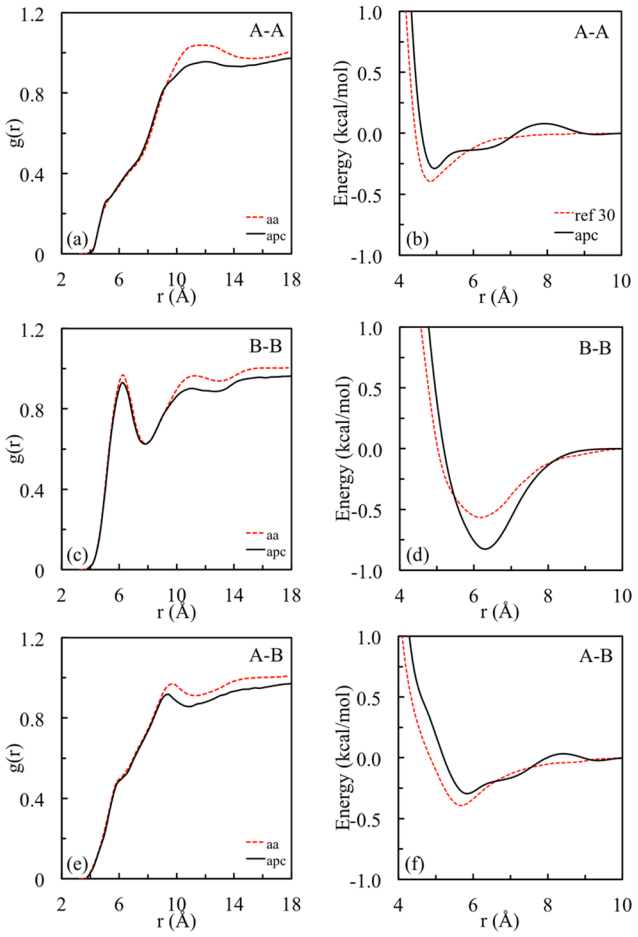

Figure 4. Left panel shows the radial distribution function of polystyrene for (a) A−A, (c) B−B, and (e) A−B. Right panel shows the nonbonded energies for (b) A−A, (d) B−B, and (f) A−B after pressure correction (apc). Dashed line in the left panels is the pair correlation function $g(r)$ obtained from all atom atomistic (aa) simulation, and in the right panels, it shows the nonbonded potential obtained from Fritz et al.[30]

Using our new potential, we calculated the density of atactic polystyrene as a function of chain length for systems reported in Table 1. Figure 5 shows the results for our potential compared to that using the Fritz et al.[30] potential for the same chain lengths and with experimental data.[48] Densities of atactic polystyrene using our potential match very well with the experimental values as seen in Figure 5.[48] The Fritz et al.[30] potential overestimates the density by 7%. Without implementing any terms to include the effect of the chain length on density in this model, these potentials could be successfully

dx.doi.org/10.1021/ma500319v | Macromolecules 2014, 47, 3210−3218

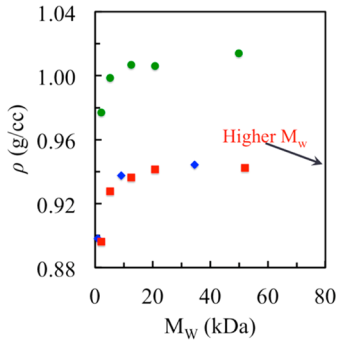

Figure 5. Density of atactic polystyrene versus molecular weight M_w at temperature 500 K and ambient pressure using the potential developed here (■), the potential of Fritz et al. (●), and experiment (♦) (ref 48). Arrow shows the experimental density of the higher molecular weight system.

used to study the effect of chain length. The thermal expansion coefficient of 20 kDa atactic polystyrene sample at 1 atm pressure was found to be 5.0×10^{-4} K^{-1} in the temperature range 400−540 K (Figure S3 in Supporting Information). This compares well with the experimental value[48] of 6.0×10^{-4} K^{-1} for 34.5 kDa sample at P = 1 atm. Compressibility of the same sample was found to be 1.8×10^{-4} MPa^{-1} in the pressure range 1−200 atm at T = 500 K (Figure S4 in Supporting Information). The experimental value of compressibility for 34.5 kDa sample at 503 K is 4.7×10^{-4} MPa^{-1}.[48]

To correctly reproduce the dynamical behavior of PS melt, a time-mapping constant based on the friction coefficients obtained from short chain atomistic and coarse-grained simulation is required similar to previous work by Harmandaris et al.[1,27,40] for PS melts and Li et al.[51] for polyisoprene melts.

4. POLY(4-*tert*-BUTYLSTYRENE)

To represent each monomer of PtBS, we extended the two-bead representation of PS to include a third CG bead. The first bead (A bead) is same for PS, the phenyl ring (C_6H_4) is represented by second bead (B bead), and third bead (C bead) is the tertiary butyl group (as shown in Figure 1b). In order to account for tacticities, we have defined two types of A bead, three types of B bead, and one type of C bead.

Distributions of bonded degrees of freedom for the coarse-grained model of atactic PtBS obtained from a fully atomistic simulation of an atactic melt are shown in Figure 6. There is one additional bond in PtBS when compared to PS, i.e., BC. Bond length distributions are shown in Figure 6a. While the AB bonds are either meso or racemic type, the BC is not affected by tacticity, which is evident from its characteristic single peak at 3.3 Å. The ABA angle distributions are shown in Figure 6b, which are comparable to atactic PS except that the mixed ABA exhibits the average behavior of meso and racemic ABA angle distributions. The BAB angle exhibits different characteristics for meso and racemic type of B beads (Figure 6c); however, the ABC shows a single peak at 160° (Figure 6d). The ABAB and BABC dihedral angle distributions show disparate characteristic for meso and racemic. The 1−5 distance distributions were also extracted for A and B beads. Since C is not directly attached to the backbone, the 1−5 distance distribution for C bead was not maintained by additional potential. These distributions were inverted in similar fashion as for PS to obtain the corresponding potential (Figure S5 of Supporting Information).

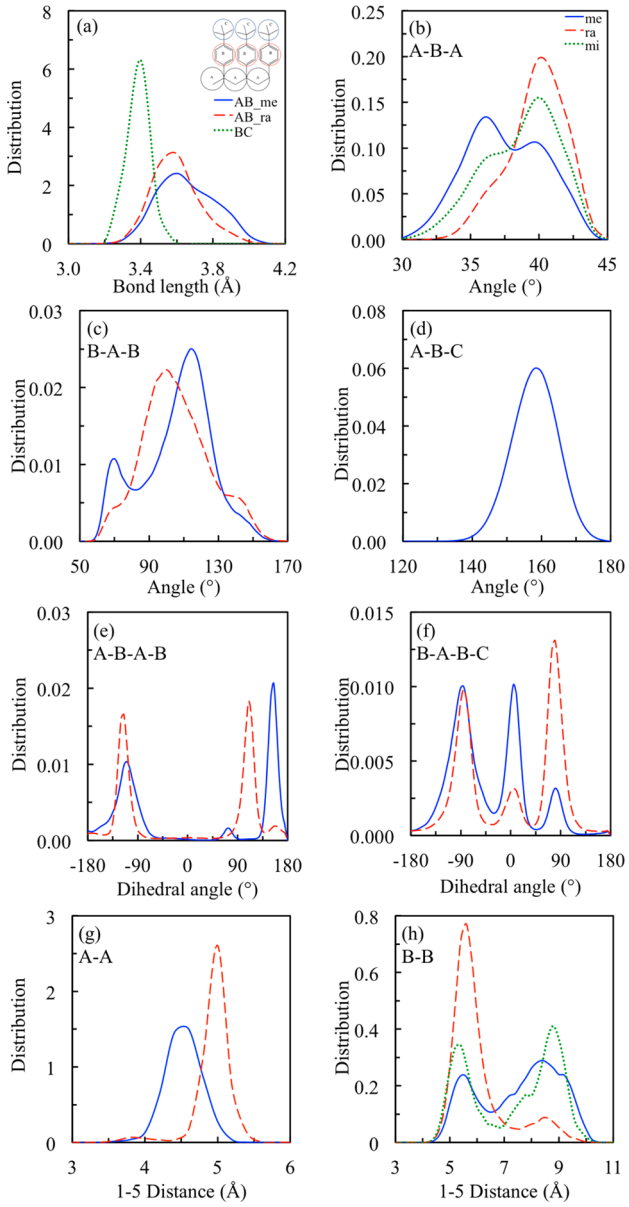

Figure 6. Bonded distribution functions for poly(4-*tert*-butylstyrene). (a) Bond distribution for AB meso type, AB racemic, and BC. (b) ABA angle distribution for meso, racemic, and mixed angles. (c) BAB angle distribution for meso and racemic and (d) ABC angle distribution. (e) ABAB dihedral angle distributions for meso and racemic and (f) BABC dihedral distriubtions for meso and racemic. The 1−5 distance distribution for (g) AA meso and racemic and (h) BB meso, racemic, and mixed.

The nonbonded potential for PtBS has six components AA, AB, AC, BB, BC, and CC. These were fitted simultaneously using the same process as described for PS. The initial guess for the nonbonded potential energy was taken from eq 6 where $g(r)$ is obtained from atomistic simulation, which was iterated using eq 8 with cutoff radius r_c = 1.0 nm and λ_1 = 0.1. A very good match with the atomistic RDF was obtained after 150 iterations with an average pressure of 400 atm. We then applied the pressure correction term as eq 9 with λ_2 = 0.05. After 17 additional iterations, we obtained very good agreement between the CG $g(r)$ and the atomistic $g(r)$ with pressure ∼1 atm. The comparison of CG and atomistic pair correlation functions is shown in Figure 7. The nonbonded potentials

dx.doi.org/10.1021/ma500319v | *Macromolecules* 2014, 47, 3210−3218

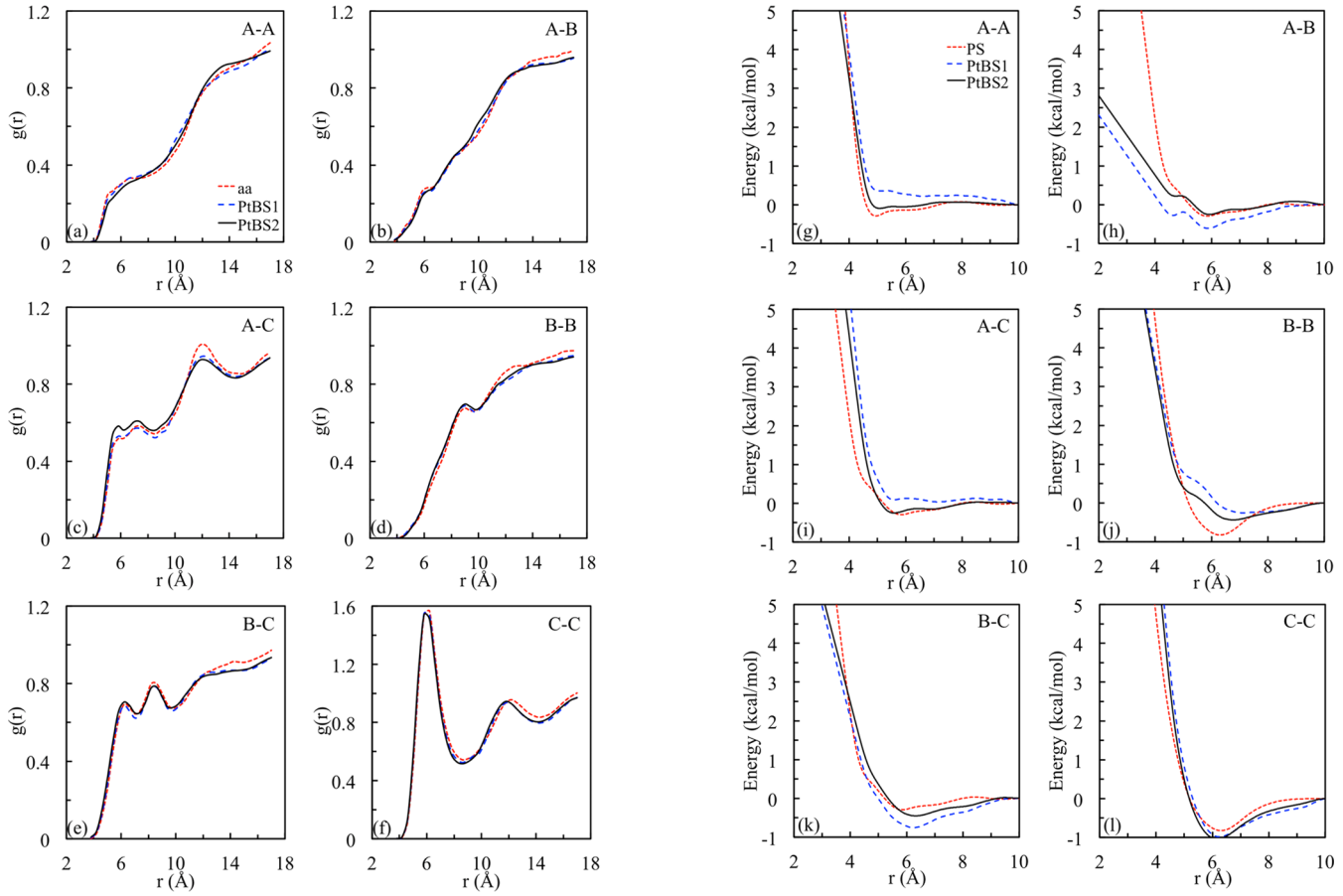

Figure 7. (a–f) Intermolecular radial distribution function of PtB obtained from PtBS1 and PtBS2. aa represents atomistic radial distribution function. (g–l) The nonbonded potential for PtBS for PtBS1 and PtBS2. The nonbonded potential PS is shown for comparison.

obtained using this methodology (labeled PtBS1) are also shown in Figure 7.

We also carried out the IBI procedure starting from the previous results for PS for the AA, AB, and BB nonbonded potential as a test of the methodology. For the nonbonded interactions involving the CG C bead, we used the AB potential of PS for the AC and BC potential of PtBS and BB potential of PS for CC. We chose BB potential to represent CC potential rather than the AA potential because B and C beads both belong to the side group whereas A represents backbone. We refer to this set of results as PtBS2. Since after a few iterations at constant volume, the pressure became negative, we applied the pressure correction term from the start such that

$$U_{i+1} = U_i + \lambda_1 k_B T \ln\left(\frac{g_i(r)}{g(r)}\right) - (P_i - P)\lambda_2 V_{atom}\left(1 - \frac{r}{r_c}\right) \quad (10)$$

with λ_1 and λ_2 are constants and their values are taken as 0.1 and 0.05, respectively. After 20 iterations, we were able to get reasonable RDF (as shown in Figure 7) and density at P = 1 atm. With additional iterations, the pressure became negative again. The potential obtained in this way show attractive minima for all the nonbonded components of PtBS. This gave AA, AB, and BB potential comparable to PS potentials. The RDF and nonbonded potentials are shown in Figure 7 as PtBS2. The agreement between $g(r)$ for AA from PtBS1 with atomistic RDF is slightly better than for PtBS2. The agreement is comparable between PtBS1 and PtBS2 for all other components of $g(r)$.

A third approach (PtBS3) is to keep A and B interactions from PS fixed and iterate only the nonbonded interactions containing C beads. We iterated the three nonbonded potentials including the C bead based on this approach; however, the pressure quickly became negative even if we include the pressure correction from the beginning of the IBI. After additional iterations, the system phase separated into a denser melt phase and vacuum. Similarly using the PtBS1 or PtBS2 potential for PS does not give a good fit to $g(r)$. Also, the pressure is 500 atm instead of 1 atm. The fact that the addition of the *tert*-butyl required a reparameterization of the original PS potential is consistent with previous results of Sun et al.,[42] who found similar effects for polystyrene/polyisoprene blends.

The two potentials PtBS1 and PtBS2 are in general similar in their characteristics, e.g., position of minima match well. However, the PtBS2 potential exhibits a stronger attractive minimum than PtBS1 for most pairs except for AB and BC. The CC interaction is essentially the same for both the potentials, which could be due to its strong RDF peak. The density of longer chain systems calculated using these potentials is given in Table 2.

The densities obtained using this coarse-grained model increase with chain length as expected. No further parameters were needed to explicitly incorporate the chain length.

dx.doi.org/10.1021/ma500319v | *Macromolecules* 2014, 47, 3210–3218

Table 2. Coarse-Grained PtBS Systems Studied in the Present Work at T = 500 K and P = 1 atm

M_w (kDa)	no. beads/chain	no. of chains	t_r (ns)	density (g/cm^3) PtBS1	density (g/cm^3) PtBS2
3.2	60	1280	1	0.847	0.846
8.0	150	384	20	0.857	0.856
32.0	600	162	15	0.862	0.862

5. CONCLUSIONS

In this paper, we have developed a methodology based on all-atom simulation of a single atactic PS melt to determine all the intramolecular and intermolecular interactions for a coarse-grained model for PS and its derivatives. We have successfully shown that once the model is developed for the base polymer, it is relatively easy to build on the model for its derivatives as we have shown for PS and PtBS. Results for the density as a function of chain length for PS are in excellent agreement with experiment. Models developed in this manner could easily be used to study the dynamics of polymers at homogeneous as well as heterogeneous interfaces. These potentials could also be extended to study block copolymers and other PS analogues.

■ ASSOCIATED CONTENT

Supporting Information

Figures S1–S5. This material is available free of charge via the Internet at http://pubs.acs.org.

■ AUTHOR INFORMATION

Corresponding Author

*E-mail dperahi@g.clemson.edu (D.P.).

Notes

The authors declare no competing financial interest.

■ ACKNOWLEDGMENTS

The authors thank Kurt Kremer for helpful discussions and gratefully acknowledge financial support from DOE Grant No. DE-FG02-12ER46843 and NSF Grant No. DMR-1006805. This research was supported in part by the National Science Foundation under Grant No. NSF PHY11-25915. This research used resources at the National Energy Research Scientific Computing Center, which is supported by the Office of Science of the United States Department of Energy, under Contract No. DE-AC02-05CH11231. This work was made possible by advanced computational resources deployed and maintained by Clemson Computing and Information Technology. This work was performed, in part, at the Center for Integrated Nanotechnology, a U.S. Department of Energy and Office of Basic Energy Sciences user facility. Sandia National Laboratories is a multiprogram laboratory managed and operated by Sandia Corporation, a wholly owned subsidiary of Lockheed Martin Corporation, for the U.S. Department of Energy's National Nuclear Security Administration under Contract No. DE-AC04-94AL85000.

■ REFERENCES

(1) Harmandaris, V. A.; Kremer, K. *Soft Matter* **2009**, *5*, 3920.
(2) Karimi-Varzaneh, H. A.; van der Vegt, N. F. A.; Müller-Plathe, F.; Carbone, P. *ChemPhysChem* **2012**, *13*, 3428.
(3) Ruocco, N.; Dahbi, L.; Driva, P.; Hadjichristidis, N.; Allgaier, J.; Radulescu, A.; Sharp, M.; Lindner, P.; Straube, E.; Pyckhout-Hintzen, W.; Richter, D. *Macromolecules* **2013**, *46*, 9122.
(4) Li, Y.; Abberton, B. C.; Kröger, M.; Liu, W. K. *Polymers* **2013**, *5*, 751.
(5) Brini, E.; Algaer, E. A.; Ganguly, P.; Li, C.; Rodriguez-Ropero, F.; van der Vegt, N. F. A. *Soft Matter* **2013**, *9*, 2108.
(6) Kremer, K.; Grest, G. S. *J. Chem. Phys.* **1990**, *92*, 5057.
(7) Tschöp, W.; Kremer, K.; Batoulis, J.; Bürger, T.; Hahn, O. *Acta Polym.* **1998**, *49*, 61.
(8) Tschöp, W.; Kremer, K.; Batoulis, J.; Bürger, T.; Hahn, O. *Acta Polym.* **1998**, *49*, 75.
(9) Müller-Plathe, F. *ChemPhysChem* **2002**, *3*, 754.
(10) Reith, D.; Pütz, M.; Müller-Plathe, F. *J. Comput. Chem.* **2003**, *24*, 1624.
(11) Tozzini, V. *Curr. Opin. Struct. Biol.* **2005**, *15*, 144.
(12) Praprotnik, M.; Delle Site, L.; Kremer, K. *J. Chem. Phys.* **2005**, *123*, 224106.
(13) Milano, G.; Müller-Plathe, F. *J. Phys. Chem. B* **2005**, *109*, 18609.
(14) Sun, Q.; Faller, R. *Comput. Chem. Eng.* **2005**, *29*, 2380.
(15) Voth, G. A., Ed.; *Coarse-Graining of Condensed Phase and Biomolecular Systems*; Taylor & Francs: London, 2008.
(16) Izvekov, S.; Parrinello, M.; Burnham, C. J.; Voth, G. A. *J. Chem. Phys.* **2004**, *120*, 10896.
(17) Lyubartsev, A. P.; Laaksonen, A. *Phys. Rev. E* **1995**, *52*, 3730.
(18) Lyubartsev, A. P.; Karttunen, M.; Vattulainen, I.; Laaksonen, A. *Soft Mater.* **2003**, *1*, 121.
(19) Soper, A. K. *Chem. Phys.* **1996**, *202*, 295.
(20) Ercolessi, F.; Adams, J. B. *Europhys. Lett.* **1994**, *26*, 583.
(21) Das, A.; Andersen, H. C. *J. Chem. Phys.* **2010**, *132*, 164106.
(22) Leon, S.; Delle Site, L.; van der Vegt, N.; Kremer, K. *Macromolecules* **2005**, *38*, 8078.
(23) Rühle, V.; Junghans, C.; Lukyanov, A.; Kremer, K.; Andrienko, D. *J. Chem. Theory Comput.* **2009**, *5*, 3211.
(24) Peter, C.; Kremer, K. *Soft Matter* **2009**, *5*, 4357.
(25) Chaimovich, A.; Shell, M. S. *J. Chem. Phys.* **2011**, *134*, 094112.
(26) Rudzinski, J. F.; Noid, W. G. *J. Chem. Phys.* **2011**, *135*, 214101.
(27) Harmandaris, V. A.; Adhikari, N. P.; van der Vegt, N. F. A.; Kremer, K. *Macromolecules* **2006**, *39*, 6708.
(28) Harmandaris, V. A.; Reith, D.; van der Vegt, N. F. A.; Kremer, K. *Macromol. Chem. Phys.* **2007**, *208*, 2109.
(29) Harmandaris, V. A.; Kremer, K. *Macromolecules* **2009**, *42*, 791.
(30) Fritz, D.; Harmandaris, V. A.; Kremer, K.; van der Vegt, N. F. A. *Macromolecules* **2009**, *42*, 7579.
(31) Fritz, D.; Koschke, K.; Harmandaris, V. A.; van der Vegt, N. F. A.; Kremer, K. *Phys. Chem. Chem. Phys.* **2011**, *13*, 10412.
(32) Rossi, G.; Monticelli, L.; Puisto, S. R.; Vattulainen, I.; Ala-Nissila, T. *Soft Matter* **2011**, *7*, 698.
(33) Spyriouni, T.; Tzoumanekas, C.; Theodorou, D.; Müller-Plathe, F.; Milano, G. *Macromolecules* **2007**, *40*, 3876.
(34) Qian, H. J.; Carbone, P.; Chen, X.; Karimi-Varzaneh, H. A.; Liew, C. C.; Müller-Plathe, F. *Macromolecules* **2008**, *41*, 9919.
(35) Ghanbari, A.; Ndoro, T. V. M; Leroy, F.; Rahimi, M.; Bohm, M. C.; Müller-Plathe, F. *Macromolecules* **2012**, *45*, 572.
(36) Sun, Q.; Faller, R. *J. Phys. Chem. B* **2005**, *109*, 15714.
(37) Sun, Q.; Faller, R. *Macromolecules* **2006**, *39*, 812.
(38) Bayramoglu, B.; Faller, R. *Macromolecules* **2012**, *45*, 9205.
(39) Bayramoglu, B.; Faller, R. *Macromolecules* **2013**, *46*, 7957.
(40) Harmandaris, V. A.; Floudas, G.; Kremer, K. *Macromolecules* **2011**, *44*, 393.
(41) Li, X.; Kou, D.; Rao, S.; Liang, H. *J. Chem. Phys.* **2006**, *24*, 204909.
(42) Sun, Q.; Pon, F. R.; Faller, R. *Fluid Phase Equilib.* **2007**, *261*, 35.
(43) Jorgensen, W. L.; Madura, J. D.; Swenson, C. J. *J. Am. Chem. Soc.* **1984**, *106*, 6638.
(44) Jorgensen, W. L.; Maxwell, D. S.; Tirado-Rives, J. *J. Am. Chem. Soc.* **1996**, *118*, 11225.
(45) Isele-Holder, R. E.; Mitchell, W.; Ismail, A. E. *J. Chem. Phys.* **2012**, *137*, 174107.
(46) Plimpton, S. *J. Comput. Phys.* **1995**, *117*, 1.
(47) "Materials Studio", Accelrys Software Inc., 2001–2007.

(48) Zoller, P.; Walsh, D. J. *Standard Pressure*; Technomic: Lancaster, 1995; Vol. *1*, pp 132−140.
(49) Mei, J.; Davenport, J. W.; Fernando, G. W. *Phys. Rev. B* **2011**, *43*, 4653.
(50) Wang, H.; Junghans, C.; Kremer, K. *Eur. Phys. J. E* **2009**, *28*, 221.
(51) Li, Y.; Kroger, M.; Liu, W. K. *Polymer* **2011**, *52*, 5867.

Healing of polymer interfaces: Interfacial dynamics, entanglements, and strength

Ting Ge,[1] Mark O. Robbins,[1] Dvora Perahia,[2] and Gary S. Grest[3]
[1]*Department of Physics and Astronomy, Johns Hopkins University, Baltimore, Maryland 21218, USA*
[2]*Department of Chemistry, Clemson University, Clemson, South Carolina 29634, USA*
[3]*Sandia National Laboratories, Albuquerque, New Mexico 87185, USA*
(Received 26 March 2014; published 25 July 2014)

Self-healing of polymer films often takes place as the molecules diffuse across a damaged region, above their melting temperature. Using molecular dynamics simulations we probe the healing of polymer films and compare the results with those obtained for thermal welding of homopolymer slabs. These two processes differ from each other in their interfacial structure since damage leads to increased polydispersity and more short chains. A polymer sample was cut into two separate films that were then held together in the melt state. The recovery of the damaged film was followed as time elapsed and polymer molecules diffused across the interface. The mass uptake and formation of entanglements, as obtained from primitive path analysis, are extracted and correlated with the interfacial strength obtained from shear simulations. We find that the diffusion across the interface is significantly faster in the damaged film compared to welding because of the presence of short chains. Though interfacial entanglements increase more rapidly for the damaged films, a large fraction of these entanglements are near chain ends. As a result, the interfacial strength of the healing film increases more slowly than for welding. For both healing and welding, the interfacial strength saturates as the bulk entanglement density is recovered across the interface. However, the saturation strength of the damaged film is below the bulk strength for the polymer sample. At saturation, cut chains remain near the healing interface. They are less entangled and as a result they mechanically weaken the interface. Chain stiffness increases the density of entanglements, which increases the strength of the interface. Our results show that a few entanglements across the interface are sufficient to resist interfacial chain pullout and enhance the mechanical strength.

DOI: 10.1103/PhysRevE.90.012602 PACS number(s): 82.35.Gh, 81.20.Vj, 68.35.Fx, 83.10.Mj

I. INTRODUCTION

Polymer interfaces are in the core of numerous devices. Understanding the structure and mechanical response of polymers in the interfacial region is a key to their utilization as coatings and adhesives, as well as in nanofabrication and many other applications [1–3]. One important mechanism for strengthening interfaces is interdiffusion of polymers between opposing sides [1,4–13]. This diffusion is an integral part of making welded joints. It also underlies the remarkable ability of polymers to heal after fracturing or being scratched. Both welding and healing processes often involve heating the polymer interface into the melt state for a certain time period and then quenching below the glass transition temperature T_g where the translational motion of the molecules is essentially arrested. The goal is to achieve an interface with strength equal to that of the bulk. The main difference between the two processes is the composition of the interface since homogeneity of welded interfaces can be well controlled, whereas damaged interfaces contain chains of multiple lengths.

The mechanical strength of a polymeric interface is achieved by molecular mechanisms that transfer stress across the boundary between the films. Numerous studies have shown that entanglements and friction between chains from opposite sides of the interface are among the major factors that control interfacial strength. Entanglements [14,15] are topological constraints that arise because polymers are long and have strong covalent bonds that prevent them from passing through each other. Friction arises from van der Waals interactions between the polymers, which resist sliding of the molecules past each other [16,17]. Both processes help anchor chains in opposing sides of the interface and impact the interfacial strength. These processes are expected to be strongly affected by the nature of the polymer, including direct chemical interactions, total length of the molecules, and their stiffness. As noted above, the distribution of chain lengths may differ for welding and healing, since fracture can produce a broad distribution of chain lengths that impacts the healing process. In this paper we contrast the evolution of strength during welding and healing and examine the effect of chain stiffness on healing.

The significance of recovering bulk strength has led to a concerted effort to extract the factors that govern the strength of an interface. Neutron reflectometry studies by Kunz and Stamm [18] followed the initial interdiffusion of polymers across an interface and distinguished different characteristic times for broadening of the interface. Experimental studies by Schnell *et al.* [16,19] and Brown [20] have shown that the mechanical tensile strength at polymer interfaces correlates very well with the interfacial width. Interfacial width was measured by neutron reflectivity, while the interfacial strength was characterized by fracture toughness determined from a double cantilever beam test. Schnell *et al.* [16] showed that the rise of interfacial toughness under tension is related to the transition of the failure mechanism from simple chain pullout to crazing at the interface. Recently, McGraw *et al.* [21] have performed crazing measurements to probe the interdiffusion between two thin films of entangled polymers and showed that it takes less than one bulk reptation time to observe the structural characteristics of bulk crazes at the interface. Similar conclusions about the recovery of interfacial strength have been obtained from lap-joint shear tests [22–25]. These studies determined the ultimate shear stress at failure and correlated it with interdiffusion time.

Theoretical and computational studies have further probed the dynamics of polymers at interfaces, providing detailed insight into the location and conformation of macromolecules. For miscible polymers, reptation dynamics, which was originally introduced by de Gennes [14] and later refined by Doi and Edwards [15] to explain the dynamics of entangled chains in bulk melt, was able to describe [1,4,6–10] diffusion across a polymer interface in a welding process. For immiscible polymers in which interpenetration of the films is limited, Helfand and Tagami [26,27] calculated the equilibrium interfacial density profile using mean-field theory.

Computer [28–33] simulations have been performed to study the interdiffusion across both miscible and immiscible polymer joints. For miscible polymers, results of Monte Carlo simulations [29] of a lattice polymer model showed that the mass uptake between polymers agrees with the prediction of reptation dynamics. However, our recent molecular dynamics (MD) simulations [31,32] of thermal welding of two thin films of identical monodispersed polymers showed that the interfacial dynamics is controlled by the motion of chain ends and is faster than predicted by reptation dynamics. For immiscible polymers, both Monte Carlo [28,30] and MD simulations [33] have found that the immiscibility arrests the interdiffusion and limits the equilibrium interfacial width.

Recently, we have probed the interfacial strength of polymer interfaces in our molecular dynamics simulations [32,33] using a shear test that is similar to lap-joint shear experiments [22–25]. For miscible polymers, the interfacial strength increases with interdiffusion time and saturates at the bulk strength. The dominant failure mode changes from pure chain pullout at the interface for short welding times to chain scission for long welding times, as in bulk failure. In contrast, even for weakly immiscible polymers, the narrow interface is unable to transfer stress upon deformation as effectively as the bulk polymer, and chain pullout at the interface is the dominant failure mode. These studies have shown that, as expected, entanglements play a critical role in resisting chain pullout and enhancing the interfacial strength.

In this work, we probe the interface between two polymeric films that were cut and allowed to heal as illustrated in Fig. 1. In contrast to thermal welding of separate parts of identical polymers [1,4–7,10,12,13,22–25], scission of polymers results in formation of interfaces that consist of chains of multiple lengths. This polydispersity is key to the dynamics of healing of polymer films. Simulation results for healing are compared with previous findings for thermal welding. The strength of a healed interface formed by polymers with different stiffness is probed and related to the molecular mechanisms of deformation and failure. These studies are correlated with the local density of entanglements extracted from primitive path analysis, a recent methodology developed to enable one to identify and track the evolution of entanglements [34–36]. These simulations allow a direct measurement of various parameters that characterize the interfacial structure and reveal correlations between them and the interfacial strength.

Section II presents the simulation model and methodology used in this study. Then Secs. III A and III B present results for the diffusion dynamics and the evolution of molecular and entanglement structure at the interface during healing. An analysis of the evolution of interfacial strength is presented in Sec. III C, highlighting the effects of polydispersity and chain stiffness. Finally a summary and conclusions are given in Sec. IV.

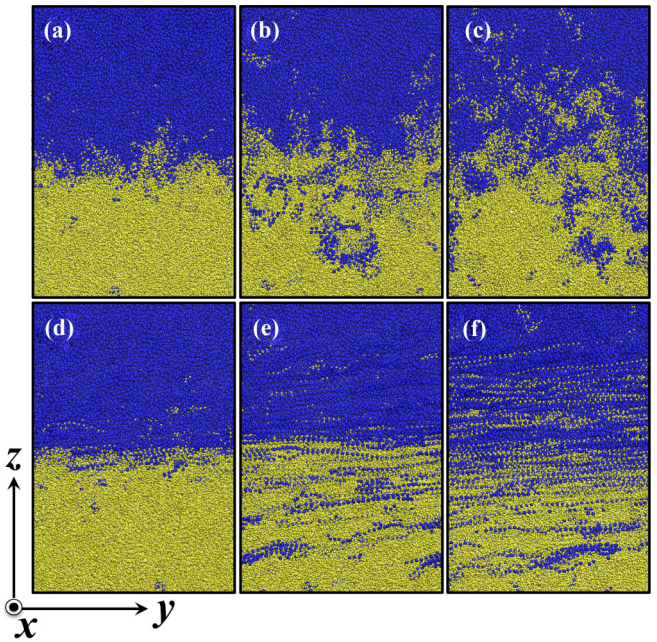

FIG. 1. (Color online) Snapshots showing the evolution of the interface due to interdiffusion and shear after bonds crossing the plane $z = 0$ are cut. Beads are colored based on their positions before the cut: $z > 0$ (blue) and $z < 0$ (yellow). For clarity only a portion of the sample, $40a$ by $60a$ in the y-z plane and $10a$ deep along x is shown. Snapshots (a)–(c) depict the interface at interdiffusion times $t = 0.01M\tau$, $0.5M\tau$, and $7M\tau$, respectively. Snapshots (d)–(f) show the corresponding states after a large shear strain $\gamma = 12$ along y. Chains have initial length $N = 500$ and $T = 0.2u_0/k_B$.

II. MODEL AND METHODOLOGY

A. Simulation model

Here we employ a coarse-grained bead-spring model [37] that captures well the properties of linear homopolymers. Each polymer chain initially contains $N = 500$ spherical beads of mass m. Beads interact via the truncated and shifted Lennard-Jones potential,

$$U_{\mathrm{LJ}}(r) = 4u_0[(a/r)^{12} - (a/r)^6 - (a/r_c)^{12} + (a/r_c)^6], \quad (1)$$

where r is the distance between beads, r_c is the cutoff radius, and $U_{\mathrm{LJ}}(r) = 0$ for $r > r_c$. All quantities are expressed in terms of the molecular diameter a, the binding energy u_0, and the characteristic time $\tau = a(m/u_0)^{1/2}$. To provide a rough mapping to hydrocarbon polymers we take $a \sim 0.5$ nm, which is a typical interpolymer distance, and a binding energy of order the glass transition temperature, $u_0 \sim 40$ meV. One then finds the units of force and stress are $u_0/a \sim 13$ pN and $u_0/a^3 \sim 50$ MPa, respectively. The latter is of the same order as yield stresses in glassy polymers.

For equilibration and healing runs we used the unbreakable finitely extensible nonlinear elastic (FENE) potential [37] to

bond adjacent monomers along the backbone,

$$U_{\mathrm{FENE}}(r) = -\tfrac{1}{2}kR_0^2 \ln[1-(r/R_0)^2], \quad (2)$$

with $R_0 = 1.5a$ and $k = 30u_0a^{-2}$ [37]. For mechanical tests, chain scission plays an essential role and a simple quartic potential was used as follows:

$$U_Q(r) = K(r-R_c)^2(r-R_c)(r-R_c-B)+U_0, \quad (3)$$

with $K = 2351u_0/k_B$, $B = -0.7425a$, $R_c = 1.5a$, and $U_0 = 92.74467u_0$. This potential provides the same equilibrium bond length as U_{FENE} and prevents chains from crossing. The bonds break at a force $f_b = 240u_0/a$ that is ~100 times higher than the maximum attractive force for the interchain U_{LJ}. This force ratio has been used in previous simulations [38–41] and is supported by typical experimental values [42,43]. From the mapping to hydrocarbons in the previous paragraph, one finds $f_b = 240u_0/a \sim 3$ nN. This is comparable to experimental estimates [42,43] and density-functional-theory results (~6 nN) for the force needed to break pentane backbone bonds [44]. Simulations with a range of potentials show that the breaking force is the most important aspect of the quartic potential and its influence is discussed briefly in Sec. III C.

An additional bond bending potential,

$$U_B(\theta) = k_{\mathrm{bend}}(1+\cos\theta), \quad (4)$$

is used to vary chain stiffness, where θ is the angle between two consecutive bonds along the chain. Varying chain stiffness serves as a means to change the entanglement spacing. As k_{bend} increases, the entanglement length N_e decreases and polymer chains become more entangled. Previous studies [45–47] find that for $k_{\mathrm{bend}}/u_0 = 0$, 0.75, and 1.5 the corresponding N_e is approximately 85, 39, and 26, respectively. Experiments and simulations [1,48] show that the mechanical response becomes independent of chain length for N/N_e larger than 6 to 12. We choose $N = 500$ to be in this limit for all k_{bend}.

All simulations were carried out using the LAMMPS parallel MD code [49]. The equations of motion were integrated using a velocity-Verlet algorithm. For equilibration and healing runs, the time step $\delta t = 0.01\tau$, while for shear strength tests the time step was reduced to $\delta t = 0.005\tau$. The temperature T was held constant for the equilibration and healing runs by a Langevin thermostat with a damping constant $\Gamma = 0.1\tau^{-1}$ [37]. For the shear runs $\Gamma = 1\tau^{-1}$, and it was applied only in the x direction to avoid biasing the flow. A million τ will be abbreviated as $1M\tau$.

B. Bulk simulations

To identify the relevant time and length scales for chain diffusion, we performed simulations of self-diffusion in bulk samples. Three samples consisting of $M = 500$ chains of length $N = 500$ and $k_{\mathrm{bend}}/u_0 = 0$, 0.75, and 1.5, respectively, were constructed using the standard methodology discussed by Auhl *et al.* [50]. The unit cell was cubic and periodic boundary conditions were applied in all directions. Samples were then equilibrated at pressure $P = 0$ and $T = 1.0u_0/k_B$ in an NPT simulation with $r_c = 2.5a$. The root-mean-square radius of gyration $\langle R_g^2\rangle^{1/2}/a = 11.9 \pm 0.1$, 13.1 ± 0.1, and 15.1 ± 0.1 for $k_{\mathrm{bend}}/u_0 = 0$, 0.75, and 1.5, respectively. The mean-squared end-to-end distance $\langle R^2\rangle = 6.0 \pm 0.02\langle R_g^2\rangle$ in all three cases, as expected for Gaussian chains.

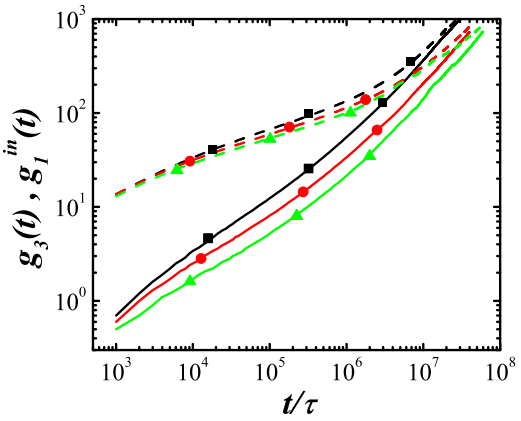

FIG. 2. (Color online) Mean-squared displacement for the center-of-mass $g_3(t)$ (solid lines) and the center 10 individual beads of the chain $g_1^{\mathrm{in}}(t)$ (dashed lines) during self-diffusion in bulk systems with $N = 500$ and $k_{\mathrm{bend}}/u_0 = 0$ (black squares), 0.75 (red circles), and 1.5 (green triangles).

After equilibration, simulations were run for $80M\tau$ for $k_{\mathrm{bend}}/u_0 = 1.5$ and $50M\tau$ for $k_{\mathrm{bend}}/u_0 = 0.75$ and 0. Results for the mean-squared displacement for the chain center of mass (c.m.) $g_3(t) = \langle(\mathbf{r}_{\mathrm{c.m.}}(t) - \mathbf{r}_{\mathrm{c.m.}}(0))^2\rangle$, and the center 10 individual beads of the chain $g_1^{\mathrm{in}}(t) = \langle(\mathbf{r}_i(t) - \mathbf{r}_i(0))^2\rangle$ are shown in Fig. 2. Based on the tube model [15,45], the increase of $g_1^{\mathrm{in}}(t)$ should cross over from $t^{1/2}$ to $t^{1/4}$ scaling, and that of $g_3(t)$ from t to $t^{1/2}$, when entanglements set in at the entanglement time τ_e. From Fig. 2 we estimate that $\tau_e = 10^4\tau$, $6\times10^3\tau$, and $4\times10^3\tau$ for $k_{\mathrm{bend}} = 0$, 0.75, and 1.5, respectively. As expected, the decrease in N_e with increasing chain stiffness lowers τ_e.

Stronger entanglement effects associated with smaller N_e prolong the disentanglement time τ_d that is required for the entire chain to diffuse by a distance on the order of $\langle R^2\rangle^{1/2}$ and get disentangled from the initial confining chains at $t = 0$. At the disentanglement time there is a crossover to the diffusive regime where both $g_1^{\mathrm{in}}(t)$ and $g_3(t)$ increase linearly with time. For $k_{\mathrm{bend}}/u_0 = 0$, the two curves in Fig. 2 overlap near $\tau_d \sim 30M\tau$ and the mean-squared displacement reaches $\langle R^2\rangle$ at about $25M\tau$. For $k_{\mathrm{bend}}/u_0 = 0.75$ and 1.5, τ_d is larger than the times which are presently accessible by simulation. Extrapolating to the points where the curves would reach $\langle R^2\rangle$ gives values of τ_d that are of order $60M\tau$ and $120M\tau$ for $k_{\mathrm{bend}} = 0.75$ and 1.5, respectively.

C. Interface simulations

For the healing studies, we constructed three films of $M = 9600$ chains of length $N = 500$ beads or a total of 4.8 million beads with $k_{\mathrm{bend}}/u_0 = 0$, 0.75, and 1.5. Periodic boundary conditions were applied along the x and y directions with dimensions $L_x = 700a$ and $L_y = 40a$. The thickness in the z direction was maintained at $L_z = 200a$ using two repulsive confining walls. Snapshots in Fig. 1 illustrate part of the cross section of such a thin film in the yz plane. After construction, all films were well equilibrated at a temperature $T = 1.0u_0/k_B$

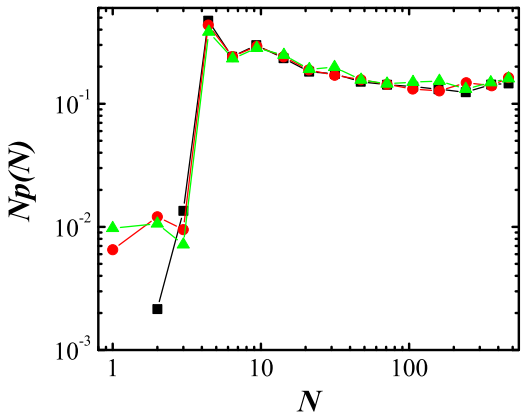

FIG. 3. (Color online) The probability $Np(N)$ that a monomer is in a cut segment of length N for $k_{\rm bend}/u_0 = 0$ (black squares), 0.75 (red circles), and 1.5 (green triangles). Uncut chains are not included in the statistics.

and pressure $P = 0$ with $r_c = 2.5a$, by allowing expansion and contraction along the x direction. The total change in L_x was minimal ($\sim$2%) and the final monomer density of all systems was $\rho a^3 = 0.89$.

A fracture plane was introduced by cutting almost all bonds that crossed the middle plane at $z = 0$. An exception was made when two crossing bonds were separated by less than three monomers. In this case only one of the bonds was cut to minimize the number of extremely short chains. A small number of bonds with length 3 and below are formed from chains that cross the midplane near a chain end. Both the bonding potential and any bond bending terms associated with cut bonds were removed from the Hamiltonian.

Figure 3 shows the resulting distribution of segment lengths from cut chains. The probability $p(N)$ that a segment has length N scales roughly as $1/N$. This means that the probability $Np(N)$ of a monomer being in a chain of length N is nearly independent of N. The probability distribution is nearly independent of chain stiffness, but there is an increase in the total number of cut segments with increasing stiffness (8691, 9507, and 10047 for $k_{\rm bend}/u_0 = 0$, 0.75, and 1.5, respectively). Stiffer chains are less likely to bend back across the interface, so more chains are cut into fewer pieces. Since n cuts produce $n + 1$ segments, the same number of cut bonds leads to more segments. The suppression of cut segments of length less than 3 also has less impact on stiffer chains.

After bond cutting, the systems were held at $k_BT = 1.0u_0$ and allowed to interdiffuse. Configurations for a series of healing times were then quenched rapidly below the glass temperature $T_g \approx 0.35u_0/k_B$. First, the cutoff radius was reduced to $r_c = 1.5a$, in order to facilitate comparison with past mechanical studies [38,48,51–53] and reduce the difference between melt and glass densities and thus chain conformations. Then the temperature was quenched at constant volume with a rate $\dot{T} = -10^{-3}u_0/(k_B\tau)$ to $T = 0.5u_0/k_B$, where $P = 0$. Subsequent quenching to $T = 0.2u_0/k_B$ was done at $\dot{T} = -2 \times 10^{-4}u_0/(k_B\tau)$ and $P = 0$. A Nose-Hoover barostat with time constant 50τ was applied to P_{xx} and P_{yy}. This quench protocol is rapid enough to preserve the interfacial structure produced by interdiffusion in the melt state at the given healing time. We verified that our conclusions were not sensitive to the details of the quench protocol or geometry. This is consistent with past experiments and simulations that find that the quench rate and aging affect the initial yield stress [54] but not strain hardening and failure [53,55]. Snapshots in the top row of Fig. 1 depict an interface during healing at three interdiffusion times after being quenched into the glassy state.

As in previous simulations [32], we determined the interfacial strength using a shear test that is similar to a lap-joint shear experiment [22–25]. To focus on a region of width H near the interface, atoms in the top ($z > H/2$) and bottom ($z < -H/2$) layers were held rigid and displaced at constant velocity in opposite directions in the xy plane. In most cases $H = 50a$ and studies with double and quadruple this value produced little change in the maximum shear stress compared to statistical fluctuations (<5%). The shear direction had a bigger effect.

Results are presented for shear along the y axis ($L_y = 40a$) because they were more reproducible. The rigid top and bottom boundaries screen elastic interactions between regions separated by more than H. When the system is sheared along the y axis these different regions are effectively independent. Averaging over the system is equivalent to averaging over independent smaller simulations. To test this we calculated the local stress on regions of length $100a$ along the x axis ($L_x = 700a$). The deviations from the mean stress in each region are uncorrelated. This confirms that our simulations are equivalent to several independent realizations and allows us to estimate the statistical error in the average stress. The error in the peak stress is $\sim$2%, while the error is $\sim$4% at early stages of the shear test where the stress is lower. Similar estimates were obtained by comparing to simulations with $L_x = 180a$ and $L_y = 40a$. In contrast, when the system is sheared along the long x axis ($L_x = 700a$) different regions are coupled because shear causes them to pass over each other. When the interface achieves bulk strength, the initial failure occurs at different heights in different regions. If the sample is sheared along the long x axis, these failure zones must be connected by diagonal shear planes and the peak stress varies by 20% with small changes in initial conditions. Experiments may involve much more complicated dissipation mechanisms and loading conditions, particularly under tensile testing [1–3].

The velocities of top and bottom rigid layers are chosen to produce an average strain rate in the film, $d\gamma/dt = 2 \times 10^{-4}\tau^{-1}$, that is low enough that it does not affect the mode of failure and stress has time to equilibrate across the system [56]. The shear stress σ is determined from the mean lateral force per unit area applied by the top and bottom layers and is consistent with the time average of the microscopic stress in the sample. All of the shear tests are run at a temperature $T = 0.2u_0/k_B$ to a large shear strain $\gamma \sim 12$. Snapshots in the bottom row of Fig. 1 illustrate the interfacial structure at large γ for different interdiffusion times.

Two additional geometries were studied to help calibrate and interpret the healing data. To determine the ideal strength of bulk samples we used systems with the same geometry and interactions but without cutting bonds. To compare healing of a fracture plane with welding of separate polymer parts, we also simulated welding of two polymer thin films using the same model [32]. Each film contained $M = 4800$ chains

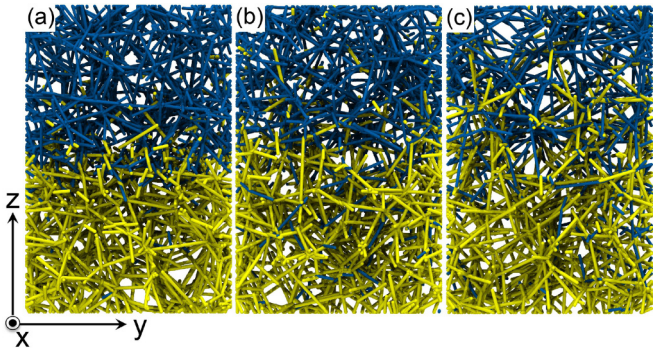

FIG. 4. (Color online) Snapshots of the primitive paths for the states in Figs. 1(a)–1(c). Beads are colored based on their positions before cutting: $z > 0$ (blue) and $z < 0$ (yellow).

of length $N = 500$ beads with $k_{\rm bend} = 0$. Dimensions in the xy plane were identical to those in the healing samples. The two films were well equilibrated, brought into close contact at the welding plane $z = 0$, and allowed to interdiffuse in the z direction at $T = 1.0u_0/k_B$. Simulation protocols for interdiffusion, quenching, and the subsequent mechanical test were all similar to those used for healing. More details can be found in our previous paper [32].

Entanglements in all states of different samples are identified using the primitive path analysis (PPA) algorithm [34]. Chain ends are frozen and tensile forces are introduced to shrink the contour length without allowing chain crossing. To limit excluded volume effects, the chain diameter is then reduced by a factor of 4 and the contour is minimized again [57]. The resulting configuration is a network of primitive paths. Figure 4 shows the primitive paths in a healing interface at different interdiffusion times. We identify the contacts between primitive paths as topological constraints (TCs) associated with entanglements. As in previous studies [36,57,58], the resulting density of TCs, $\rho_{\rm TC}$, is proportional to the density of entanglements, and variations in the density are not sensitive to the precise details of the identification procedure.

III. RESULTS

A. Interfacial dynamics

Cutting bonds at $z = 0$ introduces polydispersity in chain length near the interface that has strong consequences for both the shear strength and the dynamics of healing. Figure 5(a) shows the distribution of monomers from chains of different length shortly after cutting the $k_{\rm bend} = 0$ system. The probability of being on an uncut chain is strongly suppressed near $z = 0$, while most short segments are close to $z = 0$. The distribution of intermediate length segments has a double peak structure. While both ends of these segments are at the interface, the remainder is all on one side or the other. The longer the segment, the farther the center of mass is displaced from the midplane.

The self-diffusion constant D scales with N as N^{-1} for short chains but drops as N^{-2} for longer chains [15]. The crossover between these two regimes occurs near N_e when entanglements start to affect the dynamics. These variations in D lead to striking differences in the redistribution of segments

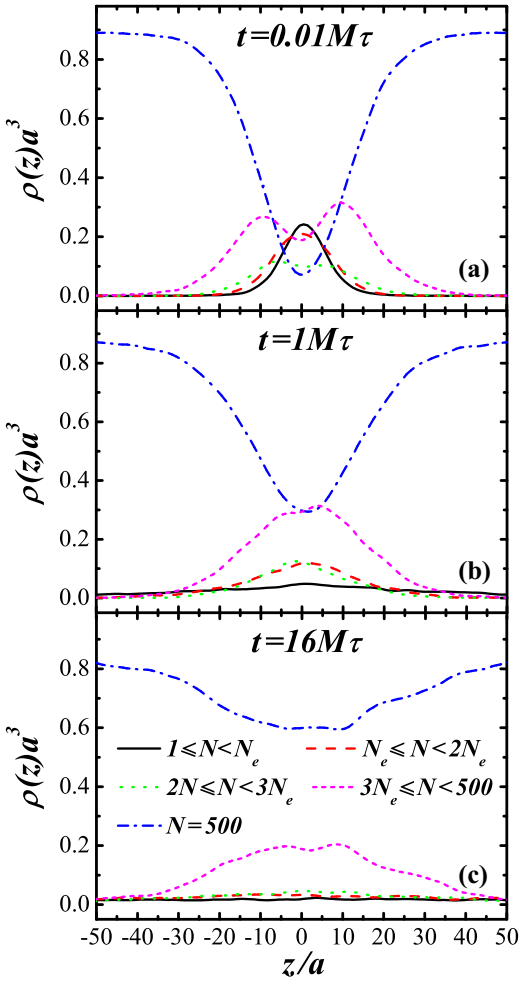

FIG. 5. (Color online) Density profiles $\rho(z)$ of monomers belonging to segments of the indicated length for fully flexible chains with $k_{\rm bend} = 0$ at (a) $t = 0.01M\tau$, (b) $1M\tau$, and (c) $16M\tau$. There are roughly equal numbers of monomers in segments of all length (Fig. 3), so the total number of monomers with $3N_e < N < 500$ is roughly 3 times larger than the number in the other length ranges which all have width N_e.

during healing. By $1M\tau$ [Fig. 5(b)], segments with $N < N_e$ have spread nearly uniformly throughout our finite system. For longer segments, the two initial peaks in $\rho(z)$ have merged into a single peak, whose width ($\sim 35a$) seems relatively insensitive to chain length. At the longest time, $16M\tau$, segments with $N < 3N_e$ have diffused away from the interface. Longer chains remain at the interface but are spread over a slightly wider range $\sim 50a$. As discussed below, the slow diffusion of these cut segments is important in the final approach to bulk strength.

Healing occurs by the diffusion of chains across the interface to create interfacial entanglements [1]. A common experimental measure is the mass uptake, which corresponds to the number of beads that have crossed to the opposite side of the initial interface. Figure 6(a) shows mass uptake per unit area, $M(t)$, as a function of time for healing samples with different stiffness and a welding sample with flexible chains. Increasing the chain stiffness lowers the rate of uptake. This is consistent with the slower diffusion of stiffer chains in Fig. 2 and each curve shows a small change in slope at a time that

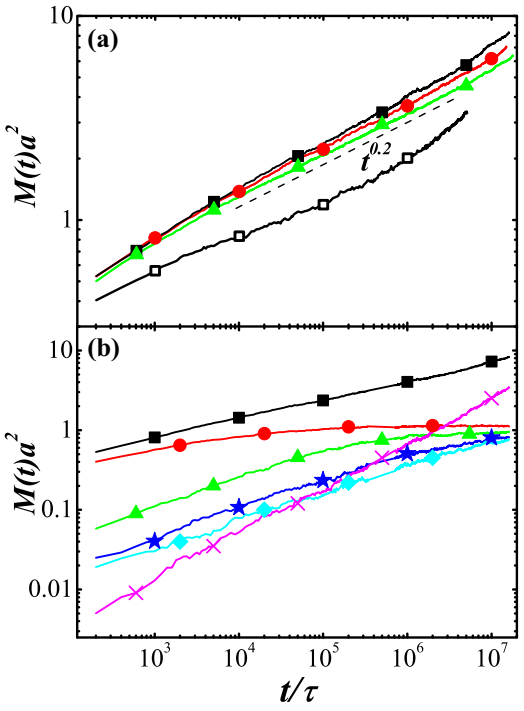

FIG. 6. (Color online) (a) Mass uptake per unit area $M(t)$ as a function of interdiffusion time t for healing samples with $k_{\rm bend}/u_0 = 0$ (black squares), 0.75 (red circles), and 1.5 (green triangles). A dashed line shows the $t^{0.2}$ scaling that curves follow at $t > t_e$. Also shown is $M(t)$ for a welding sample with $k_{\rm bend}/u_0 = 0$ (open black squares). (b) Mass uptake for all monomers (black squares) and monomers in segments with $1 \leqslant N < N_e$ (red circles), $N_e \leqslant N < 2N_e$ (green triangles), $2N_e \leqslant N < 3N_e$ (blue stars), $3N_e \leqslant N < 4N_e$ (cyan diamonds), and uncut chains (magenta crosses) during healing of a $k_{\rm bend} = 0$ sample.

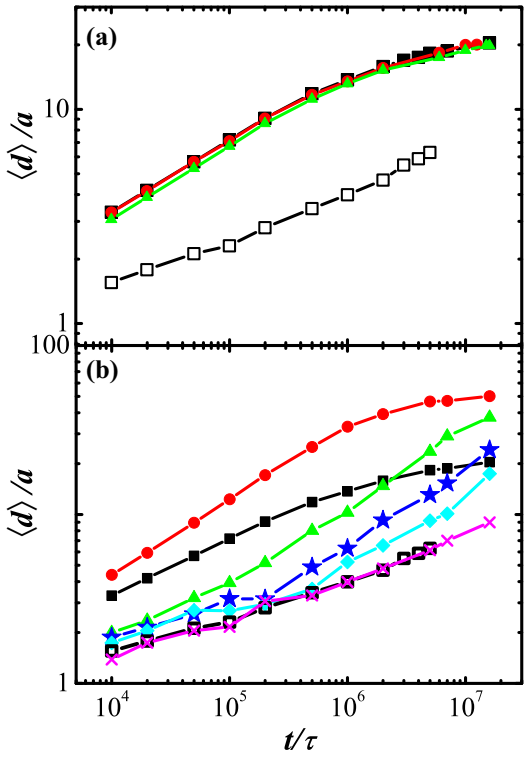

FIG. 7. (Color online) (a) Average interdiffusion depth $\langle d \rangle$ of monomers from one side into the opposite side for the same systems as in Fig. 6. (b) Separate averages for monomers in segments of the indicated lengths in healing of $k_{\rm bend} = 0$ chains and for all chains during welding (open squares). For healing, separate results are shown for all monomers (black squares) and monomers belonging to chains with $N < N_e$ (red circles), $N_e \leqslant N < 2N_e$ (green triangles), $2N_e \leqslant N < 3N_e$ (blue stars), $3N_e \leqslant N < 4N_e$ (cyan diamonds), and $N = 500$ (magenta crosses).

is comparable to the corresponding bulk τ_e. At longer times the healing curves all show an extended power-law regime $M(t) \sim t^{\alpha}$ with exponent $\alpha \approx 0.2$.

Theories for monodisperse chains predict that at short time the mass uptake should follow a power law consistent with Rouse dynamics in a tube, $M(t) \sim t^{\alpha}$ with $\alpha = 1/4$ [1,4,6–10]. The uptake should then cross over to the value of $\alpha = 1/8$ expected for reptation. All data for both healing and welding in Fig. 6 show a much faster uptake than expected from reptation. The results for welding are consistent with those obtained by Pierce *et al.* [31]. They associated the faster interdiffusion with faster motion of chain ends, which have a higher concentration near the welding interface. Here we find that diffusion of chains across the interface is significantly faster for healing than welding. Fracture produces a high density of short chains at the interface that diffuse rapidly (Fig. 5).

The importance of polydispersity is illustrated in Fig. 6(b), which shows the mass uptake associated with segments of different length for healing of flexible chains ($k_{\rm bend} = 0$). Unentangled segments ($N < N_e$) dominate the uptake at short times and progressively longer chains become important at later times. For each length the uptake saturates at long times when the chains have moved by a distance comparable to their initial distance from the interface, which is of order their radius of gyration. The curves saturate at the same uptake because they contain the same range of lengths and there are equal numbers of monomers in cut chains of each length (Fig. 3).

For each range of chain lengths the mass uptake rises with a power law higher than expected. For cut chains, $\alpha \sim 0.35$ instead of $1/4$. Over the entire time interval, the mass uptake of uncut chains increases as t^{α} with $\alpha = 0.56$. These higher-than-expected exponents do not represent superdiffusive motion of the chains in their tubes. Instead they reflect the minimum at $z = 0$ in the local density of monomers in longer chains immediately after cutting (Fig. 5). Fewer monomers in longer chains are available to diffuse across the interface at early times and the density of chains that can contribute to the mass uptake rises with time.

Another quantity of interest is how far monomers have moved across the interface, since a minimum distance is needed for entanglements to form [32,33,59]. Figure 7(a) shows the average interpenetration distance $\langle d \rangle$ for all monomers in healing samples of different stiffness and for welding of flexible chains. The rate of change decreases slightly with increasing chain stiffness and is higher for healing than welding because of the polydispersity in cut samples. Figure 7(b) shows the separate average interpenetration distances evaluated over monomers from segments of the indicated range of lengths in the case $k_{\rm bend} = 0$. For short,

unentangled chains, $\langle d \rangle$ rises in a nearly Fickian manner, $\sim t^{0.5}$, and then saturates. This saturation is a finite-size effect and the final value corresponds to monomers being evenly spread across the sample as evidenced by Fig. 5. In an infinite sample, these short segments would continue to leave the interfacial region. We show in Sec. III C 2 that their concentration is so low that they do not have a significant impact on interfacial strength.

As chain length increases, the rise in $\langle d \rangle$ approaches the $t^{1/4}$ time dependence expected for reptation. None of the entangled chains diffuse far enough for their motion to be limited by the finite system size. The behavior of uncut chains in healing and welding is nearly indistinguishable. This is surprising in light of the very different rates of mass uptake for healing and welding [Fig. 6(a)]. The suppression of $\rho(z)$ near $z = 0$ (Fig. 5) means that fewer uncut chains pass through the interface in healing than in welding. However, Fig. 7(b) shows that those that do pass through the interface travel about the same distance.

Zhang and Wool [60] calculated the concentration profile $\rho_1(z)$ for an interface between identical monodispersed polymers during welding for the minor chain model [8] and derived the time dependence of $\langle d \rangle$ and $M(t)$ from the evolution of $\rho_1(z)$. In particular, they found $M(t) \sim t^{3/4}$ from a $t^{1/4}$ increase in the number of chains crossing the interface and an average contour length rising as $t^{1/2}$. Later, Kim *et al.* [61] used the same method to study the healing of fractured polymers by interdiffusion. Compared with Zhang and Wool's results, they found that the increase of chain end density at the fracture plane leads to faster broadening of $\rho_1(z)$ and much larger $\langle d \rangle$ and $M(t)$ for the same diffusion time. Kim *et al.* also showed that the time dependence of $M(t)$ is changed from $t^{3/4}$ for welding to $t^{1/2}$ for fracture healing. While our results do show faster mass uptake for healing, they are not consistent with the predicted power laws over the time regime shown in Fig. 6. As we discuss in the next section, one reason is that the number of interfacial loops remains nearly constant, rather than rising as $t^{1/4}$.

B. Interfacial structure

Chains that diffuse across the interface do not necessarily contribute to the interfacial strength. One idea is that interfacial strength is related to loops along chains which extend into the opposing side and return. The friction needed to pull these loops out of the opposing side will resist interfacial failure and long loops will become entangled and provide even greater strength. We identified interfacial loops by searching along each chain for segments that cross $z = 0$ and return. Because thermal fluctuations lead to a blurring of the interface, only loops of length $l > 3$ monomers are included in the analysis.

The growth of the average length $\langle l \rangle$ of interfacial loops with time t for healing samples with different chain stiffness and welding of fully flexible chains is shown in Fig. 8(a). As before, increasing chain stiffness decreases diffusion and thus slows the growth of $\langle l \rangle$. More surprising is that the results for healing and welding samples with the same stiffness are almost the same.

Note that $\langle l \rangle$ does not depend explicitly on the total number of loops, which should also influence strength. Figure 8(c) shows the areal density of interfacial loops Σ for the same systems. Although $\langle l \rangle$ is nearly the same for healing and welding of flexible chains, the areal density of loops is slightly lower for welding at short times. Increasing chain stiffness increases the density of interfacial loops. In all cases, there is surprisingly little increase (<20%) in the number of loops over 3 decades in time. This is a striking contrast to the prediction of $t^{1/4}$ scaling by Zhang and Wool [60].

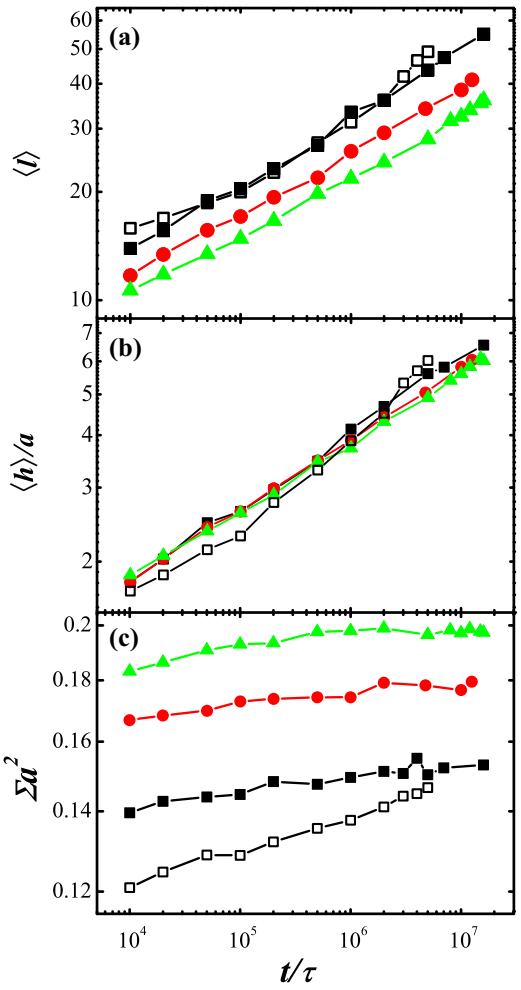

FIG. 8. (Color online) (a) Average contour length $\langle l \rangle$ and (b) average depth $\langle h \rangle$ of loops at the interface for the healing samples $k_{\text{bend}}/u_0 = 0$ (black squares), 0.75 (red circles), and 1.5 (green triangles), and the welding sample with $k_{\text{bend}} = 0$ (open black squares). (c) Time dependence of the areal density Σ of interfacial loops contributing to $\langle l \rangle$ and $\langle h \rangle$. Only interfacial loops that have more than three monomers are considered.

Loops that extend farther into the opposing surface may also provide greater strength. Figure 8(b) shows the average depth $\langle h \rangle$ of all monomers that are part of interfacial loops. Note that this differs from the interdiffusion depth $\langle d \rangle$ plotted in Fig. 7. All chain segments contribute to $\langle d \rangle$, while only loops with both ends at $z = 0$ contribute to $\langle h \rangle$. At large t, this excludes unentangled or marginally entangled short chains that have diffused deep into the opposite side, and therefore $\langle h \rangle$ could better reflect the aspects of interfacial structure related to shear strength.

The healing samples all have nearly the same $\langle h \rangle$, even though $\langle l \rangle$ decreases with stiffness. Assuming loops have a nearly equilibrium configuration, $\langle h \rangle$ should be of order the radius of gyration of segments of length $\langle l \rangle$ and related to the positions of the bumps in $\rho(z)$ for intermediate chain lengths immediately after cutting (Fig. 5). The stiffer chains have a larger radius of gyration for the same number of monomers which seems to compensate for the smaller $\langle l \rangle$.

Several theoretical models relate the interfacial strength to the areal density of bridging loops across the interface [6,9,10,17,62,63]. Some define bridging loops as chain segments intersecting both the plane at $z = \delta$ above and that at $z = -\delta$ below the interface ($z = 0$), where δ is the end-end distance of the random walk between entanglements [6,9]. Others define bridging loops as chain segments that connect two subsequent entanglements placed on different sides of the interface [10,62,63] or chain segments subject to at least one interfacial entanglement between opposite sides [17]. All of these assume that entanglements with both sides are required for effective stress transfer across the interface. From Fig. 8 one can determine when the mean loop length becomes comparable to N_e or $\langle h \rangle$ is comparable to δ, and how rapidly the number of loops grows. However, the relation between these measures and entanglements is indirect. We therefore have also followed explicitly the development of entanglements.

The increase of entanglements across the interface during healing is tracked by applying the PPA at different interdiffusion times (Fig. 4). The density of TCs between primitive paths provides a measure of the entanglement density. TCs that are near the end of a chain are not expected to contribute to mechanical strength because they can be removed by small displacements. To account for this we remove TCs when the number of monomers $n_{\rm end}$ to the nearest chain end is less than a threshold. The density profiles of TCs between chains from any side and those between chains from opposite sides (interfacial TCs) are shown in Fig. 9 for the healing sample of fully flexible chains. Here only chains with $n_{\rm end} > 30$ are included, since the distance between TCs along a chain is about 30 for $k_{\rm bend} = 0$ [36].

At short times the density of entanglements is comparable to the bulk value far from the interface but reduced almost to zero near the interface ($|z| < 10a$). Similar behavior is observed for welding samples [32,33], but they also exhibit a strong peak in entanglement density on either side of the interface at $|z| \sim 10a$. This was attributed to the higher density of chain ends and pancake like conformation produced by the prewelding interface. This interpretation is bolstered by the lack of a similar peak in our healing simulations where the chain conformations are not perturbed by reflections at an interface.

As the interdiffusion time t increases, chains form new entanglements across the interface (Fig. 4) and the dip in $\rho_{\rm TC}$ fills in. At $t = 7M\tau$, $\rho_{\rm TC}$ is statistically indistinguishable from the bulk density all across the sample. Note that the entanglement density saturates more rapidly in welding samples, where $\rho_{\rm TC}$ reaches the bulk value near $2.5M\tau$ [32]. This more rapid evolution of entanglements contrasts with the slower evolution of $\langle d \rangle$ in welding (Fig. 7) and reflects the fact that diffusion by long chains is needed to produce entanglements.

Figure 9(b) shows the rise of interfacial TCs at the interface during healing. The areal density $N_{\rm TC}^I/A$, which is shown in the inset for both the healing and welding samples, has been shown [32] to directly correlate with the interfacial strength of welds. As shown above for structural quantities characterizing the interfacial loops, $N_{\rm TC}^I/A$ is slightly larger for the healing sample due to the faster diffusion of short chains. Also shown in the inset are the areal densities of TCs with $n_{\rm end} > 50$ and $n_{\rm end} > 70$. At the same t, $N_{\rm TC}^I/A$ with $n_{\rm end} > 50$ is almost the same for healing and welding, while $N_{\rm TC}^I/A$ with $n_{\rm end} > 70$ is lower for healing. The results above are for samples of flexible chains. Similar entanglement evolution across the interface is observed for $k_{\rm bend} > 0$. However, as the interdiffusion is slower for larger $k_{\rm bend}$, it takes longer for $\rho_{\rm TC}$ to saturate at the corresponding bulk density.

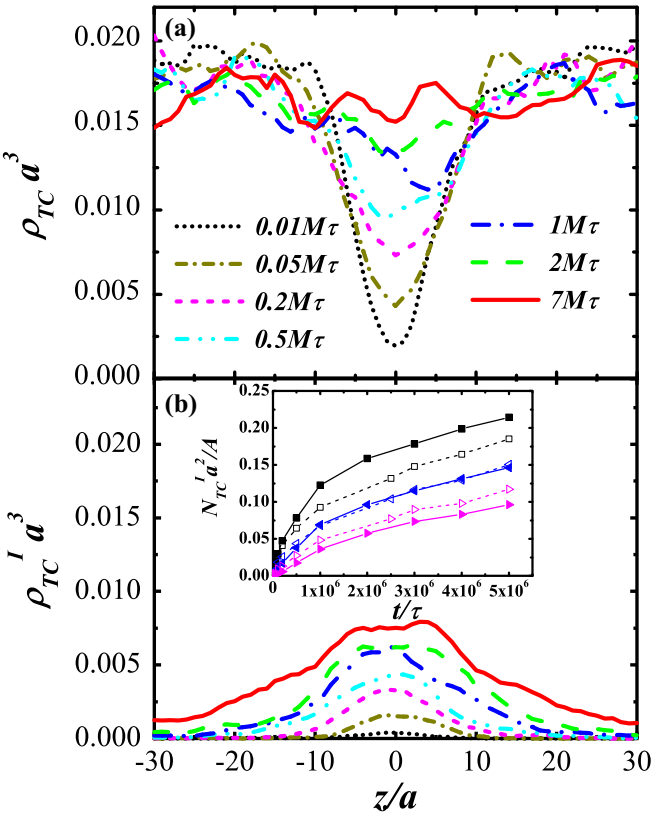

FIG. 9. (Color online) Density profiles at different interdiffusion times for TCs between chains from (a) either side and (b) opposite sides (interfacial TCs) of the interface in the healing sample of fully flexible chains ($k_{\rm bend} = 0$). Only interior TCs with the number of monomers to the nearest chain end $n_{\rm end}$ larger than 30 are included. Inset of (b) shows the development of the areal density of interfacial TCs with interdiffusion time for both healing (filled symbols) and welding (open symbols) samples with $k_{\rm bend} = 0$. Results are shown for TCs with $n_{\rm end} > 30$ (black squares), 50 (blue left triangles), and 70 (magenta right triangles), respectively.

Previous simulations of thermal welding found an almost linear correlation between the areal density of interfacial TCs and the interpenetration depth above a threshold interpenetration depth [32,33]. For healing, this correlation is complicated by the polydispersity in chain length. To reduce the effects of short cut chains, we calculated the average interpenetration depth of monomers using the chain length N of the segments they belong to as the weight. Figure 10(a) plots the density of interfacial TCs with $n_{\rm end} > 30$ against the N-weighted

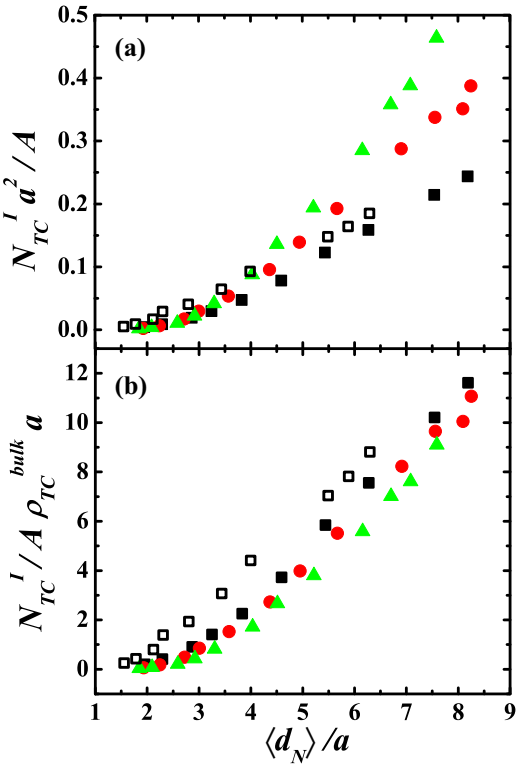

FIG. 10. (Color online) (a) The areal density of interfacial TCs and (b) the ratio of areal and bulk densities versus $\langle d_N \rangle$, the average interpenetration depth of monomers weighted by the segment length N. Only interior TCs that are more than 30 monomers from a chain end are included. Results are shown for the healing samples with $k_{\rm bend}/u_0 = 0$ (black squares), 0.75 (red circles), and 1.5 (green triangles), and the welding sample with $k_{\rm bend} = 0$ (open black squares).

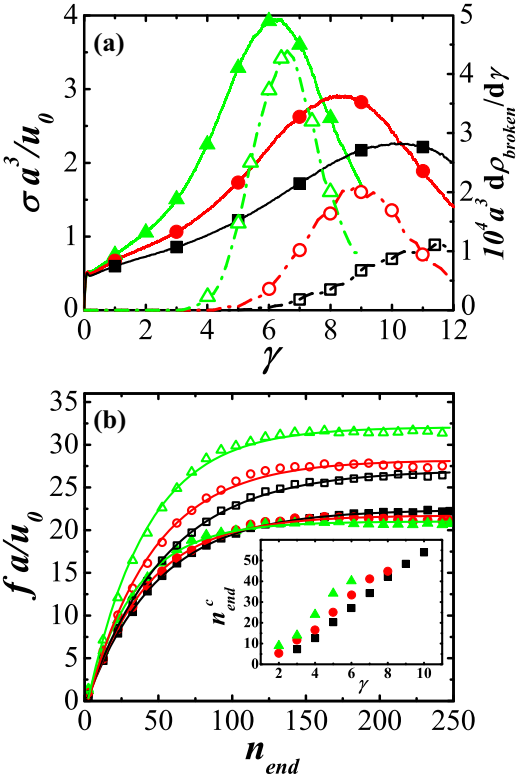

FIG. 11. (Color online) (a) Average shear stress vs. shear strain curves (solid lines and symbols) for bulk samples with $k_{\rm bend}/u_0 = 0$ (black squares), 0.75 (red circles), and 1.5 (green triangles). Dashed lines and open symbols show the rate of bond breaking $d\rho_{\rm broken}/d\gamma$, where $\rho_{\rm broken}$ is the density of broken bonds. (b) Average bond tension f along the chain as a function of $n_{\rm end}$ for bulk samples with different $k_{\rm bend}$ at the shear strain γ^c where significant bond breaking initiates (solid symbols) and $\gamma^{\rm max}$ where the shear stress reaches its peak value (open symbols). For $k_{\rm bend}/u_0 = 0$, 0.75, and 1.5, $\gamma^c = 9$, 7, and 5 and $\gamma^{\rm max} = 10$, 8, and 6, respectively. Solid lines are results from fitting the corresponding data points using $f = f_0[1 - \exp(-n_{\rm end}/n_{\rm end}^c)]$. The increase of $n_{\rm end}^c$ with shear strain γ is shown in the inset of (b) for different $k_{\rm bend}$.

average interpenetration depth $\langle d_N \rangle$ of monomers. As found previously [32,33], for welding with $k_{\rm bend} = 0$ the increase of $N_{\rm TC}^I/A$ with $\langle d_N \rangle$ is almost linear for all nonvanishing $N_{\rm TC}^I/A$. In contrast, for healing with $k_{\rm bend} = 0$, the increase is slow at small $\langle d_N \rangle$ and becomes more rapid and linear only after $\langle d_N \rangle$ rises above $\sim 3.5a$. The reason is that short chain segments dominate the diffusion at small times but they contribute less significantly to the formation of TCs.

For healing samples, as $k_{\rm bend}$ increases, the rise of $N_{\rm TC}^I/A$ becomes more rapid. This is consistent with the results shown in Sec. II that bulk samples of stiffer chains are more entangled. To separate the effects of chain stiffness and the interpenetration depth, we normalize $N_{\rm TC}^I/A$ by the corresponding bulk density $\rho_{\rm TC}^{\rm bulk}$ of TCs. As shown in Fig. 10(b), the behavior of $N_{\rm TC}^I/A\rho_{\rm TC}^{\rm bulk}$ versus $\langle d_N \rangle$ is almost the same for different healing samples. This result indicates that the different rates of increase in Fig. 10(a) merely reflect the larger bulk entanglement density of stiffer chains.

C. Interfacial strength

1. Shear response of uncut samples

The ultimate goal of healing or welding is to recover the mechanical strength of a bulk polymer. This section begins by describing this bulk response, including the role of stiffness and chain length. These results are then used to calibrate the response of healed and welded samples.

Typical stress-strain curves for samples with different chain stiffness are shown in Fig. 11(a). In all cases there is an initial elastic response followed by yield and strain softening. This initial region is confined to $\gamma < 0.2$ and is difficult to see on the scale of the plot. Further increases in γ lead to strain hardening, a steady rise in the stress with strain. Eventually the stress becomes high enough to produce chain scission. The stress then rises less rapidly with strain, reaches a maximum, and finally drops as strain localizes on a failure plane.

Chain stiffness has little effect on the initial elastic response or yield stress but greatly enhances strain hardening [52,53]. The reason is that an affine shear displacement of monomers causes chains to stretch. Stiffer, straighter chains are less able to stretch without lengthening or breaking the strong covalent backbone bonds. This has traditionally been modeled as a loss of entropy of the random walks between entanglements [64,65], but recent work shows that the stress rises because the rate of plastic activity required to avoid bond

breaking rises as chains straighten [52,53,66,67]. Since stiffer chains cannot be straightened as much without stretching backbone bonds, the strain γ^c where significant chain scission occurs and the strain $\gamma^{\max}$ where the stress peaks become smaller as $k_{\rm bend}$ increases. Figure 11(a) also shows the rate of bond breaking. We identify $\gamma^c = 9$, 7, and 5 for $k_{\rm bend} = 0$, 0.75, and 1.5 with the strain where the rate of acceleration in bond breaking is highest.

While most of the energy associated with shearing the sample is dissipated as heat in plastic rearrangements, there is also a rise in the energy and the tension along backbone bonds. Figure 11(b) shows the dependence of the average tension on the chemical distance $n_{\rm end}$ from the nearest chain end. Only bonds in unbroken chains are included in the average and results for γ^c and $\gamma^{\max}$ are shown. In all cases, the average bond tension relaxes near chain ends, which are free to retract along their tube. This relaxation can be fitted by $f = f_0[1 - \exp(-n_{\rm end}/n^c_{\rm end})]$, where f_0 corresponds to the plateau tension away from chain ends, while $n^c_{\rm end}$ characterizes the distance over which f relaxes [48]. Both the plateau tension and the characteristic relaxation length $n^c_{\rm end}$ increase with γ.

At γ^c, chains of different stiffness have nearly the same plateau bond tension, $\sim 22\ u_0/a$. This is much smaller than the bond breaking force $\sim 240\ u_0/a$, but the distribution of f has an exponential tail like that seen in craze formation [51]. The fraction of bonds that can break at any instant is of order $\exp(-240/22) \approx 2 \times 10^{-5}$ and about 1 in 10^4 has broken by γ^c for all chain stiffnesses. There is also a common value of $f_0 \sim 8u_0/a$ at the start of bond breaking, which is at strains of about 6, 5, and 3.5 for progressively stiffer chains.

The plateau bond tension at $\gamma^{\max}$ increases with $k_{\rm bend}$ and the number of broken bonds also increases. This suggests that as entanglement density increases with $k_{\rm bend}$, more bond breaking is needed to form a fracture plane across the whole sample. We find that the total number of broken bonds per entanglement is about a quarter at $\sigma^{\max}$ and a little over unity at the point of final failure.

The increase of $n^c_{\rm end}$ with γ is shown explicitly in the inset of Fig. 11(b). The characteristic relaxation length $n^c_{\rm end}$ at γ^c decreases with increasing $k_{\rm bend}$ (48, 41, and 34), but the ratio of $n^c_{\rm end}$ to N_e increases, $n^c_{\rm end}/N_e \sim 0.56$, 1.05, and 1.31. This indicates that entanglements alone do not determine $n^c_{\rm end}$ and that the friction between chains required to retract them along their tube is also important. This conclusion is bolstered by considering the effect of chain length.

The above results are all for well-entangled chains of length 500. To estimate the potential effect of polydispersity near the cut interface, we performed shear tests on monodispersed bulk samples of chains with different lengths. Cubic samples with $\sim 3 \times 10^5$ beads and periodic boundary conditions ($L_x = L_y = L_z \sim 70a$) were equilibrated as in Ref. [50]. We tested that results for this reduced system size gave the same trends with N as the larger systems used in healing and welding simulations. There is a slight ($\sim$3%) decrease in maximum stress with system size that may be related to the greater statistical likelihood of a weaker region in a larger system.

The chain length dependence of the bulk failure stress is shown in Fig. 12(a). The shear strength $\sigma^{\max}$ increases rapidly with N and then saturates at a limiting long chain value which rises with increasing chain stiffness. Even though

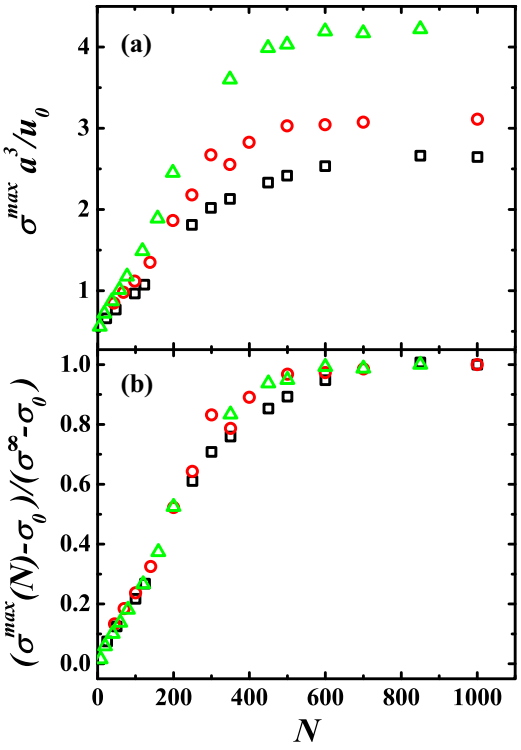

FIG. 12. (Color online) (a) The maximum shear stress $\sigma^{\max}$ for monodispersed bulk samples with different chain lengths for $k_{\rm bend}/u_0 = 0$ (black squares), 0.75 (red circles), and 1.5 (green triangles). (b) Rescaled plot showing the percentage of the increase with chain length as a function of N.

N_e decreases from about 85 to 26 with increasing $k_{\rm bend}$, the asymptotic strength is reached at roughly the same chain length. Figure 12(b) shows a scaled plot of the percentage increase toward the bulk value. About 90% of the change in strength is complete by $N = 400$ for the stiffest chains and by $N = 500$ for the most flexible. This combined with the plots of backbone tension in Fig. 11(b) suggests that interchain friction plays a critical role in determining when failure changes from pullout to scission. Only when scission is dominant does the strength become independent of N. Previous studies of tensile failure through crazing [48] had found that the fracture energy of systems with different $k_{\rm bend}$ saturated at similar values of N/N_e, indicating that chain friction was not important. However, the accepted values of N_e at the time were 64 and 32 instead of 85 and 26 for $k_{\rm bend} = 0$ and 1.5. Reexamination of the data shows that the shift in the transition is smaller than the change in N_e.

Interchain friction is difficult to measure or control in experiments, so strength saturation is normally expressed in terms of N/N_e. Using a 90% criterion in Fig. 12, one obtains N/N_e between 6 and 15. Experimental studies of tensile fracture and interfacial strength for a range of polymers typically show saturation for a similar range of N/N_e [1,9,19,62].

For the welding samples, all chains have $N = 500$ and the strength is close to the long chain limit even for flexible chains. In contrast, many of the chains near the interface of healed samples have chains in the range from 150 to 400 where strength varies rapidly with length. As we will see below this leads to a lower shear strength.

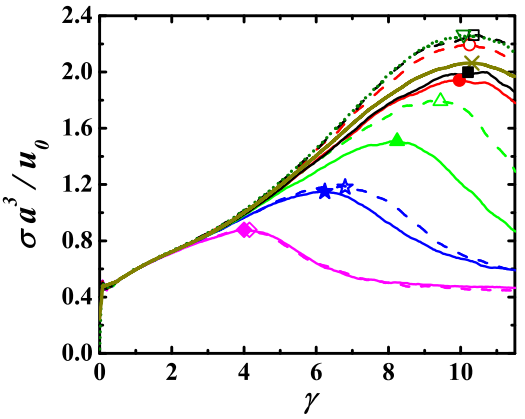

FIG. 13. (Color online) Stress-strain curves from shear tests on different states for healing (solid lines and symbols) and welding (dashed lines and open symbols) of fully flexible chains ($k_{\rm bend} = 0$). Symbols indicate the peak stress for each curve. Results are shown for interdiffusion time $t = 0.01M\tau$ (magenta diamonds), $0.1M\tau$ (blue stars), $0.5M\tau$ (green triangles), $2M\tau$ (red circles), $5M\tau$ (black squares), and $16M\tau$ (dark yellow cross, only for healing). Also shown is the corresponding average stress-strain curve for the bulk (olive dotted line and inverted triangle).

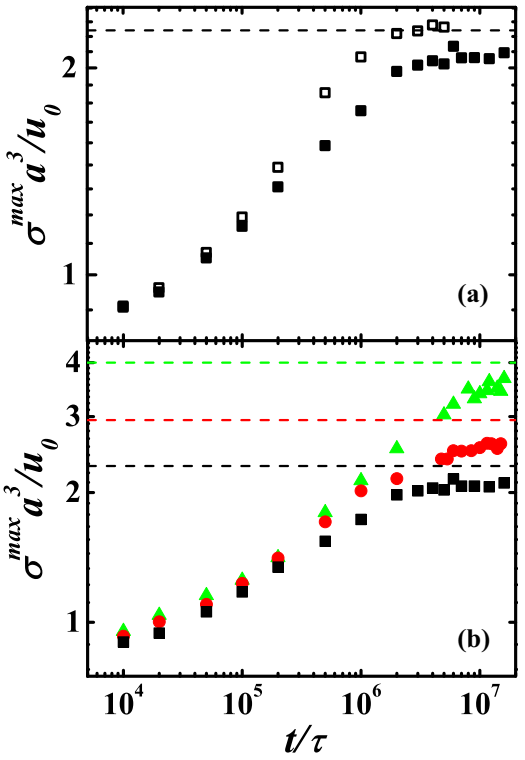

FIG. 14. (Color online) (a) The maximum shear stress $\sigma^{\rm max}$ is shown versus t for both healing (solid squares) and welding (open squares) samples of fully flexible chains. (b) Time dependence of $\sigma^{\rm max}$ for healing samples with $k_{\rm bend}/u_0 = 0$ (black squares), 0.75 (red circles), and 1.5 (green triangles). Dotted lines indicate the corresponding bulk strengths.

In Sec. II we noted that other forms of the covalent bonding potential had been used and the results were found to follow the same trends. For any reasonable stiffness, the elastic response is dominated by the intermolecular interactions. The main effect of the covalent potential comes from the breaking force f_B. As f_B decreases, the chain tension f_0 becomes large enough to break bonds at smaller strains (Fig. 11). The ratio of the strength of long to short chains decreases, as does the increase in weld strength with time. If f_B is reduced by a factor of 3 to $80u_0/a$, the difference between the failure stress of chains with N_e and $N \to \infty$ is only 50%. For $f_B = 160u_0/a$ the limiting large N failure stress is only ∼15% below that for $f_B = 240u_0$, and further increases have less effect. The factor-of-3 increase in strength with weld time found here and in Ref. [32] is similar to that found in experiments.

2. *Time-dependent strength of healed and welded interfaces*

Figure 13 contrasts the behavior of healed and welded samples of flexible chains ($k_{\rm bend} = 0$). In all cases the initial elastic response, yield, and strain hardening follow the bulk response. The youngest interfaces ($g = 0.01M\tau$) begin to deviate from the bulk response near $\gamma = 3$ and curves for healing and welding are nearly the same. The peak stress of $\sim 0.8u_0/a^3$ is comparable to values for bulk simulations with unentangled chains (Fig. 12), which is consistent with the small number of interfacial entanglements and short loop lengths described in the previous sections. As time increases, the results follow the bulk curve to larger strains and the welding results for $t > 2.5M\tau$ are indistinguishable from the bulk response. The curves for healing rise more slowly with time than welding and continue to fall below the bulk response at $16M\tau$.

Figure 1 shows the evolution in the interfacial structure before and after failure with increasing healing time. Monomers that are initially below and above the cutting plane are shown in yellow and blue, respectively. At short times the distribution of the two types of monomer sharpens with increasing strain. In Fig. 1(d), many of the chains that had diffused only part way across the interface have been pulled back to their initial side. A few small chains that had diffused completely across the interface remain on the other side and no chain scission has occurred. The final shear stress corresponds to friction between two polymer blocks with sharp interfaces.

As the healing time increases, longer segments of chains span between the two sides. Many break rather than being pulled out, and the height distribution of monomers from the two sides changes very little during failure. The strong shear alignment of individual chains that leads to high stresses and scission is clearly visible. Similar changes are observed in welding, but because there is no polydispersity, interdiffusion is slower and chain pullout produces sharper interfaces [32].

As in previous studies [32] and experiments [22], we use the maximum shear stress $\sigma^{\rm max}$ before failure to characterize the interfacial strength. Figure 14(a) shows $\sigma^{\rm max}$ versus time for the healing and welding samples of Fig. 13. Both curves rise smoothly and appear to saturate for $t > 2M\tau$. The welding results saturate at the bulk strength, while healing results are lower at all times and never reach the bulk strength.

Figure 14(b) shows healing curves for chains with different stiffness. Results for different $k_{\rm bend}$ are almost identical for $t \leqslant 2 \times 10^5$. At this stage of interdiffusion, the amount of entanglements across the interface is low in all systems and

the interface fails through chain pullout. The force required to pull short chain segments from the opposite side is determined by interchain friction, which does not depend significantly on k_{bend}. This is also why the initial yield stress is similar for all k_{bend}. Note that the strain at which systems fail does depend on stiffness. Because they strain harden more rapidly, stiffer systems reach the stress required for chain pullout at a lower strain.

At later times the interfacial strength rises slightly more rapidly for stiffer chains. As the number of interfacial entanglements increases, chain pullout is arrested and the interface begins to fail through chain scission. The interface is progressively coupled to more of the surrounding bulk material whose strength grows with stiffness. Ultimately, the interfacial strength saturates slightly below the bulk strength for all three k_{bend}. The saturation time is longer for stiffer chains because of the slower diffusion: about $2M\tau$, $5M\tau$, and $10M\tau$ for $k_{\mathrm{bend}}/u_0 = 0$, 0.75, and 1.5, respectively. To check that the reduced strength is associated with the interface, we performed additional simulations in wider systems ($H = 110a$). At failure, strain was localized in the interfacial region and the density of broken bonds was higher there. In contrast, welded samples that have recovered bulk strength show uniform distributions of strain and broken bonds.

The reduced strength of healing samples can be directly related to the residual concentration of cut chains at the interface (Fig. 5). For the flexible chains, the plateau in $\sigma^{\max}$ is comparable to the bulk strength of chains of length 3 to $4N_e$. A substantial fraction of interfacial chains have lengths in this range at $2M\tau$. There is also a residual density of very short, unentangled chains that would be smaller in an infinite system where they could continue to diffuse. To evaluate their effect we removed all chains with length less than 100 from the $7M\tau$ sample just before quenching. We found that this did not affect $\sigma^{\max}$, implying that chains of length 100 to 500 are responsible for the lower interfacial stress. Since diffusion of these chains away from the interface is slowed by entanglements, the ultimate recovery of strength to bulk values would take much longer times than are accessible in simulations.

These results suggest that recovery of the bulk strength at the interface in a healing sample is a two-step process. This arises from the separation of two time scales: the time τ_1 for the entanglement density to approach its bulk distribution and the time τ_2 for all cut chains to diffuse away from the interface. As shown in Fig. 9, τ_1 is much smaller than the disentanglement time τ_d, while τ_2 is expected to be multiple times τ_d. The strength begins to plateau near τ_1 but full strength will not be recovered until τ_2. Similar two-step healing processes based on separation of diffusion time scales have been observed in the healing behavior of γ-irradiated poly(styrene-co-acrylonitrile) [68] and blends of polystyrene with poly(2,6-dimethyl-1,4-phenylene oxide) [69].

3. *Relation between interfacial strength and structure*

As noted above, models of healing and welding have typically related shear strength to interfacial structural properties. Given the trends in Sec. III B, it is clear that no simple structural measure will collapse the different results in Fig. 14 for welding and healing. The mean length of loops $\langle l \rangle$ is nearly the same for welding and healing samples [Fig. 8(a)] and the mean depth of loops $\langle h \rangle$ is nearly the same for all systems [Fig. 8(b)]. Figure 15 shows that plotting $\sigma^{\max}$ against $\langle l \rangle$ rather than time increases the separation between results for different stiffness, although they seem to saturate at similar values of $\langle l \rangle \sim 35$. The strength imparted by loops clearly depends on their stiffness and on the length of the chains that anchor them into the opposing surface.

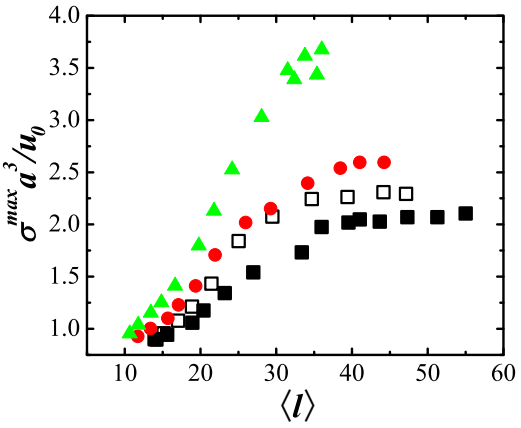

FIG. 15. (Color online) The maximum shear stress $\sigma^{\max}$ versus the average contour length $\langle l \rangle$ of interfacial loops for welding of flexible chains (open squares) and healing with $k_{\mathrm{bend}}/u_0 = 0$ (filled squares), 0.75 (circles), and 1.5 (triangles).

Our recent simulations [32] of welding showed that the recovery of bulk shear strength coincided with the approach of the entanglement density at the interface to the bulk value. Figure 16(a) shows the rise in strength with entanglement density for welding and healing samples. As with other measures, the connection between strength and entanglement density is less clear for healing because of polydispersity. Many of the entanglements involve short chains and cannot impart as much strength to the interface.

We have tried a number of ways of correcting the entanglement density to reflect the greater effectiveness of longer chains. From Fig. 11 it is clear that stress is able to relax near chain ends, and thus entanglements near chain ends are not effective in imparting strength. Excluding entanglements less than n_0 from a chain end ($n_{\mathrm{end}} < n_0$) also eliminates all entanglements involving chains of length less than $2n_0$. Figure 16(b) shows results for $n_0 = 30$, which is roughly the distance from the chain end where the stress reaches $f_0/2$ at γ_c for all chain stiffnesses (Fig. 11). Results for all healing systems follow a common curve until they saturate at a strength that grows with stiffness. Welding results follow the same curve at low strengths but then increase more rapidly and saturate at a higher level. This appears to reflect the fact that chain lengths of order 500 are needed to reach the full bulk strength. Some shorter chains are present near the interface for all healing systems.

The proportionality between interfacial strength and N_{TC}^I in Fig. 16 is sensitive to the choice of n_0. Figures 9 and 11 indicate why $n_0 \sim 30$ includes interfacial entanglements if and only if they are far enough from chain ends to prevent

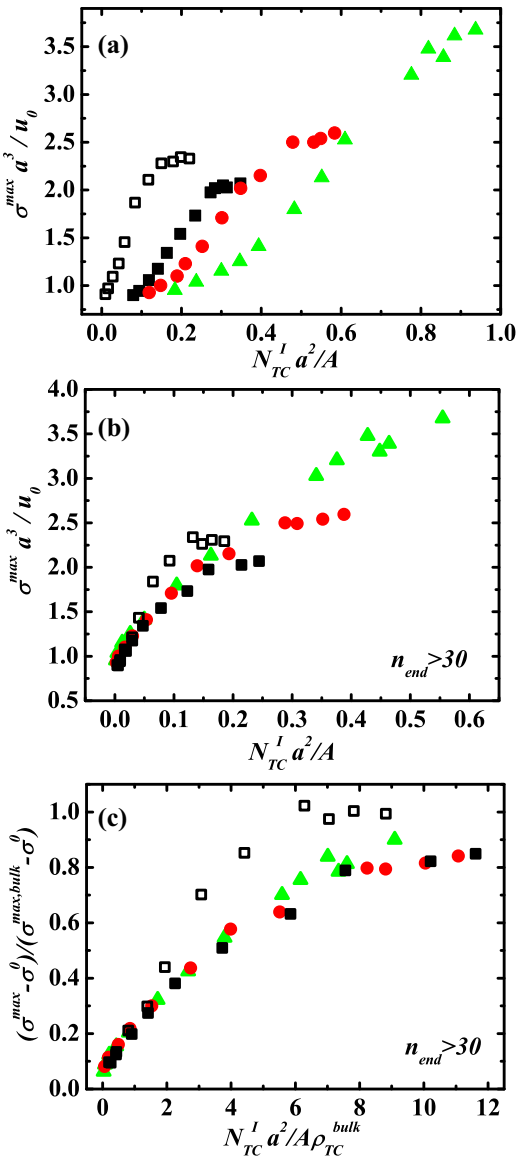

FIG. 16. (Color online) (a) Maximum shear stress $\sigma^{\max}$ versus the areal density of interfacial TCs for healing (filled symbols) and welding (open symbols) with $k_{\rm bend}/u_0 = 0$ (squares), $k_{\rm bend}/u_0 = 0.75$ (circles), and $k_{\rm bend}$ (triangles). (b) Same plot but excluding entanglements less than 30 monomers from a chain end. (c) Same data showing fraction of increase toward bulk strength against areal density of interfacial entanglements normalized by bulk density.

pullout. As expected from Fig. 11, taking n_0 much less than 30 includes regions near the chain ends where the stress can relax through motion along the tube. Taking n_0 much larger than 30 excludes regions of large stress. Curves like those in the inset to Fig. 9(b) show that choosing $n_0 < 30$ leads to a nonzero density of entanglements immediately after the quench due to motion of short chains. As for $n_0 = 0$ in Fig. 16(a), there is no corresponding increase in the shear stress. On the other hand, increasing n_0 to 50 excludes too many entanglements and there is a significant increase in strength before there are any interfacial entanglements, particularly for large $k_{\rm bend}$.

The bulk density of entanglements increases with chain stiffness and it is interesting to see if that correlates with the increasing strength of stiffer chains. Figure 16(c) shows the fractional increase from the short chain limit, $\sigma_0 \sim 0.8u_0/a^3$, to the bulk strength $\sigma^{\max,\rm bulk}$ normalized by the bulk entanglement density $\rho_{\rm TC}^{\rm bulk}$. Note that this collapses all of the healing results onto a single curve and the welding results follow the same curve at early times. This collapse is consistent with the idea that recovery towards the bulk entanglement density is related to recovery to bulk strength.

The ratio of interfacial areal density to bulk density has units of length, indicating that there is a common depth that entanglements must span to recover bulk strength. Indeed, as shown in Fig. 10(b), for healing samples with different $k_{\rm bend}$, the same $N_{\rm TC}^I/A\rho_{\rm TC}^{\rm bulk}$ corresponds to almost the same $\langle d_N\rangle$. A common interdiffusion depth for strength recovery is consistent with strength saturation at a constant loop length in Fig. 15 and a common length for stress relaxation with all $k_{\rm bend}$. It also explains why it takes longer for the interfacial strength to saturate for larger $k_{\rm bend}$. Since the interfacial dynamics slows down with increasing $k_{\rm bend}$, the time it takes to reach the same depth increases.

Experiments [16,19,20,70] show that there is a direct correlation between the width a_I of the interface and the interfacial fracture energy G. However, the increase of $G/G^{\max}$ with a_I/d_T, where $G^{\max}$ is the saturation value of G and d_T the tube diameter, is material specific. In particular, at $G_{\max}$, a_I varies between 1 and 2 times d_T. Benkoski *et al.* [17] argued that changes of interchain friction can fully account for this nonuniversal behavior.

In our simulations, the ratio of the common interdiffusion depth at strength recovery to the corresponding tube diameter varies with $k_{\rm bend}$. As in experiments [16,19,20,70], this result suggests that entanglements alone do not fully determine the strength recovery at the interface. The role of entanglements is coupled with that of interchain friction, as also demonstrated in Fig. 11(b).

IV. SUMMARY

Extensive simulations of the thermal healing of precut polymer samples were performed. The precut introduces a symmetric polymer-polymer interface with polydispersity in chain length. This polydispersity complicates the interdiffusion. The unentangled cut chains quickly diffuse away from the interface, and after a relatively short time are almost uniformly distributed across the finite simulation box. Cut chains longer than the entanglement length diffuse less rapidly and are still predominantly distributed around the interface at large diffusion times. These chains slow the development of bulk strength even though the mass uptake and increase in interpenetration depth are faster than for thermal welding of monodispersed polymers.

We examine the evolution of the interfacial structure during healing and welding. The increase of the mean length $\langle l\rangle$ and depth $\langle d\rangle$ of interfacial loops with interdiffusion time is almost the same for healing and welding samples. The mean length rises slightly more slowly for healing of stiffer chains because they diffuse more slowly. However, since the conformation of stiffer chains is more extended, $\langle d\rangle$ is nearly independent of stiffness. The number of interfacial loops is nearly independent

of time for both healing and welding, in sharp contrast to the $t^{1/4}$ increase predicted by previous theoretical work [60].

Primitive path analysis provided direct information about entanglements across the interface. The number of interfacial entanglements increases faster during healing than welding. However, a larger fraction of interfacial entanglements in healing samples are near chain ends and the number of entanglements in the center of chains rises more slowly than for welding. As a result, the density of entanglements near the interface takes longer to recover to the bulk density. Experiments often measure the interdiffusion depth as a proxy for entanglement density [16,19,20]. The primitive path analysis shows the number of interfacial entanglements rises more rapidly with interdiffusion depth for healing of stiffer chains, but the results collapse when normalized by the bulk entanglement density. The interdiffusion depth needed to produce a significant number of interfacial entanglements is roughly twice as big for healing as welding [Fig. 10(a)].

A simple shear test is applied to measure the shear strength of different samples. The strength is quantified using the maximum shear stress $\sigma^{\max}$ before failure. We first study the effects of chain stiffness and length on the bulk shear response. As chain stiffness k_{bend} increases, strain hardening is enhanced. As a result, the stress level at any given strain increases. Moreover, the strain γ^c where significant chain scission occurs and the strain $\gamma^{\max}$ that corresponds to $\sigma^{\max}$ both decrease with k_{bend}. At γ^c, the average bond tension f_0 near the center of chains and the relaxation distance n^c_{end} from chain ends are independent of k_{bend}. However, the value of f_0 at $\gamma^{\max}$ increases with k_{bend}. The resulting increase in the number of broken bonds is correlated to the increase in entanglement density. In all cases, one bond is broken for every four entanglements at $\gamma^{\max}$ and by the final failure about one bond is broken for each entanglement. The mean bond tension remains an order of magnitude smaller than the breaking force and scission is associated with bonds in the tail of an exponential distribution of local tensions.

As chain length increases, the bulk $\sigma^{\max}$ first increases and then saturates at the long chain limit. Chain stiffness increases the limiting value. However, the limit is approached at almost the same chain length for different k_{bend}. This suggests that interchain friction, which is independent of stiffness, is critical in determining the chain length for which chain pullout dominates over chain scission. More evidence comes from trends in the length n^c_{end} over which bond tension relaxes through pullout at chain ends. At a given f_0, n^c_{end} decreases only slightly (30%) with stiffness for healing samples while the ratio n^c_{end}/N_e more than doubles.

The time dependence of shear strength at healing and welding interfaces is contrasted. For healing, the bulk mechanical response is not fully recovered on the time scales of our simulations. In contrast to welding, $\sigma^{\max}$ saturates below the bulk value and the rise of $\sigma^{\max}$ before saturation is slower. We attribute the retarded strength development to the presence of cut chains with $N > N_e$ at the interface, which are less entangled than the uncut chains. The ultimate recovery of bulk strength relies on the diffusion of these entangled cut chains away from the interface, which would take a much longer time and therefore is inaccessible to our simulations.

Chain stiffness affects the development of strength in healing samples. At early times failure is through chain pullout. The value of $\sigma^{\max}$ is almost independent of k_{bend} because pullout stresses are mainly determined by interchain friction. Later, $\sigma^{\max}$ rises more rapidly and reaches a higher saturation value for larger k_{bend}, consistent with the higher stress curves and $\sigma^{\max}$ in the bulk. Moreover, the saturation occurs at a larger time for larger k_{bend} due to slower interdiffusion.

The relation between interfacial strength development and interfacial structure evolution is examined. None of the quantities considered, the interdiffusion depth, the mean length $\langle l \rangle$ of interfacial loops, or N^l_{TC}/A gave neat predictions for the relative strength development in healing and welding. Nevertheless, for healing with different k_{bend}, a good correlation is found between the fractional increase of $\sigma^{\max}$ from the short chain limit to the bulk strength and the areal density of interfacial entanglements divided by the bulk density $N^I_{\text{TC}}/A\rho^{\text{bulk}}_{\text{TC}}$. This indicates that the average interpenetration depth at strength saturation is almost the same for different k_{bend}, which is consistent with the universal correlation between $N^l_{TC}/A\rho^{\text{bulk}}_{\text{TC}}$ and $\langle d_N \rangle$ in Fig. 10. The ratio of the common interpenetration depth to the corresponding tube diameter varies for different k_{bend}. Once again, this suggests that entanglements and interchain friction are coupled to strengthen the interface.

ACKNOWLEDGMENTS

We thank E. J. Kramer and M. Rubinstein for useful discussions. This work was supported by the National Science Foundation under Grants No. DMR-1006805, No. CMMI-0923018, and No. OCI-0963185. M.O.R. acknowledges support from the Simons Foundation. D.P. and G.S.G. acknowledge support from Department of Energy Award No. DE-FG02-12ER46843. This research used resources at the National Energy Research Scientific Computing Center (NERSC), which is supported by the Office of Science of the United States Department of Energy under Contract No. DE-AC02-05CH11231. Research was carried out in part at the Center for Integrated Nanotechnologies, a US Department of Energy, Office of Basic Energy Sciences user facility. Sandia National Laboratories is a multiprogram laboratory managed and operated by Sandia Corporation, a wholly owned subsidiary of Lockheed Martin Corporation, for the US Department of Energy's National Nuclear Security Administration under Contract No. DE-AC04-94AL85000.

[1] R. P. Wool, *Polymer Interfaces: Structure and Strength* (Hanser, Munich, 1995).

[2] R. N. Haward and R. J. Young, *The Physics of Glassy Polymers* (Chapman & Hall, London, 1995).

[3] R. A. L. Jones and R. W. Richards, *Polymers at Surfaces and Interfaces* (Cambridge University Press, New York, 1999).

[4] K. Jud, H. H. Kausch, and J. G. Williams, J. Mater. Sci. **16**, 204 (1981).

[5] R. P. Wool and K. M. O'Connor, J. Appl. Phys. **52**, 5953 (1981).
[6] S. Prager and M. Tirrell, J. Chem. Phys. **75**, 5194 (1981).
[7] S. Prager, D. Adolf, and M. Tirrell, J. Chem. Phys. **78**, 7015 (1983).
[8] Y. H. Kim and R. P. Wool, Macromolecules **16**, 1115 (1983).
[9] D. Adolf, M. Tirrell, and S. Prager, J. Polym. Sci., Polym. Phys. Ed. **23**, 413 (1985).
[10] A. G. Mikos and N. A. Peppas, Polymer **30**, 84 (1989).
[11] T. R. Russell, V. R. Deline, W. D. Dozier, G. P. Felcher, G. Agrawal, R. P. Wool, and J. W. Mays, Nature **365**, 235 (1993).
[12] R. P. Wool, Soft Matter **4**, 400 (2008).
[13] B. J. Blaiszik, S. L. B. Kramer, S. C. Olugebefola, J. S. Moore, N. R. Sottos, and S. R. White, Annu. Rev. Mater. Res. **40**, 179 (2010).
[14] P. G. de Gennes, J. Chem. Phys. **55**, 572 (1971).
[15] M. Doi and S. F. Edwards, *The Theory of Polymer Dynamics* (Oxford University Press, Oxford, 1988).
[16] R. Schnell, M. Stamm, and C. Creton, Macromolecules **32**, 3420 (1999).
[17] J. J. Benkoski, G. H. Fredrickson, and E. J. Kramer, J. Polym. Sci., Part B: Polym. Phys. **40**, 2377 (2002).
[18] K. Kunz and M. Stamm, Macromolecules **29**, 2548 (1996).
[19] R. Schnell, M. Stamm, and C. Creton, Macromolecules **31**, 2284 (1998).
[20] H. R. Brown, Macromolecules **34**, 3720 (2001).
[21] J. D. McGraw, P. D. Fowler, M. L. Ferrari, and K. Dalnoki-Veress, Eur. Phys. J. E **36**, 7 (2013).
[22] D. B. Kline and R. P. Wool, Polym. Eng. Sci. **28**, 52 (1988).
[23] M. Parsons, A. Ernst, G. Smyser, A. Hiltner, and E. Baer, J. Adhesion **66**, 135 (1998).
[24] K. Akabori, D. Baba, K. Koguchi, K. Tanaka, and T. Nagamura, J. Polym. Sci., Part B: Polym. Phys. **44**, 3598 (2006).
[25] Y. M. Boiko, Macromol. Symp. **316**, 71 (2012).
[26] E. Helfand and Y. Tagami, J. Polym. Sci., Part B: Polym. Phys. **9**, 741 (1971).
[27] E. Helfand and Y. Tagami, J. Chem. Phys. **56**, 3592 (1972).
[28] H. P. Deutsch and K. Binder, J. Chem. Phys. **94**, 2294 (1991).
[29] K. R. Haire and A. H. Windle, Comput. Theor. Polym. Sci. **11**, 227 (2001).
[30] K. L. Anderson, J. T. Wescott, T. J. Carver, and A. H. Windle, Mater. Sci. Eng. A **365**, 14 (2004).
[31] F. Pierce, D. Perahia, and G. S. Grest, Europhys. Lett. **95**, 46001 (2011).
[32] T. Ge, F. Pierce, D. Perahia, G. S. Grest, and M. O. Robbins, Phys. Rev. Lett. **110**, 098301 (2013).
[33] T. Ge, G. S. Grest, and M. O. Robbins, ACS Macro Lett. **2**, 882 (2013).
[34] R. Everaers, S. K. Sukumaran, G. S. Grest, C. Svaneborg, A. Sivasubramanian, and K. Kremer, Science **303**, 823 (2004).
[35] M. Kröger, Comput. Phys. Commun. **168**, 209 (2005).
[36] C. Tzoumanekas and D. N. Theodorou, Macromolecules **39**, 4592 (2006).
[37] K. Kremer and G. S. Grest, J. Chem. Phys. **92**, 5057 (1990).
[38] J. Rottler, S. Barsky, and M. O. Robbins, Phys. Rev. Lett. **89**, 148304 (2002).
[39] S. W. Sides, G. S. Grest, and M. J. Stevens, Phys. Rev. E **64**, 050802 (2001).
[40] M. J. Stevens, Macromolecules **34**, 1411 (2001).
[41] M. J. Stevens, Macromolecules **34**, 2710 (2001).
[42] J. A. Odell and A. Keller, J. Polym. Sci., Part B: Polym. Phys. **24**, 1889 (1986).
[43] C. Creton, E. J. Kramer, C. Y. Hui, and H. R. Brown, Macromolecules **25**, 3075 (1992).
[44] T. O'Connor and J. Andzelm (private communication).
[45] M. Pütz, K. Kremer, and G. S. Grest, Europhys. Lett. **49**, 735 (2000).
[46] R. S. Hoy, K. Foteinopoulou, and M. Kröger, Phys. Rev. E **80**, 031803 (2009).
[47] J.-X. Hou, C. Svaneborg, R. Everaers, and G. S. Grest, Phys. Rev. Lett. **105**, 068301 (2010).
[48] J. Rottler and M. O. Robbins, Phys. Rev. E **68**, 011801 (2003).
[49] S. Plimpton, J. Comput. Phys. **117**, 1 (1995).
[50] R. Auhl, R. Everaers, G. S. Grest, K. Kremer, and S. J. Plimpton, J. Chem. Phys. **119**, 12718 (2003).
[51] J. Rottler and M. O. Robbins, Phys. Rev. Lett. **89**, 195501 (2002).
[52] R. S. Hoy and M. O. Robbins, Phys. Rev. Lett. **99**, 117801 (2007).
[53] R. S. Hoy and M. O. Robbins, Phys. Rev. E **77**, 031801 (2008).
[54] J. Rottler and M. O. Robbins, Phys. Rev. Lett. **95**, 225504 (2005).
[55] O. A. Hasan and M. C. Boyce, Polymer **34**, 5085 (1993).
[56] J. Rottler and M. O. Robbins, Phys. Rev. E **68**, 011507 (2003).
[57] R. S. Hoy and G. S. Grest, Macromolecules **40**, 8389 (2007).
[58] R. Everaers, Phys. Rev. E **86**, 022801 (2012).
[59] P. G. de Gennes, C. R. Acad. Sci. (Paris) Ser. II **308**, 1401 (1989).
[60] H. Zhang and R. P. Wool, Macromolecules **22**, 3018 (1989).
[61] H. J. Kim, K. Lee, and H. H. Lee, Polymer **37**, 4593 (1996).
[62] A. G. Mikos and N. A. Peppas, J. Chem. Phys. **88**, 1337 (1988).
[63] L. Silvestri, H. R. Brown, S. Carra, and S. Carra, J. Chem. Phys. **119**, 8140 (2003).
[64] R. N. Haward and G. Thackray, Proc. R. Soc. A **302**, 453 (1968).
[65] E. M. Arruda and M. C. Boyce, Int. J. Plast. **9**, 697 (1993).
[66] K. Chen and K. S. Schweizer, Phys. Rev. Lett. **102**, 038301 (2009).
[67] T. Ge and M. O. Robbins, J. Polym. Sci., Part B: Polym. Phys. **48**, 1473 (2010).
[68] T. Q. Nguyen, H. H. Kausch, K. Jud, and M. Dettenmaier, Polymer **23**, 1305 (1982).
[69] H. H. Kausch, D. Petrovska, R. F. Landel, and L. Monnerie, J. Polym. Eng. **27**, 149 (1987).
[70] J. J. Benkoski, G. H. Fredrickson, and E. J. Kramer, J. Polym. Sci., Part B: Polym. Phys. **39**, 2363 (2001).

Phase Behavior of a Single Structured Ionomer Chain in Solution[a]

Dipak Aryal, Thusitha Etampawala, Dvora Perahia,* Gary S. Grest

Structured polymers offer a means to tailor transport pathways within mechanically stable manifolds. The building block of such a membrane is examined, namely a single large pentablock co-polymer that consists of a center block of a randomly sulfonated polystyrene, designed for transport, tethered to poly-ethylene-*r*-propylene and end-capped by poly-*t*-butyl styrene, for mechanical stability, using molecular dynamics simulations. The polymer structure in a cyclohexane-heptane mixture, a technologically viable solvent, and in water, a poor solvent for all segments and a ubiquitous substance is extracted. In all solvents the pentablock collapsed into nearly spherical aggregates where the ionic block is segregated. In hydrophobic solvents, the ionic block resides in the center, surrounded by swollen intermix of flexible and end blocks. In water all blocks are collapsed with the sulfonated block residing on the surface. Our results demonstrate that solvents drive different local nano-segregation, providing a gateway to assemble membranes with controlled topology.

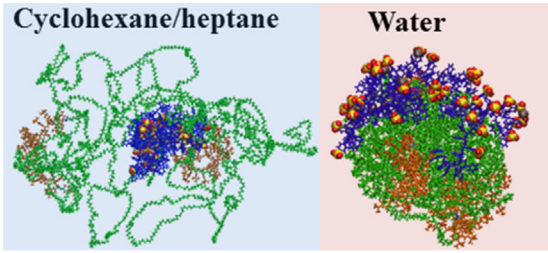

1. Introduction

Structured ionic polymers are in the core of innovative technologies where controlled transport is desired. Examples include clean energy production,[1,2] and storage[3,4] as well as actuators[5,6] and drug delivery.[7,8] Enhancing molecular complexity of the polymers, via incorporating function enabling segments while controlling their phase behavior presents an immense step toward designing controlled transport systems. Incorporating highly incompatible groups, such as ionic blocks into a hydrophobic polymer, however, results in a new set of challenges to control miscibility and long range correlations that offer mechanical stability. The ionic segments often enhance the glass transition temperature of the polymers, making solvent casting the method of choice for membrane preparation. In contrast to neutral, van der Waals polymers, the ionic blocks tend to associate posing kinetic barriers to formation of equilibrium structured membranes. Controlling the structure and dynamics of the individual polymer molecule in solution becomes imperative to controlling assembly into membranes. Here, we probe the conformation of a single molecule of structured co-polymer that consists of an ionic group tethered to an aliphatic block and terminated by bulky group, in solutions of four solvents, using atomistic molecular dynamics (MD) simulations. We show that the nature of the polymer results in phase segregation within one large molecule of molecular weight of 50 050 g mol^{-1} hold a key to understanding the association of molecules into membranes.

D. Aryal, Dr. T. Etampawala, Dr. D. Perahia
Department of Chemistry, Clemson University, Clemson, South Carolina 29634, USA
E-mail: dperahi@g.clemson.edu
Dr. G. S. Grest
Sandia National Laboratories, Albuquerque, New Mexico 87185, USA

[a]**Supporting Information** is available from the Wiley Online Library or from the author.

DOI: 10.1002/mats.201400046

The realization that topology affects polymer properties is of particular significant in presence of ionizable groups has driven significant efforts, revealing a rich manifold of control factors. In contrast to semi-flexible and flexible polymer solutions, there is hardly any insight into solution structure of ionic structures polymers.[9,10] Most studies have focused on membranes showing that the topology of the polymers impact the formation of transport pathways, however not the impact on the stability of the membrane. Among the most significant factors for homopolymers have been the degree and distribution of ionizable groups. Zhang et al.,[11] for example, have carefully mapped the degree and distribution of ionic groups along the backbone of sulfonated polystyrene. Qiao and Weiss[12] have shown that this distribution affects the rheology of the polymers. Further complexity has been introduced via crosslinking of the polymers as demonstrated by Kim et al.[1] Tailoring polymers with multiple blocks has been one of the most promising pathways to form mechanically stable transporting systems. In this frame, block copolymers that contain ionizable or ion transporting blocks are of particular interest since the incompatibility between individual blocks drives the formation of structured materials with domains that facilitate transport and hydrocarbon domains that enhance mechanical stability. Recent studies[13–16] have demonstrated the potential of ionic co-polymers for energy storage and correlated morphology with transport. Wang et al.[14] measured the ionic conductivity and degree of hydration of model membranes composed of polystyrene sulfonate-*b*-polymethybutylene copolymers and their imidazolium salts, demonstrating morphology–hydration–transport correlations.

Despite an immense effort, one significant challenge remains that under the conditions in which ionic transport is optimized, the mechanical and chemical stability of polymers are often compromised. With the rational of tailoring highly transporting blocks with segments that control mechanical stability, a number of co-polymers have been designed. As the complexity of the copolymer increases, the ability to tailor properties is enhanced, though extracting the correlations between the chemical structures of the polymers, their phase structure, and their characteristics becomes a challenge.[17]

The current study probes the fundamental building block of structured ionic polymer membranes, namely the molecular structure of the structured polymers in solution, using MD simulations. Specifically, we probe a pentablock, A-B-C-B-A, co-polymer that consists of an A block of poly-(*t*-butyl-styrene), a B block of ethylene-*r*-propylene and a C block of a randomly sulfonated styrene, shown in Figure S1, Supporting Information in a variety of solvents. The end poly(*t*-butyl-styrene) blocks, free of sulfonation, are designed to enhance mechanical strength. The flexible ethylene-*r*-propylene blocks provide additional means to prevent brittleness in dry condition, while the sulfonated styrene facilitates ion transport. As ionic polymers exhibit high glass transition temperatures, solution casting is often the pathway to formation of functional membranes. The interactions within the co-polymer and the interactions of each of the blocks with the surrounding solvent determine the conformation of the polymer and hence impact their assembly into membranes. Here, we resolve for the first time the structure of a single co-polymer in solution. We demonstrate that its overall conformation is dictated by segregation of the ionic segment.

Previous studies of this pentablock using small angle X-ray scattering and transmission electron microscopy,[18–20] concluded that for all sulfonation levels, spherical micelles are formed in 11 wt% cyclohexane/heptane mixtures, with a core of the sulfonated styrene and a corona of solvated flexible and end blocks. Recent water transport studies have shown that water sorption and absorption increase with increasing sulfonation levels as expected.[21] As the industrial process to form such membranes is solvent casting, and the three different blocks are of different nature with different T_g's and verification temperatures, controlling the structure in solution is a key element in understanding formation of a membrane.

2. Model and Methodology

Using fully atomistic MD simulation, we probe the conformation of the pentablock A-B-C-B-A of total molecular weight 50 050 g mol^{-1} containing randomly sulfonated atatic polystyrene in the center block (C) tethered to polyethylene with randomly substituted 1.1% propylene (B) and end-capped by atatic poly-*t*-butyl styrene (A) as shown in Figure S1, Supporting Information. The total wt% of the center sulfonated block is ≈40% with a random sulfonation fraction $f = 0.30$, while each of the randomly substituted polyethylene blocks is ≈20% and each of poly-*t*-butyl styrene blocks is ≈10%. Total number of monomers for the A-B-C-B-A pentablock studied here is 1 467 ($30 + 617 + 173 + 617 + 30$). For $f = 0.30$, 52 of 173 PS monomers in the center block are randomly sulfonated. The counterion in all the simulations was Na^+. Details regarding simulation code[22] and OPLS force fields for alkane[23,24] and sulfonated groups[25–27] are presented in Supporting Information. The results show that a unimolecular aggregates with well-defined hydrophilic and hydrophobic regions are formed where the interplay of solvent–polymer interactions and polymer–polymer interactions control the phase behavior and conformation of the individual blocks.

A mixture of cyclohexane and heptane, which is used industrially to cast films and water, among most ubiquitous substances, are studied. While water is a poor solvent for this polymer, similar to Nafion™,[28] membranes take up

significant amounts of water and under high-pressure, high temperature conditions are dissolved in water–alcohol to form colloidal solutions. The polymer is initially equilibrated in implicit solvents, i.e., a solvent modeled by an interaction parameter and a dielectric constant and then transferred to explicit solvents, cycling the temperature in a closed system, above the glass transition temperature of the polymer to equilibrate the chains. Results of simulations in cyclohexane heptane mixture and in water are compared to those in an implicit poor solvent with dielectric constant $\varepsilon = 1.0$ and 77.7. $\varepsilon = 1.0$ is the value for a vacuum where no screening occurs and $\varepsilon = 77.7$ is chosen to match the dielectric constant of water.

Here, we utilize an atomistic description of the solvents, which is computationally expensive, coupled with implicit solvents. While implicit solvents do not carry the chemical details of the solvents, they adequately describe most properties and allow tunability of the interaction of the polymer and solvent in a manner that is not accessible experimentally. Requiring less computational resources implicit solvents allow longer simulations, expending the range of conditions that can be realistically probed. Most importantly, a large temperature range is accessed and universal guide lines for the range of dielectric constants necessary to drive desired structures are attained.

High pressure-temperature conditions or extremely long dissolution times of weeks are required to experimentally dissolve this polymer in water. Here, preparation follows the experimental temperature cycling in a closed system. To address one of the most critical aspects of polymers in both experiments and simulations, attaining equilibrium, the pentablock was heated to 500 K and cooled back to 300 K, resulting in a significantly more compact structure than collapsing the chains directly at 300 K. Results for the radius of gyration versus time during this thermal cycling is shown in Figure S2, Supporting Information. We consider these more compact systems, obtained from heating to higher temperature and cooling back to 300 K, closer to equilibrium and then the structure obtained by directly collapsing at 300 K. All results in this paper were obtained in this manner for both explicit and implicit solvents.

3. Results and Discussion

Snapshots of the pentablock, the center block and a sulfonated PS chain identical to the center block in water are shown in Figure 1 at $T = 300$ and 500 K. At all temperatures, the polymer collapses into a unimolecular aggregate with a spherical symmetry with a clear segregation into hydrophilic and hydrophobic regions with no solvent in the core. This phase segregation to ionic blocks and the rest of the polymer provides the first insight into internal phase segregation. Additionally, we found that the

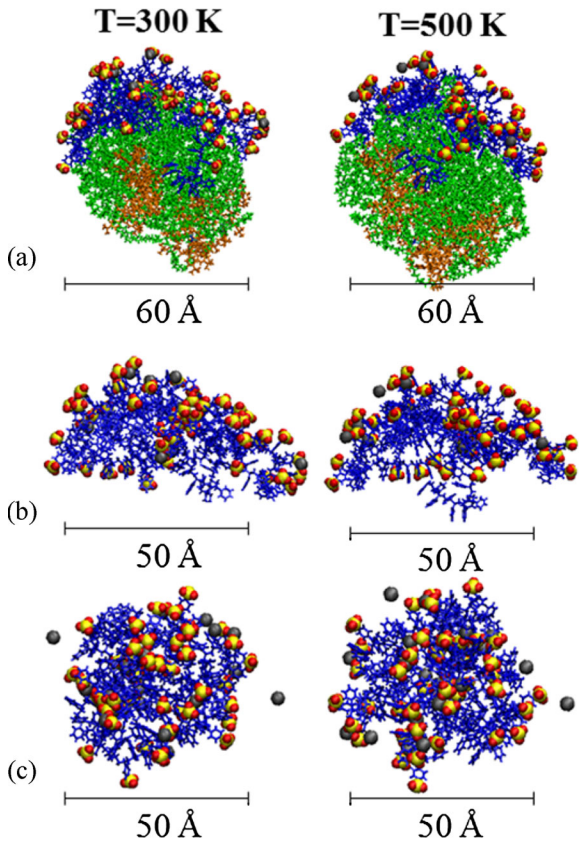

Figure 1. Snapshots of (a) pentablock, (b) center block of pentablock, and (c) sulfonated PS for $f = 0.30$ in water at $T = 300$ and 500 K. The end block is shown in orange, flexible block in green, center block in blue, oxygen atoms in red, sulfur atoms in yellow, and sodium atoms in gray.

connectivity of polymer impacts the conformation of the ionic blocks. The structure of the ionizable segment is surprisingly more extended compared with a randomly sulfonated polystyrene (PSS) chain identical to that of the center block as seen in Figure 1b,c. This visual observation is confirmed by comparing the ratio of the highest to lowest eigenvalue of the moment of inertia tensor, which at $T = 300$ K is 2.5 for the ionic center blocks and 1.4 for the PSS chain. A similar set of snapshots for the two implicit poor solvents with $\varepsilon = 77.7$ and 1.0 are shown in Supporting Information for $T = 300$, 400, 500, and 600 K.

In water and in the two implicit solvents all three blocks are collapsed as shown in Figure 2. The overall density of the core is uniform as shown in Figure S5, Supporting Information. In water, the ionic groups reside almost completely on the outer surface. The conformation of the pentablock and a sulfonated PS chain in water similar to that in the implicit poor solvent with $\varepsilon = 77.7$ where the ionic groups also reside on the outer surface. These results are in good agreement with those of Carrillo and Dobrynin[9] who reported that sulfonated PS chains in

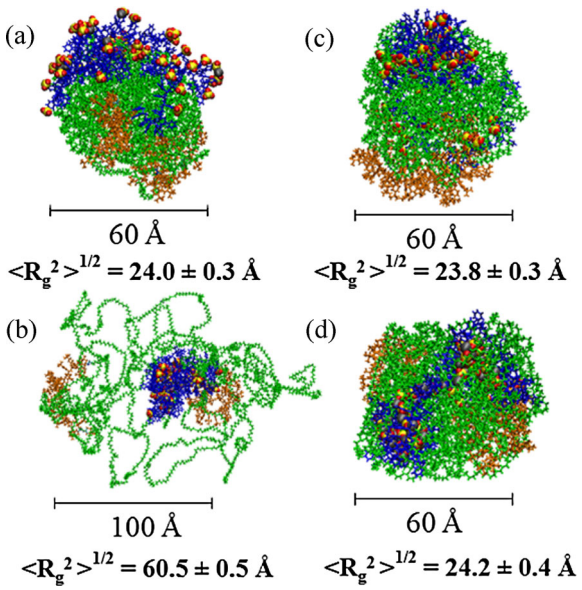

Figure 2. Snapshots of pentablock for $f = 0.30$ at $T = 300$ K (a) in water, (b) in a 1:1 mixture of cyclohexane and heptane, (c) in poor solvent with $\varepsilon = 77.7$, and (d) in poor solvent with $\varepsilon = 1.0$.

water and in the implicit poor solvent for $\varepsilon = 77.7$ form a globule-like conformation with all sulfonated groups located on the outer surface and the benzene rings of the styrene forming the inner surface.

Upon heating the system, the pentablock in water as well as in the two implicit solvents expands with most of the increase in size coming from expansion of the outer and flexible blocks. The center block and sulfonated PS are much less temperature sensitive. At all temperatures, phase segregation of the hydrophobic and ionic blocks is observed, where the open structures at higher temperatures point toward a state where interpenetration of the hydrophobic parts to form a steady network is more likely. The effects of temperature on the mean square radius of gyration $\langle R_g^2 \rangle^{1/2}$ of the pentablock, the center sulfonated block, and the PSS chain are shown in Figure S6, Supporting Information for both two implicit solvents in comparison with water. The polymer in cyclohexane/heptane follows similar trends however it is highly swollen and is discussed separately.

For both values of ε, $\langle R_g^2 \rangle^{1/2}$ of the entire pentablock increases with increasing temperature. Similarly, $\langle R_g^2 \rangle^{1/2}$ of the center block and PSS chains of the same length, increases monotonically as the temperature increases for $\varepsilon = 77.7$. These solutions behave as expected for ionic polymers in polar solvents such as water. However, for $\varepsilon = 1.0$, $\langle R_g^2 \rangle^{1/2}$ of the entire pentablock, the center block of the pentablock, and PSS, depends only weakly on the temperature.

A comparison between the dimensions of the homopolymer PSS solution and that of the center block show that the homopolymer is smaller than the center block bound in the pentablock, independent on ε. It is also significantly less sensitive to temperature variation. This dimension difference is attributed to the impact of the hydrophobic blocks that are strongly affected by temperature and essentially are pulling on the ionic segment.

To further understand the impact of the interactions with solvents, the pentablock was immersed in a 1:1 mixture of cyclohexane and heptane, which is a good solvent for the flexible and end blocks. In this case, as seen in Figure 2b both the flexible and end blocks are extended while the center ionic block is collapsed. As a function of temperature, $\langle R_g^2 \rangle^{1/2}$ for the entire pentablock is 18% larger at $T = 500$ K compared to 300 K while the center block and PSS chain by less than 2%. Note that in all four solvents the ionic block remains collapsed where the distribution and conformation of the center and end blocks vary offering different topological building blocks for membrane assembly.

The distribution of the sulfur and sodium atoms from the center of mass of the entire pentablock is shown in Figure 3. The majority of the sulfur atoms reside on the outer surface of the collapsed pentablock for both water and implicit poor solvent with $\varepsilon = 77.7$, as shown in Figure 3a, though the segregation to the surface is significantly larger in water. For $\varepsilon = 1.0$, most of sulfur atoms are distributed closer to the center of mass. This result is consistent with the conformations shown in Figure 2 in which most of the sulfur atoms are on the outer surface in water and implicit poor solvent with $\varepsilon = 77.7$. This result also shows that most of the sulfur groups are on outer surface. Figure 3b shows the distribution for the sodium counterions for the three solvents. For water and poor solvent with $\varepsilon = 77.7$, the sodium atoms are more widely dispersed compared to the case with $\varepsilon = 1.0$ as one would expect since the former two cases the Coulomb interactions are screened. At 300 K, in water only 10% of the Na^+ counterions are condensed on a SO_3^- sulfonated group. For the two implicit solvents, the fraction increases to 25 and 100% for $\varepsilon = 77.7$ and 1.0, respectively.

This computational study resolved for the first time the structure of molecular aggregate of a structured ionic polymer. These structures have been proven to be complex to the extent that scattering experiments are limited in resolving the internal structure of the aggregates, and in solutions sufficiently dilute at the detection limit of scattering. This dilute limit is essential for avoiding aggregation. Here, we calculate the static structure factor $S(q)$, where q is the momentum transfer vector. To study the size and shape of polymer chains, we calculated radius of gyration and structure factor $S(q)$. Structure factor is calculated using $S(q) = |\Sigma_i \, b_i \exp(i\mathbf{q}\bullet\mathbf{r}_i)|^2$, where b_i and $\mathbf{r}_i$ are the scattering length and position vector of atom i, respectively. All results for $S(q)$ are averaged over 500

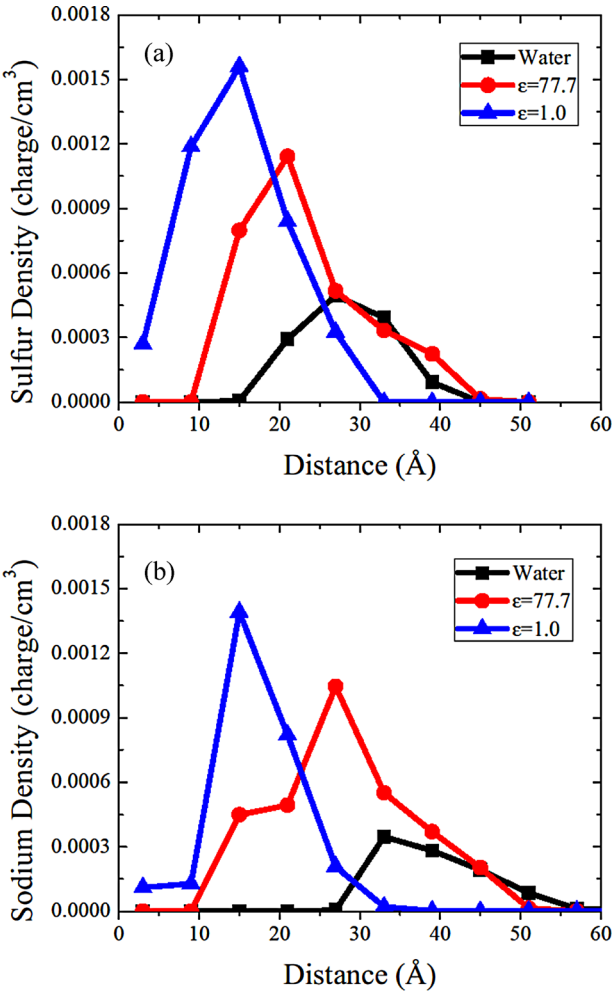

Figure 3. Density distribution function from the center of mass of pentablock for (a) sulfur atoms and (b) sodium atoms (b) at 300 K in water (black) and in poor solvent with $\varepsilon = 77.7$ (red) and $\varepsilon = 1.0$ (blue) for the entire pentablock.

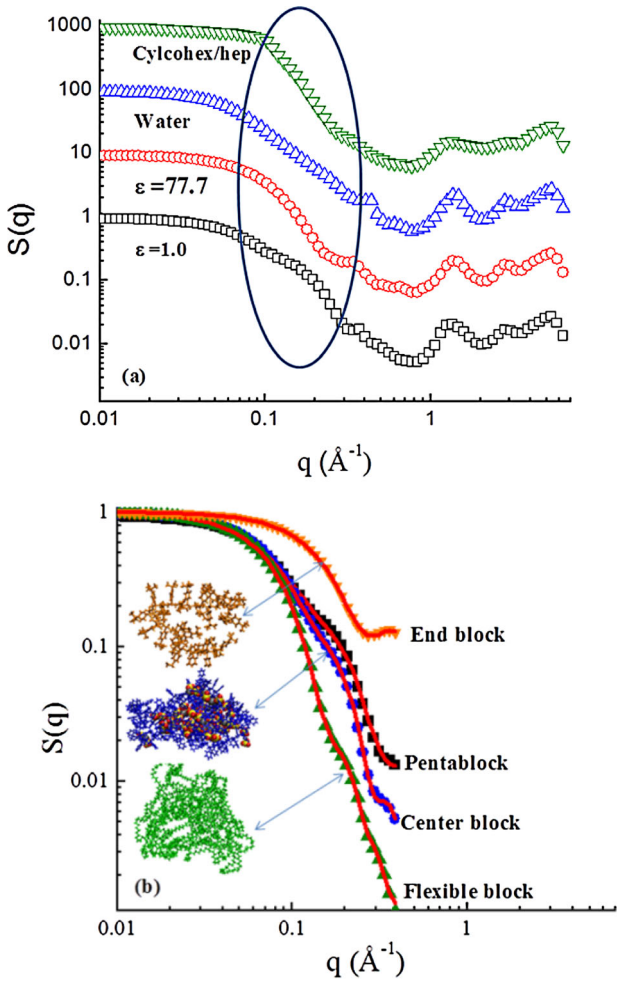

Figure 4. $S(q)$ for $f = 0.30$ at 300 K as a function of q (a) pentablock in poor solvent with $\varepsilon = 1.0$ (squares), in poor solvent $\varepsilon = 77.7$ (circles), in water (triangles), and in a 1:1 mixture of cyclohexane and heptane (down triangles). Data has been shifted vertically for clarity. (b) pentablock (squares), center block (circles), flexible block (triangles), and end block (down triangles) in poor solvent with $\varepsilon = 1.0$. Symbols represent the data and solid lines represent the best fit to the models described in text.

configurations with 500 different random **q** vectors for each q.

$S(q)$ of the pentablock in different solvents is shown in Figure 4a,b. The structure factors exhibit a characteristic slope at intermediate q region (shown by an ellipse in Figure 4a and become structured at high q. The general shape of the scattered object is determined from this intermediate q range where the slope of $S(q)$ provides a first indication of the shape. We find that magnitude of the slopes increase from 3.5 to 3.7 as ε of the implicit solvent increase from 1.0 to 77.7. These slopes indicate that the pentablock collapsed into a slightly aspherical object, which becomes more spherical as ε increases. In water and 1:1 mixture of cyclohexane and heptane, the slopes decrease to 3.0 and 2.7, respectively. The changes in presence of water are attributed to the structure inversion, i.e., hydrophilic ionic block exposed to water while hydrophobic blocks are shielded. In the presence of mutually good solvent for flexible block and end blocks, the center block is collapsed while flexible blocks float around the matrix. The structure at very high q is due to local atomic packing. These behaviors are further supported by the snapshots of pentablock as shown in Figure 2.

Further, insights of the structure are observed by fitting the data to an ellipsoid core–shell form factor,[29] which captured the characteristics of asymmetric and highly interacting blocks in solvents. This form factor is capable of capturing the overall symmetry. In an ideal core–shell model, where the core surface is smooth and well defined and the shell is homogenously distributed around the core,

this ellipsoid presents an excellent description of the system. In here however, with the presence of multiple intertwined blocks, the visualization offered by computations in imperative to in depth understanding of the structure as shown in Figure 4b, where the partial structure factors, fits for elliptical models and visualization are presented for implicit poor solvent with $\varepsilon = 1.0$. The ionic block is collapsed to a slightly asymmetric shape captured by an elliptical form factor, where the roughness is described by the shell. The end blocks and aliphatic chains are interwoven and segregate from the ionic block. With increasing complexity of the polymers, and diversion from highly symmetric shapes, the visualization obtained from computations is essential to resolve the structure.

4. Conclusion

A single chain of pentablock and sulfonated PS of the same molecular weight as that of the center block has been studied as a function of solvent quality. All blocks of pentablock are collapsed nearly spherical shape in water and in both implicit poor solvents with $\varepsilon = 1.0$ and $\varepsilon = 77.7$. Pentablock in water is very close to that in the implicit poor solvent for $\varepsilon = 77.7$ where the ionic groups are on outer surface. The three different blocks of pentablock segregate from each other in the 1:1 mixture of cyclohexane and heptane. Both the flexible and end blocks in the 1:1 mixture of cyclohexane and heptane are swollent while the center block is collasped. Comparing $\langle R_g^2 \rangle^{1/2}$ of the sulfonated PS with that of the center block of the pentablock, $\langle R_g^2 \rangle^{1/2}$ of center block is slightly higher than that of sulfonated PS. In both water and $\varepsilon = 77.7$, center block of pentablock and sulfonated PS chains are a globule-like conformation with all sulfonated groups located on the outer surface and the benzene rings of the styrene forming the inner surface. Similarly, the sodium counterions are more widely dispersed whereas for $\varepsilon = 1.0$ the counterions are largely condensed. The distribution of the sulfur atoms and sodium atoms from the center of mass of the entire pentablock revealed that the majority of the sulfur atoms are on the outer surface of the collapsed pentablock and sodium atoms are more widely dispersed in both water and implicit solvent with $\varepsilon = 77.7$.

This study shows for the first time that the blocks of a single pentablock chain locally phase separate into distinct regions depending on the solvent. By varying the solvent and temperature, the local morphology of membranes formed from by solvent processing of these pentablocks can be varied depending on how readily the different blocks can associate. Future studies are on underway to explore membranes and micelles made from these pentablock molecules.

Acknowledgements: The authors gratefully acknowledge financial support from DOE Grant No. DE-FG02-12ER46843. This research used resources at the National Energy Research Scientific Computing Center, which is supported by the Office of Science of the United States Department of Energy under Contract No. DE-AC02-05CH11231. This work was made possible by advanced computational resources deployed and maintained by Clemson Computing and Information Technology. This work was performed, in part, at the Center for Integrated Nanotechnologies, a U.S. Department of Energy and Office of Basic Energy Sciences user facility. Sandia National Laboratories is a multi-program laboratory managed and operated by Sandia Corporation, a wholly owned subsidiary of Lockheed Martin Corporation, for the U.S. Department of Energy's National Nuclear Security Administration under Contract No. DE-AC04-94AL85000.

The authors declare no competing financial interest.

Received: May 26, 2014; Revised: June 27, 2014; Published online: August 14, 2014; DOI: 10.1002/mats.201400046

Keywords: ionic polymers; ionomers; molecular simulations; structured polymers

[1] D. S. Kim, M. Guiver, J. E. McGrath, B. S. Pivovar, Y. S. Kim, *Polym. Electrolyte Fuel Cell* **2010**, *33*, 711.
[2] J. Kim, B. Kim, B. Jung, *J. Membr. Sci* **2002**, *207*, 129.
[3] D. T. Wong, S. A. Mullin, V. S. Battaglia, N. P. Balsara, *J. Membr. Sci.* **2012**, *394*, 175.
[4] A. E. Ozcam, N. Petzetakis, S. Silverman, A. K. Jha, N. P. Balsara, *Macromolecules* **2013**, *46*, 9652.
[5] A. J. Duncan, J. M. Layman, M. P. Cashion, D. J. Leo, T. E. Long, *Polym. Int.* **2010**, *59*, 25.
[6] A. J. Duncan, B. J. Akle, T. E. Long, D. J. Leo, *Smart Mater. Struct.* **2009**, *18*, 104005.
[7] T. Yoshida, T. C. Lai, G. S. Kwon, K. Sako, *Expert Opin. Drug Deliv.* **2013**, *10*, 1497.
[8] A. K. Shakya, K. S. Nandakumar, in: *Responsive Materials and Methods* (Eds: A. Tiwari, H. Kobayashi), Wiley, Hoboken, NJ, USA **2014**, p. 123.
[9] J. Y. Carrillo, A. V. Dobrynin, *J. Phys. Chem. B* **2010**, *114*, 9391.
[10] S. Park, X. Zho, A. Yethiraj, *J. Phys. Chem. B* **2012**, *116*, 4319.
[11] L. Zhang, B. C. Katzenmeyer, K. A. Cavicchi, R. A. Weiss, C. Wesdemiotis, *ACS Macro Lett.* **2013**, *2*, 217.
[12] X. Qiao, R. A. Weiss, *Macromolecules* **2013**, *46*, 2417.
[13] M. J. Park, N. P. Balsara, *Macromolecules* **2008**, *41*, 3678.
[14] X. Wang, K. M. Beers, J. B. Kerr, N. P. Balsara, *Soft Matter* **2011**, *7*, 4446.
[15] K. M. Beers, N. P. Balsara, *ACS Macro Lett.* **2012**, *1*, 1155.
[16] R. Yuan, A. A. Teran, I. Gurevitch, S. A. Mullin, N. S. Wanakule, N. P. Balsara, *Macromolecules* **2013**, *3*, 914.
[17] A. A. Teran, N. P. Balsara, *J. Phys. Chem. B* **2014**, *118*, 4.
[18] J. Choi, A. Kota, K. I. Winey, *Ind. Eng. Chem. Res.* **2010**, *49*, 12093.
[19] J. Choi, C. L. Willis, K. I. Winey, *J. Membr. Sci.* **2013**, *428*, 516.
[20] G. M. Geise, B. D. Freeman, D. R. Paul, *Polymer* **2010**, *51*, 5815.
[21] G. M. Geise, C. M. Doherty, A. J. Hill, B. D. Freeman, D. R. Paul, *J. Membr. Sci.* **2014**, *453*, 425.
[22] S. Plimpton, *J. Comput. Phys.* **1995**, *117*, 1.
[23] W. Jorgensen, J. Madura, C. Swenson, *J. Am. Chem. Soc.* **1984**, *106*, 6638.

[24] W. Jorgensen, D. Maxwell, J. TiradoRives, *J. Am. Chem. Soc.* **1996**, *118*, 11225.
[25] X. He, O. Guvench, A. D. MacKerell, Jr., M. L. Klein, *J. Phys. Chem. B.* **2010**, *114*, 9787.
[26] W. R. Cannon, B. M. Pettitt, J. A. McCammon, *J. Phys. Chem.* **1994**, *98*, 6225.
[27] J. Chandrasekhar, D. C. Spellmeyer, W. Jorgensen, *J. Am. Chem. Soc.* **1984**, *106*, 903.
[28] G. Gebel, *Polymer* **2000**, *15*, 5829.
[29] J. S. Pederson, M. C. Gerstenberg, *Macromolecules* **1996**, *29*, 1363.

Association of a multifunctional ionic block copolymer in a selective solvent

Thusitha N. Etampawala, Dipak Aryal, Naresh C. Osti, Lilin He, William T. Heller, Carl L. Willis, Gary S. Grest, and Dvora Perahia'

Citation: J. Chem. Phys. **145**, 184903 (2016); doi: 10.1063/1.4967291
View online: http://dx.doi.org/10.1063/1.4967291
View Table of Contents: http://aip.scitation.org/toc/jcp/145/18
Published by the American Institute of Physics

Association of a multifunctional ionic block copolymer in a selective solvent

Thusitha N. Etampawala,[1] Dipak Aryal,[1] Naresh C. Osti,[1] Lilin He,[2] William T. Heller,[2] Carl L. Willis,[3] Gary S. Grest,[4] and Dvora Perahia[1,a)]

[1]*Department of Chemistry, Clemson University, Clemson, South Carolina 29634, USA*
[2]*Biology and Soft Matter Division, Oak Ridge National Laboratory, Oak Ridge, Tennessee 37831, USA*
[3]*Kraton Polymers US LLC, 16400 Park Row, Houston, Texas 77084, USA*
[4]*Sandia National Laboratories, Albuquerque, New Mexico 87185, USA*

(Received 7 September 2016; accepted 25 October 2016; published online 14 November 2016)

The self-assembly of multiblock copolymers in solutions is controlled by a delicate balance between inherent phase segregation due to incompatibility of the blocks and the interaction of the individual blocks with the solvent. The current study elucidates the association of pentablock copolymers in a mixture of selective solvents which are good for the hydrophobic segments and poor for the hydrophilic blocks using small angle neutron scattering (SANS). The pentablock consists of a center block of randomly sulfonated polystyrene, designed for transport, tethered to poly-ethylene-*r*-propylene and end-capped by poly-*t*-butyl styrene, for mechanical stability. We find that the pentablock forms ellipsoidal core-shell micelles with the sulfonated polystyrene in the core and Gaussian decaying chains of swollen poly-ethylene-*r*-propylene and poly-*t*-butyl styrene tertiary in the corona. With increasing solution concentration, the size of the micelle, the thickness of the corona, and the aggregation number increase, while the solvent fraction in the core decreases. In dilute solution the micelle increases in size as the temperature is increased, however, temperature effects dissipate with increasing solution concentration. *Published by AIP Publishing.* [http://dx.doi.org/10.1063/1.4967291]

INTRODUCTION

Diblock copolymers in selective solvents form rich phase diagrams that include micellar phases, gels as well as ordered complex fluids. Diverse micellar structures are observed where the shape and the stability of the assemblies depend on the relative dimensions of the block, their interactions, as well as the interaction of each block with the solvent.[1–4] These structured solutions often serve as precursors for casting membranes, where the morphology of the micelles impacts the film structure and properties. Enhancing the complexity of the copolymer by tailoring polymers with multiple blocks, each with a specific role, has been one of the most promising pathways to new multi-functional materials. Most experimental and theoretical studies, however, have provided insight into assembly of di and tri-block copolymers only in the low segregation regime.[5–11] The effect of complex architectures present in assemblies of multiple blocks containing highly interacting blocks on their structure and dynamics remains to be resolved.

One important example is a multiblock copolymer in which one of the blocks facilitates transport and the others provide mechanical stability. These copolymers are of particular interest in applications such as fuel cells, organic photovoltaic devices, battery separators, electro-dialysis, as well protective breathable cloth.[12–14] Despite immense efforts to generate new transport controlled materials,[1–11] under the conditions that transport is optimized, the mechanical or the chemical stability is compromised. Structured polymers exhibit a potential to form mechanically stable multi-functional materials capable of transporting electrons, ions, as well as guest molecules. An in-depth understanding of the association of structured polymers in solution and the propagation of solution structures into thin films is warranted in order to design membranes with well-defined properties. Here we present an insight into the shape and stability of assemblies formed by a pentablock copolymer that consist of a highly interacting ionic segment tethered to blocks which provide mechanical stability as resolved by small angle neutron scattering (SANS). The inherent contrast of the scattering length density of hydrogen and deuterium to neutrons offers a means to probe a uniquely detailed internal structure of aggregates formed by structured polymers with several highly incompatible blocks. In contrast to microscopy studies, solvent distribution as well as interfacial boundaries within the micelle are resolved. Here we demonstrate that in contrast to copolymers in the low segregation limit, one block, the ion bearing one, controls the overall stability and shape of the micelles.

Among the most extensively studied structured polymers are flexible diblocks in the weak segregation regime with ca. $\chi N < 10$ where χ is the Flory Higgins interaction parameter and N is the polymerization number.[5–11] When dissolved in a selective solvent, a preferential solvate for one blocks, these diblocks form core-shell structures with different geometries, such as spherical, ellipsoidal and cylindrical where the less soluble blocks are surrounded by a corona formed by the soluble blocks. The dimensions, geometries, and stability of block copolymer micelles are mainly determined by minimization of the overall free energy.[15,16] Most of the

a)Email: dperahi@g.clemson.edu

previous studies were carried out in the weak segregation limit. However, with increasing incompatibility of the block copolymers, interfacial tension between the blocks in the core and corona increases and becomes a significant contribution to the free energy.[17,18] Overall, the delicate balance between entropy loss due to confinement and the tendency to minimize unfavorable interactions control the stability of the micelles.

With the realization of the technological potential of structured polymers, complexity of their architecture increased significantly, leading to new phase behavior. Among the many examples were studies by Geise *et al.*[14,19,20] who showed that sulfonation of random copolymers such as poly(styrene-*b*-hydrogenated butadiene-*b*-styrene) leads to uncontrolled swelling in polar solvents. The solvent penetration results in poor mechanical stability. Eisenberg *et al.*[21] realized that the diblock copolymer topology in which only one of the blocks swells provides a mechanically stable manifold. They showed that polystyrene-*b*-poly(cesium acrylate) and polystyrene-*b*-poly(cesium methacrylate) form spherical micro-domains surrounded by a non-ionic polystyrene corona in the presence of toluene, a solvent selective for the polystyrene block. Increasing the topological complexity by tailoring multiple blocks with significantly different chemistries provides pathways to form stable multifunctional polymers.

One example for a topology controlled polymer is a pentablock co-polymer of the form ABCBA. This structured polymer was designed by Kraton Polymers LLC, with the rationale of tailoring an ion transport-facilitating block surrounded by aliphatic chains for flexibility and a sturdy end block for stability. Specifically, this block copolymer shown in Figure 1 consists of a randomly sulfonated polystyrene midblock bound on both sides to poly-ethylene-*r*-propylene blocks to allow control of mobility and rearrangements of the polymer, terminated on both sides by poly-*t*-butyl styrene a block that contributes to mechanical stability.[14] Recently, Choi *et al.*[13] reported X-ray scattering and transmission electron microscopy studies revealing spherical micelles with a core of sulfonated polystyrene block and a corona of solvated poly-ethylene-*r*-propylene and poly-*t*-butyl styrene blocks regardless of sulfonation level of the center block in hydrophobic solvents. These studies, which focused on relatively high polymer concentrations of approximately 11 wt. %, provided the first indication of the morphology of micelles formed by structured ionic polymers. Griffin *et al.*[22] found by x-ray scattering that at low weight fractions of polar solvent, these pentablocks form spherical micelles with the sulfonated center block in the core. Further studies by Geise *et al.*[14,23] followed transport across these membranes. They found that the transport increases with increasing sulfonation levels and is strongly dependent on the counterion.

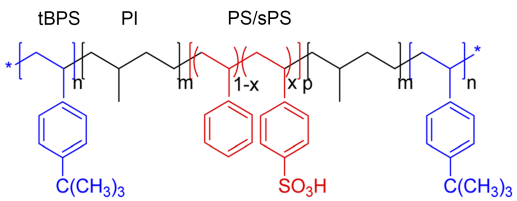

FIG. 1. Chemical structure of a randomly sulfonated block copolymer, poly(*t*-butyl-styrene)-*b*-ethylene-*r*-propylene-*b*-styrene-*r*-styrenesulfonate-*b*-ethylene-*r*-propylene-*b*-poly(*t*-butyl-styrene). The weight distribution = 15-10-28-10-15 kg/mol for the five blocks. The sulfonated polystyrene block is randomly sulfonated to x ~ 42 mol. %. n, m, and p, are approximately 94, 142, and 203, respectively.

The morphology of the micelles and the structural details of the segregation of the blocks within the assembly determine the association of the polymer into films in solution cast process. Building on the knowledge acquired by Choi *et al.*,[13] we probed the assembly process of the micelles and their stability in a mixed solvent of cyclohexane and heptane, which is used industrially to cast films, using neutron scattering. In contrast to previous solution studies, we probed the low concentration regime, following the transition from a single molecule to a micelle. Our temperature and concentration studies revealed extremely stable assemblies whose symmetry is impacted by the assembly of the ionic groups. We found that the complexity of the polymer and the incompatibility of the blocks results in divergence of the micelles' shape from sphericity and their internal structure diverges from a simple core-shell model.

EXPERIMENTAL

Materials

The pentablock copolymer was provided by Kraton Polymers LLC. The polymer was synthesized via anionic polymerization and the middle styrene block was selectively sulfonated.[24] This study focuses on a pentablock with molecular weight of the unsulfonated blocks 15-10-28-10-15 kg/mol with a 42 mol. % randomly sulfonated middle styrene block. The polymers were obtained in concentrated solutions in protonated solvents and were diluted with a 1:1 volume ratio of deuterated cyclohexane and deuterated n-heptane purchased from Cambridge Isotope Laboratories, Inc., USA to form solutions with concentrations ranging from 0.025 wt. % to 6.0 wt. %. All calculations and solvents were corrected for the presence of small quantities of protonated solvents.

SMALL ANGLE NEUTRON SCATTERING

SANS experiment

SANS measurements were carried out on several instruments including the Extended Q–Small Angle Neutron Scattering (EQ-SANS)[25] at the Spallation Neutron Source (SNS) and the General Purpose Small Angle Neutron Scattering (GP-SANS)[26] at High Flux Isotope Reactor (HFIR) both at Oak Ridge National Laboratory. The data were collected over a broad momentum transfer vector range. The momentum transfer vector q is given by $q = 4\pi \sin(\theta)/\lambda$, where 2θ is the scattering angle and λ is the neutron wave length.

Measurements of pentablock copolymer solutions ranging from 0.5 wt. % to 6 wt. % were carried out on EQ-SANS over two q ranges, keeping nominal detector-to-sample distance constant at 4 m using a frame-skipping mode at chopper frequency of 60 Hz. Two wavelength bands, 2.6–5.7 Å and 13.4–16.5 Å, were used to obtain a desired momentum transfer vector range.

Dilute solutions from 0.025 wt. % to 0.1 wt. % were studied on GP-SANS with two different configurations covering a

q range from ca. 0.003–0.06 $Å^{-1}$ and ca. 0.028–0.38 $Å^{-1}$ while keeping the wave length constant at 4.72 Å and varying the detector-to-sample distances of 18.5 m and 2 m, respectively. Measurements were performed on the pentablock copolymer solutions, empty cell, and the solvents of d_{12}-cyclohexane and d_{16}-heptane with traces of protonated solvent to match the sample, in each configuration. The scattering of solvents and empty cell was subtracted from the data. Data were normalized to a calibrated, standard porosil-B[25] and corrected for their transmission to obtain absolute intensity. Data were recorded on 2-dimensional detectors and integrated into one dimensional scattering patterns using Mantid,[25] the default software at EQ-SANS and the standard data reduction procedure using SPICE,[26] the default software at GP-SANS.

SANS data analysis

The SANS data were analyzed using the SASfit[27] version 0.93.5 developed by Kohlbrecher and Bressler. Neutron scattering length densities (SLD); 0.71×10^{-6} $Å^{-2}$ for *t*-butyl styrene, -0.30×10^{-6} $Å^{-2}$ for ethylene, 1.69×10^{-6} $Å^{-2}$ for sulfonated styrene blocks, and 6.35×10^{-6} $Å^{-2}$ for 1:1 volume ratio of d_{12}-cyclohexane and d_{16}-heptane, were determined using their chemical formula and their bulk densities (tBPS = 1.08 g cm^{-3}, PE = 0.87 g cm^{-3}, PS/sPS = 1.47 g cm^{-3}, d_{12}-cyclohexane = 0.78 g cm^{-3}, and d_{16}-heptane = 0.68 g cm^{-3}). These values were used as the starting SLDs in the fitting routine.

The average dimensions of the scattering objects were initially estimated by calculating the radius of gyration from the Guinier approximation for spherical particles,

$$I(q) \approx SLD^2 V^2 exp\left(-\frac{1}{3}q^2 R_g^2\right), \quad (1)$$

where I(q) is the measured intensity, *SLD* is the scattering length density, *V* is the volume of the particle, *q* is the momentum transfer vector, and R_g is the radius of gyration. The Guinier approximation is valid for dilute and homogeneous solutions, where particles in the system scatter independently and are randomly orientated.[28]

Micellar form factor

Previous studies reported spherical core shell micelles. While the spherical core-shell model as well as an onion-model did match some of the low q data, they do not capture the scattering function across the broad q measured. To capture the behavior of the micelles across a broad q range, an ellipsoidal core-shell with Gaussian decaying chains was used to analyze the scattering data. This model has successfully captured the characteristics of asymmetric and highly interacting diblock copolymer micelles in solutions.[29–34] Pedersen *et al.*,[31] for example, described the micellar structure of an asymmetric polystyrene-polyisoprene diblock copolymer in a slightly selective solvent for polystyrene, di-n-butyl phthalate, and Ratnaweera *et al.*[34] determined the shape of a diblock copolymer, polytrifluoro propyl methylsiloxane-*b*-polystyrene, in toluene, a selective solvent for polystyrene.

Four different contributions including self-correlation terms of core and corona together with the cross terms between the core-corona and the corona-corona chains are encapsulated in this form factor[29–33]

$$\begin{aligned} F_{Micelle} &= N\beta_{Core}^2 F_{Core}(q) + N\beta_{Brush}^2 F_{Brush}(q) \\ &\quad + 2N^2 \beta_{Core}\beta_{Brush} S_{Core-Brush}(q) \\ &\quad + N(N-1)\beta_{Brush}^2 S_{Brush-Brush}(q), \end{aligned} \quad (2)$$

where N is the number of chains associated to form a micelle, β_{Core} and β_{Brush} are the total excess scattering length densities of the core and the shell. Here brush refers to the polymer chains in corona. The self-correlation term of core and corona is given by F_{Core} and F_{Brush}, respectively. F_{Core} describes the interaction of chains in the core and defines it as a homogeneous core in the center and decaying core-chain density at the core-corona interface. F_{Brush} describes Gaussian chains and obeys the Debye function. The cross terms between the core-corona and the corona-corona chains are given in $S_{Core\text{-}Brush}$ and $S_{Brush\text{-}Brush}$, respectively. The $S_{Core\text{-}Brush}$ consists of roughness of the interfaces between the two while $S_{Brush\text{-}Brush}$ reflects the interactions among the corona chains themselves. Mathematical description of F_{Core}, F_{Brush}, $S_{Core\text{-}Brush}$, and $S_{Brush\text{-}Brush}$ is given by[29,30,32,33,35]

$$F_{Core}(q, R_{Core}, \varepsilon) = \int_0^{\pi/2} \Phi^2 \left[qr\left(R_{Core}, \varepsilon, \alpha\right)\right] \sin\alpha \, d\alpha, \quad (3)$$

$$F_{Brush}\left(q, R_g\right) = \frac{2\left(e^{-x} + x - 1\right)}{x^2}, \; x = (qR_g)^2, \quad (4)$$

$$\begin{aligned} &S_{Core-Brush}\left(q, R_{Core}, \varepsilon, R_g, d\right) \\ &\quad = \Psi(qR_g) \int_0^{\pi/2} \Phi\left[qr\left(R_{Core}, \varepsilon, \alpha\right)\right] \omega \sin\alpha \, d\alpha, \end{aligned} \quad (5)$$

$$S_{Brush-Brush}\left(q, R_{Core}, R_g, d\right) = \Psi^2(qR_g) \int_0^{\pi/2} \omega^2 \sin\alpha \, d\alpha. \quad (6)$$

σ is the interface thickness, $\Phi(qR_{Core}) = 3\left[\sin(qR_{Core}) - qR_{Core}\cos(qR_{Core})\right]/(qR_{Core})^3$ is the form factor amplitude of solid sphere and $\Psi(qR_g) = \left[1 - \exp\left(-q^2R_g^2\right)\right]/q^2R_g^2$ is the form factor amplitude of the brush. $\omega = \sin\left(q\left[R_{Core} + dR_g\right]\right)/q\left[R_{Core} + dR_g\right]$. A sharp interface between the core and corona is represented by d = 1 while penetration of the corona into core is represented by $d < 1$. Essentially, d is a scaling factor that reflects the roughness. The orientation-dependent radius of the ellipsoid is given by $r\left(R_{Core}, \varepsilon, \alpha\right) = R_{Core}(\sin^2\alpha + \varepsilon^2\cos^2\alpha)^{1/2}$, where α is the angle of the long axis of ellipsoid with respect to q.

Scattering length densities of 1:1 volume ratio of d_{16}-heptane and d_{12}-cyclohexane, each polymer block, sPS, PE, and tBPS were used as initial input parameters with initial R_g of the micelles estimated from the Guinier analysis. The dimensions of the core, corona, aggregation numbers, and eccentricity of the ellipsoidal micelles as well as the volume fraction of solvent in the micellar core were allowed to vary. Best fits were obtained by minimizing χ^2. It is noted that attempts to analyze the data with form factors of a spherical core-shell micelle and a core with two shells were not successful.

MOLECULAR DYNAMICS SIMULATION

Molecular dynamics simulations of an ionic pentablock in dilute solution were carried out using Large-Scale Atomic/Molecular Massively Parallel Simulator (LAMMPS).[36] A single pentablock of total molecular weight of 52 853 g/mol in a 1:1 mixture of 21 600 cyclohexane molecules and 21 600 heptane molecules was modeled using the Optimized Potentials for Liquid Simulations - All Atoms (OPLS-AA) framework of Jorgensen *et al.*[37,38] The counter ion was Na^+. Non-bonded interactions were calculated between all atom pairs of different molecules and all pairs on the same molecule separated by three or more bonds, though the interaction is reduced by a factor of 1/2 for atoms separated by three bonds. All Lennard-Jones interactions were cut-off at r_c = 12 Å. For atom pairs, all electrostatic interactions closer than 12 Å were calculated in real space; those outside this range are calculated in reciprocal Fourier space by using the particle-particle particle-mesh algorithm (PPPM)[39] with precision of 10^{-4}. The Newton equations of motion were integrated using a velocity-Verlet algorithm with a time step δt = 1 fs. To maintain the system temperature, a Langevin thermostat with a 100 fs damping constant was used. The system was equilibrated for 30 ns at P = 1 atm using a Nose-Hoover thermostat with the same damping constant followed by a run of 20 ns at constant volume to obtain $S(q) = \left|\sum_i b_i e^{iqr_i}\right|^2$ of the pentablock, where b_i and r_i are the scattering length and position vector of atom i, respectively.

RESULTS AND DISCUSSION

The structure of the aggregates was first studied as a function of concentration at 25 °C. Scattering patterns are presented in Figures 2(a) and 2(b). The patterns appear rather similar at concentrations above 0.025 wt. %. Further structural features are observed in a Kratky plot, presented in Figure 2(b). At 0.01 wt. %, the scattering intensity decreases significantly and the high q-range is no longer detectable. This concentration will be separately discussed following the analysis of the micellar structure.

The intensity of the scattering patterns at intermediate q regime decreases as $I(q) \sim q^{-\alpha}$. In scattering of isolated objects in the intermediate q range, the exponent α is characteristic of the shape of the scattering objects. As shown in Figure 2(a), α is approximately 3.8 at low concentrations and decreases to approximately 3.2 at highest concentration. For a spherical object, α = 4. In the high q range, the scattering function is dominated by internal dimensions of the micelle. This initial scaling analysis shows that the overall symmetry of the micelle diverges from a sphere. The divergence from sphericity is a result of the sulfonated groups that affect the rigidity of the center block and consequently its packing. Our on-going SANS studies have shown that at lower sulfonation levels the core of the micelles is spherical.

A crossover from the intermediate q region is observed at approximately 0.04 $Å^{-1}$. At low concentrations, the slopes crossed over to approximately 2.0. With increasing the concentration the slopes cross over to approximately 1.5. These crossover regions are essentially a crossover from the q range that captures the dimensions of the entire micelle to that of internal features, as will be further discussed together with the full analysis of the scattering patterns.

The data are plotted as a generalized Kratky plot $q^2I(q)$ vs. q in Figure 2(b). This presentation offers a clearer view of the scattering features at different q and provides a more accurate insight into the shape and internal structure of the micelle. At low q region a clear peak, accompanied by a shoulder is observed. Its intensities grow with increasing concentration, where some overlap of the curves is observed at lower concentrations and increases at higher concentrations. This behavior is consistent with an assembly process in which the micellar size increases with increasing concentration up to a dimension in which the energetics of the system are balanced. Further increase in concentration results in the formation of more micelles. This behavior is reflected in the values of R_g of the micelles, extracted from the Guinier analysis presented in Figure 3. Above 0.01 wt. %, R_g increases linearly with concentration and then levels off. R_g values determined from the Guinier analysis are used as initial values for full form factor analysis.

A close look at the high q regime, presented in Figure 2(b), provides further insight into the internal structure of the micelles. At the crossover dimension of approximately 0.04 $Å^{-1}$,

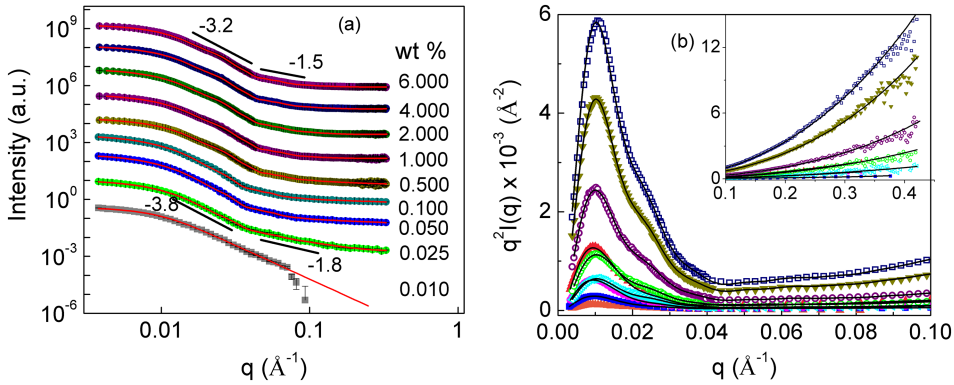

FIG. 2. SANS profiles in terms of (a) log I(q) vs. log q, (b) $q^2I(q)$ vs. q for the pentablock copolymer solution at concentration from 0.01 wt. % to 6 wt. % (orange—0.01 wt. %, blue—0.025 wt. %, pink—0.05 wt. %, cyan—0.1 wt. %, green—0.5 wt. %, red—1 wt. %, violet—2 wt. %, yellow green—4wt. %, and navy blue—6 wt. %) at 25 °C. The symbols represent the experimental data and the solid lines represent the best fits to the models described in text. Curves in (a) shifted for clarity.

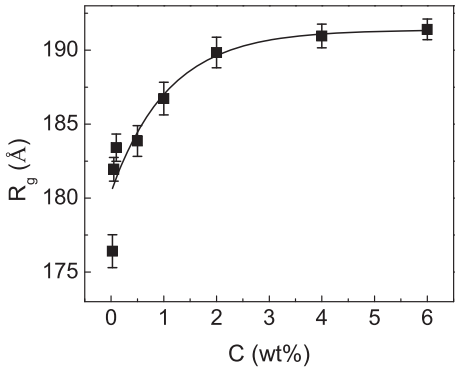

FIG. 3. Radius of gyration R_g extracted from Guinier analysis for the pentablock copolymer as a function of polymer concentration at 25 °C. The error bars in the profiles denote the standard deviation for each of the fits.

all curves exhibit a minimum beyond which q increases monotonically, however no plateau is observed, supporting the divergence from sphericity. The features at low q are the result of well-defined micelles, where the monotonic increase of $q^2I(q)$ at higher q is consistent with a Gaussian distribution of the corona segments swollen with solvent.[40]

The form factor of an ellipsoidal core-shell with Gaussian decaying chains at the corona captures well the features of all the scattering patterns. The best fits are shown as solid lines in Figure 2. As discussed above, the association of the pentablock into micelles is driven by mutually exclusive interactions between the blocks and the affinities of the blocks to the solvent. Since the solvent is hydrophobic, the ionizable block segregates to the center of the micelle and the rest of the blocks are Gaussian. These results show that the shape of the ionizable domain dominates the overall shape of the micelle. Our molecular dynamics simulations[41,42] have shown that the ionic segment of the pentablock assumes a slightly elongated shape. These results are consistent with previous findings that have shown elongated ionizable domains in melt homopolymers and random copolymers such as Nafion®.[43,44] In this study, the presence of multiple highly incompatible blocks along with the mutual compatibilities of solvent results in the breaking of a fully spherical symmetry, resulting in elongation captured by an ellipsoidal core-shell model.

The dimensions of the aggregates including that of the micellar core and corona together with the volume fraction of solvent in the core and aggregation number were extracted from the fits presented in Figures 4(a)–4(d). With increasing concentrations, both the core and the corona size increased rapidly up to about 2 wt. % and then level off as shown in Figures 4(a) and 4(b). The long and the short dimensions of the core retain relatively similar eccentricities with increasing concentrations providing a first insight into the growth pathways of the micelle. At the initial stage of association the number of polymer molecules increases and consequently, the size of the micelle increases. In this regime, the overall dimension of the micelle is determined by an internal balance of interfacial energies between the ionizable domain and the area per chain in the corona. Above the concentration in which an optimal structure in which the area per corona chain is optimized, no further changes in the dimensions of the micelle take place and the number of micelles increases. The plateau in dimensions of a micelle without the development of an interaction peak is rather unusual for both polymers and surfactant micelles. It suggests that the growth is limited by the excluded volume of the corona chains rather than balance of interfacial energies at the interfaces between the core and corona. This is further supported by the compactness of the ionizable block in comparison with the highly swollen state of the corona.

Even though the core size increases with increasing the concentration, the volume fractions of the trapped solvent, Φ, in the micellar core decrease. Φ varies from ~0.68 to 0.26 as the polymer concentration increases as shown in Figure 4(d). In contrast to van der Waals co-polymers, the core consists of both hydrophilic and hydrophobic groups, allowing the solvent to reside in the core. As the sulfonated groups are hydrophilic, with increasing concentration, the hydrophilic nature of the core is enhanced as a result of aggregation of more sulfonated PS groups. This results in repulsion of hydrophobic solvent molecules out of the micellar core. Nguyen *et al.*[21,45] found similar effects for highly incompatible block copolymers. They observed that these systems tend to optimize their size by reducing the amount of solvent in the core. Further, the entropy cost for the expansion of core and corona chains at equilibrium is balanced by surface energy gained by an increase in size.

At 0.01 wt. %, the data can no longer be described by an elliptical micelle form factor. The data were therefore analyzed in terms of a form factor of an ellipsoid coupled to a Gaussian chain. This analysis reflects the fact that the sulfonated center block assumes an elliptical shape, whereas the hydrophobic chains assume a Gaussian conformation. Since they are not constrained to surround the ellipsoid, they can explore all of the space with only a single tether point. The fit is shown in Figure 2(a) giving dimensions of approximately 40 Å for the radius of major core and 176 Å for the R_g of the whole object and 0.78 for the eccentricity of the ellipsoid. At this low concentration, the pentablock consists of an ionic collapsed block with an ellipsoid shape surrounded by highly swollen chains from the middle and outer blocks. The ionic cluster holds a significant amount of solvent, though it retained a collapsed configuration. Molecular dynamics simulations of a single molecule in heptane and cyclohexane reveal a similar configuration as shown in Figure 5.[41,42] The corresponding calculated S(q) is shown as well. Note that the scattering function of an experimental low concentration solution is scattering from an ensemble and is impacted by its variability. These results, however, clearly demonstrate that in this hydrophobic solvent, the ionic block remains collapsed.

The stability of the micelles and their structure was studied as a function of temperature in the low concentration regime 0.025–2 wt. %. The samples were heated up to 75 °C (limited by the boiling temperature of the solvents). The scattering profiles are presented in Figures 6(a)–6(d). In this temperature range, the micelles remain stable. Only small changes are observed in the low q region for all concentrations. The slopes of the scattering patterns, at intermediate q range, decrease slightly, i.e., the micelles become less spherical with increasing temperature. At high q, however, the slope changes significantly at low concentrations and is less pronounced as

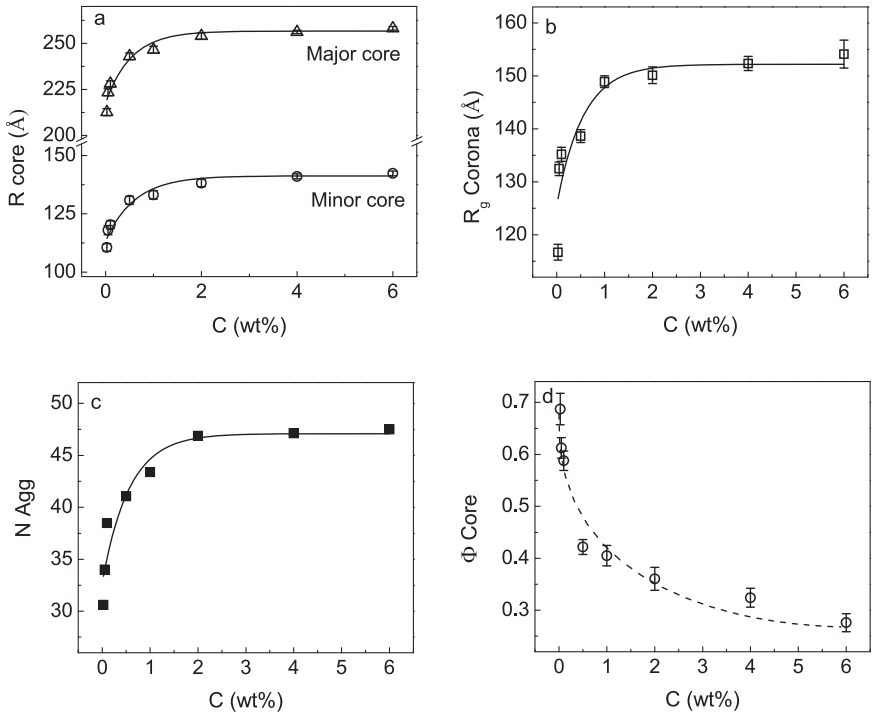

FIG. 4. Calculated parameters from the ellipsoidal core-shell model for the pentablock copolymer solutions as a function of polymer concentration at 25 °C. (a) Radii of core, (b) R_g of corona, (c) aggregation number, and (d) solvent fraction in the core.

the concentration increases. In the high q range, changes in internal structure of the micelles are reflected. These changes are observed predominantly at the low concentration regime. At the lowest concentration, a slope of approximately 2 is observed. This is consistent with conformation of a Gaussian chain. Upon heating the chains, they stretch out into the solvent. As the corona becomes more miscible in the solvent, there is no clear distinction between the solvent and the corona and S(q) is dominated by the scattering from the ionic core. With increasing concentration, the corona becomes more defined and the impact of temperature less pronounced.

All the profiles were analyzed in terms of the form factor of ellipsoidal core-shell micelles with Gaussian decaying chains at the corona. The best fits are given in solid lines in Figures 6(a)–6(d). The eccentricities of the micelles are hardly affected by temperature. The overall shape of the scattering profile does not change significantly with increasing temperature, which we attribute to the fact that the micelles do not dissociate in this temperature range.

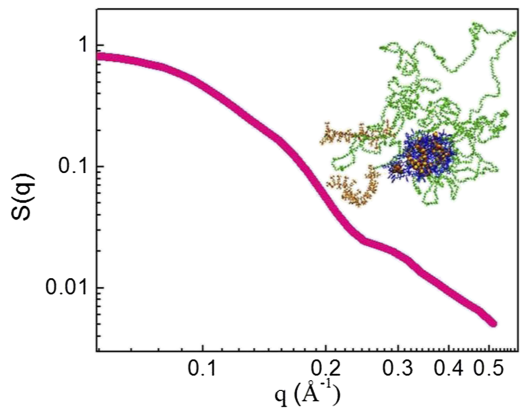

FIG. 5. Snapshot and S(q) of a pentablock with a total molecular weight of 52 853 gm/mol with a weight fraction of 10:20:40:20:10 and sulfonation fraction is 0.4 in 1:1 a mixture of cyclohexane and heptane at 27 °C from a molecular dynamics simulation. The end block is shown in orange, flexible block in green, middle block in blue, oxygen atoms in red, sulfur atoms in yellow, and sodium atoms in gray.

The dimensions of the micelles, including those of the core and corona together with the volume fraction of solvent in the core and the aggregation number, were extracted from the full data analysis as a function of concentration and temperature. The parameters as a function of concentration are presented in Figures 7(a)–7(d). The insets represent the changes of the corresponding parameter at low concentrations.

The size of the micelles increases with increasing temperature regardless of the concentration as shown in Figures 7(a) and 7(b), where the degree of changes of core size is higher than that of the corona. Fairly large micelles with more trapped solvents were observed even at 0.025 wt. % in comparison with higher concentrations. At the highest temperature, the core size changes only slightly compared to the changes at room temperature. This supports our assertion that the ionic segment dominates the structure and provides stability. Extensions of the outer two blocks do not result in pulling out molecules from the micelle.

The number of polymer chains associated for the micellar assembly or the aggregation number increases with increasing concentration and temperature as shown in Figure 7(c). The results are in agreement with the increase in core size. The increase of aggregation number with increasing the temperature is rather slow at higher concentrations. We calculated the enthalpy, ΔH, of association of chains to micelles at room temperature using the changes of aggregation number as a function of the concentration using $N_{agg} = Ae^{-\Delta H}/RT$, where N_{agg} is the

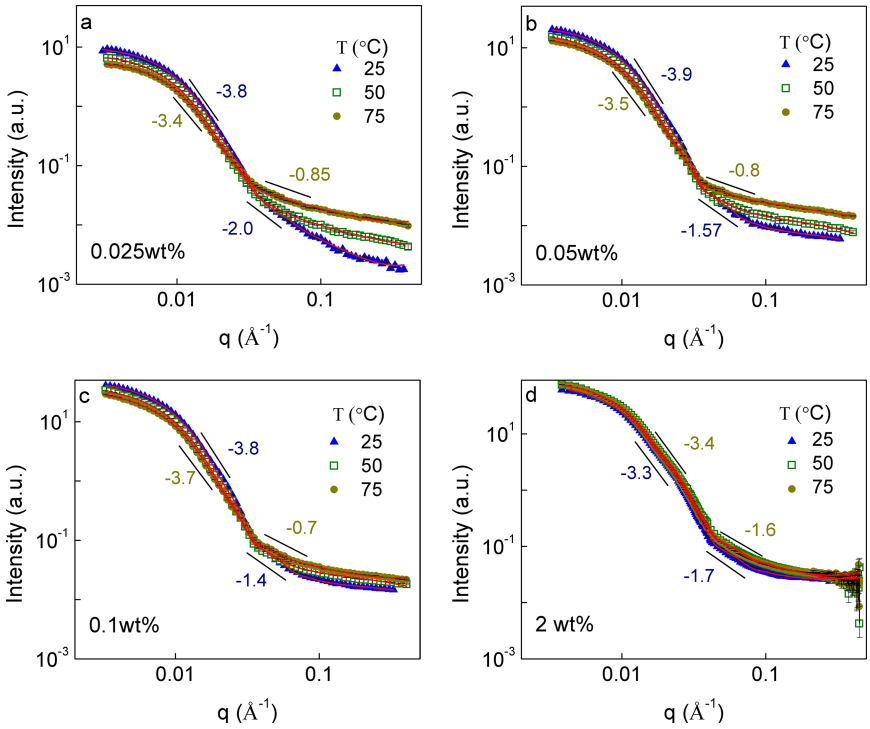

FIG. 6. SANS profiles of the pentablock copolymer as a function of temperature and polymer concentration, (a) 0.025 wt. %, (b) 0.05 wt. %, (c) 0.1 wt. %, and (d) 2 wt. %. The symbols represent the experimental data and the solid lines represent the best fits.

aggregation number, A is the pre-exponential factor, R is the universal gas constant, and T is the temperature. The values of the enthalpy of association are shown in Figure 8. The enthalpy of association is positive and decreases with increasing concentration. The positive values of ΔH of micellization show that this process is endothermic. As concentration increases, the solvent fraction in the core decreases at all temperatures as shown in Figure 7(d). With association of more ionic groups at the core, the poor solvent is repelled. With increasing temperature, the system becomes more dynamic allowing further segregation between incompatible components. Hence, the solvent is expelled from the core.

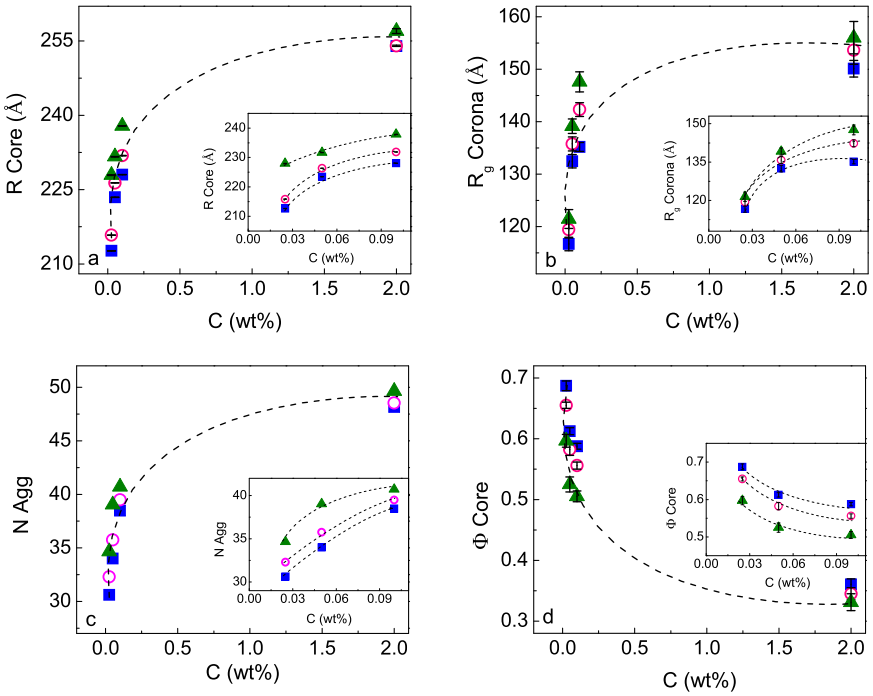

FIG. 7. Calculated parameters from the ellipsoidal core-shell form factor for the pentablock copolymer as a function of temperature (25 °C—solid squares, 50 °C—open circles, and 75 °C—solid triangles) and polymer concentration for (a) major radius of core, (b) R_g of corona, (c) aggregation number, and (d) solvent fraction in the core. Insets represent the changes at lower concentrations. Units of the insets are identical to the main axis. The dotted lines are guideline to the eye.

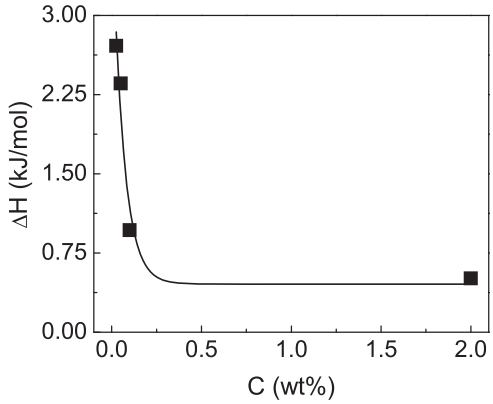

FIG. 8. Enthalpy of micellization determined from the Arrhenius relation of the change of aggregation number.

The ΔH of micellization of the pentablock copolymer in a mixture of non-polar solvents is higher than that observed for the well-known polar block copolymer, pluronic [poly(ethylene oxide) poly(propylene oxide) poly(ethylene oxide)]. Trong *et al.*[46] found that the enthalpy of micellization of a pluronic, triblock copolymer in aqueous solution is approximately 25 J/g using differential scanning calorimetry which shows that the micellization is also endothermic. They assumed that the endothermic process is mainly due to the micelle formation whereas at high concentrations a small contribution also comes from the ordering of micelles.

SUMMARY

Self-assembly of a pentablock copolymer in a cyclohexane and heptane mixture has been investigated as a function of concentration and temperature by SANS. In solution, the pentablock copolymer self-assembles into ellipsoidal micelles with a sulfonated polystyrene center surrounded by solvated rubbery poly-ethylene-*r*-propylene and poly-*t*-butyl styrene block. The radius of the micelle, the thickness of the corona, and the aggregation number increase rapidly and level off with increasing concentrations, while the solvent fraction in the core decreased with increasing the polymer concentration. The increase of micellar size with increasing concentration is attributed to enhance incompatibilities between the ionic center block and the two outer blocks. The size of the micelle and aggregation number increase slightly with increasing temperature, while the solvent fraction in the core decreases. The thermal responsiveness of the micelle solutions decreased with increasing the polymer concentrations. We attribute the changes of the size of the core and corona with increasing concentration and temperature to minimization of the surface energy. In very dilute solutions, single structured molecules are solvated with a swollen ionic core surrounded by a Gaussian chain.

These findings provide first insight into the assembly process of a multifunctional polymer that contains an ionic block. We found that in a selective solvent for the non-ionic block, the ionic block dominated the assembly process and the shape of the micelles. This in turn will impact the formation of membranes from solution casting process.

ACKNOWLEDGMENTS

This work was supported by the U.S. Department of Energy under Contract No. DE-SC007908. The SANS measurements conducted using the EQ-SANS at ORNL's Spallation Neutron Source and GP-SANS at ORNL's High Flux Isotope Reactor were sponsored by the Scientific User Facilities Division, Office of Basic Energy Sciences, U.S. Department of Energy. Travel to Oak Ridge National Laboratory to carry out this work was supported by a Travel Fellowship from the DOE-EPSCoR Grant to the University of Tennessee, Grant No. DE-FG02-08ER46528. This work was performed, in part, at the Center for Integrated Nanotechnologies, a U.S. Department of Energy and Office of Basic Energy Sciences user facility. Sandia National Laboratories is a multi-program laboratory managed and operated by Sandia Corporation, a wholly owned subsidiary of Lockheed Martin Corporation, for the U.S. Department of Energy's National Nuclear Security Administration under Contract No. DE-AC04-94AL85000. The authors would also like to thank Dr. Karen Winey for helpful discussions.

[1] Y. Sheng, T. Wang, W. M. Chen, and H. Tsao, J. Phys. Chem. B **111**, 10938 (2007).
[2] J. Bang, K. Viswanathan, T. P. Lodge, M. J. Park, and K. Char, J. Chem. Phys. **121**, 11489 (2004).
[3] G. Cristobal, J.-P. Berret, C. Chevallier, R. Talingting-Pabalan, M. Joanicot, and I. Grillo, Macromolecules **41**, 1872 (2008).
[4] N. Torikai, N. Takabayashi, J. Suzuki, I. Noda, and Y. Matsushita, Polymer **54**, 929 (2013).
[5] C. Huang, B. Chapman, T. P. Lodge, and N. P. Balsara, Macromolecules **31**, 9384 (1998).
[6] Z. Tuzar and P. Kratochvil, Adv. Colloid Interface Sci. **6**, 201 (1976).
[7] R. Nagarajan and K. Ganesh, Macromolecules **22**, 4312 (1989).
[8] C. Dyer, P. Driva, S. W. Sides, B. G. Sumpter, J. W. Mays, J. Chen, R. Kumar, M. Goswami, and M. D. Dadmun, Macromolecules **46**, 2023 (2013).
[9] L. Gwee, J. Choi, K. I. Winey, and Y. A. Elabd, Polymer **51**, 5516 (2010).
[10] J. H. Park, Y. Sun, Y. E. Goldman, and R. J. Composto, Macromolecules **42**, 1017 (2009).
[11] G. Cheng, F. Hua, Y. B. Melnichenko, K. Hong, J. W. Mays, B. Hammouda, and G. D. Wignall, Macromolecules **41**, 4824 (2008).
[12] A. M. Castagna, W. Wang, K. I. Winey, and J. Runt, Macromolecules **43**, 10498 (2010).
[13] J. Choi, A. Kota, and K. I. Winey, Ind. Eng. Chem. Res. **49**, 12093 (2010).
[14] G. M. Geise, B. D. Freeman, and D. R. Paul, Polymer **51**, 5815 (2010).
[15] I. LaRue, M. Adam, E. B. Zhulina, M. Rubinstein, M. Pitsikalis, N. Hadjichristidis, D. A. Ivanov, R. I. Gearba, D. V. Anokhin, and S. S. Sheiko, Macromolecules **41**, 6555 (2008).
[16] A. Halperin, M. Tirrell, and T. P. Lodge, Adv. Polym. Sci. **100**, 31 (1992).
[17] L. Fang, M. Wei, Y. Shang, D. Kazmer, C. Barry, and J. Mead, Langmuir **28**, 10238 (2012).
[18] H. Retsos, D. Lee, M. Lim, J.-C. Lee, K. Char, and C. Creton, Langmuir **24**, 10169 (2008).
[19] R. A. Weiss, A. Sen, L. A. Pottick, and C. L. Willis, Polymer **32**, 2785 (1991).
[20] R. A. Weiss, A. Sen, C. L. Willis, and L. A. Pottick, Polymer **32**, 1867 (1991).
[21] D. Nguyen, S. K. Varshney, C. E. Williams, and A. Eisenberg, Macromolecules **27**, 5086 (1994).
[22] P. J. Griffin, G. B. Salmon, J. Ford, and K. I. Winey, J. Polym. Sci., Part B: Polym. Phys. **54**, 254 (2016).
[23] G. M. Geise, H. Lee, D. J. Miller, B. D. Freeman, J. E. McGrath, and D. R. Paul, J. Polym. Sci., Part B: Polym. Phys. **48**, 1685 (2010).
[24] C. L. Willis, D. L. Handlin, J. S. R. Trenor, and B. D. Mather, "Sulfonated block copolymers, method for making same, and various uses for such block copolymers," U.S. patent 7737224 B2, Kraton Polymers US LLC, Houston, TX (15 June 2010).

[25]J. K. Zhao, C. Y. Gao, and D. Liu, J. Appl. Crystallogr. **43**, 1068 (2010).
[26]G. D. Wignall, K. C. Littrell, W. T. Heller, Y. B. Melnichenko, K. M. Bailey, G. W. Lynn, D. A. Myles, V. S. Urban, M. V. Buchanan, D. L. Selby, and P. D. Butler, J. Appl. Crystallogr. **45**, 990 (2012).
[27]J. Kohlbrecher and I. Bressler, SASfit version 0.93.5, https://kur.web.psi.ch/sans1/ SANSSoft/sasfit.html.
[28]R.-J. Roe, *Methods of X-Ray and Neutron Scattering in Polymer Science* (Oxford University Press, NY, 2000).
[29]J. S. Pedersen and M. C. Gerstenberg, Macromolecules **29**, 1363 (1996).
[30]J. S. Pedersen, J. Appl. Crystallogr. **33**, 637 (2000).
[31]J. S. Pedersen, I. W. Hamley, C. Y. Ryu, and T. P. Lodge, Macromolecules **33**, 542 (2000).
[32]C. Svaneborg and J. S. Pedersen, Macromolecules **35**, 1028 (2002).
[33]J. S. Pedersen and C. Svaneborg, Curr. Opin. Colloid Interface Sci. **7**, 158 (2002).
[34]D. R. Ratnaweera, U. M. Shrestha, N. Osti, C. Kuo, S. Clarson, K. Littrell, and D. Perahia, Soft Matter **8**, 2176 (2012).
[35]A. Guinier and G. Fournet, *Small-Angle Scattering of X-Rays* (John Wiley and Sons, New York, 1955).
[36]S. Plimpton, J. Comput. Phys. **117**, 1 (1995).
[37]W. Jorgensen, J. Madura, and C. Swenson, J. Am. Chem. Soc. **106**, 6638 (1984).
[38]W. Jorgensen, D. Maxwell, and J. Tirado-Rives, J. Am. Chem. Soc. **118**, 11225 (1996).
[39]R. W. Hockney and J. W. Eastwood, *Computer Simulation Using Particles* (Adam Hilger-IOP, Bristol,1988).
[40]A. Tuteja, M. E. Mackay, C. J. Hawker, B. Van Horn, and D. L. Ho, J. Polym. Sci., Part B: Polym. Phys. **44**, 1930 (2006).
[41]D. Aryal, T. Etampawala, D. Perahia, and G. S. Grest, Macromol. Theory Simul. **23**, 543 (2014).
[42]D. Aryal, D. Perahia, and G. S. Grest, J. Chem. Phys. **143**, 124905 (2015).
[43]L. Rubatat, G. Gebel, and O. Diat, Macromolecules **37**, 7772 (2004).
[44]L. Rubatat, A. Rollet, O. Diat, and G. Gebel, J. Phys. IV **12**, 197 (2002).
[45]D. Nguyen, C. Williams, and A. Eisenberg, Macromolecules **27**, 5090 (1994).
[46]L. C. P. Trong, M. Djabourov, and A. Ponton, J. Colloid Interface Sci. **328**, 278 (2008).

Water dynamics in rigid ionomer networks

N. C. Osti, T. N. Etampawala, U. M. Shrestha, D. Aryal, M. Tyagi, S. O. Diallo, E. Mamontov, C. J. Cornelius, and D. Perahia

Citation: J. Chem. Phys. **145**, 224901 (2016); doi: 10.1063/1.4971209
View online: http://dx.doi.org/10.1063/1.4971209
View Table of Contents: http://aip.scitation.org/toc/jcp/145/22
Published by the American Institute of Physics

Water dynamics in rigid ionomer networks

N. C. Osti,[1,a),b)] T. N. Etampawala,[1] U. M. Shrestha,[1] D. Aryal,[1] M. Tyagi,[2,3] S. O. Diallo,[4] E. Mamontov,[4] C. J. Cornelius,[5] and D. Perahia[1,a)]
[1]*Department of Chemistry, Clemson University, Clemson, South Carolina 29634, USA*
[2]*NIST Center for Neutron Research, National Institute of Standards and Technology, Gaithersburg, Maryland 20899, USA*
[3]*Department of Materials Science and Engineering, University of Maryland, College Park, Maryland 20742, USA*
[4]*Chemical and Engineering Materials Division, Oak Ridge National Laboratory, Oak Ridge, Tennessee 37831, USA*
[5]*Chemical and Biomolecular Engineering Department, University of Nebraska-Lincoln, Lincoln, Nebraska 68588, USA*

(Received 17 August 2016; accepted 16 November 2016; published online 8 December 2016)

The dynamics of water within ionic polymer networks formed by sulfonated poly(phenylene) (SPP), as revealed by quasi-elastic neutron scattering (QENS), is presented. These polymers are distinguished from other ionic macromolecules by their rigidity and therefore in their network structure. QENS measurements as a function of temperature as the fraction of ionic groups and humidity were varied have shown that the polymer molecules are immobile while absorbed water molecules remain dynamic. The water molecules occupy multiple sites, either bound or loosely constrained, and bounce between the two. With increasing temperature and hydration levels, the system becomes more dynamic. Water molecules remain mobile even at subzero temperatures, illustrating the applicability of the SPP membrane for selective transport over a broad temperature range. *Published by AIP Publishing.* [http://dx.doi.org/10.1063/1.4971209]

I. INTRODUCTION

Polymers decorated by ionic groups are in the core of numerous technologies where selective and timed transport is a key to their function. These polymers are incorporated in a large number of applications ranging from clean energy generation[1,2] and storage[3] to biotechnology.[4,5] Of particular interest are ionomers, where in contrast to polyelectrolytes, their overall conformation is determined by a balance between electrostatic interactions and the effect of the backbone rigidity. Ionomers are in the core of numerous current technologies such as hydrogen fuel cells,[6–8] sensors,[9,10] water purification,[11] and drug delivery.[12,13] Striving to enhance current technologies and controlling selective timed transport has driven a large number of studies to resolve the three prong correlations of the polymer: chemical structure, phase structure, and transport.

Among the most studied ionomers are Nafion™ [14–21] and sulfonated polystyrene (SPS).[22,23] These flexible and semi-flexible polymers form networks where the ionic groups tend to associate into clusters. The size and shape of these aggregates depend on a large number of parameters including the chemistries of the ionic groups, their distribution along the backbone as well as the polymer topology. These ionic clusters play contradicting roles, where on one hand, they serve as physical cross links, enhancing stability and concurrently forming transport pathways, where hydrophilic solvents such as water and alcohols accumulate. The dynamics within ionic-polymeric networks including the motion of the polymer backbone and that of the ionic moieties and solvents, determine the transport ability of these macromolecules and their mechanical stability.[24,25] As such, the topography of the backbone and its rigidity constitute a critical control over the dynamics of ionic polymer networks.

Here using quasi-elastic neutron scattering (QENS), we probe the dynamic processes within one ionic polymer network that consists of macromolecules with a rigid backbone[26–29] whose structure is shown in Figure 1(a). The backbone of sulfonated poly-phenylene (SPP) is significantly more rigid than most common ionomers including sulfonated polystyrene (SPS)[30] and Nafion®.[31] Small-angle neutron scattering (SANS) studies have shown that SPP molecules form a rather extended conformation in dilute solutions as is visualized in the SPP image captured by molecular dynamics simulations are presented in Figure 1(b). Details of these simulations, carried out under a limited number of molecules for visualization only, are presented in the supplementary material. The rigidity of its backbone leads to the formation of bundles that serve as the building blocks of the ionic structure as shown in the schematic presented in Figure 1(c). This schematic was derived from previous SANS[27] and NMR[32] studies.

When hydrated, the water molecules associate with the ionic groups of the ionomers and often induce phase transformations. The local dynamics of the water molecules was found to be strongly coupled with macroscopic proton transport.[17,33–35] The significance of water transport in polymeric membrane has driven numerous studies to probe the

a)Authors to whom correspondence should be addressed. Electronic addresses: nosti@g.clemson.edu and dperahi@clemson.edu
b)Present address: Oak Ridge National Laboratory, Oak Ridge, TN 37831, USA.

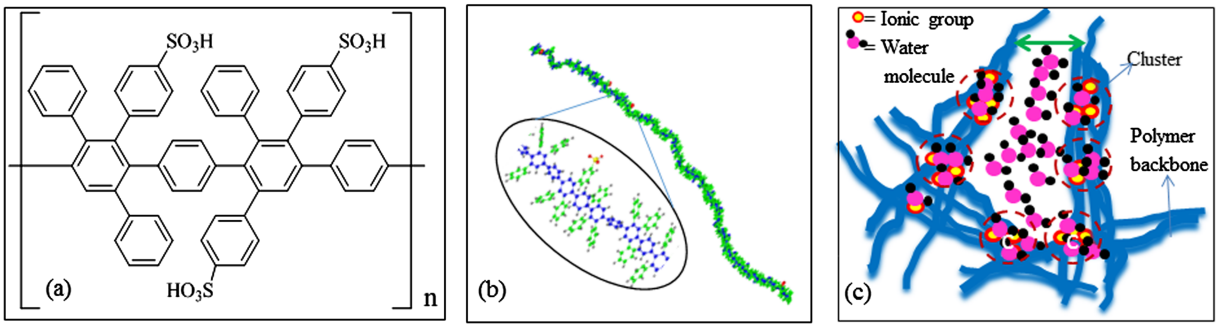

FIG. 1. (a) Chemical formula of the SPP monomer. (b) Molecular dynamics simulation snapshot of SPP chain in implicit good solvent with ε = 33.3, t = 100 ns, and n = 60. The phenyl backbone is shown in blue, side phenyl ring in green, oxygen atoms in red, sulfur atoms in yellow, and hydrogen atoms in gray. (c) Schematic of SPP network showing bundle structure.[27,32]

dynamics within ionomers, where QENS was able to capture the local motion of both segmental motion and that of guest molecules. Volino and co-workers reported fast and slow modes of water dynamics in hydrated Nafion membranes, with bulk like diffusion at length scale smaller than 10 Å.[14] Similar results were observed by Pivovar and Pivovar[36] who resolved a jump-exchange between the different sites. Further, using molecular dynamic simulation, Devanathan *et al.*[34] have shown multiple water environments for water including bound, weakly bound, and unbound water in Nafion membranes, which increase with increasing hydration levels.[37] The mobility of the solvents, ions, and the polymer backbone determines the stability and transport in these ionic networks, spanning a broad range of dynamical process whose characterization requires a conjunction of technique.

The time and length scales over which solvent dynamics takes place as well as some segmental dynamics are captured by QENS. For organic materials, QENS predominantly follows the incoherent scattering of hydrogen. The inherently large difference in the scattering cross section between proton (H, σ = 80.26 b) and deuterium (D, σ = 2.05 b) makes QENS the technique of choice to study segmental dynamics of ionomers[38,39] as well as that of water in confinement.[40–42] Here, using QENS, we explore the effects of chain rigidity on the local dynamics in membranes that consist of substituted polyphenylene backbone with sulfonated ionic groups shown in Figure 1. We find that similar to other ionomers, water occupies multiple sites with a different degree of association and displays fast and slow dynamic modes; however, the distribution of the molecules is strongly affected by the bundle structure arising from the chain rigidity. The paper is organized as follows: experimental details will be first presented followed by results on the dynamics of the polymer networks themselves. Results for water confined in these ionic networks will be then presented.

II. EXPERIMENTAL

A. Material

The SPP polymers were synthesized by Diels-Alder polymerization as described by Fujimoto *et al.*[26,43] with the average molecular weight of 70,000 g/mol and polydispersity index of 2.2. Specifically, the polymers were synthesized from 1,4-bis(2,4,5-triphenylcyclopendienone) benzene and 1,4-diethynylbenzene followed by sulfonation with chlorosulfonic acid. Membranes were made by evaporating a 10 wt. % solution of SPP in *N*,*N*-dimethylacetamide (DMAc) from a flat glass container and the solvent was allowed to evaporate at ambient condition. The ion exchange capacities (IECs) of the SPP polymers were measured by titration with 0.01M NaOH. IEC corresponds the reciprocal mass equivalent of the polymer between adjacent ionic groups. This quantity is a measure of the degree of decoration with ionic groups. It determines the ability of the dry SPP membranes to exchange ions. Two polymers of IECs 1.6 and 2.2 with a corresponding sulfonation level of 22.0% and 33.3% were studied. Table I summarizes the characteristics of the membranes studied. Deuterium oxide, D_2O (99.9%), was purchased from Cambridge Isotope Laboratories. The protonated membranes were kept in vacuum overnight at room temperature.

1. Hydration

Samples were studied in ambient and saturated conditions. Ambient here corresponds to membranes kept at room temperature (295 K) and humidity. Membranes were dried under vacuum for 72 h and then exposed to H_2O/D_2O depending on the experiment. The experimental cell was first flushed with nitrogen followed by exposure of the samples to saturated vapors. The weight of the membranes was measured periodically. In parallel, the water NMR signal (for samples with equal dimensions and processing history) was measured and its intensity integrated to follow the uptake. We find that in ambient conditions, the samples absorb water instantaneously and hardly any further changes take place after several minutes. The samples of IEC of 1.6 and 2.2 absorbed 4-4.8 wt. % of water with small variations between samples. Saturated samples were exposed to boiling water for 5 min. IEC of 1.6 absorbed 50 wt. % and IEC of 2.2 absorbed 140 wt. %

TABLE I. IEC, sulfonation levels (S), and water uptake of SPP membranes.

			Water uptake (wt. %)		
Sample ID	IEC (mmol/g)	S level (%)	Dry	Ambient	Saturated
SPP22	2.2	33.3	0	4.8	140
SPP16	1.6	22.0	0	4.0	50

of water. Differential Scanning Calorimetry (DSC) measurements were carried out with an effort to reveal distinctive possible states of water. Conclusive results could not be obtained because of the presence of multiple water containing sites.

B. Neutron scattering

The dynamics processes in SPP ionomer membranes were measured on two QENS spectrometers. Membranes saturated with D_2O were measured on NG-2 high flux backscattering spectrometer[44] (HFBS) at National Institute of Standards and Technology (NIST). Wavelength of neutron beam used was, λ_0 = 6.27 Å, corresponding to an energy E_0 = 2.08 meV. Sixteen Si (111) analyzer crystal detectors covering Q ranges of 0.25 $Å^{-1}$ to 1.74 $Å^{-1}$ were used with an instrument dynamic energy range of ±11 μeV and 0.8 μeV energy resolutions. Membranes saturated by H_2O were studied on the backscattering spectrometer (BASIS)[45] at the Spallation Neutron Source, Oak Ridge National Laboratory. A band of polychromatic incident neutrons was used; the wavelength of the detected neutrons was λ_0 = 6.267 Å, as selected by Si (111) Bragg reflection at 88°. Data were obtained from a dynamic range of −100 to + 100 μeV with an overall energy resolution of 3.5 μeV. This value provides the average of the resolution at the Q range covered. The data from multiple detectors were binned into nine Q values to cover the Q range of 0.20 $Å^{-1}$ to 1.85 $Å^{-1}$.

Data were collected on both instruments for 10 h at different temperatures using a standard top loading closed cycle refrigerators with helium gas as the refrigerant. All data were reduced and analyzed using the DAVE[46] software package.

1. Neutron cross sections and scattering functions

The intensity, $I(Q,E)$, of the QENS spectra is given by

$$I(Q,E) = A(Q)\left[p_1(Q)\delta(E) + \left(1 - p_1(Q)\right)S(Q,E) + B(Q,E)\right] \otimes R(Q,E), \quad (1)$$

where $A(Q)$ and $p_1(Q)$ are scaling factor and contribution of elastic scattering, respectively. The elastic scattering is captured by $\delta(E)$, a Dirac delta function. The quasi-elastic scattering function $S(Q,E)$ contains the dynamic information; the background is described by $B(Q,E)$ and $R(Q,E)$ is the instrument resolution function.

Inelastic cross section of hydrogen is significantly higher than that of the other elements that constitute most soft materials. The coherent and incoherent scattering cross sections of the atoms that constitute SPP are[47] σ_{coh}(H) = 1.76 b, σ_{inch}(H) = 80.26 b, σ_{coh}(D) = 5.59 b, σ_{inch}(D) = 2.04 b, σ_{coh}(C) = 5.56 b, σ_{inch}(C) = 0 b, σ_{coh}(S) = 1.02 b, and σ_{inch}(S) = 0.007 b. In SPP membranes, the dominant incoherent scattering originates from the protons on the aromatic rings and residual water.

III. RESULTS AND DISCUSSION

QENS spectra of SPP membranes dry and saturated with D_2O, as a function of temperature at representative Q values, are shown in Figure 2. As mentioned above, the signal arises predominantly from incoherent scattering of protons, thus the observed signals correspond to the polymer network. The spectra, obtained from the membranes for two ionic levels over the Q range that corresponds to potential segmental motion, do not exhibit any dynamics signature as evident by the over-

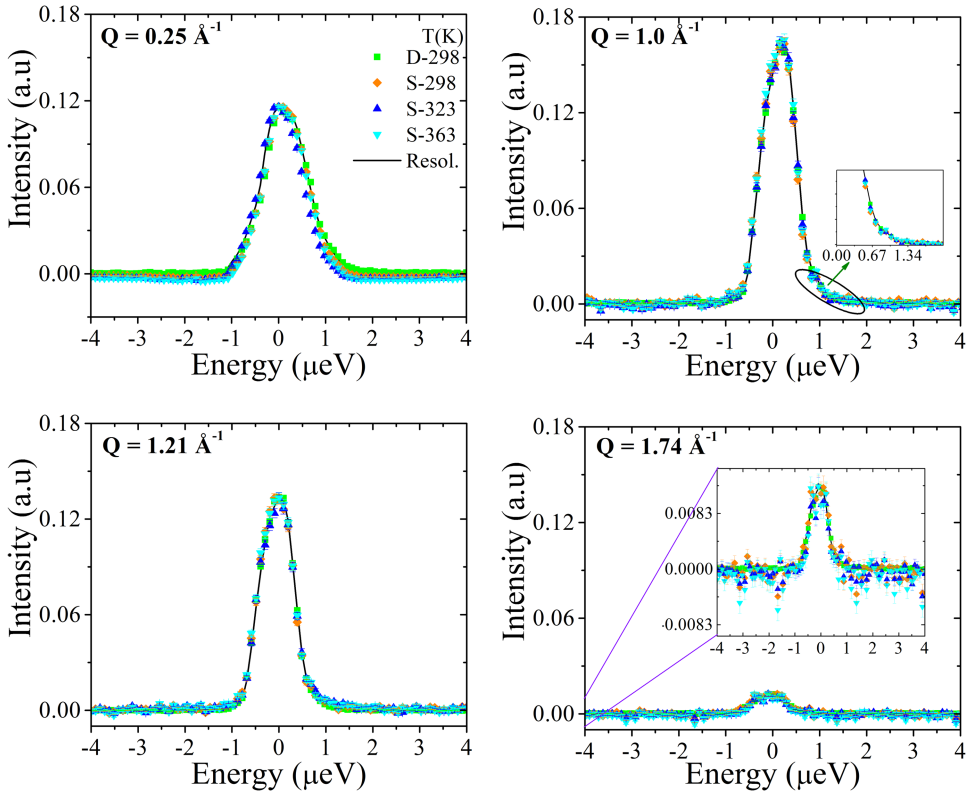

FIG. 2. QENS spectra as a function of energy from dry (D) and D_2O saturated (S) protonated SPP membranes with IEC = 2.2 at indicated temperatures and Q values. These measurements were carried out at HFBS in NIST. The symbols correspond to the polymer and a line corresponds to vanadium reference. The insets in figures at Q = 1.0 $Å^{-1}$ and Q 1.74 $Å^{-1}$ are magnification of the marked regions.

lap of the signal with a vanadium standard for all measured Q values. Lack of broadening, in comparison to a vanadium standard, is a clear indication that on the time and length scales captured by the instrument, the polymer molecules hardly move. Lack of dynamics on the time and length scales detected by QENS for the dry membranes is consistent with the high glass transition (T_g) of SPP which is ca. 400 K. The much faster vibrational dynamics expected in organic networks is outside the range of energies detected by the backscattering spectrometer.

The membranes were kept below their glass transition temperature and were hydrated with D_2O. The temperature was not raised above T_g to avoid any processing impacts to the direct environment of the water molecules. Surprisingly, the membranes, saturated with D_2O, did not exhibit any signature of network dynamics in all measured Q and E values. These results show that even though these membranes are saturated with water, the polymeric network remained rigid and displayed a glassy behavior. These characteristics are rationalized in terms of the bundle structure of SPP[27] that persists across a broad humidity range. The lack of dynamics on the length and time scales of QENS suggests that the water molecules hardly penetrate the densely packed bundles of SPP and therefore T_g of these nano-domains is not affected even though water occupies inter bundle sites. From the I(Q) spectrum in Figure 3, we conclude that the incoherent scattering does not dominate the QENS signal only below Q = 0.5 Å^{-1}.

The dry membranes were then hydrated with H_2O. As the measurements of the polymer in D_2O did not reveal any dynamics of the network, the incoherent scattering measured for the hydrated samples consists of contributions from the polymer and the water. As the measurements of the polymer in D_2O did not reveal any dynamics of the network and, the quasi-elastic spectra broadening arise from the incoherent signal of the water, membranes exposed to two humidity conditions were probed: ambient and saturated. Measurements were carried out over a Q range of 0.20 Å^{-1} to 1.85 Å^{-1} corresponding to distances in real space of ~31 Å to 4 Å. QENS spectra of SPP (IEC = 1.6) membranes measured at Q = 1.0 Å^{-1} at the two hydration levels are shown in Figure 4.

Data at additional Q values are presented in Figure 2S of the supplementary material. For both hydration conditions, at all Q ranges, the lines broaden with increasing temperature,

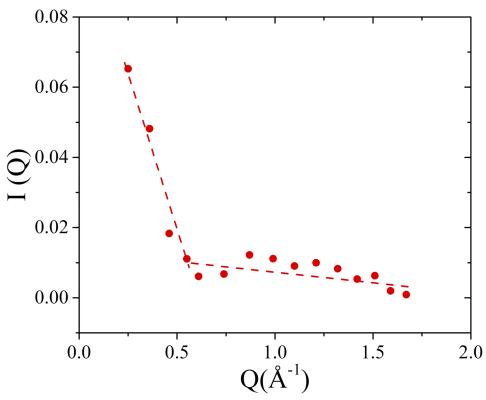

FIG. 3. Integrated intensity of QENS spectra, I(Q), as a function of Q of a D_2O saturated SPP 2.2 membrane. Dotted lines are a guide to the eye.

revealing increasing mobility of water molecules. It is notable that even for limited numbers of water molecules present under ambient conditions, they remain dynamic. This indicated that the water molecules are only loosely bound to the polymer network. Certain amount of water might be associated with the polymer network, but it is hard to quantify the amount and the position of such water. Qualitatively, water dynamics appear similar as a function of water content as illustrated in Figure 5, where the spectra at 233 K and 343 K at Q = 1.0 Å^{-1} are presented. Detailed analysis however, discussed below, distinguishes different dynamics. The spectra at other Q values are given in Figure 3S of the supplementary material.

A delta function was used to account for the contributions from polymer chains and residual water molecules whose dynamics remain outside the range of the experiment resolution. A flat background was also introduced to take account of any vibrational motion that falls outside the instrument dynamics range (±100 μeV). After convolution with the instrument resolution, water dynamics was followed through the analysis of $S(Q,E)$, given by Equation (1).

In an effort to analyze the water dynamics, we have tested common models often used including stretched exponential,[48] Gaussian dynamics,[49] and single Lorentzian.[41,50,51] These models were not able to capture the dynamics in the system. We attribute this to the unusual water dynamics in physical nano-confinement, originated from the rigid bundle structure of the SPP membranes providing both inter- and intra-bundle sites. Confined water dynamics depend on the nature of the confining matrices and their geometrics. A number of different models have been used to understand the dynamics of confined water in different media, including Nafion from QENS experiments.[41] Especially for Nafion, a variety of models, such as diffusion inside a sphere,[52] a single Lorentzian,[36] and a Gaussian model,[53] have been used to extract the length scale and time scale of water dynamics in hydrated membranes. In SPPs, the backbone and bundle are rigid compared to Nafion, the membrane form non-conforming structures that remain rigid in presence of water, forming larger vacancies compared with Nafion and polystyrene sulfonate.

Further insight is obtained from the dynamics susceptibility, $\chi(Q,E)$. It provides a measure of temperature-induced dynamic fluctuations and accounts for experimentally multipoint correlator that identifies the dynamic heterogeneities. $\chi(Q,E)$ is obtained by converting $S(Q,E)$ using Bose occupation factor[54] that accounts for the energy difference between species occupying different sites and the temperature. Practically, it helps to separate the contribution coming from different dynamics processes, manifested in different peaks. The presence of a minimum in the susceptibility of both ambient and saturated membranes as a function of energy transfer suggests the presence of two peaks, one at low energy transfer and another at higher energy transfer, as shown by arrows, thus indicating two different relaxation processes at two different time scales. Note that the data contain the onset of the second peak, limited by the signal to noise of the system. In order to capture those separate dynamic processes, a sum of two Lorentzian functions representing a different characteristics time was essential to capture the dynamics

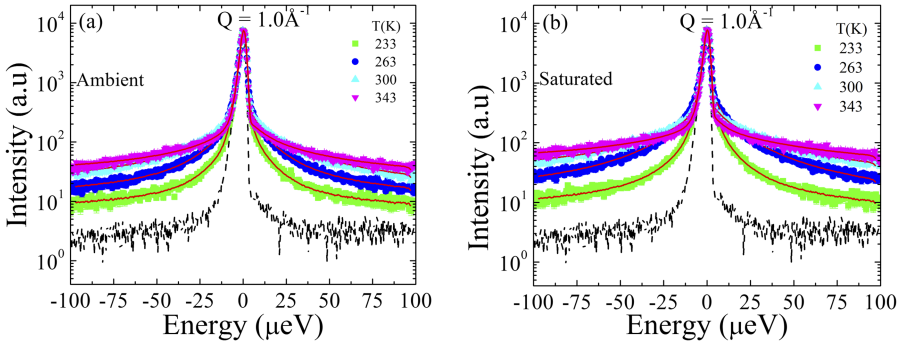

FIG. 4. Representative QENS spectra as a function of energy of SPP membranes of IEC = 1.6 measured on BASIS (ORNL). (a) Ambient condition and (b) saturated with H_2O. Symbols correspond to the data at the indicated temperatures. Solid lines correspond to Lorentzian fits discussed in the text. The dashed line corresponds to the vanadium reference.

in the entire measured range. Therefore, $S(Q,E)$ is modeled as

$$S(Q,E) = p_2(Q)\frac{1}{\pi}\frac{\Gamma_1(Q)}{\Gamma_1^2(Q)+E^2} + \left(1-p_2(Q)\right)\frac{1}{\pi}\frac{\Gamma_2(Q)}{\Gamma_2^2(Q)+E^2}, \quad (2)$$

where $\Gamma_1(Q)$ and $\Gamma_2(Q)$ correspond to the HWHM of two Lorentzians, with the broader one describing the faster dynamics and the narrower, the slower one, respectively.

The relative weights of the fast and slow components of the overall dynamics are given by $p_2(Q)$ and $(1-p_2(Q))$, respectively. The best fits obtained for $S(Q,E)$ incorporating the elastic component and the resolution function are described by the solid lines in Figures 4 and 5. $\Gamma_1(Q)$ and $\Gamma_2(Q)$ extracted from the best fits at ambient and saturated conditions are presented as a function of Q^2 in Figure 6. For a simple Fickian diffusion, $\Gamma(Q) = DQ^2$ where D is the translational diffusion coefficient. Both $\Gamma_1(Q)$ and $\Gamma_2(Q)$ initially increase with Q at all measured temperatures, where $\Gamma_1(Q)$ is significantly higher than $\Gamma_2(Q)$. However, $\Gamma_1(Q)$ is not a linear function of Q^2, diverting from simple Fickian diffusion. We find a fast increase of $\Gamma_1(Q)$ for low Q, which crosses over to a plateau at ~7 Å (Q = 1 Å^{-1}) for all measured temperatures. This Q-temperature dependence is typical of jump diffusion.[55,56]

$\Gamma_2(Q)$ exhibits similar behavior at low Q and becomes rather random at high Q. The slow component is attributed to bound water that is impacted by small structural changes that take place with increasing temperature.[27] The changes in $\Gamma_1(Q)$ and $\Gamma_2(Q)$ for the fully hydrated membranes are shown in Figure 6(b). Both $\Gamma_1(Q)$ and $\Gamma_2(Q)$ for the saturated membrane are higher than the values at ambient conditions (Figure 6(a)) but show a similar trend as a function of temperature. These results show that though water molecules in saturated membranes are significantly more dynamic, they occupy similar sites to those in ambient conditions. In saturated membrane, HWHM at certain Q (high Q) values is at the edge of the resolution, and therefore a large error is associated with their values.

In order to extract the heterogeneous dynamics of water molecules at different length and time scales, the dynamics reflected in $\Gamma_1(Q)$ and $\Gamma_2(Q)$ were analyzed using the random jump diffusion model[57] given by Equation (3), the simplest exchange model between two different sites. This model has been used to capture water dynamics in heterogeneous environments including ionomers membrane[36] and porous media.[55] It assumes that water molecules oscillate around an equilibrium position for an average time τ_o, before jumping a distance L to another equilibrium position. $\Gamma_i(Q)$ for site i = 1 and 2 for the jump model are correlated with the translational diffusion coefficient, D and the residence time, τ_o, as described in the following equation:[58]

$$\Gamma_i(Q) = \frac{DQ^2}{1+DQ^2\tau_o}, \quad (3)$$

and the jump length, L is described by the following:

$$L = \sqrt{6D\tau_0}. \quad (4)$$

We find that $\Gamma_1(Q)$ extracted from this model was well behaved across the entire measured Q range where $\Gamma_2(Q)$ deviated at larger Q for both hydration levels. The jump diffusion constants extracted from the fit for ambient and saturated hydration levels are presented in Table II and the results for the jump length are given in Table III. The jump diffusion constants for both fast and slow dynamics for the

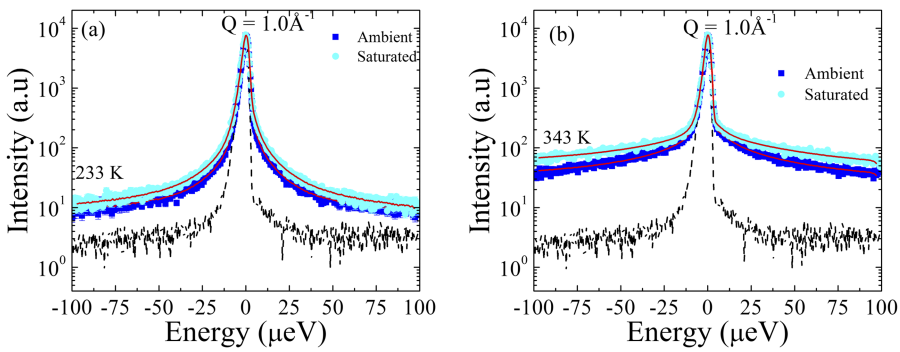

FIG. 5. QENS spectra of SPP (IEC = 1.6) membrane in ambient and saturated conditions at Q = 1.0 Å^{-1}. (a) 233 K, (b) 343 K. Symbols correspond to the data and solid lines correspond to model fits. Dashed lines correspond to the vanadium resolution.

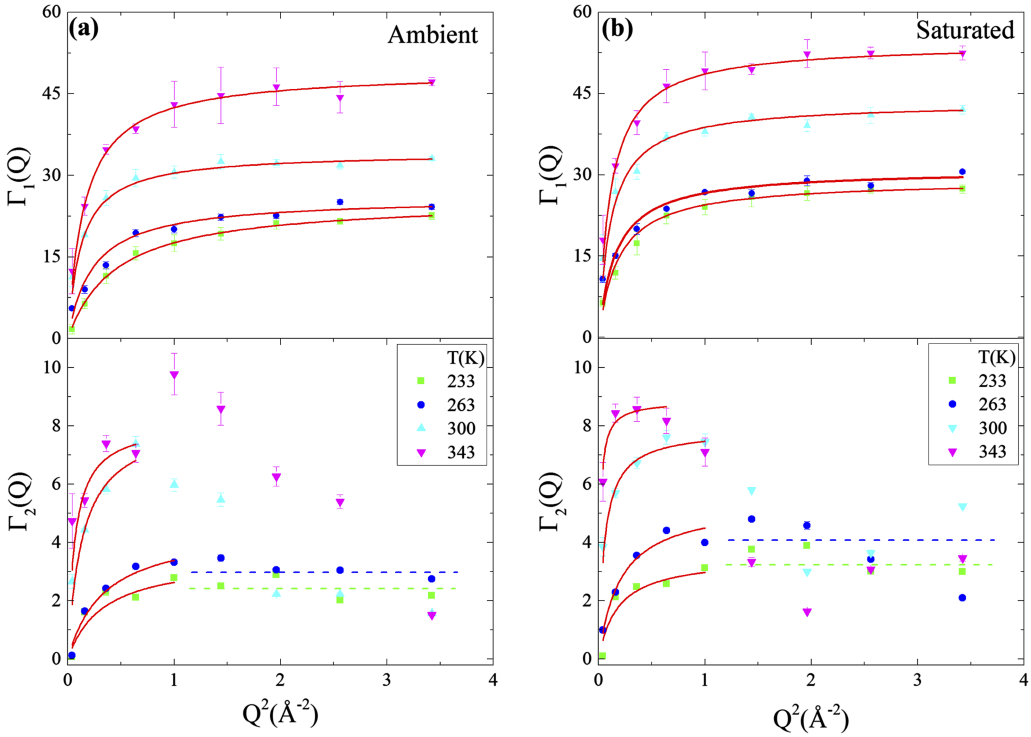

FIG. 6. Temperature dependence of $\Gamma_i(Q)$ from best fits to the data for protonated SPP 1.6. Solid lines represent the fit to jump diffusion model. (a) Ambient condition. (b) Saturated with H_2O. Solid lines represent best fit to the model. Horizontal lines for the lower panels are the guide to the eye showing that $\Gamma_2(Q)$ is independent of Q for high Q.

saturated membranes are larger than for those at ambient conditions.

SPP membrane structure has been previously studied using SANS and x-ray scattering experiments.[27] The structure at high Q, where chain packing is reflected, exhibits one broad line centered around 4.6 Å which slightly broadens with hydration and shifts to higher dimensions. The linewidths, however, are rather broad and no quantitative information can be extracted. In higher dimensions, where bundles and ion clustering have been traditionally detected, SANS revealed the presence of larger domains of ~35-60 nm in dry membranes. With increasing water content, this line becomes slightly pronounced, indicating the penetration of water into hydrophobic regions. The water penetration is attributed to the presence of ionic groups within the bundles. At ~32 Å, a temperature insensitive peak attributed to hydrophilic/ionic domain is observed. Therefore, the higher values of water diffusivity in saturated membrane are attributed to the increase in the size of the hydrophilic domain, forming a less constraint environment. This is further corroborated by the jump length extracted from the analysis as shown in Table III. The jump length increases with increasing temperature and hydration levels of the SPP membranes. The jump lengths are 2-5 times larger than the bulk water values (1.3 Å), which is commonly observed for water molecules in confinement,[59] except for the slow component at 343 K in saturated membrane, where it is large. This data point is clearly affected by some ambiguity due to internal structure changes.

The diffusion coefficients increase with increasing temperature for both ambient and saturated hydration levels. The jump diffusion constants for the slow component are smaller than the fast components in both hydration levels at a given temperature. At 343 K, uncharacteristically high values are obtained for $\Gamma_1(Q)$ which are higher than those obtained for $\Gamma_2(Q)$, and the slow-fast model breaks down. At this temperature, structural changes take place where the bundle structure itself is affected, allowing penetration of

TABLE II. Diffusion constants of SPP 1.6 membranes in ambient and saturated membranes conditions as extracted from fit to jump diffusion model. Bulk water diffusion coefficient at 298 K = 25.5×10^{-10} m^2 s^{-1}.[47]

	Ambient		Saturated	
T(K)	*Fast* (10^{-10} m^2 s^{-1})	*Slow* (10^{-10} m^2 s^{-1})	*Fast* (10^{-10} m^2 s^{-1})	*Slow* (10^{-10} m^2 s^{-1})
233	9.0 ± 0.5	2.0 ± 1	24 ± 2	3.0 ± 1
263	17 ± 3	2.0 ± 1	29 ± 5	4.0 ± 1
300	42 ± 2	9.0 ± 2	54 ± 9	22 ± 4
343	47 ± 2	19 ± 1	69 ± 3	94 ± 1

TABLE III. Jump length L (Å) of SPP 1.6 membranes at two conditions calculated from diffusion constant extracted from the fit of $\Gamma_i(Q)$ to the jump diffusion model.

	Ambient		Saturated	
T(K)	*Fast*	*Slow*	*Fast*	*Slow*
233	3.6 ± 0.1	4.2 ± 1.5	5.7 ± 0.3	5.8 ± 1.1
263	5.0 ± 0.5	4.2 ± 1.2	6.1 ± 0.6	5.4 ± 0.6
300	7.0 ± 0.1	6.6 ± 1.0	6.2 ± 0.6	10.7 ± 1.2
343	6.2 ± 0.1	9.5 ± 0.8	7.0 ± 0.2	20.2 ± 0.5

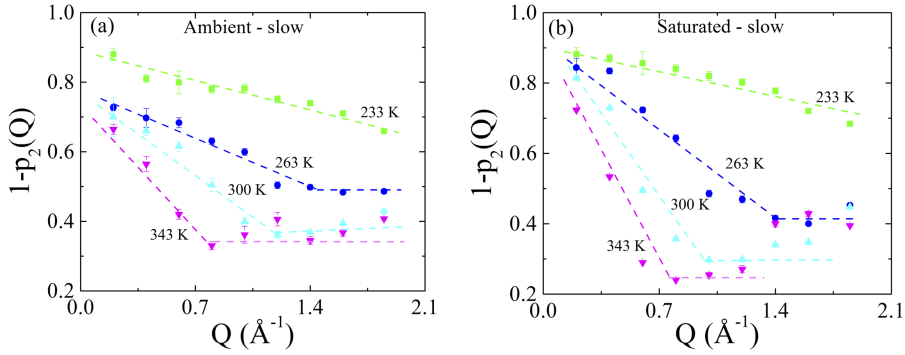

FIG. 7. Temperature dependence of relative weight of slower component of Lorentzian functions showing the variation of 1-p_2(Q) with Q of SPP (IEC = 1.6) membrane. (a) Ambient condition. (b) Saturated with H_2O. Dotted lines are guide to the eyes.

the water into the bundles themselves as shown by He *et al.*[27] The direct correlation of the structure and dynamics of these saturated membranes at high temperatures though remain an open question. We found that water remains dynamic below its freezing point in this ionomer membrane due to their confined geometry that does not allow the formation of hydrogen bonds that often promote crystallization. Similar phenomena have been observed in water in confined geometry.[41,60]

Here the measured value of diffusion coefficients is slightly higher than that of bulk water.[50] Similar type of higher value for water diffusion in confinement has been previously reported[61,62] and rationalized through the breaking of highly regular hydrogen bonding for water confined to small pores. With increasing temperature, more sulfonate groups migrate to the interface, disturbing much of the bulk hydrogen bonding, and may facilitate water diffusivity in SPP membranes. This high value of diffusivity is local and does not propagate across the sample and remains confined on some length scale that may be larger than the lowest Q of the QENS experiment. Therefore, leveling off of the low Q data is not detectable.

Contribution of slow and fast components in the overall dynamics has been determined. The Q dependence of the relative weight of the slow components, 1-p_2(Q), for membranes at both ambient and saturated conditions is presented in Figures 7(a) and 7(b), respectively. In both cases, 1-p_2(Q) decreases as Q increases and levels off at high temperature for higher Q values. The crossover at higher Q values at higher temperatures reflects the capturing of some coherent scattering at smaller length scale. As the temperature increases, the molecular motion of the water molecules increases, leading to an increase in the jump length of the water. In principal, the geometry of water motion can be obtained from the elastic incoherent structure factor of water diffusing translationally in confined geometry. It is however a challenge in highly heterogeneous systems.

Here we showed that water in the ionomer follows two diffusion processes. The temperature dependence of the diffusion coefficients of both populations of water at ambient and saturated condition is illustrated in Figure 8.

The diffusion constants of water extracted for both types of water follow the Arrhenius process of $D = Ae^{-\frac{E_a}{RT}}$, where D is the self-diffusion coefficient, A is a constant, and R is the universal gas constant. The diffusion coefficients at 233 K for the slow water component could not be included in the Arrhenius fit, reflecting the fact that slow population of water molecules do not show Arrhenius behavior at T ≤ 233 K. The activation energies of the diffusion mechanism at both conditions were calculated and summarized in Table IV. Activation energy of the slow population of water is comparable to the bulk water hydrogen bonding[63] but is lower for the fast population. Precaution must be taken while using the activation energies derived for slow moving water population because of the limited number of points that could be included in the Arrhenius fit.

This smaller value of E_a, compared to bulk water, is attributed to the presence of bundles of polymers, along with sulfonated groups that accelerate the water diffusion. The activation energy for fast population of water at saturated membrane is smaller than at ambient condition. This smaller value of activation energy corresponds to a lowering of the energy barrier for water diffusion and is consistent with the diffusion in swollen membranes. The interfacial diffusion of water molecules is facilitated by the backbone rigidity giving rise to faster diffusion with smaller activation energy.

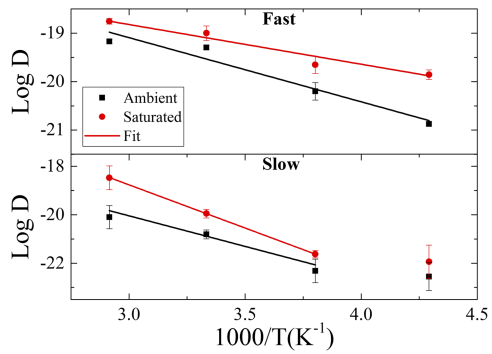

FIG. 8. Temperature dependence of diffusion coefficients of two different motions of water confined in SPP (IEC = 1.6) in ambient and saturated conditions. The data points represent the diffusion coefficient at different temperatures and the solid line represents fit to an Arrhenius function.

TABLE IV. Activation energy of two types of motion in SPP (IEC = 1.6) at ambient and saturated conditions obtained from the Arrhenius fit parameters. Bulk water activation energy = 23.3 kJ/mol.[57]

	Activation energy (kJ/mol)	
Samples	Fast motion	Slow motion
Ambient	10.9	20.9
Saturated	6.8	29.6

IV. CONCLUSIONS

Dynamics of water in SPP ionomers membranes was investigated by QENS as a function of water content and temperature. Our study shows that on the time scale of measurement, the polymer molecules are immobile, while the water in the membrane molecules is exchanged between multiple sites resulting in slow and fast dynamics. We attribute the fast components to water molecules that reside predominantly in inter-bundle space and the slow one to water molecules associated with the polar groups. Water dynamics is characterized by jump diffusion for both components. We found that diffusion of both populations of water molecules rises with increasing water content and temperature and is higher than the values reported for Nafion.[36] These higher values are attributed to the rigidity of SPP polymer backbone. As in porous materials,[60] water molecules remain non-frozen even at subzero temperature in SPP ionomer membranes.

SUPPLEMENTARY MATERIAL

See supplementary material for molecular dynamics simulation detail, QENS spectra and dynamics susceptibility plots.

ACKNOWLEDGMENTS

This work was supported by the U.S. Department of Energy under the Contract Nos. DOE-DE-FG02-07ER46456 and DE-FG02-12ER46843. The use of neutron scattering facility at Oak Ridge National Laboratory is supported by the U.S. Department of Energy, Office of Basic Energy Sciences. Travel to Oak Ridge National Laboratory to carry out this work was supported by a Travel Fellowship from the DOE-EPSCoR Grant to the University of Tennessee, DE-FG02-08ER46528. This work utilized facilities supported in part by the National Science Foundation under Agreement No. DMR-0944772. We acknowledge the support of the National Institute of Standards and Technology, U.S. Department of Commerce, in providing the neutron research facilities used in this work. Any mention of commercial products within NIST web pages is for information only; it does not imply recommendation or endorsement by NIST.

[1] D. Ebenezer, A. P. Deshpande, and P. Haridoss, J. Power Sources **304**, 282 (2016).
[2] L. Zhang, N. R. Brostowitz, K. A. Cavicchi, and R. A. Weiss, Macromol. React. Eng. **8**, 81 (2014).
[3] M. Zhang, L. Zhang, M. Zhu, Y. G. Wang, N. W. Li, Z. J. Zhang, Q. Chen, L. N. An, Y. H. Lin, and C. W. Nan, J. Mater. Chem. A **4**, 4797 (2016).
[4] R. K. Nagarale, G. S. Gohil, and V. K. Shahi, Adv. Colloid Interface Sci. **119**, 97 (2006).
[5] D. Filip, D. Macocinschi, S. Vlad, G. Lisa, M. Cristea, and M. F. Zaltariov, J. Appl. Polym. Sci. **133**, 42921 (2016).
[6] M. A. Hickner, J. Polym. Sci., Part B: Polym. Phys. **50**, 9 (2012).
[7] A. Donnadio, M. Pica, A. Carbone, I. Gatto, T. Posati, G. Mariangeloni, and M. Casciola, J. Mater. Chem. A **3**, 23530 (2015).
[8] A. Strong, B. Britton, D. Edwards, T. J. Peckham, H. F. Lee, W. Y. Huang, and S. Holdcroft, J. Electrochem. Soc. **162**, F513 (2015).
[9] G. Hatipoglu, Y. Liu, R. Zhao, M. Yoonessi, D. M. Tigelaar, S. Tadigadapa, and Q. M. Zhang, Smart Mater. Struct. **21**, 055015 (2012).
[10] A. Giuliani, M. Placidi, F. Di Francesco, and A. Pucci, React. Funct. Polym. **76**, 57 (2014).
[11] J. Li, J. K. Park, R. B. Moore, and L. A. Madsen, Nat. Mater. **10**, 507 (2011).
[12] K. T. Oh, T. K. Bronich, L. Bromberg, T. A. Hatton, and A. V. Kabanov, J. Controlled Release **115**, 9 (2006).
[13] S. H. Wu, L. C. Zheng, C. C. Li, S. D. Huo, Y. N. Xiao, G. H. Guan, and W. X. Zhu, Polym. Chem. **6**, 1495 (2015).
[14] F. Volino, M. Pineri, A. Dianoux, and A. De Geyer, J. Polym. Sci., Polym. Phys. Ed. **20**, 481 (1982).
[15] G. Ye, C. A. Hayden, and G. R. Goward, Macromolecules **40**, 1529 (2007).
[16] K. A. Mauritz and R. B. Moore, Chem. Rev. **104**, 4535 (2004).
[17] Z. J. Lu, G. Polizos, D. D. Macdonald, and E. Manias, J. Electrochem. Soc. **155**, B163 (2008).
[18] G. Gebel, Polymer **41**, 5829 (2000).
[19] D. E. Moilanen, D. B. Spry, and M. D. Fayer, Langmuir **24**, 3690 (2008).
[20] S. A. Eastman, S. Kim, K. A. Page, B. W. Rowe, S. H. Kang, S. C. DeCaluwe, J. A. Dura, C. L. Soles, and K. G. Yager, Macromolecules **45**, 7920 (2012).
[21] K. A. Page, B. W. Rowe, K. A. Masser, and A. Faraone, J. Polym. Sci., Part B: Polym. Phys. **52**, 624 (2014).
[22] B. P. Kirkmeyer, R. A. Weiss, and K. I. Winey, J. Polym. Sci., Part B: Polym. Phys. **39**, 477 (2001).
[23] N. C. Zhou, C. D. Chan, and K. I. Winey, Macromolecules **41**, 6134 (2008).
[24] K. Lu, J. K. Maranas, and S. T. Milner, Soft Matter **12**, 3943 (2016).
[25] C. L. Kinsinger, Y. Liu, F. Liu, Y. Yang, S. Seifert, D. M. Knauss, A. M. Herring, and C. M. Maupin, J. Phys. Chem. C **119**, 24724 (2015).
[26] C. H. Fujimoto, M. A. Hickner, C. J. Cornelius, and D. A. Loy, Macromolecules **38**, 5010 (2005).
[27] L. He, C. H. Fujimoto, C. J. Cornelius, and D. Perahia, Macromolecules **42**, 7084 (2009).
[28] L. He, H. L. Smith, J. Majewski, C. H. Fujimoto, C. J. Cornelius, and D. Perahia, Macromolecules **42**, 5745 (2009).
[29] S. G. Jo, T.-H. Kim, S. J. Yoon, S.-G. Oh, M. S. Cha, H. Y. Shin, J. M. Ahn, J. Y. Lee, and Y. T. Hong, J. Membr. Sci. **510**, 326 (2016).
[30] B. Smitha, S. Sridhar, and A. A. Khan, J. Membr. Sci. **225**, 63 (2003).
[31] W. G. Grot, Macromol. Symp. **82**, 161 (1994).
[32] L. He, C. J. Cornelius, and D. Perahia, Eur. Polym. J. **56**, 168 (2014).
[33] T. A. Zawodzinski, M. Neeman, L. O. Sillerud, and S. Gottesfeld, J. Phys. Chem. **95**, 6040 (1991).
[34] R. Devanathan, A. Venkatnathan, and M. Dupuis, J. Phys. Chem. B **111**, 13006 (2007).
[35] J. C. Perrin, S. Lyonnard, and F. Volino, J. Phys. Chem. C **111**, 3393 (2007).
[36] A. A. Pivovar and B. S. Pivovar, J. Phys. Chem. B **109**, 785 (2005).
[37] R. Devanathan, A. Venkatnathan, and M. Dupuis, J. Phys. Chem. B **111**, 8069 (2007).
[38] K. Sinha and J. K. Maranas, Macromolecules **44**, 5381 (2011).
[39] K. Sinha, W. Wang, K. I. Winey, and J. K. Maranas, Macromolecules **45**, 4354 (2012).
[40] J. M. Y. Carrillo, M. A. Sakwa-Novak, A. Holewinski, M. E. Potter, G. Rother, C. W. Jones, and B. G. Sumpter, Langmuir **32**, 2617 (2016).
[41] N. C. Osti, A. Cote, E. Mamontov, A. Ramirez-Cuesta, D. J. Wesolowski, and S. O. Diallo, Chem. Phys. **465**, 1 (2016).
[42] M. Laurati, P. Sotta, D. R. Long, L. A. Fillot, A. Arbe, A. Alegria, J. P. Embs, T. Unruh, G. J. Schneider, and J. Colmenero, Macromolecules **45**, 1676 (2012).
[43] B. R. Cherry, C. H. Fujimoto, C. J. Cornelius, and T. M. Alam, Macromolecules **38**, 1201 (2005).
[44] A. Meyer, R. Dimeo, P. Gehring, and D. Neumann, Rev. Sci. Instrum. **74**, 2759 (2003).
[45] E. Mamontov and K. W. Herwig, Rev. Sci. Instrum. **82**, 085109 (2011).
[46] R. T. Azuah, L. R. Kneller, Y. M. Qiu, P. L. W. Tregenna-Piggott, C. M. Brown, J. R. D. Copley, and R. M. Dimeo, J. Res. Natl. Inst. Stand. Technol. **114**, 341 (2009).
[47] M. Bee, *Quasielastic Neutron Scattering: Principles and Applications in Solid State Chemistry, Biology, and Materials Science* (Adam Hilger, Bristol, 1998).
[48] A. Faraone, K. H. Liu, C. Y. Mou, Y. Zhang, and S. H. Chen, J. Chem. Phys. **130**, 134512 (2009).
[49] L. Liu, A. Faraone, C. Mou, C. W. Yen, and S. H. Chen, J. Phys.: Condens. Matter **16**, S5403 (2004).
[50] J. Teixeira, M. C. Bellissentfunel, S. H. Chen, and A. J. Dianoux, Phys. Rev. A **31**, 1913 (1985).
[51] M. C. Bellissentfunel, S. H. Chen, and J. M. Zanotti, Phys. Rev. E **51**, 4558 (1995).
[52] F. Volino and A. J. Dianoux, Mol. Phys. **41**, 271 (1980).
[53] F. Volino, J. C. Perrin, and S. Lyonnard, J. Phys. Chem. B **110**, 11217 (2006).
[54] J. H. Roh, J. E. Curtis, S. Azzam, V. N. Novikov, I. Peral, Z. Chowdhuri, R. B. Gregory, and A. P. Sokolov, Biophys. J. **91**, 2573 (2006).

[55]S. O. Diallo, E. Mamontov, W. Nobuo, S. Inagaki, and Y. Fukushima, Phys. Rev. E **86**, 021506 (2012).
[56]N. C. Osti, M. Naguib, A. Ostadhossein, Y. Xie, P. R. C. Kent, B. Dyatkin, G. Rother, W. T. Heller, A. C. T. van Duin, Y. Gogotsi, and E. Mamontov, ACS Appl. Mater. Interfaces **8**, 8859 (2016).
[57]K. Singwi and A. Sjölander, Phys. Rev. **119**, 863 (1960).
[58]M. Bee, Chem. Phys. **292**, 121 (2003).
[59]M. A. Anderson, F. R. Trouw, and C. N. Tam, Clays Clay Miner. **47**, 28 (1999).
[60]C. E. Bertrand, Y. Zhang, and S. H. Chen, Phys. Chem. Chem. Phys. **15**, 721 (2013).
[61]A. Filippov, S. V. Dvinskikh, A. Khakimov, M. Grahn, H. Zhou, I. Furo, O. N. Antzutkin, and J. Hedlund, Magn. Reson. Imaging **30**, 1022 (2012).
[62]V. Skirda, A. Filippov, A. Sagidullin, A. Mutina, R. Archipov, and G. Pimenov, *Fluid Transport in Nanoporous Materials* (Springer, Netherlands, 2006), p. 255.
[63]S. J. Suresh and V. M. Naik, J. Chem. Phys. **113**, 9727 (2000).

Clustering effects in ionic polymers: Molecular dynamics simulations

Anupriya Agrawal,[1,*] Dvora Perahia,[1] and Gary S. Grest[2]
[1]*Department of Chemistry, Clemson University, Clemson, South Carolina 29634, USA*
[2]*Sandia National Laboratories, Albuquerque, New Mexico 87185, USA*
(Received 18 December 2014; revised manuscript received 18 March 2015; published 18 August 2015)

Ionic clusters control the structure, dynamics, and transport in soft matter. Incorporating a small fraction of ionizable groups in polymers substantially reduces the mobility of the macromolecules in melts. These ionic groups often associate into random clusters in melts, where the distribution and morphology of the clusters impact the transport in these materials. Here, using molecular dynamic simulations we demonstrate a clear correlation between cluster size and morphology with the polymer mobility in melts of sulfonated polystyrene. We show that in low dielectric media ladderlike clusters that are lower in energy compared with spherical assemblies are formed. Reducing the electrostatic interactions by enhancing the dielectric constant leads to morphological transformation from ladderlike clusters to globular assemblies. Decrease in electrostatic interaction significantly enhances the mobility of the polymer.

DOI: 10.1103/PhysRevE.92.022601 PACS number(s): 82.35.Lr, 82.35.Jk, 83.10.Mj, 83.80.Sg

I. INTRODUCTION

Cluster formation in ionomers, macromolecules that consist of ionizable groups, is driven by a balance of electrostatic interactions and inherent segregation between hydrophilic and hydrophobic groups [1]. In contrast to polyelectrolytes [2,3] where the properties of the polymers are dominated by electrostatic interactions, the characteristics of ionomers are a result of a balance of both the conformation of the backbone and electrostatic forces. The ionic groups impart conductivity and electrolytic transport characteristics as well as mechanical behavior and adhesion strength [1]. Segregation of the hydrophobic matrix and ionic clusters dominates the structure of melts of flexible and semiflexible ionomers such as sulfonated polystyrene (SPS), polystyrene methacrylate, and Nafion [4–7]. The size, shape, number, and distribution of the ionic assemblies, all affect the overall structure and dynamics of the polymers as well as their transport characteristics. Surprisingly, even the addition of a small number of ionizable groups impacts both the dynamics of the melts and the ability to transport ions and solvents. This impact is strongly manifested in recent rheology studies of Weiss and co-workers who have shown that lightly sulfonated short polystyrene melts, below the entanglement length are highly viscous and diffusion is significantly hindered in comparison with the nonsulfonated polymer with identical chain length [8–11]. The role of ionic clusters in the mobility of these polymers is one critical factor in controlling both transport characteristics and mechanical stability. Experimental studies revealed clusters with a predominantly spherical symmetry in melts, whose presence significantly reduces the mobility of the macromolecules. The direct correlation of clustering with mobility of ionic polymers, however, remains one critical open question. Here we probe the *clustering process and its impact on mobility* in sulfonated polystyrene, using molecular dynamics (MD) simulations. The rich manifold of available experimental data for polystyrene allows validation of our initial choice of force fields to describe polystyrene. Here the atomistic insight obtained from MD studies correlates the clustering effects on the polymer dynamics. We find that the morphology of the aggregates evolves with electrostatic interactions and impacts the polymer mobility.

The role of the ionic clusters in transport has driven numerous studies, pioneered by Eisenberg and co-workers [1,12–14]. They initially observed that the ionic groups segregate into multiplets—small, tightly packed ionic assemblies that in turn form clusters—using x-ray scattering [13]. They rationalized the stability of the clusters in terms of balance between electrostatic and elastic pulling forces of the polymer chains [13]. This initial model was further generalized by Forsman [15], Dreyfus [16], Datye and Taylor [17], and later by Mauritz [18]. Eisenberg *et al.* [14] have successfully extended the original model of clustering to different types of ionomer environments. This model predicts that the mobility of atoms immediately surrounding the clusters is significantly reduced; however, they were not able to predict the morphology of the clusters. These clusters were further probed by several groups. Cooper and co-workers identified spherical ionic aggregates of size ∼3 nm using electron microscopy and x-ray scattering in SPS [6,19]. Using scanning transmission electron microscopy and x-ray scattering, Winey and co-workers have observed ∼2 nm spherical ionic aggregates that were independent of the percent of sulfonation and the degree of ionization [7,20,21]. The clusters comprise multiplets—small, tightly packed ionic groups whose association is driven by Columbic forces. The clusters' size and shape are generally affected by residual electrostatic energy between multiplets, the steric repulsion between monomers, and the energies needed to deform the polymer coils from their free, natural configuration due to confinement.

The significance of these ionic aggregates has driven further studies zooming in on the conformation of single molecules. Single chains of SPS with varying sulfonation, tacticity, and ionization levels in different solvents were probed computationally [22–26]. Xie and Weiss have shown that the increase in sulfonation of SPS molecules resulted in the increase of the radius of gyration of chains [22]. Chialvo

*Present address: Department of Mechanical Engineering and Materials Science, Washington University, St. Louis, MO 63130, USA.

and Simonson have observed the like-charge attraction in the solvation of short chain SPS in aqueous solutions [23]. Carrillo and Dobrynin showed that with increasing fraction of sulfonation, a SPS chain adopts an elongated conformation [25]. Hall *et al.* have shown that pendant ions as present in SPS form discrete clusters as opposed to percolated aggregates formed in polymers with ions in the polymer backbone [27]. Here, using MD simulations we probe the formation of ionic clusters in SPS melts and their impact on the polymer mobility. We demonstrate a quantitative correlation between cluster size and polymer dynamics. For low dielectric media, we find predominantly nonspherical, ionic clusters, predicted by Dreyfus [16] that transform into spherical ones with reduction of electrostatic interaction strength.

II. METHODOLOGY

Simulations were performed using the parallel molecular dynamics code Large Atomic Molecular Massive Parallel Simulator (LAMMPS) [28]. Atactic polystyrene chains of length $N = 40$ (20 chains) and 80 (40 chains) were made using Accelrys Materials Studio [29] with 0%, 5%, and 10% random sulfonation levels. The $N = 80$ system was further replicated by a factor of 8 for a total system size of 320 chains. The percent sulfonation is defined as the number of monomers which are sulfonated with respect to the total number of monomers per chain. Polystyrene is modeled using the all atom optimized potential for liquid simulations force field by Jorgensen *et al.* [30,31]. Additional parameters for the sulfonated group are obtained from Refs. [26,32,33]. The attractive r^{-6} dispersion term in the Lennard-Jones interaction as well as the electrostatic interactions were calculated using a particle-particle particle-mesh algorithm [34]. As a result the Lennard-Jones interaction becomes a fully long range potential. Interactions closer than 1.2 nm are calculated in real space; those outside this range are calculated in reciprocal Fourier space with precision of 10^{-4}. The repulsive r^{-12} Lennard-Jones interaction was truncated at 1.2 nm. To understand the effect of the strength of the electrostatic interactions on the structure and dynamics of SPS melts, the dielectric constant ε of the $N = 80$, 10% sulfonation system was varied from $\varepsilon = 1$ to $\varepsilon = 30$.

The polymer chains were placed randomly in the simulation cell. After overlaps were removed using the "nve/limit" fix in LAMMPS, each system was run for 1−2 ns using *NPT* ensemble with temperature 600 K and 1 atm pressure where temperature and pressure were controlled using the Nosé-Hoover thermostat and barostat, respectively, to set the density. Production runs for each sulfonation level and dielectric constant were run for at least 300 ns at constant volume. As discussed in more detail below, the average size of SO_3^- clusters increases over first 100 ns and then stabilizes. Newton equations of motion were integrated using a velocity Verlet algorithm. The reference system propagator algorithm [35] with a multi-time-scale integrator with a time step of 1.0 fs for the bond, angle, dihedral, van der Waals interactions and direct interactions part of the electrostatic interactions and a time step 4.0 fs for long range electrostatic interactions was used to accelerate the simulation. For all constant volume runs, each monomer was coupled weakly to a Langevin thermostat with a damping constant of 100 fs to maintain a constant temperature.

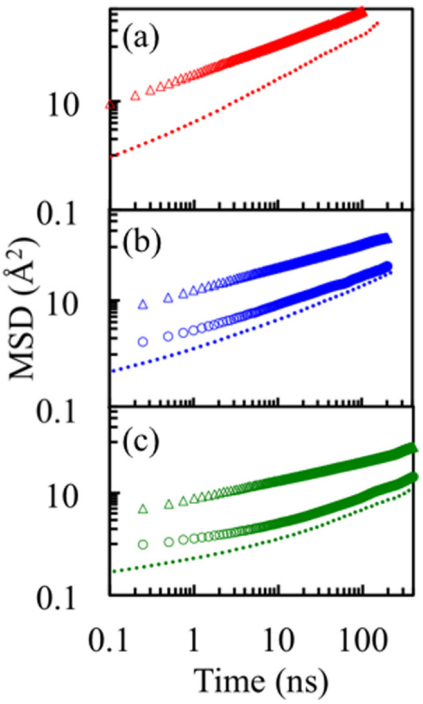

FIG. 1. (Color online) Mean square displacement versus time at 600 K of a sulfonated polystyrene melt with (a) 0%, (b) 5%, and (c) 10% sulfonation for chain length $N = 40$. MSD of phenyl rings (Δ), sulfonated phenyl rings (○), and chain center of mass (dashed line).

III. RESULTS

The mobility of the polymer was followed by determining the mean square displacement (MSD) of the center of mass of the chains for three melts of 0%, 5%, and 10% sulfonation at $T = 600$ K as shown in Fig. 1. With increasing sulfonation level, the mobility of the chains is considerably reduced as was previously observed experimentally by rheology studies [4,11]. We further probed the internal dynamics of the polymers by comparing the MSD of nonsulfonated and sulfonated phenyl rings within SPS chains. As seen in Fig. 1 the sulfonated phenyl ring motion is significantly slower than that of the nonsulfonated rings, whereas the overall motion of chains is similar to that of the sulfonated phenyl groups.

A snapshot of various clusters for a melt of chains of length $N = 40$ for 10% SPS at $T = 600$ K is shown in the left panel of Fig. 2. Surprisingly, the sulfonated groups form ladderlike clusters, as shown in the zoomed-in image in the right panel. This cluster consists of eight $SO_3^-Na^+$ groups originating from three different chains. Assuming a dipole from SO_3^- to Na^+, the geometry of this particular cluster can be described by ↑↓↑↓↑↓↑↓ where the arrows represent a dipole with the arrowhead representing Na^+. This ladderlike cluster was first postulated by Dreyfus [16]. Building on basic ionic pairs which constitute electrical dipoles, he showed that electrostatic interactions drive these dipole pairs to organize into multiplets of quadrupoles which further grow to form clusters. The size of a multiplet is limited by steric hindrance since each

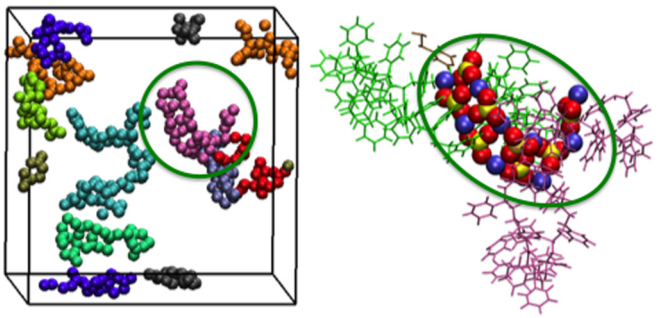

FIG. 2. (Color online) Left panel shows the snapshot of different ionic clusters for $N = 40$ with 10% sulfonation at 600 K after 160 ns, where 0 represents the start of the constant volume simulation. Different colors represent distinct clusters. The zoomed-in cluster encircled in green at right shows individual atoms: S (yellow), O (red), and Na (blue).

ionic pair is attached to the polymer backbone. The residual electrical energy between multiplets, the steric repulsion between monomers, and entropy loss due to disruption of polymer conformation all contribute to the overall shape of the cluster. In low dielectric media, the linear arrangement of these dipoles as found here minimizes the cluster energy.

To explore the thermal stability of the ladder morphology we probed the melt at 700 K, which is feasible in our model since the bonds are unbreakable. We find that the clusters remain stable even at this higher temperature as shown in Fig. 3. The mobility of the ionomers increases with increasing temperature as shown in the MSD data presented in Fig. 3(b). While the clusters become more dynamic with increasing temperature, they do not dissociate under the conditions of our measurement. The tendency of the ionic groups to form clusters, also leads to an increase in density with sulfonation level. The densities measured at 600 K and pressure $P = 1$ atm are 0.84, 0.89, and 0.95 g/cc for sulfonation 0%, 5%, and 10%, respectively. Concurrently, the average end-to-end distance of chains decreases with increasing sulfonation levels where $\langle R_g^2 \rangle^{1/2} \sim 17.2$, 14.8, and 13.6 Å for 0%, 5%, and 10% sulfonation, respectively.

As clustering affects the mobility, the impacts of the electrostatic interactions were further probed via increasing

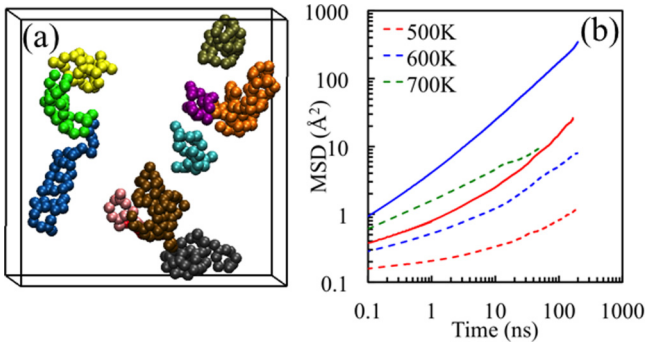

FIG. 3. (Color online) (a) Clusters depicted in a melt of sulfonated polystyrene, $N = 40$ with 10% sulfonation at 700 K. (b) Mean square displacement for the same system (dashed lines). Solid lines are for zero sulfonation.

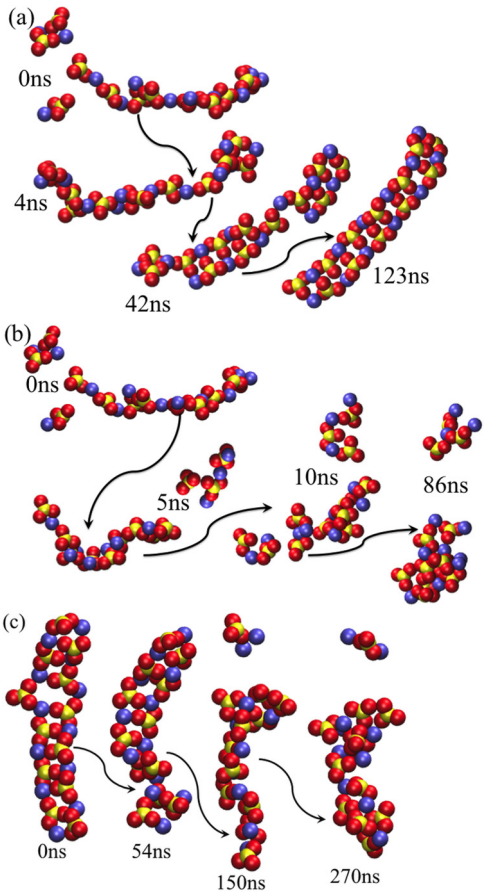

FIG. 4. (Color online) Time evolution of association and rearrangement of multiplets for (a) $\varepsilon = 1$, (b) $\varepsilon = 2$, and (c) ε increased to 2 from 1 after 230 ns of simulation in (a).

the dielectric constant ε of the melt. The dielectric constant impacts the residual electrostatic screening, which along with the hard core repulsion between monomers and polymer entropy determine the shape and stability of the ionic assemblies [16]. Here ε was varied between 1 and 30 as a means to tune this energetic term. Though increasing ε slightly decreases the density at constant pressure, all simulations for $\varepsilon = 1-30$ were carried out at the equilibrium density for $\varepsilon = 1$ for a direct comparison. Cluster evolution was followed as a function of time for different ε values. A wide variety of cluster morphology was observed for these melts similar to those found previously by Bolintineanu *et al.* [36] for poly(ethylene-co-acrylic acid) ionomers with precise spacing between acid groups. One typical cluster is shown Fig. 4(a) as time progresses for $\varepsilon = 1$ melt. Initially there are three smaller clusters as shown in Fig. 4(a). With time, the clusters form one stringlike large aggregate. Once merged, the cluster rearranges and by 42 ns there are two $\uparrow\downarrow\uparrow\downarrow$ multiplets joined by a string cluster. By 123 ns, all $SO_3^-Na^+$ ions form a single large multiplet. This cluster remains stable for an additional 300 ns apart from slight motion of the atoms.

The electrostatic interactions were then decreased by increasing the dielectric constant to $\varepsilon = 2$ for the same starting state as for $\varepsilon = 1$ described above. In this case, the clusters are significantly more dynamic; they break up and merge forming

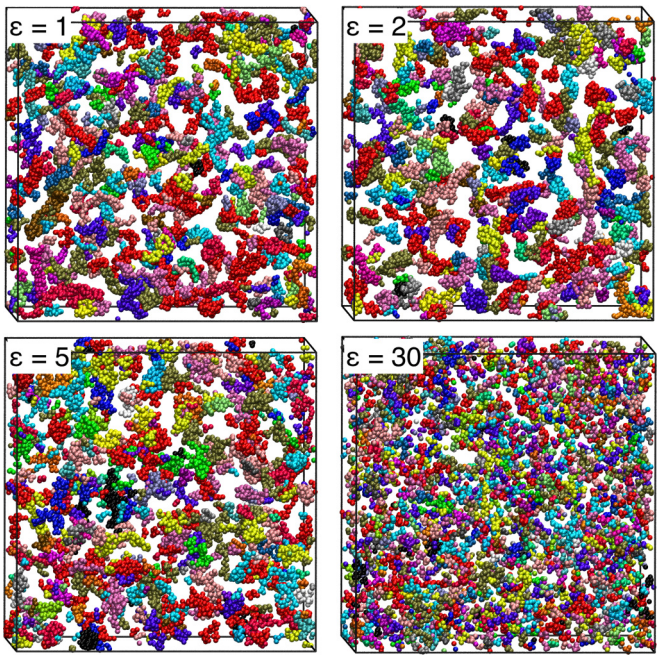

FIG. 5. (Color online) Ionic clusters for 10% sulfonated polystyrene ($N = 80$) for different values of ε at $T = 600$ K.

more globular assemblies as shown for one cluster after ~83 ns in Fig. 4(b). The clusters are much more globular or spherical for $\varepsilon = 2$ than for $\varepsilon = 1$ with an average cluster size of 6 to 7 SO_3^- groups. On further increasing ε, the average cluster size decreases to 4.0 for $\varepsilon = 5$ and 1.7 SO_3^- for $\varepsilon = 10$. Distribution of SO_3^- for $\varepsilon = 1$, 2, 5, and 30 melt is shown in Fig. 5. Overall, as the strength of the electrostatic interaction decreases, cluster size decreases.

Finally, starting at time 230 ns for the $\varepsilon = 1$ system, we followed the changes in the cluster shown in Fig. 4(a) with time after increasing ε from 1 to 2. Results are shown in Fig. 4(c). After ~40–50 ns, the ladder morphology begins to distort but does not break up until ~150 ns. This cluster continues to deform as the simulation progresses. When switching back ε from 2 to 1 the globular clusters stretch out again to form ladderlike aggregates after approximately 100 ns. This morphological change as a function of ε is attributed to screening of the residual electrostatic energy between ion pairs or multiples.

To further understand the morphological changes as a function of electrostatic strength, we compared the energy of ladderlike and spherical aggregates of equal size and found that the potential energy is 32 kcal/mol lower in a ladderlike structure than in a spherical aggregate per SO_3^- group for $\varepsilon = 1$. This result was determined by calculating the potential energy of each aggregate for the melt with $\varepsilon = 1$ and comparing it with the melt run with $\varepsilon = 5$ but setting $\varepsilon = 1$. This shows that for $\varepsilon = 1$, ladderlike type clusters are most stable. However, for large screening ($\varepsilon = 5$) the ladderlike and spherical aggregates of the same size have comparable potential energies. In this case the spherical aggregates would be likely favored due to a combination of entropy and interfacial energy, in agreement with our simulation results. This result is consistent with the overall energy of the ladderlike melt which is lower by 31 kcal/mol

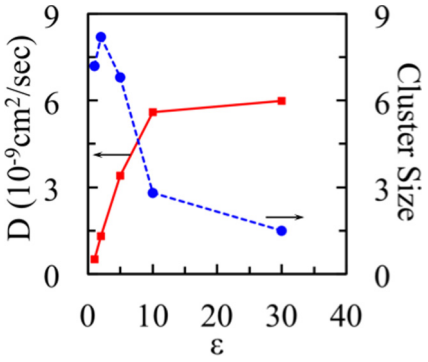

FIG. 6. (Color online) Diffusion constant D (red squares) and average cluster size (blue circles) for $N = 80$ SPS with 10% sulfonation at $T = 600$ K as a function of ionic strength.

per SO_3^- group in comparison to that of a melt that consists of predominantly globular aggregates. This difference is due to a large gain in electrostatic energy at the expense of a small loss in the interfacial energy [37]. This result further demonstrates that the cluster morphology is dominated by the residual electrostatic interactions between multiplets and is consistent with previous observations by coarse grained models [38,39] that the cluster shape changes from disklike to spherical as the strength of the attraction interaction between associating groups decreases.

Using the dielectric constant as a means to control the overall degree of association of the sulfonated groups, we probed the effects of cluster formation on the overall mobility of the polymers. The correlation between cluster formation and the mobility of the polymers with varying dielectric constant is summarized in Fig. 6 for a melt of chain length $N = 80$ with 10% sulfonation. With increasing ε the cluster size decreases, and their number increases as seen in Fig. 7. The mobility of the polymers as reflected in the diffusion constant increases as the size of the clusters decreases. In this range the average end-to-end distance of chains remain constant (41.3, 41.2, 44.8, and 45.4 Å for $\varepsilon = 1$,2,5, and 30, respectively). The difference in the local mobility of the sulfonated versus

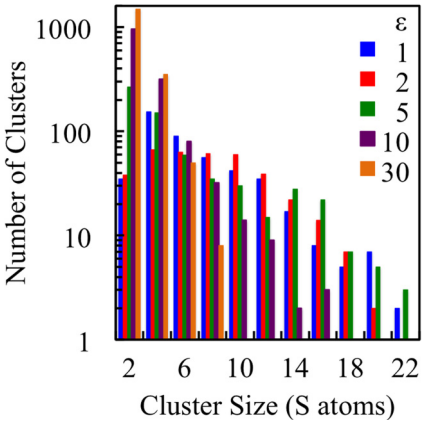

FIG. 7. (Color online) Cluster distribution for $N = 80$ polystyrene at $T = 600$ K for 10% sulfonation with varying ionic strength.

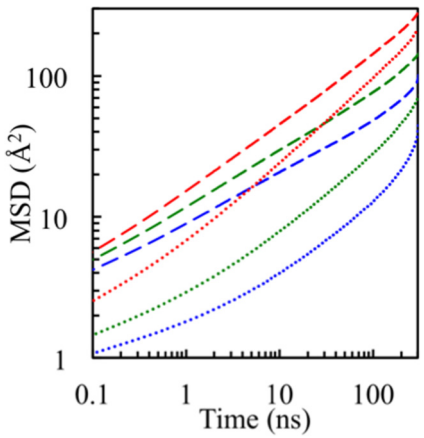

FIG. 8. (Color online) Mean square displacement of sulfonated (dotted) and nonsulfonated (dashed) benzene rings for chain length $N = 80$ with 10% sulfonation at 600 K for $\varepsilon = 1$ (blue), $\varepsilon = 2$ (green), and $\varepsilon = 5$ (red).

nonsulfonated benzene rings also decreases as ε increases as shown in Fig. 8. Even though the mobility of the polymers increases with increasing ε, for SPS, it remains slower in comparison with that of zero sulfonation polystyrene. The diffusion constant calculated for zero sulfonation polystyrene ($N = 80$) is $1.7 \times 10^{-8}\,\mathrm{cm}^2/\mathrm{s}$, which is considerably faster than all of the sulfonated systems and is in good agreement with experiment [40]. Part of this increase could be attributed to the reduction in density at $P = 1$ atm (0.84 g/cc for zero sulfonation compared to 0.95 g/cc for 10%).

IV. CONCLUSIONS

In summary, we have shown that the constrained dynamics in sulfonated polystyrene is directly correlated with cluster formation and is affected by the local movements of the group to which the ionizable group is tethered. The mobility of the SPS molecules decreases significantly with increasing sulfonation fraction in agreement with recent experiments [4]. However, increasing the dielectric constant of the media decreases the dimensions of the clusters and consequently enhances dynamics. Surprisingly, the study revealed ladderlike cluster morphologies dominate at low dielectric media as predicted by Dreyfus [16] regardless of the percent sulfonation and chain length. These ladderlike clusters exhibit a lower potential energy compared to a globular morphology. We further show that small change in the electrostatic strength leads to more spherical or globular clusters. In addition to unique new cluster morphologies, this study has demonstrated the delicate balance that controls cluster formation in ionic polymers and its correlation with the dynamics of the polymers in melts.

ACKNOWLEDGMENTS

We gratefully acknowledge financial support from Grant No. DE-SC007908. We acknowledge computational resources at the National Energy Research Scientific Computing Center, which is supported by the Office of Science of the United States Department of Energy, under Contract No. DE-AC02-05CH11231 and Clemson Computing and Information Technology. This work was performed, in part, at the Center for Integrated Nanotechnology, a U.S. Department of Energy and Office of Basic Energy Sciences user facility. Sandia National Laboratories is a multiprogram laboratory managed and operated by Sandia Corporation, a wholly owned subsidiary of Lockheed Martin Corporation, for the U.S. Department of Energy's National Nuclear Security Administration under Contract No. DE-AC04-94AL85000.

[1] A. Eisenberg and J.-S. Kim, *Introduction to Ionomers* (Wiley, New York, 1998).
[2] D. T. Hallinan, Jr. and N. P. Balsara, Annu. Rev. Mater. Res. **43**, 503 (2013).
[3] C. E. Sing, J. W. Zwanikken, and M. Olvera de la Cruz, Nat. Mater. **13**, 694 (2014).
[4] Q. Chen, G. J. Tudryn, and R. H. Colby, J. Rheol. **57**, 1441 (2013).
[5] D. G. Peiffer, R. A. Weiss, and R. D. Lundberg, J. Polym. Sci., Polym. Phys. Ed. **20**, 1503 (1982).
[6] C. Li, R. A. Register, and S. L. Cooper, Polymer **30**, 1227 (1989).
[7] N. C. Zhou, C. D. Chan, and K. I. Winey, Macromolecules **41**, 6134 (2008).
[8] X. Qiao and R. A. Weiss, Macromolecules **46**, 2417 (2013).
[9] R. A. Weiss and H. Zhao, J. Rheol. **53**, 191 (2009).
[10] R. A. Weiss, J. J. Fitzgerald, and D. Kim, Macromolecules **24**, 1071 (1991).
[11] R. A. Weiss and W.-C. Yu, Macromolecules **40**, 3640 (2007).
[12] M. Rigdahl and A. Eisenberg, J. Polym. Sci., Polym. Phys. Ed. **19**, 1641 (1981).
[13] A. Eisenberg, Macromolecules **3**, 147 (1970).
[14] A. Eisenberg, B. Hird, and R. B. Moore, Macromolecules **23**, 4098 (1990).
[15] W. C. Forsman, Macromolecules **1**, 343 (1968).
[16] B. Dreyfus, Macromolecules **18**, 284 (1985).
[17] V. K. Datye and P. L. Taylor, Macromolecules **18**, 1479 (1985).
[18] K. A. Mauritz, in *Ionomers: Synthesis, Structure, Properties and Applications*, edited by M. R. Tant, K. A. Mauritz, and G. L. Wilkes (Chapman and Hall, London, 1997), pp. 95–157.
[19] D. J. Yarusso and S. L. Cooper, Macromolecules **16**, 1871 (1983).
[20] B. P. Kirkmeyer, R. A. Weiss, and K. I. Winey, J. Polym. Sci., Part B: Polym. Phys. **39**, 477 (2001).
[21] A. M. Castagna, W. Wang, K. I. Winey, and J. Runt, Macromolecules **44**, 2791 (2011).
[22] R. Xie and R. A. Weiss, Comput. Theor. Polym. Sci. **7**, 65 (1997).
[23] A. A. Chialvo and J. M. Simonson, J. Phys. Chem. B **109**, 23031 (2005).
[24] A. Vishnyakov and A. V. Neimark, J. Chem. Phys. **128**, 164902 (2008).
[25] J.-M. Y. Carrillo and A. V. Dobrynin, J. Phys. Chem. B **114**, 9391 (2010).

[26] X. He, O. Guvench, A. D. J. Mackerell, and M. L. Klein, J. Phys. Chem. B **114**, 9787 (2010).
[27] L. M. Hall, M. J. Stevens, and A. L. Frischknecht, Phys. Rev. Lett. **106**, 127801 (2011).
[28] S. Plimpton, J. Comput. Phys. **117**, 1 (1995).
[29] Materials Studio, Accelrys.©2001–2007 Accelrys Software Inc.
[30] W. L. Jorgensen, J. D. Madura, and C. J. Swenson, J. Am. Chem. Soc. **106**, 6638 (1984).
[31] W. L. Jorgensen, D. S. Maxwell, and J. Tirado-Rives, J. Am. Chem. Soc. **118**, 11225 (1996).
[32] W. R. Cannon, B. M. Pettitt, and A. A. McCammon, J. Phys. Chem. **98**, 6225 (1994).
[33] J. Chandrasekhar, D. C. Spellmeyer, and W. L. Jorgensen, J. Am. Chem. Soc. **106**, 903 (1984).
[34] R. E. Isele-Holder, W. Mitchell, and A. E. Ismail, J. Chem. Phys. **137**, 174107 (2012).
[35] M. Tuckerman, B. J. Berne, and G. J. Martyna, J. Chem. Phys. **97**, 1990 (1992).
[36] D. S. Bolintineanu, M. J. Stevens, and A. L. Frischknecht, ACS Macro Lett. **2**, 206 (2013).
[37] J. L. Brédas, R. R. Chance, and R. Silbey, Macromolecules **21**, 1633 (1988).
[38] A. N. Semenov, I. A. Nyrkova, and A. R. Khokhlov, Macromolecules **28**, 7491 (1995).
[39] P. G. Khalatur, A. R. Khokhlov, I. A. Nyrkova, and A. N. Semenov, Macromol. Theory Simul. **5**, 713 (1996); **5**, 749 (1996).
[40] G. Fleischer, Polym. Bull. **11**, 75 (1984).

Solvent controlled ion association in structured copolymers: Molecular dynamics simulations in dilute solutions

Dipak Aryal, Dvora Perahia, and Gary S. Grest

Citation: J. Chem. Phys. **143**, 124905 (2015); doi: 10.1063/1.4931657
View online: http://dx.doi.org/10.1063/1.4931657
View Table of Contents: http://aip.scitation.org/toc/jcp/143/12
Published by the American Institute of Physics

Solvent controlled ion association in structured copolymers: Molecular dynamics simulations in dilute solutions

Dipak Aryal,[1] Dvora Perahia,[1] and Gary S. Grest[2]
[1]*Department of Chemistry, Clemson University, Clemson, South Carolina 29634, USA*
[2]*Sandia National Laboratories, Albuquerque, New Mexico 87185, USA*

(Received 31 July 2015; accepted 14 September 2015; published online 28 September 2015)

Tailoring the nature of individual segments within ion containing block co-polymers is one critical design tool to achieve desired properties. The local structure including the size and distribution of the ionic blocks, as well as the long range correlations, are crucial for their transport ability. Here, we present molecular dynamics simulations on the effects of varying the concentrations of the ionizable groups on the conformations of pentablock ionomer that consist of a center block of ionic sulfonated styrene tethered to polyethylene and terminated by a bulky substituted styrene in dilute solutions. Sulfonation fractions $f(0 \leq f \leq 0.55)$, spanning the range from ionomer to polyelectrolytes, were studied. Results for the equilibrium conformation of the chains in water and a 1:1 mixture of cyclohexane and heptane are compared to that in implicit poor solvents with dielectric constants $\varepsilon = 1.0$ and 77.73. In water, the pentablock collapses with the sulfonated groups on the outer surface. As f increases, the ionic, center block increasingly segregates from the hydrophobic regions. In the 1:1 mixture of cyclohexane and heptane, the flexible blocks swell, while the center ionic block collapses for $f > 0$. For $f = 0$, all blocks swell. In both implicit poor solvents, the pentablock collapses into a nearly spherical shape for all f. The sodium counterions disperse widely throughout the simulation cell for both water and $\varepsilon = 77.73$, whereas for $\varepsilon = 1.0$ and mixture of cyclohexane and heptane, the counterions largely condense onto the collapsed pentablock. © *2015 AIP Publishing LLC.* [http://dx.doi.org/10.1063/1.4931657]

I. INTRODUCTION

Transporting ions, electrons, and solvents are the key requirements of ionic polymers for varieties of applications such as in fuel cell,[1,2] for clean energy production and storage,[3,4] in actuators,[5–7] and in drug delivery.[8,9] Tailoring multiple blocks into one polymer has been one promising pathway to multi-functional materials. Tethering ionic blocks and non-ionic blocks provides potential design tool for ionic morphologies in which transport properties are tailored. The presence of these incompatible blocks leads to the segregation of the polymer matrix into hydrophobic and hydrophilic regions resulting in a new set of challenges to control miscibility and long range correlations. This phase segregation manifests itself on multiple length scales from that of an individual polymer molecule to that of the macroscopic membranes.

One such example of multifunctional macromolecules is a pentablock copolymer of the form ABCBA shown in inset of Figure 1. The center block consists of randomly sulfonated atactic polystyrene tethered to polyethylene with randomly substituted propylene, which we refer as the flexible blocks, end-capped by atactic *tert*-butyl polystyrene. The end poly(*t*-butyl-styrene) blocks, free of sulfonation, give strong mechanical strength and do not swell on wetting. The flexible ethylene-*r*-propylene blocks provide toughness to prevent brittleness in dry condition, which is a critical attribute in membrane. Architecture of this material provides an opportunity to understand and control the interface between the hydrophilic and hydrophobic sections. Building on the understanding obtained in our previous study,[10] here we probed isolated molecules in solvents as a function of the ionic fractions using molecular dynamics (MD) simulations. It is particularly significant to probe the ionizable groups on the internal phase segregation on the length scale of isolated molecules since solution is the casting media for membranes. One critical challenge though is that the ionic groups drive clustering even in dilute solutions. This clustering is essentially the initial path to forming transport channels in membranes; however, they form physical crosslinking that in turn may trap the polymers in far from equilibrium state. With solvent casting as the main path to membrane formation, tuning the structure through polymer-solvent interactions in the dilute regime, below the critical micellar concentration, offers a tool to tune membrane structures. Here, using extensive set of simulations, we probed the dilute regime with the insight that only a large number of solvent molecules can provide. This regime is the optimal media to tune the initial conformation and association of this complex polymer. In contrast to non-ionic polymers, we find that the degree of ionic substitution even of one block plays a critical role, with a distinction between the ionomer and polyelectrolyte regions.

Though computational methods provide a unique molecular insight into the nano and mesoscopic length scales, the association of the ionic groups which drive the properties of the pentablock presents a challenge that one can easily be trapped in metastable states. Here, in parallel to the insight into the impact of the concentration of ionic groups, we

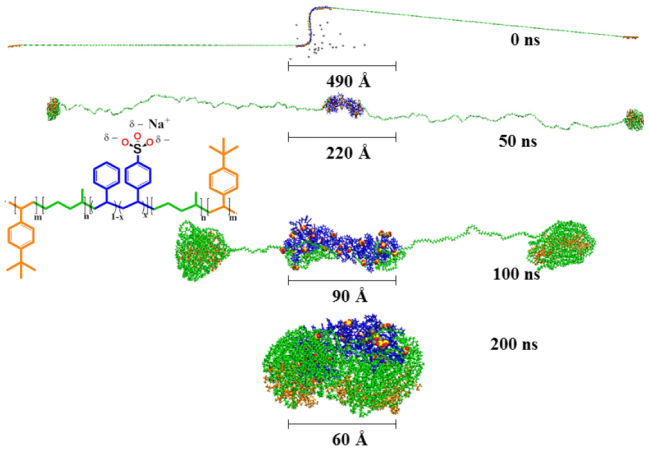

FIG. 1. Sample images of pentablock molecule for $f = 0.15$ in an implicit poor solvent for $\varepsilon = 1.0$ at 300 K at four different times. The chemical structure of poly(t-butyl-styrene)-b-ethylene-r-propylene-b-styrene-r-styrenesulfonate-b-ethylene-r-propylene-b-poly(t-butyl-styrene) pentablock molecule in the inset. The end block is shown in orange, flexible block in green, middle block in blue, oxygen atoms in red, sulfur atoms in yellow, and sodium atoms in gray.

demonstrate the use of temperature cycling to address this challenge.

Experimental studies have probed concentrated solution and bulk properties of this pentablock for different sulfonation fractions.[11–16] Choi *et al.*[11] have shown that above 10 wt. %, this pentablock associates to form micelles with spherical symmetry. Most studies have focused in the transport in membranes. Geise *et al.*[12] found that water uptake, water permeability, and salt permeability increase with increase in degree of sulfonation. Choi *et al.*[17] and Geise *et al.*[14] have shown that aluminum neutralization affects the structure and the mechanical and transport properties of membranes of this pentablock copolymer. Recently, Etampawala *et al.*[16] studied the association of multichains sulfonated pentablock copolymers in dilute solutions of the polymer in a mixture of cyclohexane and heptane using small angle neutron scattering. They reported that micelles are formed for all sulfonation levels with a core of the sulfonated styrene and a corona of the solvated flexible and end blocks. The micellar shape however diverges from sphericity.

Molecular level understanding of interactions between the polymer-solvent, block–block, ion-ion, and ion-counterion determines the conformation of polymer and hence impact their assembly into membranes. Resolving the factors that affect the conformation of this type of structured polymer is essential to control the processing in dilute solution where intramolecular interactions can be resolved. The ionizable block, namely, the styrene sulfonate segregates from the rest of the polymer and essentially facilitates transport of polar solvents and ions. Its conformation is therefore critical to the understanding of the overall behavior of the pentablock. A number of computational studies have investigated the conformation of single chains of sulfonated polystyrene (sPS) in dilute solution.[18–22] Among them are Xie and Weiss[19] who carefully mapped the conformation of sPS chain in poor solvents using molecular dynamics simulations. They found that as the sulfonation fraction increased, the radius of gyration R_g of collapsed ionomers increased slightly and the conformation became less globule-like. Further insight was obtained by Carrillo and Dobrynin[18] who studied single sPS chains in aqueous solutions. They showed that with the increasing sulfonated groups, the chains adopt an elongated conformation where the ionic groups lie on the outer surface. Chialvo and Simonson[21] showed that the solvent, degree of sulfonation, and its distribution along the sPS chain strongly effect the polymer chain conformation.

Enhancing molecular complexity of the polymers by tailoring blocks with specific roles while controlling their phase behavior presents an immense step towards designing controlled transport systems. While introducing a highly interacting block such as an ionizable one into block co-polymers is one effective way to attain functionality, there is yet no theoretical framework to predict their phase diagrams. Recently, we[10] studied for the first time the behavior of a single chain of pentablock copolymer in different solvents at sulfonation fraction $f = 0.30$. In hydrophobic solvents, the ionic block resides in the center, surrounded by a swollen intermix of the flexible and end blocks. In water, all blocks collapse with the sulfonated block residing on the surface of the collapsed molecule. Present study investigates the conformation of a single pentablock chain and sulfonated polystyrene of the same molecular weight as that of the center block as a function of temperature, sulfonation fraction f, and solvent quality using molecular dynamics simulations. Specifically, this study explores the single chain conformations for six sulfonation fractions $0 \le f \le 0.55$, spanning the range from ionomer to polyelectrolyte, in solvents of different qualities. The interplay of solvent-polymer interactions and polymer-polymer interactions in controlling the phase behavior and conformation of individual block was studied in water and in a 1:1 mixture of cyclohexane and heptane. Water is a poor solvent for all the blocks except for the ionic regions, and the 1:1 mixture of cyclohexane and heptane is a good solvent for the end blocks and flexible blocks and a poor solvent for center block when it is sulfonated. Along with these explicit solvents, implicit solvents have been used to tune the dielectric constants without changing any additional factors. The dielectric properties of the solvent affect the size and orientation of ionic domain as well as counter ions. One of the implicit solvents was modeled to be similar to water with the dielectric constant $\varepsilon = 77.73$[18] and $\varepsilon = 1$ captures hydrocarbon chains.

This paper is organized as follows: Section II describes the simulation methodology followed by introducing the computational challenge of obtaining equilibrium configurations for sulfonated chains, described in Section III; Section IV presents the results for the pentablock and sPS for six sulfonation fractions in different solvents. A brief summary and outlook are presented in Section V.

II. MODEL AND METHODOLOGY

The single chain of pentablock ionomer, sPS chain, and solvent molecules is modeled using the Optimized Potentials for Liquid Simulations-All Atoms (OPLS-AAs) framework of Jorgensen *et al.*[23,24] which is composed of bonded and

non-bonded interactions. The non-bonded interaction $U_{nb}(r_{ij})$ is a sum of standard 12-6 Lennard-Jones (LJ) and electrostatic potentials,

$$U_{nb}(r_{ij}) = 4\varepsilon_{ij}\left[\left(\frac{\sigma_{ij}}{r_{ij}}\right)^{12} - \left(\frac{\sigma_{ij}}{r_{ij}}\right)^{6}\right] + \frac{q_i q_j}{4\pi\varepsilon r_{ij}}, \quad (1)$$

where r_{ij} is the distance between atoms i and j, ε_{ij} is the LJ energy, and σ_{ij} is the LJ diameter for atoms i and j, q_i and q_j are their partial charges. Geometric mixing rules are used for atoms of different species: $\varepsilon_{ij} = (\varepsilon_i\varepsilon_j)^{1/2}$ and $\sigma_{ij} = (\sigma_i\sigma_j)^{1/2}$. Non-bonded interactions are calculated between all atom pairs of different molecules. In addition, all pairs on the same molecule are separated by three or more bonds, though the interaction is reduced by a factor of 1/2 for atoms separated by three bonds. All LJ interactions are cutoff at r_c = 12 Å. All electrostatic interactions closer than r_c are calculated in real space; those beyond this range are calculated in reciprocal Fourier space by using the particle-particle particle-mesh (PPPM) algorithm[25] with precision of 10^{-4}. In the OPLS-AA, covalent bonds consist of distance and angles. The bonded potentials include two-body bond, three-body angle, and four-body dihedral interactions.[23]

The pentablock, sPS, and 1:1 mixture of cyclohexane and heptane molecules were constructed separately using polymer builder and amorphous cell modules in Accelrys Materials Studio©.[26] Since OPLS potentials are not available in Material Studio, the conformation energy of each polymer molecule was initially minimized with the polymer consistent force field (pcff). The pentablock molecules, ABCBA, had a total molecular weight of ~50 000 g/mol and contained randomly sulfonated atactic polystyrene in the center block (C) tethered to polyethylene with randomly substituted 1.1% propylene (B) and end-capped by atactic poly-*t*-butyl styrene (A) as shown in inset of Figure 1. The total wt. % of the center sulfonated block is ~40%, while each of the randomly substituted polyethylene blocks is ~20% and each of poly-*t*-butyl styrene blocks is ~10%. Total number of monomers for each pentablock molecules (ABCBA) studied here is 1467 (30 + 617 + 173 + 617 + 30) with f = 0, 0.08, 0.15, 0.30, 0.40, and 0.55. The counterion is Na^+ in all cases.

The LAMMPS classical MD code[27] was used to perform all the simulations. The Newton equations of motions were integrated using a velocity-Verlet algorithm with a time step δt = 1 fs for simulation for the polymer in water and in implicit solvents. The reference system propagator algorithm (REPSA)[28] with multi-time scale integrator with a time step of 1.0 fs for the bond, angle, dihedral, van der Waals interactions and direct interactions part of the electrostatic interactions and a time step 4.0 fs for long range electrostatic interactions was used to accelerate simulation of system for the polymer in 1:1 mixture of cyclohexane and heptane. Temperature of the system was maintained by using a Langevin thermostat with a 100 fs damping constant. The Nose-Hoover thermostat was used with the same damping constant to equilibrate the system at constant pressure and temperature after merging the polymer chain with the solvent. An in-house conversion code was used to convert the potential parameters to OPLS as well as to modify the Material Studio data files into a form readable by LAMMPS.

Simulations of six pentablock and six sPS molecules with $0 \le f \le 0.55$ in TIP4P/2005 water[29] and 1:1 mixture of cyclohexane and heptane as well as two implicit poor solvents were carried out. The five pentablocks and sPS chain with $f > 0$ were randomly sulfonated. For both explicit solvents, the dielectric constant in Eq. (2) was set ε = 1.0. All the interactions between atoms on the polymer molecule for the implicit solvent simulations were the same as in Eq. (2) with r_c = 12 Å. To model water implicitly, we set the dielectric constant ε = 77.73, while to model a nonpolar, poor solvent implicitly, we set ε = 1.0.

Before merging pentablocks in explicit solvents, we first equilibrated systems of 256 000 water molecules and 1:1 mixture of 21 600 cyclohexane and 21 600 heptane molecules at 300 K in a cubic simulation cell. Periodic boundary conditions were used for all explicit atom simulations. The collapsed pentablocks were then combined with the solvent to form solutions. Overlapping atoms that resulted from merging the pentablock molecules and the explicit solvents were removed by running for a few thousand steps with the *fix nve/limit* routine in LAMMPS. We ran the water system for 30 ns and mixed solvent system for 40 ns at 500 K and then cooled each to 300 K. Each system was then run for 30 ns at constant pressure of P = 0 at T = 300 K to equilibrate the mixture, followed by a run of 30 ns at constant volume to obtain statistics. The dimensions of the simulation cell after equilibration were between 19.3 and 19.5 nm for water and 21.6–21.8 nm for the mixed solvent, which is sufficient to prevent interaction of pentablock with its periodic image.

To study the size and shape of polymer chains, we calculated the radius of gyration and the principal moment of inertia. Radius of gyration is given by

$$R_g^2 = \sum_{i=1}^{N} m_i (r_i - r_{COM})(r_i - r_{COM}) / \sum_{i=1}^{N} m_i, \quad (2)$$

where m_i is the mass of atom i and r_{COM} is the center of mass of the polymer. This calculation includes the atomic positions and masses which account for molecular conformations. Similarly, the principal of moments of inertia, i.e., eigenvalues of the moment of inertia tensor are given by

$$R_g^2 = \lambda_1 + \lambda_2 + \lambda_3, \quad (3)$$

where $\lambda_1 < \lambda_2 < \lambda_3$ are the eigenvalues of moment of inertia tensor. The sphericity of the polymer can be characterized by a number of

$$A(a_1, a_2, a_3) = \frac{(a_1 - a_2)^2 + (a_1 - a_3)^2 + (a_2 - a_3)^2}{2(a_1 + a_2 + a_3)^2}, \quad (4)$$

where a_i are the lengths of the principal axis of the moment of inertia tensor, $a_i = \sqrt{3\lambda_i}$, $i = 1,2,3$. The sphericity $A(a_1, a_2, a_3)$ is a number between zero for a spherical shape and 1 for a rod. The shape of the ellipsoid is characterized by

$$P(a_1, a_2, a_3) = \frac{(2a_1 - a_2 - a_3)(2a_2 - a_1 - a_3)(2a_3 - a_1 - a_2)}{2(a_1^2 + a_2^2 + a_3^2 - a_1a_2 - a_1a_3 - a_2a_3)^{3/2}}. \quad (5)$$

The prolateness, $P(a_1, a_2, a_3)$, ranges from −1 for a perfectly oblate ellipsoid ($a_1 = a_2 > a_3$) to 1 for a perfectly prolate

ellipsoid ($a_1 > a_2 = a_3$).[30] Structure factor is calculated using $S(q) = \left|\sum_i b_i e^{iqr_i}\right|^2$, where b_i and r_i are the scattering length and position vector of atom i, respectively.

III. COMPUTATIONAL CHALLENGES

A computational challenge in any simulation is to assure that the systems are fully equilibrated. This is particularly relevant for the present simulations since all blocks are collapsed at room temperature forming a dense state and both the polystyrene and *t*-butyl polystyrene are below their glass transition temperature. The introduction of sulfonated groups further reduces the chain mobility as the ionic groups interact strongly and form long-lived ionic clusters. An example of this challenge can be seen by following the collapse of a nearly fully stretched chain for $f = 0.15$ in an implicit poor solvent with $\varepsilon = 1.0$ as a function of time at 300 K as shown in Figure 1. At first, the two end blocks collapse after approximately 10 ns, followed by the partially sulfonated center block after approximately 40 ns. Then, the two flexible blocks rolled up with end blocks merging with the center block. After approximately 200 ns, the entire pentablock remains elongated as shown in Figure 1. Similar results were obtained for other specified value of f and for $\varepsilon = 77.73$.

The instantaneous radius of gyration R_g is shown in Figure 2 as a function of time for $f = 0.15$ at 300 K. Initially, R_g decreases linearly from its fully extended state at 0 ns and becomes constant after 170 ns. While R_g has reached a plateau at later times as shown in the inset of Fig. 2, the system has not reached equilibrium; it is simply trapped in a metastable state which is effectively frozen over the accessible simulation times. To overcome being trapped in long-lived metastable states, we thermally annealed all of our systems at 500 K and 700 K and then cooled back down to 300 K. Note that experimentally these temperatures are accessible under inert environment. Snapshots of the resulting configurations are shown in Figure 3 for $f = 0.15$ where the pentablock is more

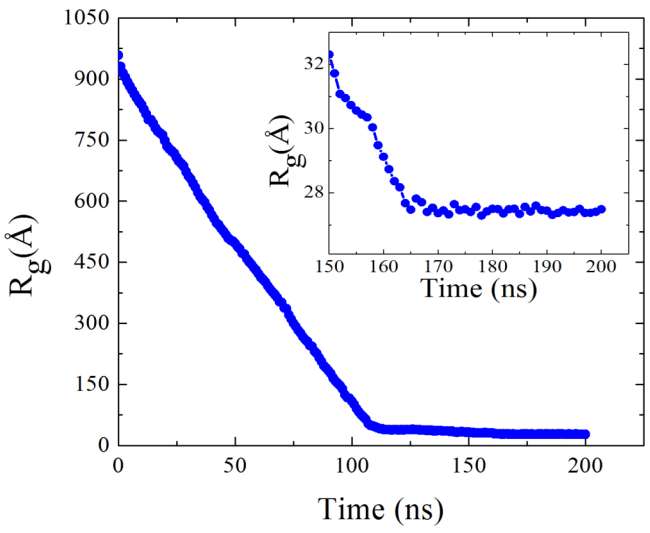

FIG. 2. Radius of gyration R_g as the function of time for pentablock in an implicit poor solvent for $\varepsilon = 1.0$ at 300 K.

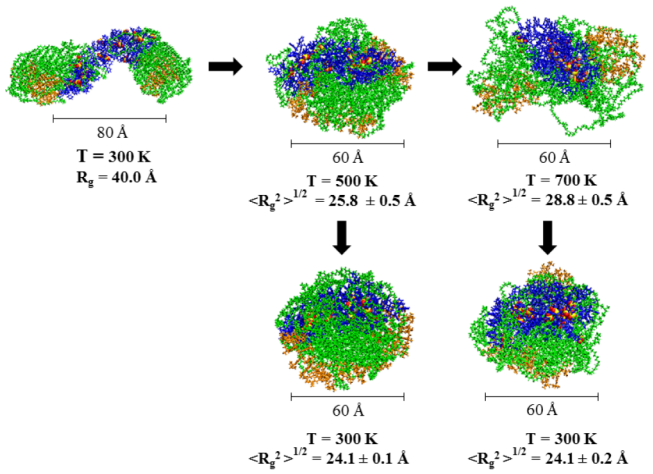

FIG. 3. Sample images of pentablock for $f = 0.15$ in an implicit poor solvent at different temperatures for $\varepsilon = 1.0$.

expanded at 700 K compared to 500 K as one would expect at elevated temperature. These systems were then cooled back to 300 K at a rate of 40 K/ns. Starting from either 500 or 700 K states, the final configuration at 300 K has the same mean square radius of gyration $\langle R_g^2 \rangle^{1/2}$ as shown at the two lower panels in Figure 3. This process of thermally annealing the pentablock and cooling back to 300 K resulted in a much more compact structure than obtained from collapsing the chain directly at 300 K. All results in the remaining of the paper were obtained by thermal annealing at high temperature both for implicit and explicit solvents.

IV. RESULTS AND DISCUSSION

This section introduces the effects of degree of substitution by ionizable groups on the packing and the conformation of single pentablock molecules in several solvents including water, implicit poor solvents, and mixture of cyclohexane and heptane, an industrially important casting environment. These studies are carried out on isolated polymers in solvents to be able to resolve the parameters that dominate the conformation of structured ionic block co-polymers; parameters that determine their micellization characteristics and essentially their assembly into membranes. The results obtained for water will be first discussed followed by those obtained for implicit poor solvents as the dielectric constants are varied and those derived for the mixture of cyclohexane and heptane. The results present direct observations of the conformation and location of all blocks and further elucidate the distribution of sulfur and the ions, critical components for any transport application. Detailed insight regarding the shape of the molecules is obtained from moment of inertia calculations and finally, the static structure factor is calculated as a potential bridge with experiments.

A. Water

A typical conformation of the pentablock in water at 300 K for four values of f. Pentablock in water collapses into

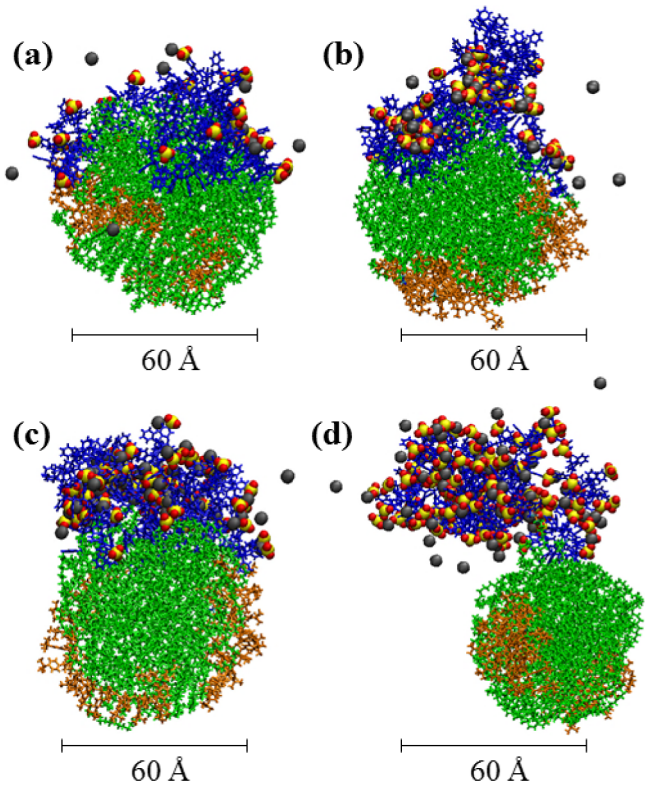

FIG. 4. Sample images of pentablock in water at 300 K (a) $f = 0.15$, (b) $f = 0.30$, (c) $f = 0.40$, and (d) $f = 0.55$.

a nearly spherical shape for $f = 0.15$ as shown in Figure 4. With increasing f, a more elliptical shape is observed, which we attribute to the balance of electrostatic repulsion between sulfonated groups and the hydrophobic attraction between the flexible blocks and the end blocks. All blocks are collapsed in water, however, the center block forms a more globular structure with more ionic groups on the outer surface with increasing f as observed in Figure 4. As f increases, the flexible and end blocks collapse into a globule in order to and essentially minimize the number of unfavorable block-solvent interactions, while electrostatic interactions force the ionic block to extend to minimize the electrostatic repulsion between charged groups. As shown in Figure 4(d), for the highest sulfonation fraction $f = 0.55$, the ionic block is completely segregated from the flexible and end blocks.

The dimension and shape of entire pentablock, center block, and sPS have been further quantified through calculations of the root mean square radius of gyration $\langle R_g^2 \rangle^{1/2}$, the three eigenvalues of the moment of inertia tensor $\lambda_1 < \lambda_2 < \lambda_3$, sphericity $A(a_1, a_2, a_3)$, and prolateness $P(a_1, a_2, a_3)$. Results are presented in Table I. $\langle R_g^2 \rangle^{1/2}$ of pentablock, the center block, and sPS all increase as f increases. These results in water are in good agreement with those of Park *et al.*[20] for sPS who reported that with increasing the degree of sulfonation, $\langle R_g^2 \rangle^{1/2}$ increases and that all the sulfonated groups are on the outer surface and the benzene rings of the styrene are in the inner surface.

As shown in Table I, the ratios of the two largest eigenvalues to the smallest (λ_2/λ_1 and λ_3/λ_1), $A(a_1, a_2, a_3)$, and $P(a_1, a_2, a_3)$ for pentablock, center block, and sPS in water all increase as f increases. Visual observations shown in Figure 4 confirm this asymmetry. At 500 K, $\langle R_g^2 \rangle^{1/2}$ for the entire pentablock, center block, and sPS is ~7% higher than at 300 K. However, the overall shape of pentablock is hardly affected by increasing the temperature.

The ion distribution, an important factor affecting the polymer properties, particularly its transport characteristics, was calculated resolving the distribution for sulfur (S) and sodium (Na) atoms for $f > 0$. The distribution as a function of the distance from the center of mass of the entire pentablock for sodium and sulfur is shown in Figure 5. In water for all $f > 0$, the sodium atoms are widely dispersed across the pentablock as is shown in Figure 5(a), while the sulfur atoms are largely distributed toward the surface of the pentablock and are segregated from other blocks, as is apparent in Figure 5(b). This distribution is consistent with the conformations of the polymer presented in Figure 4. Also, as f increases, the cluster size of the sulfonated groups increases.

The effect of electrostatic interactions on the sulfur and sodium ions was then probed comparing the distribution in water and in implicit poor solvents with $\varepsilon = 1.0$ and 77.73. Implicit solvents allow longer simulations requiring less computational resources. They also enable change in dielectric constants without changing any other parameter. The results for one sulfonation level $f = 0.15$ are shown in Figures 5(c) and 5(d) for sodium and sulfur, respectively. For low dielectric constant, $\varepsilon = 1.0$, both groups lie towards the center of the pentablock. With increasing dielectric constant to $\varepsilon = 77.73$, the dielectric constant of water, both the sulfur and the sodium migrate to the middle of the globule. In actual water, however, a clear migration of the sulfur atoms to the interface is observed. This is a clear demonstration that while the dielectric interaction impacts the distribution and association of the sulfur and the sodium, the polarity of the water is a critical driving force for the sulfur distribution.

Further insight has been obtained following the conformation of the pentablock as the temperature was raised to 700 K. The temperature dependence of $\langle R_g^2 \rangle^{1/2}$ of the entire pentablock and its center block along with that of sPS chains are presented in Figure 6 for both $\varepsilon = 1.0$ and 77.73 and water. For all f and for both $\varepsilon = 1.0$ and 77.73, $\langle R_g^2 \rangle^{1/2}$ for the entire pentablock chain increases with increasing the temperature from 300 K to 700 K as shown in Figure 6(a). Also, $\langle R_g^2 \rangle^{1/2}$ of both the center block and the sPS chain increases monotonically with temperature for all f for $\varepsilon = 77.73$ as seen in Figures 6(b) and 6(c). This system behaves similar to what one would expect for the pentablock in water where the ionic groups are on the outer surface, resulting in an increase in the size of the center block as the temperature is increased. For $\varepsilon = 1.0$, however, $\langle R_g^2 \rangle^{1/2}$ first increases as the temperature is increased to 500 K for all f. But, for $f > 0.15$, $\langle R_g^2 \rangle^{1/2}$ slightly decreases as the temperature is increased further to 700 K, whereas for $\varepsilon = 77.73$ systems, there is a slight increase in $\langle R_g^2 \rangle^{1/2}$ as f increases. Comparing $\langle R_g^2 \rangle^{1/2}$ of sPS for both $\varepsilon = 1.0$ and 77.73 with that of the center block of the pentablock, $\langle R_g^2 \rangle^{1/2}$ of center block is slightly higher than that of sPS. This is reasonable because center block is connected with others flexible blocks which do not allow the center block to completely collapse.

TABLE I. Root mean square of average radius of gyration $\langle Rg^2\rangle^{1/2}$ (Å), moments of inertia, asphericity $A(a_1, a_2, a_3)$, and prolateness $P(a_1, a_2, a_3)$ for entire pentablock, center block, and sPS chain at T = 300 K.

	Implicit poor solvent ε = 1.0				Implicit poor solvent ε = 77.73				Water				1:1 mixture of cyclohexane and heptane			
f	0	0.15	0.30	0.55	0	0.15	0.30	0.55	0	0.15	0.30	055	0	0.15	0.30	0.55
Pentablock																
$\langle Rg^2\rangle^{1/2}$	23.9 ± 0.2	24.1 ± 0.3	24.3 ± 0.4	24.65 ± 0.4	23.95 ± 0.3	24.0 ± 0.2	24.4 ± 0.3	24.8 ± 0.5	23.8 ± 0.2	24.2 ± 0.3	24.70 ± 0.3	31.0 ± 0.5	63.20 ± 0.6	65.0 ± 0.5	61.0 ± 0.4	64.30 ± 0.5
λ_2/λ_1	1.10	1.10	1.30	1.30	1.20	1.25	1.30	1.60	1.15	1.20	1.25	1.30	2.00	1.90	1.20	1.70
λ_3/λ_1	1.15	1.63	1.90	2.00	1.55	1.60	1.75	2.30	1.50	1.60	2.50	4.30	3.50	3.15	6.70	8.95
$A(a_1, a_2, a_3)$	0.00	0.006	0.015	0.02	0.005	0.003	0.008	0.015	0.003	0.004	0.02	0.075	0.30	0.09	0.10	0.15
$P(a_1, a_2, a_3)$	−0.40	0.55	0.60	0.75	−0.60	0.65	0.70	0.80	0.15	−0.80	0.85	1.00	−0.05	−0.65	1.00	0.90
Center block																
$\langle Rg^2\rangle^{1/2}$	17.5 ± 0.3	17.7 ± 0.3	17.8 ± 0.4	18.1 ± 0.4	17.4 ± 0.4	17.8 ± 0.4	17.9 ± 0.3	18.2 ± 0.5	17.5 ± 0.2	18.0 ± 0.2	18.6 ± 0.5	20.6 ± 0.5	31.40 ± 0.4	19.0 ± 0.3	18.70 ± 0.5	18.30 ± 0.3
λ_2/λ_1	1.45	1.50	1.65	1.70	1.55	1.25	1.55	1.25	1.20	1.25	1.35	1.70	2.00	1.15	1.70	1.75
λ_3/λ_1	1.90	2.55	3.70	2.15	2.10	2.20	2.30	2.35	2.40	2.45	2.60	4.50	4.50	2.10	2.50	2.40
$A(a_1, a_2, a_3)$	0.01	0.02	0.05	0.03	0.01	0.03	0.04	0.05	0.01	0.02	0.02	0.07	0.10	0.015	0.02	0.02
$P(a_1, a_2, a_3)$	−0.08	0.40	0.60	0.70	0.40	0.50	−0.60	0.90	0.60	0.70	0.70	0.80	0.90	0.80	0.60	0.15
Sulfonated PS																
$\langle Rg^2\rangle^{1/2}$	15.7 ± 0.3	16.0 ± 0.2	16.2 ± 0.4	16.7 ± 0.2	15.8 ± 0.4	16.1 ± 0.3	16.4 ± 0.5	17.3 ± 0.4	16.0 ± 0.3	16.4 ± 0.3	17.20 ± 0.4	20.5 ± 0.5	29.0 ± 0.5	21.3 ± 0.3	19.5 ± 0.4	18.5 ± 0.2
λ_2/λ_1	1.27	1.55	1.58	1.65	1.40	1.45	1.46	1.70	1.15	1.25	1.30	1.70	2.00	1.80	1.70	1.65
λ_3/λ_1	1.90	3.0	3.5	2.00	2.00	2.10	2.30	2.40	1.60	1.74	1.80	3.00	4.00	3.50	3.00	2.50
$A(a_1, a_2, a_3)$	0.008	0.01	0.02	0.02	0.009	0.02	0.02	0.04	0.01	0.01	0.05	0.07	0.09	0.07	0.05	0.04
$P(a_1, a_2, a_3)$	0.15	0.50	0.70	−0.75	−0.20	0.55	0.75	−0.80	0.50	−0.55	0.80	−0.90	0.90	0.80	0.70	−0.50

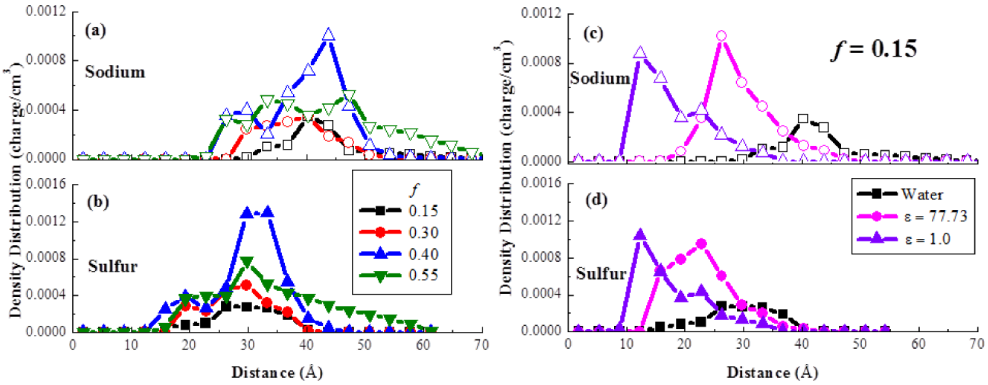

FIG. 5. Density distribution functions of sulfur and sodium as a function of the distance from center of mass of pentablock at 300 K. (a) Na and (b) S are in water at different sulfonation fractions. (c) Na and (d) S for $f = 0.15$ as a function of solvents.

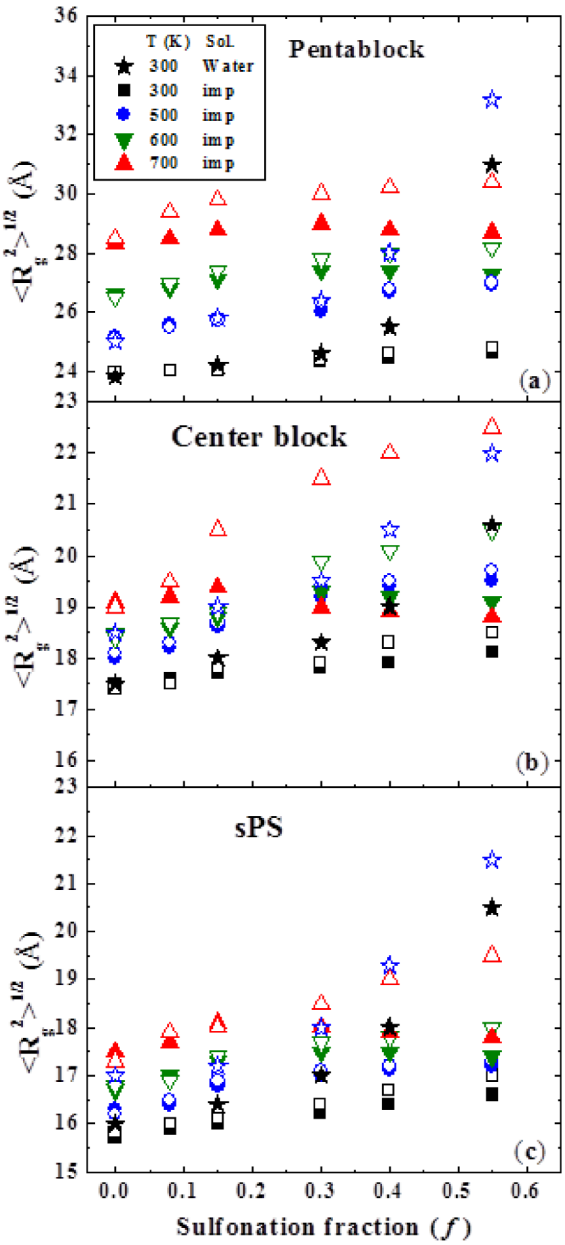

FIG. 6. Root mean square of average radius of gyration $\langle R_g^2 \rangle^{1/2}$ of (a) pentablock, (b) center block, and (c) sPS chain at 300 K (squares), 500 K (circles), 600 K (down triangles), and 700 K (up triangles) as a function of f in poor solvent with $\varepsilon = 1.0$ (solid) and $\varepsilon = 77.73$ (open). Results in water are shown as stars for 300 K (solid) and 500 K (open).

Results of simulations in an implicit poor solvent with 77.73 are compared to those in water. For $f < 0.3$, the conformation of the pentablock in the implicit poor solvent with $\varepsilon = 77.73$ is very close to that in water. However, for $f \geq 0.3$, the implicit solvent does not capture segregation of the center block from the flexible and outer blocks as it occurs for the pentablock in water (see Figure 4). As shown in Figure 6, $\langle R_g^2 \rangle^{1/2}$ for pentablock, center block, and sPS with $\varepsilon = 77.73$ is close to that found for the pentablock in water for $f < 0.3$, while for $f \geq 0.3$, $\langle R_g^2 \rangle^{1/2}$ in water is larger than in the implicit solvent.

To determine the effect of sulfonation fractions on the shape of pentablock, center block, and sPS, the eigenvalues of moment of inertia tensor were calculated together with the sphericity and prolateness given in Table I. The sphericity $A(a_1, a_2, a_3)$ for the pentablock for all values of f studied for both $\varepsilon = 1.0$ and 77.73 is close to zero with the largest value of <0.02, indicating that the collapsed pentablocks are nearly spherical in shape. A strong effect of f is observed on the prolateness $P(a_1, a_2, a_3)$ which shows that the pentablock changes from oblate for $f = 0$ to prolate for $f > 0$ in both values of ε. Since the sphericity is small for all these cases, the meaning of the prolateness should be taken with some caution. In both systems of the center block of pentablock and sPS, $\langle R_g^2 \rangle^{1/2}$ increases slightly as f increases for both $\varepsilon = 1.0$ and 77.73. These results for $\varepsilon = 1.0$ are in a good agreement with those of Xie and Weiss,[19] who found that as the sulfonation level increases, $\langle R_g^2 \rangle^{1/2}$ of the collapsed sPS increases slightly. For $\varepsilon = 77.73$, our results are in good agreement with those of Carrillo and Dobrynin[18] who reported that with increase of degree of sulfonation, sPS chains form a more open structure. Further, our results agree with their findings that sPS chains take a globule-like conformation with all f located on the outer surface and the benzene rings of the styrene forming the inner surface. The sphericity $A(a_1, a_2, a_3)$ and prolateness $P(a_1, a_2, a_3)$ of the sPS chain for both $\varepsilon = 1.0$ and 77.73 are slightly smaller than those of center block of pentablock. However, the prolateness $P(a_1, a_2, a_3)$ for both systems of center block of pentablock and sPS is increasing on increasing $\varepsilon = 1.0$–77.73.

Overall, the results of $\langle R_g^2 \rangle^{1/2}$ along with the sphericity $A(a_1, a_2, a_3)$ and the prolateness $P(a_1, a_2, a_3)$ clearly demonstrate that the shape of the pentablock in implicit poor solvent with $\varepsilon = 77.73$ is well modeled by water only for $f < 0.3$.

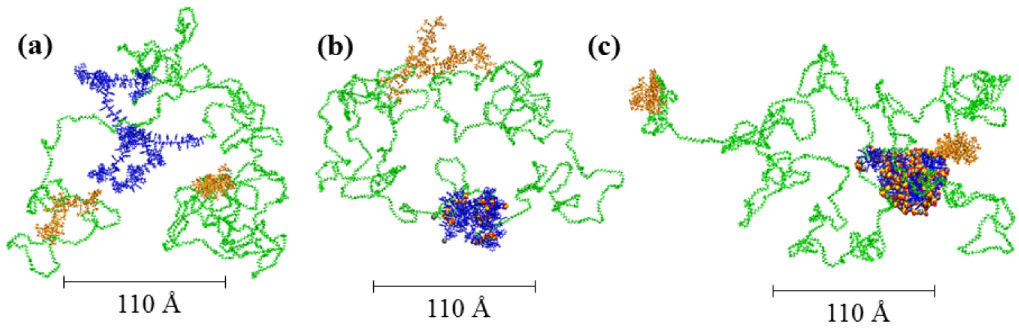

FIG. 7. Sample images of pentablock in mixture of 1:1 cyclohexane and heptane at 300 K (a) $f = 0$, (b) $f = 0.15$, and (c) $f = 0.55$.

B. Cyclohexane and heptane mixture

In the 1:1 mixture of cyclohexane and heptane, all blocks of pentablock are extended for $f = 0$ as seen in Figure 7(a). In this case, block-solvent interaction is stronger than block-block interaction. However, only the flexible and end blocks are extended, while the ionic block is collapsed for $f > 0$ as seen in Figures 7(b) and 7(c). It is important to point out that addition of very small amount of sulfonated groups ($f = 0.15$) to center blocks is large enough to segregate in the center of molecule. As seen from Table I, $\langle R_g^2 \rangle^{1/2}$ of the entire pentablock in 1:1 mixture of cyclohexane and heptane is ~63 Å for all f. $\langle R_g^2 \rangle^{1/2}$ of the entire pentablock is hardly affected by f. However, $\langle R_g^2 \rangle^{1/2}$ of the center block and sPS decreases as f increases. At 500 K, $\langle R_g^2 \rangle^{1/2}$ for the entire pentablock is ~10% higher than at 300 K. The ratios of the eigenvalues, λ_2/λ_1 and λ_3/λ_1 for entire pentablock in 1:1 mixture of cyclohexane and heptane, as shown in Table I, are much larger than those in an implicit poor solvent and in water as expected. Since the 1:1 mixture of cyclohexane and heptane is a good solvent for end blocks and flexible blocks and a poor solvent for the sulfonated center block, it is hard to define a shape for the entire pentablock from the ratios of the eivenvalues of the moment of inertia tensor for the individual blocks. For example, for $f = 0.15$, $\lambda_2/\lambda_1 = 4.5$, $\lambda_3/\lambda_1 = 15.5$, $A(a_1, a_2, a_3) = 0.35$, and $P(a_1, a_2, a_3) = 0.65$ for the end blocks, while for the flexible blocks, $\lambda_2/\lambda_1 = 3.1$, $\lambda_3/\lambda_1 = 5.8$, $A(a_1, a_2, a_3) = 0.45$, and $P(a_1, a_2, a_3) = 0.20$. The center block and sPS chain have a sphericity very close to 0 as expected. Similar results are obtained for other f. However, for $f = 0$, the sphericity is greater than zero. These results are consistent with the conformations shown in Figure 7.

These calculations have shown that the content of ions affects cluster size and distribution and hence the overall symmetry of the molecule. The ion distribution was calculated resolving the distribution for sulfur and sodium for $f > 0$. The distribution as a function of the distance from the center of mass of the pentablock for sodium and sulfur is shown in Figure 8 along with the dimensions of the core. Unexpectedly, the dimension of the ionic clusters decreases with increasing sulfonation levels. At low sulfonation levels, the ionic block is swollen, whereas increasing f results in expelling the solvent molecules from the ionic groups. In contrast to water and high dielectric media, the sodium ions are condensed on the sulfonated groups and are immobile, as observed from the similar positions of the sulfur and sodium groups.

At low sulfonation fractions, both sulfur and sodium are equally distributed within the ionic region. With increasing f, a well-defined region close to the ionic cluster surface is observed. Number of clusters increases as f decreases, while cluster size increases with higher value of $f \geq 0.3$.

C. Structure comparison

The static structure factor S(q), where q is the momentum transfer vector, was also calculated. This quantity is an ideal bridge with experimental structural studies where S(q) of the individual blocks coupled with visualization provides further insight into molecular conformation. Results for S(q) for the pentablock in water and in 1:1 mixture of cyclohexane and heptane, averaged over 500 configurations with 500 different random q vectors for each q, are shown in Figures 9(a) and 9(b), respectively. At intermediate q (0.10–0.27 $Å^{-1}$), S(q) exhibits a characteristic power law of $q^{-\alpha}$, with $\alpha = 3.3, 3.0, 2.7$, and 1.8 for $f = 0.15, 0.30, 0.40$, and 0.55, respectively, for the pentablock in water. These scaling factors diverge from 4, the characteristic value for spherical objects. These results are consistent with our previous analysis that shows that though in water, the entire polymer is collapsed and in mixture of cyclohexane and heptane, the ionic block is

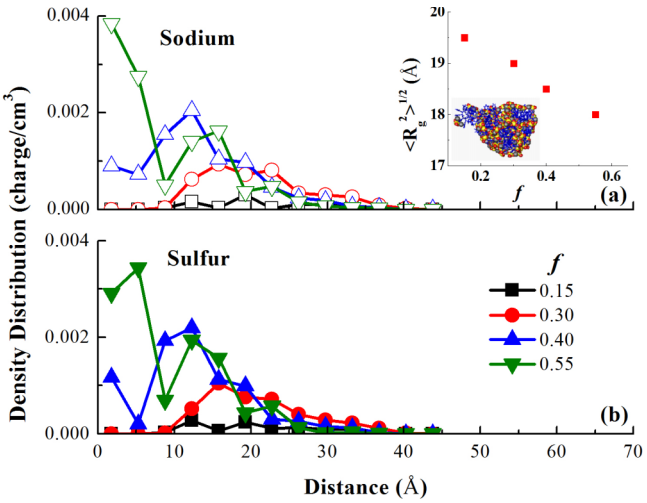

FIG. 8. Density distribution functions at 300 K for (a) sodium atoms and (b) sulfur atoms as a function of the distance from center of mass of pentablock in the mixture of cyclohexane and heptane for different sulfonation fractions. Inset shows results for $\langle R_g^2 \rangle^{1/2}$ for center block. Image is for f = 0.55.

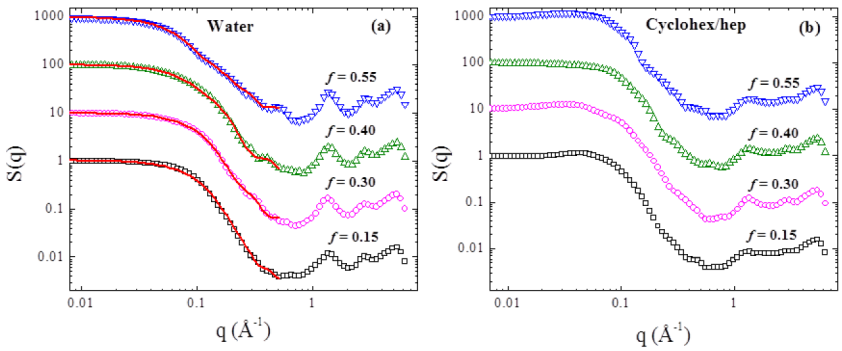

FIG. 9. S(q) of pentablock in water (a) and in mixture of 1:1 cyclohexane and heptane (b) at 300 K as a function of q for $f = 0.15$ (squares), $f = 0.30$ (circles), $f = 0.40$ (up triangles), and $f = 0.55$ (down triangles). Symbols represent the data and solid lines represent the best fit to the models described in text. Data have been shifted vertically for clarity.

collapsed into globules, the symmetry diverges from that of fully spherical objects. Further, these exponents are consistent with a collapsed, nearly spherical shape, for $f = 0.15$ and that transforms into a more ellipsoidal shape as f increases in agreement with the configurations shown in Figure 4. For $f = 0.55$, S(q) exhibits a narrow peak at q ~ 0.50 Å^{-1} (13 Å) which is signature of ionic groups residing on outer surface. The peak becomes broader as the sulfonation fraction decreases.

For intermediate q region (0.15–0.35 Å^{-1}), the exponent $\alpha = 3.0$, 2.7, 2.9, and 2.3 for $f = 0.15$, 0.30, 0.40, and 0.55, respectively, for the pentablock in the 1:1 mixture of cyclohexane and heptane. At high q region, the peaks are broader for all f which signify internal structure as shown in Figure 9(b). These results indicate that the conformations of pentablock in 1:1 mixture of cyclohexane and heptane are a Gaussian coil with little structure in the high q region and little dependence on f.

The validation of structural studies of the pentablock in the low q region is important factor in mapping our results to experiment. S(q) data for pentablock in water were fit[31] with a form factor of oblate core-shell[32] for $f = 0.15$ and prolate core-shell for $f > 0.15$. As seen in Figure 9(a), these two models capture the features of the pentablock very well. The models and parameters from fit are consistent with our results for the eigenvalues of the moment of inertia tensor as well as prolateness $P(a_1, a_2, a_3)$ as shown in Table I. These models successfully capture the characteristics of asymmetric and highly interacting blocks in water.

V. CONCLUSIONS

The conformation of a single chain of pentablock and sPS has been studied as a function of temperature, sulfonation fraction f, and solvent quality using molecular dynamic simulations. The study focused on dilute regime which enables probing the solvent effects of each of the blocks which is a significant tuning processing parameter. We find that the degree of substitution by ionizable groups is one critical parameter that together with interaction with the solvents controls the size, segment distribution, and ionic distribution of the polymer. In all solvent studies, the ionic blocks segregate from the non-ionic ones. In all poor solvents, the entire macromolecule collapses, whereas in cyclohexane and heptane mixture, only the ionizable block does. The degree of segregation is enhanced with enhancing sulfonation fraction for all solvents, where at low sulfonation levels, some mixing is observed where at high sulfonation levels, well define segregated domains are formed.

The distribution of the ionic groups strongly depends on the interactions of the different blocks with the solvents. In water and poor solvent of a dielectric constant similar to that of water, the dimensions of the entire polymer and its segments grow with increasing f where the sulfur groups tend to lie towards the surface of the polymer. In low dielectric media including poor solvent and cyclohexane and heptane mixture, the sodium is condensed, whereas increasing the dielectric constant such as in water and implicit poor with higher dielectric constants, the sodium ions are distributed across the entire ionizable block. In water, some of the ions appear fully solvated.

Future studies are on underway to explore micelles and membranes of these pentablock molecules. Having knowledge of the structure and dynamics of the individual polymer molecule in solution becomes imperative to controlling the structure of membranes, where the morphology of the micelles impacts the film structure and properties.

ACKNOWLEDGMENTS

The authors gratefully acknowledge financial support from DOE under Grant No. DE-SC007908. This research used resources at the National Energy Research Scientific Computing Center, which is supported by the Office of Science of the United States Department of Energy under Contract No. DE-AC02-05CH11231. This work was made possible by advanced computational resources deployed and maintained by Clemson Computing and Information Technology. This work was performed, in part, at the Center for Integrated Nanotechnology, a U.S. Department of Energy and Office of Basic Energy Sciences user facility. Sandia National Laboratories is a multi-program laboratory managed and operated by Sandia Corporation, a wholly owned subsidiary of Lockheed Martin Corporation, for the U.S. Department of Energy's National Nuclear Security Administration under Contract No. DE-AC04-94AL85000.

[1]D. S. Kim, M. Guiver, J. E. McGrath, B. S. Pivovar, and Y. S. Kim, ECS Trans. **33**, 711 (2010).
[2]Y. A. Elabd and M. A. Hickner, Macromolecules **44**, 1 (2011).
[3]N. P. Balsara and J. Newman, J. Chem. Educ. **4**, 446 (2013).
[4]D. T. Wong, S. A. Mullin, V. S. Battaglia, and N. P. Balsara, J. Membr. Sci. **394**, 175 (2012).
[5]A. J. Duncan, J. M. Layman, M. P. Cashion, D. J. Leo, and T. E. Long, Polym. Int. **59**, 25 (2010).
[6]A. J. Duncan, B. J. Akle, T. E. Long, and D. J. Leo, Smart Mater. Struct. **18**, 104005 (2009).

[7]R. Gao, D. Wang, J. R. Heflin, and T. E. Long, J. Mater. Chem. **22**, 13473 (2012).
[8]A. K. Shakya and K. S. Nandakumar, in *Responsive Materials and Methods*, edited by A. Tiwari and H. Kobayashi (Wiley, Hoboken, NJ, USA, 2014), p. 123.
[9]T. Yoshida, T. C. Lai, G. S. Kwon, and K. Sako, Expert Opin. Drug Delivery **10**, 1497 (2013).
[10]D. Aryal, T. Etampawala, D. Perahia, and G. S. Grest, Macromol. Theory Simul. **23**, 543 (2014).
[11]J. Choi, A. Kota, and K. I. Winey, Ind. Eng. Chem. Res. **49**, 12093 (2010).
[12]G. M. Geise, B. D. Freeman, and D. R. Paul, Polymer **51**, 5815 (2010).
[13]G. M. Geise, C. M. Doherty, A. J. Hill, B. D. Freeman, and D. R. Paul, J. Membr. Sci. **453**, 425 (2014).
[14]G. M. Geise, C. L. Willis, C. M. Doherty, A. J. Hill, T. J. Bastow, J. Ford, K. I. Winey, B. D. Freeman, and D. R. Paul, Ind. Eng. Chem. Res. **52**, 1056 (2013).
[15]Y. Fan and C. J. Cornelius, J. Mater. Sci. **48**, 1153 (2013).
[16]T. Etampawala, D. Aryal, N. Osti, L. He, W. Heller, C. Willis, G. S. Grest, and D. Perahia, "Association of a Multifunctional Ionic Block Copolymer in a Selective Solvent" (unpublished).
[17]J. Choi, C. L. Willis, and K. I. Winey, J. Membr. Sci. **428**, 516 (2013).
[18]J. Y. Carrillo and A. V. Dobrynin, J. Phys. Chem. B **114**, 9391 (2010).
[19]R. Xie and R. Weiss, Comput. Theor. Polym. Sci. **7**, 65 (1997).
[20]S. Park, X. Zhu, and A. Yethiraj, J. Phys. Chem. B **116**, 4319 (2012).
[21]A. Chialvo and J. Simonson, J. Phys. Chem. B **109**, 23031 (2005).
[22]A. Lyulin, B. Dunweg, O. Borisov, and A. Darinskii, Macromolecules **10**, 3264 (1999).
[23]W. Jorgensen, J. Madura, and C. Swenson, J. Am. Chem. Soc. **106**, 6638 (1984).
[24]W. Jorgensen, D. Maxwell, and J. Tirado-Rives, J. Am. Chem. Soc. **118**, 11225 (1996).
[25]R. W. Hockney and J. W. Eastwood, *Computer Simulation Using Particles* (Adam Hilger-IOP, Bristol, 1988).
[26]Accelrys Materials Studio©, Accelrys Software, Inc., 2001-2007.
[27]S. Plimpton, J. Comput. Phys. **117**, 1 (1995).
[28]M. Tuckerman, B. Berne, and G. Martyna, J. Chem. Phys. **97**, 1990 (1992).
[29]J. Abascal and C. Vega, J. Chem. Phys. **123**, 234505 (2005).
[30]E. J. Rawdon, J. C. Kern, M. Piatek, P. Plunkett, A. Stasiak, and K. C. Millett, Macromolecules **41**, 8281 (2008).
[31]S. R. Kline, J. Appl. Crystallogr. **39**, 895 (2006).
[32]J. Pedersen and M. Gerstenberg, Macromolecules **29**, 1363 (1996).

Cluster Morphology-Polymer Dynamics Correlations in Sulfonated Polystyrene Melts: Computational Study

Anupriya Agrawal,[1,2] Dvora Perahia,[1] and Gary S. Grest[3]
[1]Department of Chemistry, Clemson University, Clemson, South Carolina 29634, USA
[2]Department of Mechanical Engineering and Materials Science, Washington University in St. Louis, St. Louis, Missouri 63130, USA
[3]Sandia National Laboratories, Albuquerque, New Mexico 87185, USA

(Received 4 December 2015; revised manuscript received 19 February 2016; published 11 April 2016)

Reaching exceptionally long times up to 500 ns in equilibrium and nonequilibrium molecular dynamics simulations studies, we have attained a fundamental molecular understanding of the correlation of ionomer clusters structure and multiscale dynamics, providing new insight into one critical, long-standing challenge in ionic polymer physics. The cluster structure in melts of sulfonated polystyrene with Na^+ and Mg^{2+} counterions are resolved and correlated with the dynamics on multiple length and time scales extracted from measurements of the dynamic structure factor and shear rheology. We find that as the morphology of the ionic clusters changes from ladderlike for Na^+ to disordered structures for Mg^{2+}, the dynamic structure factor is affected on the length scale corresponding to the ionic clusters. Rheology studies show that the viscosity for Mg^{2+} melts is higher than for Na^+ ones for all shear rates, which is well correlated with the larger ionic clusters' size for the Mg^{2+} melts.

DOI: 10.1103/PhysRevLett.116.158001

Ionomers are in the core of many applications including ion exchange membranes, water separation, sensors, and others [1–3]. Their mechanical and viscoelastic response as well as their transport characteristics strongly depend on the number of ionizable groups on the polymer chain. These ionizable groups segregate into long-lived clusters independent of anions and cations present [2]. Examples include ionomers containing sulfonates [4,5], carbonates [6,7], or phosphonates [8,9], which all form ionic domains with various morphologies. As the ionic aggregates serve as physical cross-linkers, the morphology of these assemblies and their internal dynamics is one critical component in determining the overall properties of ionomers. While the formation of clusters in ionomers has been observed, the factors that control their shape and size remain an open question despite immense efforts. Being able to probe computationally long times commensurate with the actual segmental dynamics time scales in ionomers, now possible with new computational tools, this study provides a new fundamental insight into the factors that impact the dynamics of ionic polymers.

The size and shape of the ionic cluster result from a balance between electrostatic interactions, size of the ionic groups, and counterions as well as the behavior of the polymeric chains that is determined by the dielectric constant of the environment [10]. The counterion is one important entity that is not only responsible for electrical neutrality but also impacts the cluster formation and their size in ionic polymers [11]. Using equilibrium and nonequilibrium molecular dynamics (MD) simulations, we obtained a molecular level insight into the effects of the counterions on the size and shape of the ionic clusters in one model polymer, polystyrene sulfonate (PSS), and directly correlated these characteristics with dynamics of the polymers for the first time on multiple length scales through measuring the dynamic structure factor $S(q, t)$ and the macroscopic shear rheology of the melts.

Specifically we have investigated melts of PSS fully neutralized with two counterions Na^+ and Mg^{2+} (PSS/Na^+ and PSS/Mg^{2+}), correlating cluster morphology with multiscale dynamics. This polymer has been extensively studied, offering a wealth of knowledge to compare with and validate the choice of the force fields. We show a direct correlation between the polymer dynamics as the morphology of the ionic clusters changes from ladderlike with extended ribbons that consist of SO_3^- and Na^+ pairs for PSS/Na^+ melts to elongated, disordered structures for PSS/Mg^{2+}.

The significance of ionic clusters for both transport and stability of ionomers has led to numerous studies of the size and shape of clusters and their impact on rheology of the polymers. While a variety of different clusters were observed, one universal conclusion has been that the ionic groups impede the dynamics of the polymers. However, there is hardly any explanation for the dramatic effects on mobility induced by a small fraction of ionizable groups. Kirkmeyer *et al.* [12], for example, showed that the cluster morphology changes from spherical to vesicular with the change in neutralization levels of PSS. Zhou *et al.* [5] reported that the size of the ionic aggregates increased with increasing cation radius independent of the cation valency; however, the cation concentrations of the ionic aggregates are higher for monovalent cations than for divalent cations. In contrast, Castagna *et al.* [13] found that ionic aggregate

size is independent of sulfonation fraction, degree of neutralization, and ionic radius of cations. They observed one broad segmental relaxation process for monovalent cations and two distinct segmental relaxation processes for divalent cations, in Na^+, Cs^+, and Zn^{2+} neutralized PSS melts. The impact on dynamics is slightly less explored where Weiss and Zhao [14] reported that increasing sulfonation and decreasing cation size of monovalent alkali metal cations result in higher melt viscosity in PSS melts. Ling *et al.* [15] have shown that the rheology and response to elongation flow of PSS are similar to that of highly entangled polymers. Further, Qiao and Weiss [16] have shown that nonlinear rheological behavior of PSS melts significantly differed from entangled polystyrene melts. These comprehensive experimental studies have clearly demonstrated that the cations impact the size and shape of the clusters and often the mobility of the polymers.

Further insight was obtained from MD simulations for a variety of ionomer melts [10,17,18] and aqueous polyelectrolyte solutions [19,20]. Using a coarse-grained polymer model Hall *et al.* [21] have shown that polymer architecture impacts the fluidity of the ionic aggregates. Melt studies using atomistic simulation by Bolintineanu *et al.* [17] revealed that in ionomers with precisely spaced ionizable groups, for Na^+, Li^+, Zn^{2+}, and Cs^{2+} counterions, aggregate with morphologies ranging from small spherical clusters and stringlike chains to large percolating network exists. Buitrago *et al.* [18] have shown that the calculated structure factors of these ionomer melts are in agreement with x-ray studies, further validating the complex structures of the ionic clusters and the ability to probe these types of polymers by MD studies. Both experimental and simulation studies have demonstrated that electrostatic interactions impact cluster morphology in a wide range of ionomers. Using atomistic MD simulations, Agrawal *et al.* have shown that morphological transformation from ladderlike clusters to globular assemblies in PSS/Na^+ melts can be induced by increasing the dielectric constant of the media. They have clearly demonstrated that the decrease in electrostatic interaction impacts the cluster morphology, and in turn enhances significantly the mobility of the ionomers [10]. These studies pointed to correlations of cluster morphology and viscoelastic behavior, though the direct effects on the ionomers' dynamics remains unresolved. Here, using all-atom MD simulations of PSS melt with Na^+ or Mg^{2+} counterions, we probed cluster morphology and their impact on segmental dynamics and viscosity on multiple length scales.

Sulfonated polystyrene is modeled using the All Atom Optimized Potential for Liquid Simulations (OPLS-AA) force field by Jorgensen *et al.* [22,23]. Additional parameters for sulfonate SO_3^- group are given in Refs. [24–26]. The nonbonded interaction is a sum of standard 12-6 Lennard-Jones (LJ) and electrostatic potentials. Nonbonded interactions are calculated between all atom pairs of different molecules. In addition, all pairs on the same molecule separated by three or more bonds are included in nonbonded interactions, though the interaction is reduced by a factor of 1/2 for atoms separated by three bonds. The attractive (r^{-6}) dispersion term in the LJ interaction as well as the electrostatic interactions were calculated using the particle-particle particle-mesh (PPPM) algorithm [27]. As a result, the LJ interaction becomes a fully long-range potential. Interactions closer than 1.2 nm are calculated in real space; those outside this range are calculated in reciprocal Fourier space with precision of 10^{-4}. The repulsive (r^{-12}) LJ interaction was truncated at 1.2 nm. The simulations were performed using the Large Atomic Molecular Massive Parallel Simulator (LAMMPS) molecular dynamics code [28]. The Newton equations of motion were integrated using a velocity-Verlet algorithm with each atom coupled weakly to a Langevin thermostat with a damping constant of 100 fs to maintain a constant temperature. The reference system propagator algorithm (RESPA) with multi-time-scale integrator [29,30] was used to accelerate the simulation. A time step of 1.0 fs for the bond, angle, dihedral, van der Waals interactions, and direct interactions part of the electrostatic interactions and a time step 4.0 fs for long-range electrostatic interactions were used in all of the simulations.

All of the results presented here are for randomly sulfonated atactic polystyrene chains of 80 monomers (8320 g/mol) with sulfonation levels 0%, 5%, and 10% with either Na^+ or Mg^{2+} counterions. The 0%, 5%, and 10% systems contained 160, 312, and 320 chains, respectively. Periodic boundary conditions were used in all simulations. These systems were first equilibrated at 600 K at constant pressure of 1 atm using the Nosé-Hoover thermostat and barostat. The resulting densities of the melts at 1 atm at 600 K are 0.903 and 0.95 g/cm^3 for sulfonation 5% and 10%, respectively, for PSS/Na^+ and 0.898 g/cm^3 for 5% sulfonation PSS/Mg^{2+}, compared to 0.84 g/cm^3 at 600 K and 0.905 g/cm^3 at 500 K for the neat polystyrene (PS). Each of these systems then was run at constant volume for 300–500 ns. To measure the viscosity, we integrated the SLLOD (which adopts the transpose of the qp-DOLLS tensor) equations of motion [31,32] at strain rates of $\dot{\gamma} = 10^7$ to 10^{10}/s with a damping constant of 1 ps. The shear viscosity is calculated using $\eta = -\langle P_{xz}\rangle/\dot{\gamma}$, where $\langle P_{xz}\rangle$ is the xz component of the pressure tensor along the flow and gradient directions, respectively. In LAMMPS, the PPPM algorithm has been implemented for nonrectangular simulation cells only for the Coulomb interactions; therefore, the LJ potential was truncated at 1.2 nm for the shear simulations.

As previously discussed, ionic clusters are formed in PSS melts with both Na^+ and Mg^{2+} [1,2,5]. The ionic clusters, and their size distributions are depicted in Fig. 1 for 5% sulfonation level. We have defined a cluster by SO_3^- groups that are within 6 Å of each other. For 5% and 10% sulfonation, all of the clusters are finite in size and do not percolate across the sample. A close look at the cluster

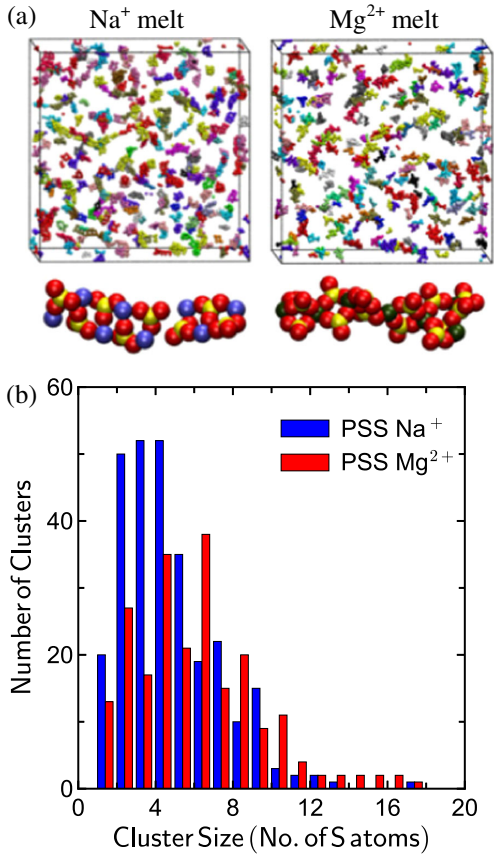

FIG. 1. (a) Representative clusters and (b) cluster distribution for 5% sulfonated polystyrene melts with Na^+ and Mg^{2+} counterions. PS chains in (a) are not shown for clarity. S (yellow), O (red), Na^+ (blue), and Mg^{2+} (green).

morphology of both melts in Fig. 1(a) show that in PSS/Na^+ melts many of the clusters are highly ordered, with ladderlike structure, whereas in PSS/Mg^{2+} while the clusters are elongated, they are more disordered. The cluster size distributions for both melts are presented in Fig. 1(b) are both very broad. The average cluster size in PSS/Na^+ melts is 4.1 sulfonation groups with cluster size that varies from 1 to 17 sulfonated groups, where the majority of clusters consist of 2 to 5 SO_3^- groups. The cluster distribution in the PSS/Mg^{2+} melts exhibits a similar size distribution with an average cluster size of 5.2 SO_3^- groups. The charge-neutral clusters with an even number of SO_3^- groups are dominant and positively and negatively charged clusters with an odd number SO_3^- groups appear to be less favored. The clusters in PSS/Mg^{2+} melts are more disordered and varied in morphology. Each Mg^{2+} ion is shared by 4 or more SO_3^- groups whereas in PSS/Na^+ melts, the counterion is shared by 2–3 SO_3^- groups. This new molecular insight distinguishes ordered and disordered clusters arising from the packing of ions with different charges.

Further insight into the clusters' structure was obtained from the static structure factor $S(q)$ for both melts. Ionic

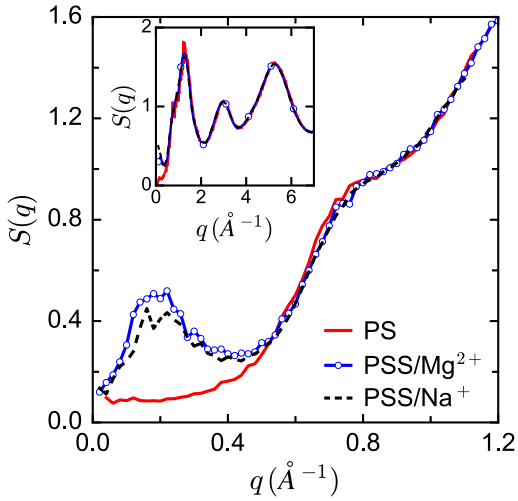

FIG. 2. $S(q)$ vs q for polystyrene and 5% sulfonated polystyrene with Na^+ and Mg^{2+} counterions. Inset shows the $S(q)$ for the full q range.

clustering was initially detected by scattering experiments and microscopy techniques [5,12–14,33,34]. $S(q)$ calculated from MD simulations were found to be in close agreement with the experimental ones [18]. The static structure factor is given by $S(q) = |\sum_i b_i e^{iq_i r_i}|^2 / \sum_i b_i^2$, where b_i, q_i, and r_i are the scattering length, momentum transfer vector, and position vector of atom i, respectively [35]. The results for polystyrene and for the two PSS melts are presented in Fig. 2. The patterns at high q values are identical for all polymers and the features correspond to intramolecular distances as shown in the inset. The ionic clusters signature is expressed as a broad peak centered around $q = 0.2$ Å^{-1}, presented in the main panel, which corresponds to an average cluster distance of ~30 Å. The $S(q)$ for polystyrene does not exhibit any features at the low q range as expected for a polymer without any ionic groups. These patterns are similar to those measured experimentally by Zhou *et al.* [5] for both PSS/Na^+ and PSS/Mg^{2+}. They observed a broad peak centered ~0.15 Å^{-1} for a similar range of sulfonation fractions at room temperature. The simulations point to smaller dimensions than the experimental data. The difference is attributed to slightly better packing of the chains obtained in atomistic simulation as a result of higher temperatures. Further, in contrast to the experiments where PSS absorbs water at ambient conditions, the simulation melts are water free. The signature of the ionic domains provides one important length scale associated with the confinement of the motion of the PSS molecules.

The dynamics of PSS was explored by calculating $S(q,t)$ [36,37]. Similar to Weiss and co-workers [14,16], who demonstrated that a small fraction of ionizable groups on polystyrene below its entanglement length results in constrained dynamics, our recent MD studies [10] have shown that the diffusion constant decreases from 1.7×10^{-8} cm^2/s

for 0 to 4.0×10^{-9} cm^2/s for 5% and 6.2×10^{-10} cm^2/s for 10% sulfonation in PSS/Na^+ melts. Here we first studied the center of mass diffusion for both melts; however, we did not detect any differences within the times we were able to access. We then probed segmental motion following the dynamic structure factor at different length scales. $S(q,t)$ for PSS melts with Na^+ and Mg^{2+} as counterions for different q values are shown in Fig. 3. On the length scales of the ionic domains reflected in $S(q)$ for PSS, i.e., q in the range of 0.1–0.5 Å^{-1}, the overall relaxation time surprisingly does not decrease monotonically with decreasing q as expected of diffusion of nonionic polymers in melts. Instead, $S(q,t)$ decays the slowest for $q = 0.2$ Å^{-1}, which corresponds to the ionic cluster signature in $S(q)$. This slow relaxation for $q \sim 0.2$ Å^{-1} is a result of quenching of the local motion on the length scale of the ionic clusters.

$S(q,t)$ differs in its decay from a single exponential that characterizes simple diffusion. It was analyzed in terms of a sum of two exponentials $S(q,t) = A_1 e^{-\Gamma_1 t} + A_2 e^{-\Gamma_2 t}$, where A_1 and A_2 are constants and Γ_1 and Γ_2 are effective diffusion coefficients (by definition $\Gamma_1 < \Gamma_2$). The fits are shown in Fig. 3 for Na^+ and Mg^{2+} PSS melts and their respective effective diffusion coefficients are shown in the inset. The slowest relaxation times $\sim 1/\Gamma_1$ decrease monotonically with increasing q. This q dependence shows that the slower decay in q around the low q peak in $S(q)$ is thus not due to a decrease in the long time effective diffusion constant (Γ_1) but is a consequence of reduction in the amplitude A_2 of the fast component (Γ_2) for $q \sim 0.2$ Å^{-1}. This is consistent with the ionic clusters acting as physical cross-linkers and inhibiting relaxation of the chains locally. Comparing the effective diffusion for PSS melts of both counterions shows that the slow component of the diffusion is similar for both melts; however, the faster component Γ_2 is larger for the Mg^{2+} melts than for the Na^+ ones. These differences could be attributed to disruption of packing of the chains around the magnesium clusters, which are more disordered, resulting in slightly less confined PS chains. These measurements of $S(q,t)$, coupling time, and length scales have provided a direct observation of the impact of clustering on dynamics that has been long postulated by rationalizing numerous experimental results.

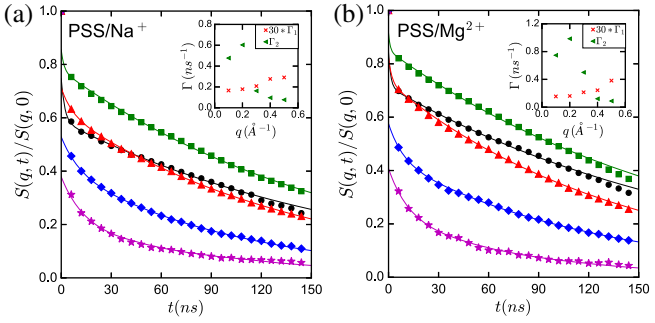

FIG. 3. $S(q,t)/S(q,0)$ vs time for various q values (symbols) and double exponential fit (solid line) to the data and gamma value with q in the inset for 5% sulfonated polystyrene with (a) Na^+ and (b) Mg^{2+} counterions. $S(q,t)/S(q,0)$ is plotted for q values of 0.1, 0.2, 0.3, 0.4, and 0.5 Å^{-1} represented by (circle, square, triangle, diamond and star), respectively.

To probe the macroscopic dynamics we measured the stress and calculated the shear viscosity of the sulfonated melts at 600 K as a function of strain rates. While for PS melt at both 500 and 600 K the viscosity has reached the shear rate independent plateau, the 5% and 10% PSS melts remain in the shear thinning regime for the computationally accessible lowest shear rate of 10^7/s. Over the entire range of shear rates studied, the shear viscosity of the 5% Mg^{2+} PSS melt is higher than that of the Na^+ PSS one, as demonstrated in the inset of Fig. 4. At the lowest shear rate accessible (10^7/s) the Na^+ PSS melt is beginning to cross over to the shear-rate-independent regime while PSS/Mg^{2+} melt is still in the shear-thinning regime.

The average radius of gyration of chains as a function of shear rate is shown in Fig. 5(a) for 5% sulfonation. For comparison, the mean squared radius of gyration is $\langle R_g^2 \rangle^{1/2} = 18.5$ Å for PSS/Na^+ and 19.0 Å for PSS/Mg^{2+}. As the melt is sheared, chains extend in the shear direction resulting in some clusters breaking up and forming new clusters. While the average cluster size increases with decreasing shear rates for both Mg^{2+} and Na^+, as shown in Fig. 5(b), the average cluster size is always larger for Mg^{2+}. This increase in the size of the long-lived ionic clusters for Mg^{2+} compared to Na^+ is consistent with the difference in the shear viscosity for the melts of the two counterions. The effect of shear strain on the ionic clusters is illustrated in Fig. 6, where t = 0 is the time when the shear is applied. With increasing strain, the chains opened up as evident from the increase in radius of gyration.

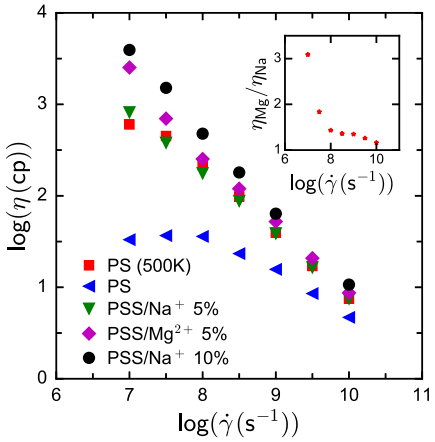

FIG. 4. Shear viscosity as a function of shear strain rate at 600 K for the indicated systems. The inset corresponds to the ratio of viscosities of PSS melts with Mg^{2+} and Na^+ counterions as a function of strain rate.

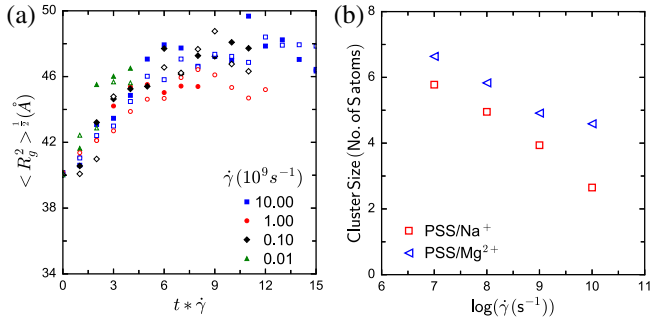

FIG. 5. (a) Radius of gyration as a function of shear cycles at indicated shear rates for 5% sulfonated polystyrene with Na^+ (open symbols) or Mg^{2+} (filled symbols) counterions. (b) Average cluster size with the shear rate.

With the chain opening up, clusters could break, grow, or rearrange depending on how ionic groups are distributed on the chain. A representative of a cluster rearranging in PSS/Na^+ melt is shown in Fig. 6(a). Here, a distorted cluster transforms into a ladderlike cluster with shear resulting in increase in the number of ordered ladderlike clusters in the melt. The cluster itself didn't break up due to the opening of the chains because the random ionic groups on different chains are involved. Because of the random distribution of the sulfonate groups on the polystyrene chain and given the small sulfonation fraction, there can be chains where sulfonate groups are distributed relatively evenly. When such chains stretch, ionic clusters may break up followed by rearrangements afterwards. A representative of this type of rearrangement is shown in Fig. 6(b) for PSS/Mg^{2+} melt, where there are three ionic clusters at the start of shearing which break and rearrange to give one large ionic cluster and a couple of smaller ionic groups as the aftermath of chain opening.

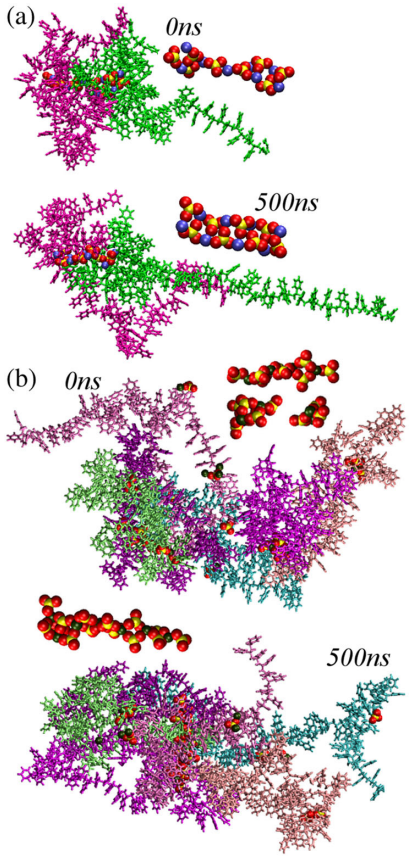

FIG. 6. Representative ionic cluster and chains with time at shear rate of 10^7 s^{-1} for 5% randomly sulfonated polystyrene with (a) Na^+ and (b) Mg^{2+} counterions.

In summary, accessing long simulation times, this study provides a fundamental molecular understanding that underlines the dynamics in ionic polymers. The structure, cluster size, and morphology of PSS melts with Na^+ and Mg^{2+} counterions were determined and correlated with chain dynamics, attained through measurements of $S(q,t)$ and shear viscosity, spanning multi time and length scales of motion. We find that PSS/Na^+ melts consist of well-defined ladderlike clusters and in PSS/Mg^{2+} more disorder clusters are formed. Although changing the counterion from Na^+ to Mg^{2+} did not have significant effect on the center of mass dynamics, on the time scales we were able to access, $S(q,t)$ revealed for the first time the correlation between the dimensions of the ionic clusters and the dynamics of the chains surrounding them. Upon applying of steady state shear, the viscosity of PSS/Mg^{2+} melt is much higher than that of PSS/Na^+ melt, which correlates directly with the larger cluster size of the Mg^{2+} melts. Overall, these observations through computational studies provided a new fundamental direct molecular insight into a long-lasting challenge in ionomers with an immense technological impact.

We gratefully acknowledge financial support from DOE Grant No. DE-SC007908 at Clemson University. We acknowledge computational resources at the National Energy Research Scientific Computing Center, which is supported by the Office of Science of the U.S. Department of Energy, under Contract No. DE-AC02-05CH11231 and Clemson Computing and Information Technology. This work was performed, in part, at the Center for Integrated Nanotechnologies, a U.S. Department of Energy and Office of Basic Energy Sciences user facility. Sandia National Laboratories is a multiprogram laboratory managed and operated by Sandia Corporation, a wholly owned subsidiary of Lockheed Martin Corporation, for the U.S. Department of Energy's National Nuclear Security Administration under Contract No. DE-AC04-94AL85000.

[1] A. Eisenberg and J.-S. Kim, *Introduction to Ionomers* (Wiley, New York, 1998).
[2] B. P. Grady, Polym. Eng. Sci. **48**, 1029 (2008).
[3] L. Zhang, N. R. Brostowitz, K. A. Cavicchi, and R. A. Weiss, Macromol. React. Eng. **8**, 81 (2014).

[4] D. G. Peiffer, R. A. Weiss, and R. D. Lundberg, J. Polym. Sci., Part B: Polym. Phys. **20**, 1503 (1982).
[5] N. C. Zhou, D. C. Chan, and K. I. Winey, Macromolecules **41**, 6134 (2008).
[6] B. Hird and A. Eisenberg, J. Polym. Sci., Part B: Polym. Phys. **28**, 1665 (1990).
[7] S. H. Kim and J. S. Kim, Macromolecules **36**, 2382 (2003).
[8] Q. Wu and R. A. Weiss, J. Polym. Sci., Part B: Polym. Phys. **42**, 3628 (2004).
[9] Q. Wu and R. A. Weiss, Polymer **48**, 7558 (2007).
[10] A. Agrawal, D. Perahia, and G. S. Grest, Phys. Rev. E **92**, 022601 (2015).
[11] B. Dreyfus, Macromolecules **18**, 284 (1985).
[12] B. P. Kirkmeyer, R. A. Weiss, and K. I. Winey, J. Polym. Sci., Part B: Polym. Phys. **39**, 477 (2001).
[13] A. M. Castagna, W. Wang, K. I. Winey, and J. Runt, Macromolecules **44**, 5420 (2011).
[14] R. A. Weiss and H. Zhao, J. Rheol. **53**, 191 (2009).
[15] G. H. Ling, Y. Wang, and R. A. Weiss, Macromolecules **45**, 481 (2012).
[16] X. Qiao and R. A. Weiss, Macromolecules **46**, 2417 (2013).
[17] D. S. Bolintineanu, M. J. Stevens, and A. L. Frischknecht, Macromolecules **46**, 5381 (2013).
[18] C. F. Buitrago, D. S. Bolintineanu, M. E. Seitz, K. L. Opper, K. B. Wagener, M. J. Stevens, A. L. Frischknecht, and K. I. Winey, Macromolecules **48**, 1210 (2015).
[19] J.-M. Y. Carrillo and A. V. Dobrynin, J. Phys. Chem. B **114**, 9391 (2010).
[20] S. Park, X. Zhu, and A. Yethiraj, J. Phys. Chem. B **116**, 4319 (2012).
[21] L. M. Hall, M. J. Stevens, and A. L. Frischknecht, Phys. Rev. Lett. **106**, 127801 (2011).
[22] W. L. Jorgensen, J. D. Madura, and C. J. Swenson, J. Am. Chem. Soc. **106**, 6638 (1984).
[23] W. L. Jorgensen, D. S. Maxwell, and J. Tirado-Rives, J. Am. Chem. Soc. **118**, 11225 (1996).
[24] X. He, O. Guvench, A. D. J. Mackerell, and M. L. Klein, J. Phys. Chem. B **114**, 9787 (2010).
[25] W. R. Cannon, B. M. Pettitt, and A. A. McCammon, J. Phys. Chem. **98**, 6225 (1994).
[26] J. Chandrasekhar, D. C. Spellmeyer, and W. L. Jorgensen, J. Am. Chem. Soc. **106**, 903 (1984).
[27] R. E. Isele-Holder, W. Mitchell, and A. E. Ismail, J. Chem. Phys. **137**, 174107 (2012).
[28] S. J. Plimpton, Comparative physiology **117**, 1 (1995).
[29] D. Evans and G. P. Morris, Comput. Phys. Rep. **1**, 297 (1984).
[30] J. W. Rudisill and P. T. Cummings, Rheol. Acta **30**, 33 (1991).
[31] D. J. Evans and G. P. Morriss, *Statistical Mechanics of Nonequilibrium Liquids* (Academic, New York 1990).
[32] M. E. Tuckerman, C. J. Mundy, S. Balasubramanian, and M. L. Klein, J. Chem. Phys. **106**, 5615 (1997).
[33] Y. S. Ding, S. R. Hubbard, K. O. Hodgson, R. A. Register, and S. L. Cooper, Macromolecules **21**, 1698 (1988).
[34] D. J. Yarusso and S. L. Cooper, Macromolecules **16**, 1871 (1983).
[35] C. M. Sorensen, Aerosol Sci. Technol. **35**, 648 (2001).
[36] B. Nystrom, J. Roots, J. S. Higgins, D. G. Peiffer, F. Mezei, and B. Sarkissian, J. Polym. Sci., Part C: Polym. Lett. **24**, 273 (1986).
[37] T. Kanaya, K. Kaji, R. Kitamaru, J. S. Higgins, and B. Farago, Macromolecules **22**, 1356 (1989).

Resolving Dynamic Properties of Polymers through Coarse-Grained Computational Studies

K. Michael Salerno,[1] Anupriya Agrawal,[2,3] Dvora Perahia,[3] and Gary S. Grest[1]
[1]Sandia National Laboratories, Albuquerque, New Mexico 87185, USA
[2]Department of Mechanical Engineering and Materials Science, Washington University, St. Louis, Missouri 63130, USA
[3]Department of Chemistry, Clemson University, Clemson, South Carolina 29634, USA
(Received 16 October 2015; published 5 February 2016)

Coupled length and time scales determine the dynamic behavior of polymers and underlie their unique viscoelastic properties. To resolve the long-time dynamics it is imperative to determine which time and length scales must be correctly modeled. Here we probe the degree of coarse graining required to simultaneously retain significant atomistic details and access large length and time scales. The degree of coarse graining in turn sets the minimum length scale instrumental in defining polymer properties and dynamics. Using linear polyethylene as a model system, we probe how the coarse-graining scale affects the measured dynamics. Iterative Boltzmann inversion is used to derive coarse-grained potentials with 2–6 methylene groups per coarse-grained bead from a fully atomistic melt simulation. We show that atomistic detail is critical to capturing large-scale dynamics. Using these models we simulate polyethylene melts for times over 500 μs to study the viscoelastic properties of well-entangled polymer melts.

DOI: 10.1103/PhysRevLett.116.058302

Polymer properties depend on a wide range of coupled length and time scales, with unique viscoelastic properties stemming from interactions at the atomistic level. The need to probe polymers across time and length scales to capture polymer behavior makes probing dynamics, and particularly computational modeling, inherently challenging. With increasing molecular weight, polymer melts become highly entangled and the long-time diffusive regime becomes computationally inaccessible using atomistic simulations. In these systems the diffusive time scale increases with polymerization number N faster than N^3, becoming greater than 10^{10} times larger than the shortest time scales even for modest molecular weight polymers. While it is clear that the largest length scales of polymer dynamics are controlled by entanglements, the shortest time and length scales required to resolve dynamic properties are not obvious. This knowledge is critical for developing models that can transpose atomistic details into the long time scales needed to model long, entangled polymer chains.

One path to overcoming this computational challenge is to coarse grain the polymer, reducing the number of degrees of freedom and increasing the fundamental time scale. The effectiveness of this process depends on retaining the smallest length scale essential to capturing the polymer dynamics. The process of coarse graining amounts to combining groups of atoms into pseudoatom beads and determining the bead interaction potentials [1,2]. Simple models like the bead-spring model [3] capture characteristics described by scaling theories, but disregard atomistic details and cannot quantitatively describe properties like structure, local dynamics, or densities. Immense efforts have been made to systematically coarse grain polymers and bridge the gap of time and length scales while retaining atomistic characteristics [4]. One critical issue underlying the coarse-graining process is the degree to which a polymer can be coarse grained while still appropriately capturing polymer properties and dynamics [5]. The current study probes the effects of the degree of coarse graining of polymers on their dynamic and static properties.

With the vast efforts to coarse grain polymers, many models have emerged with differences in the number of atoms combined in each bead and the procedure for determining the interaction potentials. One of the most common coarse-grained (CG) models for polymers is the united atom (UA) model, which combines each CH_n group into a pseudoatom. The UA interaction parameters are determined phenomenologically to reproduce physical properties such as densities and critical temperatures [6–9]. Another model commonly used is the MARTINI model, which utilizes the same approach, matching bulk densities and compressibilities of short alkane chains at a larger scale of four CH_2 groups per CG bead [10]. More advanced methods such as force matching, iterative Boltzmann inversion, and optimized relative entropy [11–13] have recently been developed to incorporate atomistic detail into the CG model. With these methods there is an open question as to the number of atoms to represent by a single bead and the effect of this coarse-graining scale on the measured properties of the system. One critical physics question remains unresolved: namely, defining the shortest length scale in a polymer that is fundamental to the macroscopic dynamics and properties [1,3,4,6–13]. Here, this issue is addressed through the development of CG models with increasing degree of

coarse graining using iterative Boltzmann inversion. By examining how well these CG models describe both the static and dynamic properties of a polymer melt, using polyethylene (PE) as a model system, we probe this outstanding question. The backbone of PE consists of -CH_2- methylene groups that provide a natural unit or scale for coarse graining. Though the chemical structure of PE is simple, it is a thermoplastic material useful in a large number of applications, with tunable mechanical properties determined by the degree of branching.

Polyethylene chains have previously been studied using CG models with beads of $\lambda = 3 - 48$ methylene groups per bead [14–19]. These studies were able to capture the radius of gyration as a function of molecular weight and the pair correlation function between CG beads. As most of these studies used a large degree of coarse graining ($\lambda \sim 20$) to study dynamical properties, an extra constraint was needed to prevent chains cutting through each other [20]. With this extra constraint, the mean squared displacement (MSD), stress autocorrelation function, and shear viscosity of linear and branched PE [20–22] have been studied for long, entangled chains. However, these studies did not account for or study the effects of the coarse-graining degree λ on dynamic properties.

Here, for the first time, we elucidate the effect of coarse-graining degree on the ability to capture both the structure and dynamics of PE. We are able to capture polymer chain dynamics for lengths up to $C_{1920}H_{3842}$ and time scales of 400 μs using models that accurately represent atomistic detail. Accessing large length and time scales allows us to measure quantities like the plateau modulus which depend on a hierarchy of length and time scales.

Coarse-grained beads shown in Fig. 1 represent λ methylene groups. We study $\lambda = 2$, 3, 4, and 6 and refer to these models as CGλ. We find that for surprisingly small λ the chains cross and diffuse rapidly, indicating that CG features directly link to macroscopic polymer motion. With this result, we further probed the CG6 model polymer including noncrossing constraints, and comparing with models with unconstrained dynamics.

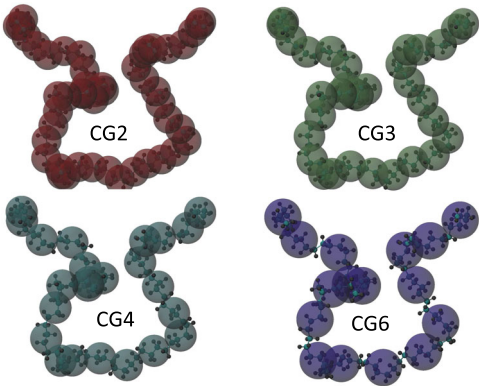

FIG. 1. A single $C_{96}H_{194}$ PE chain represented with increasing degree of coarse graining $\lambda = 2$, 3, 4, and 6 methylene groups per CG bead. Bead diameter corresponds to the minimum in the nonbonded interaction for each CG model.

The tabulated CG PE potentials were derived from a single fully atomistic simulation of a melt of $C_{96}H_{194}$ PE chains at 500 K. The simulation details are given in the Supplemental Material [23]. The study was then generalized to melts of C_nH_{2n+2} with $n = 96$, 480 for the fully atomistic model, and $n = 96$, 480, 960, and 1920 at 500 K using the CG models. Atomistic simulations used a version of the Optimized Potentials for Liquid Simulations (OPLS) potential with modified dihedral coefficients that better reproduce the properties of long alkanes [27]. With this modified potential the mean squared radius of gyration $\langle R_g^2 \rangle$ and end to end distance $\langle R^2 \rangle$ match experimental values [28,29] better than with original OPLS parameters [30]. For the CGλ models, $\langle R^2 \rangle$ for $n = 96$ chains is within 20% of the atomistic value, while $\langle R^2 \rangle$ for the MARTINI model is 50% too high. Static properties for different chain lengths are reported in the Supplemental Material [23].

Tabulated CG angle and bond potentials were determined by Boltzmann inversion of the atomistic bond and angle distributions in Fig. S1. Torsion terms were omitted in all CG models, which may account for the shorter end-to-end distances listed in Table SI for the CG2 model. Tabulated nonbonded potentials were determined by iterative Boltzmann inversion [4]. The intermolecular radial distribution function $g(r)$ from the atomistic simulation, shown in Fig. S2, was used as the target for iteration of the nonbonded potentials shown in Fig. 2. Also shown are 6–12 Lennard-Jones pair potentials for the united atom (UA) model of Paul *et al.* [6], and the MARTINI (CG4-M) model [10]. The MARTINI parameter ϵ was reduced from 0.8365 kcal/mol to 0.803 kcal/mol to match the density $\rho = 0.72$ g/cm^3 of atomistic simulations for $n = 96$ chains. For each CG model a pressure correction is applied to match the density $\rho = 0.72$ g/cm^3 for $n = 96$. The similarity in length and energy scales between the CG4 and CG4-M models is evident in Fig. 2. For each CGλ model all beads have identical interactions; however, end beads have an extra hydrogen atom mass.

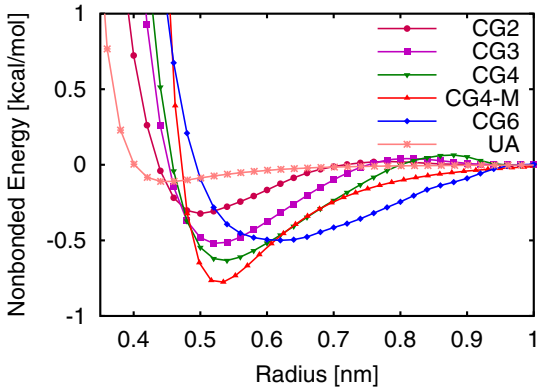

FIG. 2. Tabulated pair potential between CG beads. The UA and CG4-*M* potentials are included for comparison.

The CG6 model has a surprisingly large equilibrium bond distance relative to the bead diameter. Therefore, a modified soft segmental repulsive potential [31] was added between CG beads to inhibit chain crossing. We used a segmental bead diameter of 0.5 nm. This scheme increases the pressure in our samples by about 80 atm at fixed density compared to simulations with no constraint. We do not rederive the potential including the soft segmental bead; however, Fig. S3 in [23] shows that the noncrossing bead induces only small changes in $g(r)$ relative to a model with no constraint. By eliminating the finest degrees of freedom, CG models allow a significantly larger time step than atomistic models. We use a time step $\delta t = 20$ fs for the CG6, CG4, and CG4-M models, 10 fs for the CG3 model, and 2 fs for the CG2 model, compared to 1 fs for the atomistic model.

Coarse graining reduces the number of degrees of freedom in a system, creating a smoother free-energy landscape compared with fully atomistic simulations. This speedup can be addressed by including frictional and stochastic forces [15]. This approach allows large CG scales; however, rigorously correct dissipation requires a sophisticated generalized Langevin kernel, and simplifications are usually employed [5]. It has been shown that for small λ, CG models without added friction or stochastic forces can be employed, but CG dynamics are significantly faster than in atomistic simulations [32–39]. To determine the dynamic scaling factor of the CG models we compare the MSD of the inner 24 methylene groups (4, 6, 8, or 12 beads) for CG models and the inner 24 carbon atoms for atomistic simulations for $n = 96$ and 480 as shown in Fig. 3(a). The mobility of the chains in the CG models is larger than in atomistic simulations. By scaling the time for each of the CG models we create a single collapsed curve for each chain length for both the atomistic and CG data as shown in Fig. 3(b). Notably, a single scaling factor α is required to collapse atomistic and CG data for each model, independent of chain length. As seen in Fig. 3(b), the MSD has reached the diffusive regime where MSD $\sim t^1$ even for the longest chain length $n = 1920$. Over intermediate time scales, the chains show the expected $t^{1/4}$ scaling predicted by reptation theory [40]. These results demonstrate that one can capture long time and length scales with CG models while accounting for atomistic details.

The MSD of the center of mass was then measured to test the scaling factor α. Figure 4 shows the MSD of the chain center of mass for chain lengths $n = 96$, 480, 960, and 1920. These data have been scaled by the same α as the monomer MSD, producing an excellent collapse. The scale factor α as a function of the CG model is shown as an inset in Fig. 4 along with α for the MARTINI [10] and UA [6] models. Our CG potentials have a much larger time scaling factor than the MARTINI and UA models, similar to the time-scaling factor found previously for PE for a single λ [33]. Values of α are also comparable to those found previously for polystyrene, modeled at a similar coarse-graining level [37]. The UA model has long been considered approximate to the fully atomistic simulation and indeed is ≈40% faster than fully atomistic simulations. Interestingly, the time scaling factor is not monotonic in the CG level, with the CG2 and CG6 models exhibiting the largest speedup. The potential depths in Fig. 2, relate to the value of α, as described previously by Depa and Maranas [33].

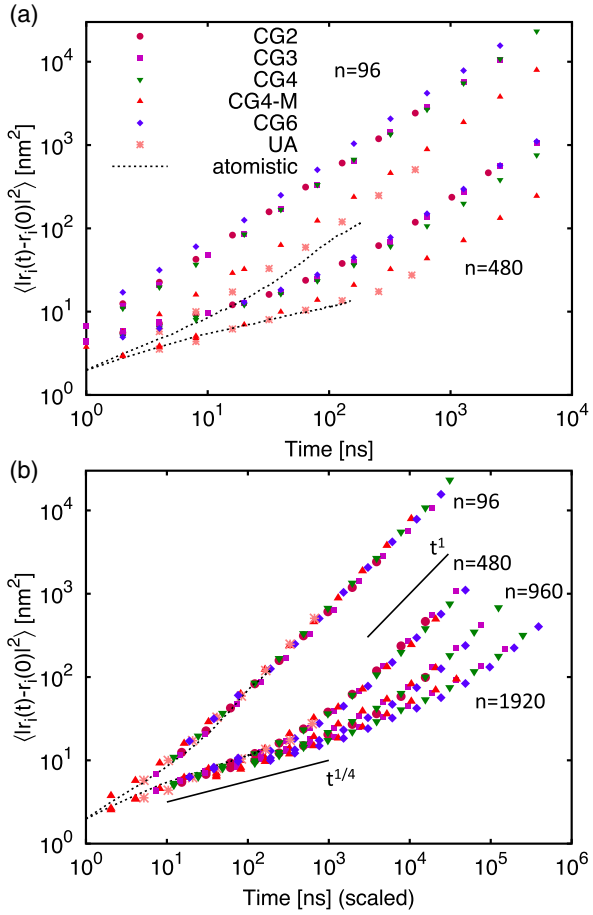

FIG. 3. (a) The MSD of the inner 24 -CH_2- groups of each polymer chain at 500 K. (b) Same data as in (a), scaled by α. The solid lines represent the scaling predictions t^1 for the diffusive regime and $t^{1/4}$ for the reptation regime.

The polymer entanglement mass M_e governs many properties of the polymer melt and provides information about chain mobility within the polymer mesh. Experimentally, $M_e = \rho RT/G_N^0$ is determined from the plateau modulus G_N^0 of the stress relaxation function $G(t)$ [28]. Experimental values for polyethylene are 1.6–2.5 MPa, corresponding to M_e of 1300–2000 g/mol [28,29,41,42].

The relaxation modulus in each of our CG models was measured for the four different chain lengths via equilibrium stress correlations using the Green-Kubo relation $G(t) = (V/k_BT)\langle \sigma_{\alpha\beta}(t)\sigma_{\alpha\beta}(0)\rangle$, where $\sigma_{\alpha\beta}$ are the off-diagonal components xy, xz, and yz of stress. Figure 5

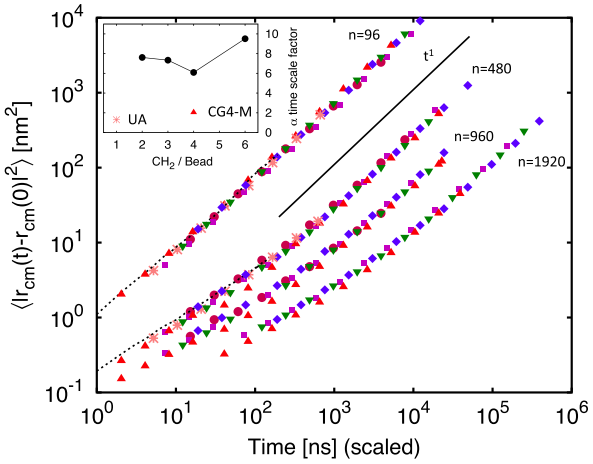

FIG. 4. MSD of center of mass scaled with the same α scale factor as for the inner -CH_2- groups in Fig. 3(b). The solid line has slope t^1. Inset: The alpha scale factor for different coarse-grained models and the UA and Martini models.

shows G_N^0 for each of the CG models for $n = 96$ and 480 and for $\lambda \geq 3$ for $n = 1920$. The times for each model have been scaled by the corresponding value of α. Though it shows similar behavior, the UA model is omitted because the zero-pressure density is higher than the other models, making comparison difficult. The curves collapse for the short-time $t^{-1/2}$ regime, with longer, more entangled chains forming progressively more distinct plateau regions. The plateau modulus is measured as the value of the relaxation modulus in the plateau region, roughly between 20 and 600 ns. Using the longest chain length, $n = 1920$, the plateau modulus $G_N^0 = 2.2 \pm 0.3$ MPa for CG6, 2.1 ± 0.3 MPa for CG4, and 2.1 ± 0.7 MPa for CG3, all within the experimental range. For CG4-M G_N^0 is significantly higher, $G_N^0 = 3.7 \pm 0.4$ MPa, and does not agree with experimental values. Uncertainties are measured by dividing the data sets in two and measuring the variation in the plateau value. Similar plateau modulus values were found by Padding and Briels [20] for $n \leq 1000$ with $\lambda = 20$ model with a noncrossing constraint.

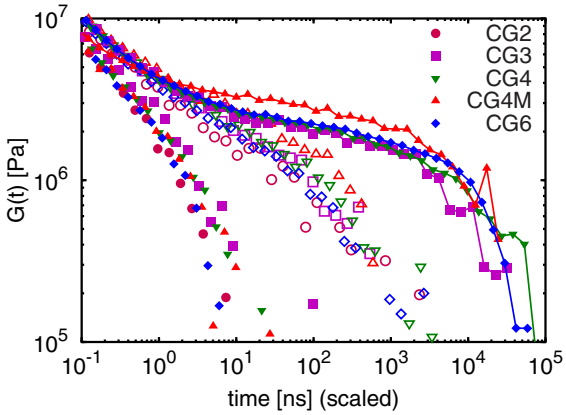

FIG. 5. Modulus $G(t)$ for each of the CG polymer models at 500 K. Closed and open symbols represent the $n = 96$ and $n = 480$ chain length, respectively. Solid lines represent the $n = 1920$ length, while $n = 960$ chains are omitted for clarity.

The thermal expansion coefficient is another way to assess the validity of the CG models. The linear thermal expansion coefficients for the $n = 96$ samples in the temperature range from 495 to 480 K are 5.0, 3.4, 3.5, 3.3, $3.4 \times 10^{-4} T^{-1}$, respectively, for the CG2, CG3, CG4, CG4-M, and CG6 models, compared with $3.1 \times 10^{-4} T^{-1}$ for the atomistic model. Hence, all the CG models with $\lambda \geq 3$ agree with the atomistic thermal expansion.

Although one can derive CG potentials using multiple temperatures [43], our CG models are developed in the traditional way at a single temperature. Hence, there is uncertainty about the validity of these models away from the chosen point [44]. Shown in Fig. 6 are temperature-density data for the CG models from 400 to 200 K. For $\lambda \leq 4$, the curves show a pronounced density increase between 250 and 330 K, corresponding to a semicrystalline state. The CG6 model does not capture crystallinity and we expect that coarser models will not, either. Previous studies of bead-spring polymer models indicated that a commensurate bond length and bead diameter leads to crystallization [45]. The melting temperature for $n = 96$ is about 400 K, so crystallization occurs at a lower temperature than expected, yet observation of any semicrystalline phase is remarkable. This surprising feature indicates that although our potentials are derived at 500 K they may be useful away from this temperature.

Here we have shown that the smallest length scale needed in the hierarchy of length scales to correctly describe macroscopic behavior and properties is rather small, between 4 and 6 monomers. The CG4 model offers a speedup of more than four orders of magnitude over atomistic simulations, which includes contributions from the time step δt, scale factor α, and $(3\lambda)^2$ reduction in the number of pairwise interactions. The speedup of the CG4 model is about 3 times faster than the CG3 model and is comparable the CG6 model. However, because the CG4

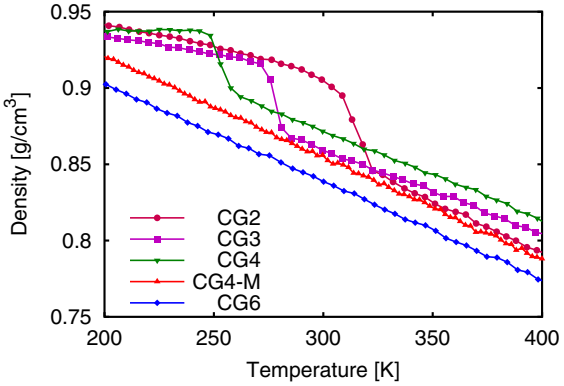

FIG. 6. Density versus temperature for the $n = 96$ samples cooled at 1.4 K/ns.

model does not require a crossing constraint, we prefer this model. With this realized speedup polymers as long as $n = 1920$ can now be simulated for over 500 μs. Reaching this time scale allows probing some of the most unique and intrinsic properties of polymers including the plateau modulus and intermediate $t^{1/4}$ scaling in the mean squared displacement. From the computational viewpoint, the CG models developed significantly reduce the resources needed to study polymers for long times. Our results for the plateau modulus and diffusion dynamics show that without adding extra constraints the CG4 model captures the atomistic detail needed for correct dynamics from monomer to polymer scale.

A. A. and D. P. acknowledge financial support from Grant No. DE-SC007908 and an allotment of time on the Clemson University Palmetto cluster. This research used resources at the National Energy Research Scientific Computing Center, which is supported by the Office of Science of the U.S. Department of Energy under Contract No. DE-AC02-05CH11231. This work was supported by the Sandia Laboratory Directed Research and Development Program. Research was carried out in part, at the Center for Integrated Nanotechnologies, a U.S. Department of Energy, Office of Basic Energy Sciences user facility. Sandia National Laboratories is a multiprogram laboratory managed and operated by Sandia Corporation, a wholly owned subsidiary of Lockheed Martin Corporation, for the U.S. Department of Energy's National Nuclear Security Administration under Contract No. DE-AC04-94AL85000.

[1] S. O. Nielsen, C. F. Lopez, G. Srinivas, and M. L. Klein, J. Phys. Condens. Matter **16**, R481 (2004).
[2] Y. Li, B. C. Abberton, M. Kröger, and W. K. Liu, Polymers **5**, 751 (2013).
[3] K. Kremer and G. S. Grest, J. Chem. Phys. **92**, 5057 (1990).
[4] F. Müller-Plathe, ChemPhysChem **3**, 754 (2002).
[5] J. T. Padding and W. J. Briels, J. Phys. Condens. Matter **23**, 233101 (2011).
[6] W. Paul, D. Y. Yoon, and G. D. Smith, J. Chem. Phys. **103**, 1702 (1995).
[7] S. K. Nath, F. A. Escobedo, and J. J. de Pablo, J. Chem. Phys. **108**, 9905 (1998).
[8] M. G. Martin and J. I. Siepmann, J. Phys. Chem. B **102**, 2569 (1998).
[9] M. Mondello and G. S. Grest, J. Chem. Phys. **103**, 7156 (1995).
[10] S. J. Marrink, H. J. Risselada, S. Yefimov, D. P. Tieleman, and A. H. de Vries, J. Phys. Chem. B **111**, 7812 (2007).
[11] S. Izvekov and G. A. Voth, J. Phys. Chem. B **109**, 2469 (2005).
[12] M. S. Shell, J. Chem. Phys. **129**, 144108 (2008).
[13] V. Rühle and C. Junghans, Macromol. Theory Simul. **20**, 472 (2011).
[14] H. Fukunaga, J.-i. Takimoto, and M. Doi, J. Chem. Phys. **116**, 8183 (2002).
[15] J. T. Padding and W. J. Briels, J. Chem. Phys. **115**, 2846 (2001).
[16] H. S. Ashbaugh, H. A. Patel, S. K. Kumar, and S. Garde, J. Chem. Phys. **122**, 104908 (2005).
[17] X. Guerrault, B. Rousseau, and J. Farago, J. Chem. Phys. **121**, 6538 (2004).
[18] L.-J. Chen, H.-J. Qian, Z.-Y. Lu, Z.-S. Li, and C.-C. Sun, J. Phys. Chem. B **110**, 24093 (2006).
[19] D. Curcó and C. Alemán, Chem. Phys. Lett. **436**, 189 (2007).
[20] J. T. Padding and W. J. Briels, J. Chem. Phys. **117**, 925 (2002).
[21] J. T. Padding and W. J. Briels, J. Chem. Phys. **118**, 10276 (2003).
[22] L. Liu, J. T. Padding, W. K. den Otter, and W. J. Briels, J. Chem. Phys. **138**, 244912 (2013).
[23] See Supplemental Material at http://link.aps.org/supplemental/10.1103/PhysRevLett.116.058302 for simulation details and static chain properties, which includes Refs. [24–26].
[24] M. Tuckerman, B. J. Berne, and G. J. Martyna, J. Chem. Phys. **97**, 1990 (1992).
[25] R. E. Isele-Holder, W. Mitchell, and A. E. Ismail, J. Chem. Phys. **137**, 174107 (2012).
[26] S. Plimpton, J. Comput. Phys. **117**, 1 (1995).
[27] S. W. I. Siu, K. Pluhackova, and R. A. Böckmann, J. Chem. Theory Comput. **8**, 1459 (2012).
[28] L. J. Fetters, D. J. Lohse, S. T. Milner, and W. W. Graessley, Macromolecules **32**, 6847 (1999).
[29] L. J. Fetters, D. J. Lohse, and W. W. Graessley, J. Polym. Sci., Part B **37**, 1023 (1999).
[30] W. L. Jorgensen, D. S. Maxwell, and J. Tirado-Rives, J. Am. Chem. Soc. **118**, 11225 (1996).
[31] T. W. Sirk, Y. R. Slizoberg, J. K. Brennan, M. Lisal, and J. W. Andzelm, J. Chem. Phys. **136**, 134903 (2012).
[32] P. Depa, C. Chen, and J. K. Maranas, J. Chem. Phys. **134**, 014903 (2011).
[33] P. K. Depa and J. K. Maranas, J. Chem. Phys. **123**, 094901 (2005).
[34] I. Y. Lyubimov and M. G. Guenza, J. Chem. Phys. **138**, 12A546 (2013).
[35] I. Y. Lyubimov, J. McCarty, A. Clark, and M. G. Guenza, J. Chem. Phys. **132**, 224903 (2010).
[36] V. Harmandaris, Korea-Aust. Rheol. J. **26**, 15 (2014).
[37] V. A. Harmandaris and K. Kremer, Soft Matter **5**, 3920 (2009).
[38] D. Fritz, K. Koschke, V. A. Harmandaris, N. F. A. van der Vegt, and K. Kremer, Phys. Chem. Chem. Phys. **13**, 10412 (2011).
[39] B. Hess, S. Leon, N. van der Vegt, and K. Kremer, Soft Matter **2**, 409 (2006).
[40] P. G. de Gennes, J. Chem. Phys. **72**, 4756 (1980).
[41] J. F. Vega, S. Rastogi, G. W. M. Peters, and H. E. H. Meijer, J. Rheol. **48**, 663 (2004).
[42] V. R. Raju, G. G. Smith, G. Marin, J. R. Knox, and W. W. Graessley, J. Polym. Sci. Pol. Phys. **17**, 1183 (1979).
[43] T. C. Moore, C. R. Iacovella, and C. McCabe, J. Chem. Phys. **140**, 224104 (2014).
[44] P. Carbone, H. A. K. Varzaneh, X. Chen, and F. Müller-Plathe, J. Chem. Phys. **128**, 064904 (2008).
[45] R. S. Hoy and N. C. Karayiannis, Phys. Rev. E **88**, 012601 (2013).

Eur. Phys. J. Special Topics **225**, 1707–1722 (2016)

DOI: 10.1140/epjst/e2016-60142-7

THE EUROPEAN PHYSICAL JOURNAL SPECIAL TOPICS

Regular Article

Dynamics in entangled polyethylene melts

K. Michael Salerno[1], Anupriya Agrawal[2], Brandon L. Peters[1], Dvora Perahia[3], and Gary S. Grest[1]

[1] Sandia National Laboratories, Albuquerque, NM, 87185, USA
[2] Department of Mechanical Engineering and Materials Science, Washington University in St. Louis, MO 63130, USA
[3] Department of Chemistry, Clemson University, Clemson, SC 29634, USA

Received 28 April 2016 / Received in final form 27 July 2016
Published online 10 October 2016

Abstract. Polymer dynamics creates distinctive viscoelastic behavior as a result of a coupled interplay of motion at the atomic length scale and motion of the entire macromolecule. Capturing the broad time and length scales of polymeric motion however, remains a challenge. Using linear polyethylene as a model system, we probe the effects of the degree of coarse graining on polymer dynamics. Coarse-grained (CG) potentials are derived using iterative Boltzmann inversion with λ methylene groups per CG bead (denoted CGλ) with $\lambda = 2, 3, 4$ and 6 from a fully-atomistic polyethylene melt simulation. By rescaling time in the CG models by a factor α, the chain mobility for the atomistic and CG models match. We show that independent of the degree of coarse graining, all measured static and dynamic properties are essentially the same once the dynamic scaling factor α and a non-crossing constraint for the CG6 model are included. The speedup of the CG4 model is about 3 times that of the CG3 model and is comparable to that of the CG6 model. Using these CG models we were able to reach times of over 500 μs, allowing us to measure a number of quantities, including the stress relaxation function, plateau modulus and shear viscosity, and compare directly to experiment.

1 Introduction

The distinctive viscoelastic behavior of polymers arises from coupled dynamics over many length and time scales. To resolve the dynamics of macromolecules it is imperative to probe processes that occur at the monomer level and those that occur on the time scale of the entire molecule. This challenge transcends experimental and computational efforts. Experimentally, dynamics are probed by several techniques, each probing limited windows of time and space.

Computationally, polymers have been studied by two distinct methods: CG models, and with recent increases in computational power, fully atomistic models. The bead-spring description [1] is perhaps the most basic CG model, and with its simplicity it has been able to probe phenomena on long length and time scales. However, by construction it ignores local structure and chemical properties and cannot

quantitatively describe properties such as the local packing, segmental dynamics or density. Atomistic models account for the chemical details but cannot access the long time scales necessary for highly entangled polymer molecules to move their own dimensions. Numerous recent studies have worked to bridge the divide between atomistic and coarse models, developing new approaches to drive computational studies to larger length and time scales while maintaining relevant sub-nanometer details [2–5].

Coarse-graining approaches all aim to combine groups of atoms into pseudoatom beads and determine the bead interaction potentials [2–5]. CG polymer models vary in detail, from the bead-spring description to United Atom (UA) models, which combine each CH_2/CH_3 group into a single pseudoatom. UA interactions are often fit to a functional form with several parameters chosen to reproduce physical properties such as densities and critical temperatures of small molecules [6–9]. Another CG model that uses a similar approach is the MARTINI model, where each bead represents of order four CH_2/CH_3 groups. In this model, parameters for Lennard-Jones interactions are fit to match bulk densities and compressibilities for short chains [10].

Newer methods such as force matching, iterative Boltzmann inversion, and optimized relative entropy [11–13] encode atomistic detail into the CG model interactions and have truly begun to bridge the gap between CG and atomistic descriptions. Significant advances have been made with these methods in coarse graining of polymers, retaining atomistic characteristics while attaining large length and time scales. The resulting CG models effectively predict many structural characteristics, due to the atomic scale information encoded in the bead interactions [2–5]. One critical issue underlying the coarse graining process is the effect of the model coarseness (λ) on the ability to appropriately capturing polymer properties [14].

The optimal number of atoms represented by a CG bead and the effect of this coarse-graining scale on the measured properties of the system remains a critical, open question. This issue is directly correlated with resolving the shortest length scale in a polymer that is fundamental to the macroscopic dynamics and properties. Here, using linear polyethylene as a model system, we probe the effects of the degree of coarse-graining on macromolecular dynamics. The backbone of PE consists of -CH_2– methylene groups, which are a natural coarse-graining unit. Figure 1 illustrates how the CG models with different λ represent an underlying atomistic configuration. We find that for PE, potentials derived using iterative Boltzmann inversion with 2, 3, 4 and 6 methylene groups per CG bead from a fully atomistic polyethylene melt simulation can capture the long-time dynamics of entangled polymer melts.

Polyethylene chains have previously been studied using CG models with beads of $\lambda = 3$–48 methylene groups per bead [15–20]. As most of these studies used a large degree of coarse graining ($\lambda \sim 20$) to study dynamical properties, an extra constraint was needed to prevent chains cutting through each other [21]. With this extra constraint, the mean squared displacements (MSD), stress autocorrelation functions and shear viscosities of linear and branched PE [21–23] have been studied for long, entangled chains. However, these studies did not address the effect of the coarse-graining degree λ on dynamic properties.

Here we elucidate the effect of coarse-graining degree on the ability to capture the structure and dynamics of PE. We are able to capture polymer chain dynamics for lengths up to $C_{1920}H_{3842}$ and time scales of 500 μs using models that accurately represent atomistic detail. Accessing these large length and time scales allows us to measure a wide range of properties from the single chain dynamics to the stress relaxation function and shear viscosity which depend on a hierarchy of length and time scales.

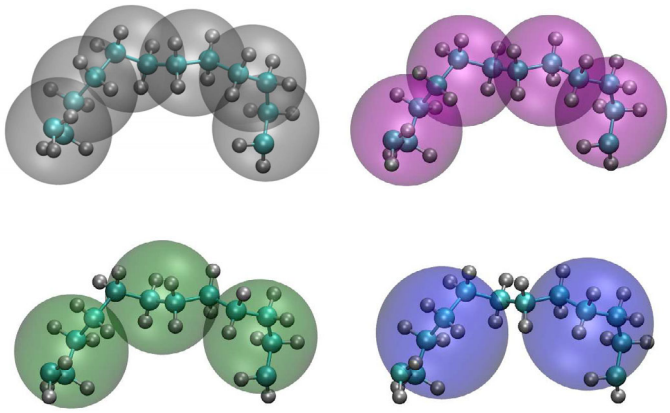

Fig. 1. $C_{12}H_{24}$ segment of a PE chain represented with degree of coarse graining $\lambda = 2$, 3, 4, and 6 methylene groups per CG bead. The bead diameter corresponds to the position of the minimum in the nonbonded interaction for each CG model.

2 Model and methodology

Each of the CG potentials was derived from an atomistic simulation of 345 chains of C_nH_{2n+2} with $n = 96$ at 500 K. The simulation pressure was ~30 atm with density 0.72 g/cm^3. The atomistic simulations used the All Atom Optimized Potentials for Liquid Simulations (OPLS-AA) potential [24,25] with modified dihedral coefficients [26]. These modified OPLS-AA parameters reproduce the experimental static and dynamic chain properties for long alkanes better than the original OPLS-AA parameters [25].

Most of the simulations were run at constant volume with a Langevin thermostat with damping time constant t_v. The equation of motion for each atom in the atomistic simulations and each bead in the CG simulations is [27,28],

$$m\ddot{\mathbf{r}}_i = -\nabla U_i - m\dot{\mathbf{r}}_i/t_v + \mathbf{W}_i(t), \tag{1}$$

where U_i is the sum of the intramolecular bond, angle and dihedral potentials and nonbonded potentials. $\mathbf{W}_i(t)$ describes the random stochastic force of the heat bath acting on each CG bead or atom. $\mathbf{W}_i(t)$ is a Gaussian white noise with

$$\langle \mathbf{W}_i(t) \cdot \mathbf{W}_j(t') \rangle = 6k_BTm\delta_{ij}\delta(t - t')/t_v. \tag{2}$$

In the atomistic simulations, the nonbonded potential is the sum of Lennard-Jones and long-range Coulomb interactions, while for the CG models the nonbonded potential is short-ranged as discussed below. In the atomistic simulations the Langevin damping constant is 1 ps, a weak damping that serves to maintain the temperature and integration stability. However in the CG simulations the Langevin damping has a more important role. The viscous damping can be used to slow down the mobility of the polymer chains, compensating for a smoother free-energy landscape as discussed below.

For the atomistic simulations, the attractive r^{-6} dispersion term in the Lennard-Jones interaction and the electrostatic interactions are calculated using the particle-particle-particle-mesh (PPPM) algorithm [29]. Interactions closer than 1.2 nm are calculated in real space; those outside this range are calculated in reciprocal space with precision of 3×10^{-5}. The repulsive r^{-12} term in the Lennard-Jones interaction is truncated at 1.2 nm. For the CG models the nonbonded interactions are truncated at

1.0 nm. Simulations are performed using the Large Atomic Molecular Massive Parallel Simulator (LAMMPS) molecular dynamics code [30]. Atomistic bond, angle, dihedral and nonbonded interactions are integrated with a 1 fs time step, and long-range interactions are integrated with a 4 fs time step using the RESPA integrator [31].

Before generating the CGλ potentials the $n = 96$ sample was equilibrated for 30 ns, after which particle configurations were sampled every 0.1 ns for 7 ns. Over this time the chains moved a significant distance relative to their end-to-end size, and many local conformations were sampled. Atomistic simulations for a system of 216 chains of length $n = 480$ were also run at 500 K at mass density $\rho = 0.73\,\mathrm{g/cm^3}$ for 675 ns. Both the $n = 96$ and 480 systems were used to calibrate the time scaling for the CG potentials.

The CG bond and angle potentials are derived from the atomistic simulations in a single Boltzmann inversion step. The bond potential is calculated from the distribution of bond lengths $P(l)$,

$$U_B(l) = -k_B T \log\left[\frac{P(l)}{l^2}\right], \tag{3}$$

where l is the bond length for CG beads overlaid on the atomistic reference configurations. The bond potentials for the CG models with $\lambda = 2$, 3, 4, and 6 are shown in Fig. 2(a). Similarly, the angle potential

$$U_A(\theta) = -k_B T \log\left[\frac{P(\theta)}{\sin(\theta)}\right] \tag{4}$$

is computed from the distribution $P(\theta)$, where θ is the angle between CG bead triplets from the atomistic reference configuration. These CGλ potentials $U_A(\theta)$ for $T = 500$ K are shown in Fig. 2(b). Previously we showed the angle distribution $P(\theta)$ with the convention $\theta = 0^\circ$ aligned as consecutive bead-bead vectors ($i-1 \to i$ and $i \to i+1$) [32]. Here $\theta = 180^\circ$ represents this orientation.

The CG nonbonded potentials are derived through a multi-step iterative Boltzmann inversion process. In the first iteration the nonbonded potential is calculated from the intermolecular radial distribution function (RDF) $g(r)$ of CG beads overlaid on the atomistic reference configuration as

$$U^0_{NB}(r) = -k_B T \log[g(r)]. \tag{5}$$

The nonbonded potential U^{i+1}_{NB} is then determined iteratively from the previous potential U^i_{NB}, the reference RDF $g(r)$, and RDF $g^i(r)$ calculated from a CG simulation using the $U^i_{NB}(r)$ potential

$$U^{i+1}_{NB}(r) = U^i_{NB}(r) + \Lambda k_B T \log\left[\frac{g^i(r)}{g(r)}\right]. \tag{6}$$

Here i is the iteration number and Λ determines how quickly updates change the nonbonded potential. During the iteration procedure $\Lambda = 0.5$ initially, but is decreased to $\Lambda = 0.1$ as $g^i(r)$ converges toward the target $g(r)$.

The potential and force are required to go smoothly to zero at the cutoff by multiplying the potential by the Mei-Davenport-Fernando taper function [33]

$$f(x) = \begin{cases} 1, & r \le r_m \\ (1-x)^3(1+3x+6x^2), & r_m \le r \le r_c \\ 0, & r_c \le r \end{cases} \tag{7}$$

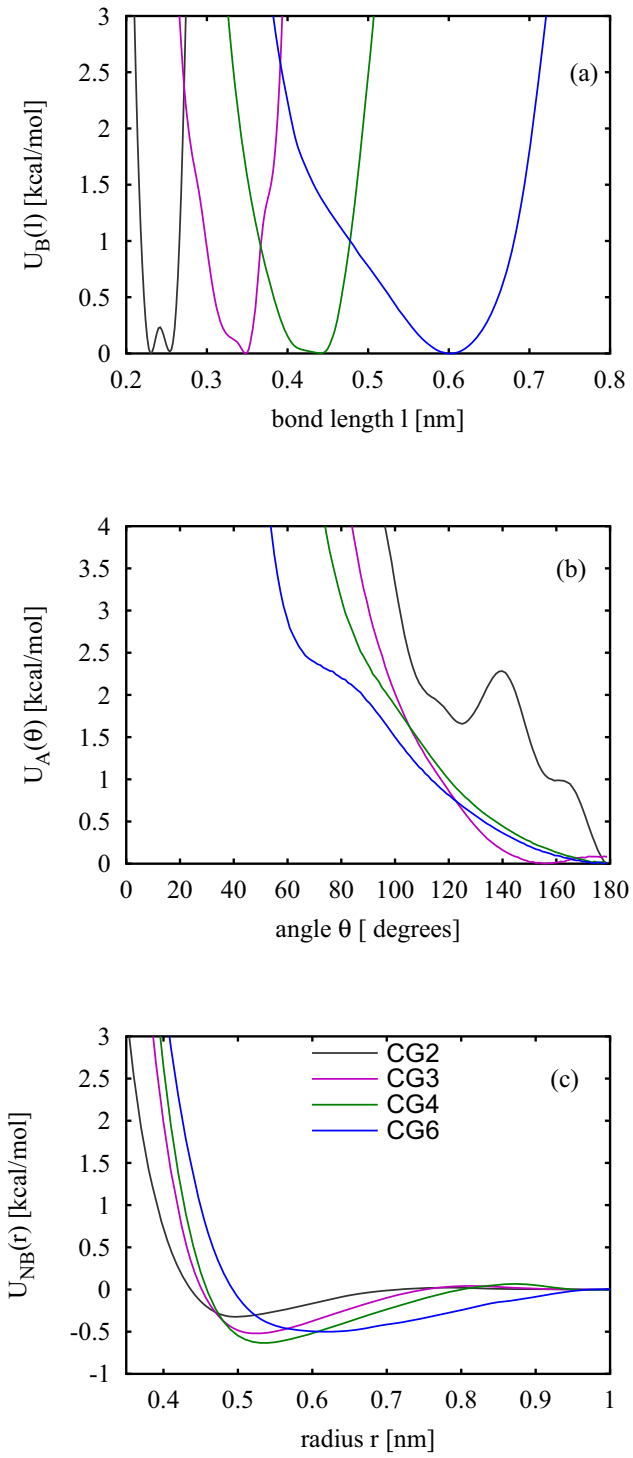

Fig. 2. Potentials for (a) bond, (b) angle and (c) non-bonded interactions for the CGλ models at $T = 500\,\mathrm{K}$.

where $x = (r - r_m)/(r_c - r_m)$, $r_m = 0.9\,\text{nm}$ is the start of the taper range and $r_c = 1.0\,\text{nm}$ is the cutoff distance. After 20–25 iterations, a pressure correction [34–36]

$$\Delta U_{i+1}^{pc}(r) = -(P_i - P)V_0\gamma\left(1 - \frac{r}{r_c}\right) \tag{8}$$

is applied. Here P_i is the average pressure during iteration i, P is the target pressure, and γ is a damping factor to control convergence. The density is set to match that of the atomistic system for n = 96, $\rho = 0.72\,\text{g/cm}^3$. The target and final RDF are shown in the supplement to ref. [32].

The final nonbonded potentials are shown in Fig. 2(c). Comparing Fig. 2(a) and (c) it is clear that for $\lambda = 6$, the equilibrium bond distance $b \approx 0.6\,\text{nm}$ is larger than the characteristic size of the CG bead $\sigma_6 \approx 0.5$ nm ($U_{NB}(\sigma_6) = 0$). This led to chain crossing. As a result we adopted a modified segmental repulsive potential developed by Sirk et al. to prevent chain crossing for this model. See the Appendix for details [37].

Due to larger bead diameters and masses, the CG models allow a longer simulation time step than the atomistic model. With the damping constant $t_v = 20\,\text{ps}$, the systems were stable with a time step $\delta t = 20\,\text{fs}$ for $\lambda = 4$ and 6, 10 fs for the $\lambda = 3$ and 2 fs for $\lambda = 2$, compared to 1 fs for the atomistic model. To test the effect of the damping on the dynamics of the system, we ran a series of simulations for $n = 480$ for $\lambda = 4$ with $0.01\,\text{ps} \leq t_v \leq 100\,\text{ps}$. While for all $t_v \leq 100\,\text{ps}$, the systems were stable with $\delta t = 20\,\text{ps}$, for the weakest damping, $t_v = 100\,\text{ps}$, the average temperature increased to 520 K compared to the target temperature $T = 500\,\text{K}$. Reducing δt kept the temperature at its target for $t_v = 100\,\text{ps}$. However, we found it most efficient to set $t_v = 20\,\text{ps}$ and run with the larger time step which, as we show below, has little effect on our results.

3 Results

3.1 Chain structure and mobility

The effect of the different levels of coarse graining on the local structure can best be seen from the single chain structure factor $S(q)$ at $T = 500\,\text{K}$ shown in Fig. 3. As shown in Fig. 3(a), $S(q)$ in the intermediate q range for $\lambda = 3$, 4 and 6 are all in good agreement with that of the fully atomistic simulations for $q \lesssim 0.2\,\text{Å}^{-1}$. For larger q values, the effect of the increasing CG bead size with increasing λ is evident. The local signatures in $S(q)$ in this q range correspond to the atomic bond lengths, which are averaged out by the CG process. The conformation of the polymers is reflected in the Kratky plot for the longest chain length $n = 1920$ shown in Fig. 3b. At this chain length PE assumes a Gaussian conformation which, is manifested in the Kratky plot as a plateau. The q^{-2} power-law regime, characteristic of ideal Gaussian chains in the intermediate q regime is clearly seen for all three CG models.

The plateau propagates across a relatively narrow q range due to the local stiffness of the chains. Previous UA model simulations and rotational isomeric state modeling found that polyethylene oligomers do not become Gaussian in the melt until n is significantly larger than 200 [38]. One signature of Gaussian behavior is the ratio of the mean-squared end-to-end distance $\langle R^2 \rangle$ to the mean squared radius of gyration $\langle R_g^2 \rangle$. For Gaussian chains $\langle R^2 \rangle / \langle R_g^2 \rangle = 6$. As shown in Fig. 4, $\langle R^2 \rangle / 6\langle R_g^2 \rangle > 1$ for the shorter chains as expected from previous studies [38]. For $n = 96$, the ratio increases significantly with increasing λ, indicating that care must be exercised in using a high level of coarse graining for short chains. In all cases $\langle R^2 \rangle / 6\langle R_g^2 \rangle \to 1$

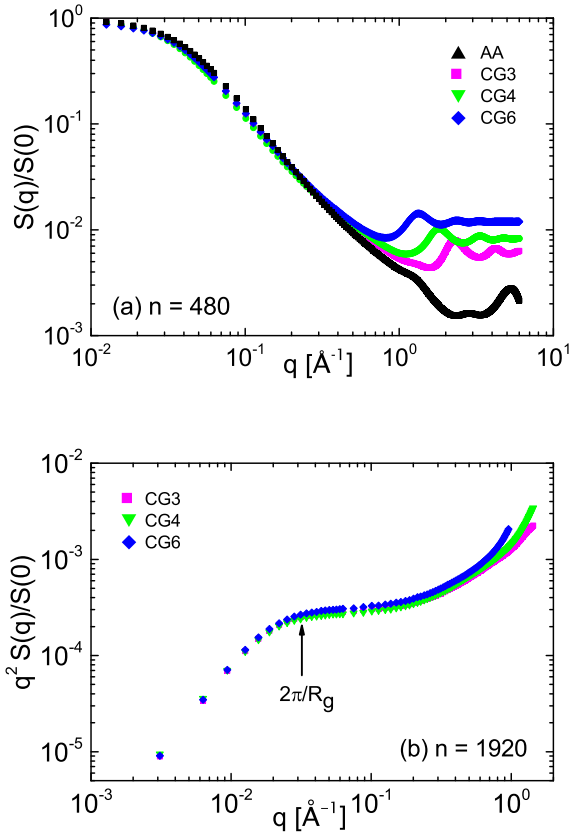

Fig. 3. Single chain structure factor S(q) for (a) n = 480 comparing atomistic model to CG models with $\lambda = 3$, 4 and 6. (b) Kratky plot for n = 1920 for CG models with $\lambda = 3$, 4 and 6.

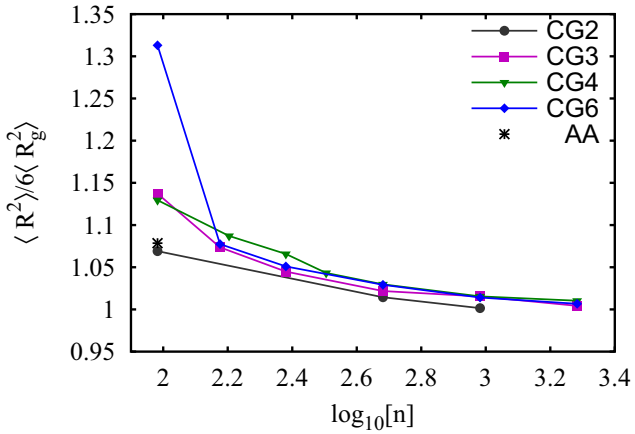

Fig. 4. Ratio of the mean squared end-to-end distance and radius of gyration $\langle R^2\rangle/(6\langle R_g^2\rangle)$. Results for atomistic system for $n = 96$ is shown by *.

as n increases. For the largest n studied here, the chains are Gaussian for all λ. For large n, $\langle R^2\rangle/M = 1.42 \pm 0.05$ Å^2 mol/g for $\lambda = 3$, 1.5±0.05 Å^2 mol/g for $\lambda = 4$, and 1.35±0.05 Å^2 mol/g for $\lambda = 6$, in good agreement with the experimental value from small angle neutron scattering of 1.25 Å^2 mol/g at 413 K [39]. These results give a packing length [40] $p = M/(\langle R^2\rangle \rho_m N_A) = 1.54$ Å for $\lambda = 3$, 1.45 Å for $\lambda = 4$ and $p = 1.61$ Å for $\lambda = 6$ at 500 K, compared to the experimental result $p = 1.69$ Å at 413 K [39].

Coarse graining reduces the number of degrees of freedom in a system, creating a smoother free-energy landscape compared with fully atomistic simulations. This results in faster dynamics for the polymer chain than for the fully atomistic model [41–47]. This enhancement in the chain dynamics has been addressed two ways. The first is to include frictional and stochastic forces [16,48–53] to compensate for the faster chain dynamics. Often by choosing the damping constant t_v appropriately one can adjust the particle dynamics for the CG model to match that of the atomistic model. For example, Padding and Briels compared the decay of autocorrelation of the random force in atomistic simulations to their coarse grained model to calibrate the strength of viscous damping [21]. However, rigorously correcting for the dissipation on all length scales requires a sophisticated generalized Langevin kernel and simplifications are usually employed [14,48,52]. Alternatively, one can take advantage of this increase in dynamics for the CG model to simulate effectively longer time scales [46,47]. While the former approach may be useful for coarse graining small molecules, for entangled polymers which already have inherently slow dynamics, this additional speed up for CG models can be advantageous. Here we explore both approaches.

Previously, we [32] showed that mean squared displacement (MSD) of the of the center of mass (cm)

$$g_3(t) = \langle (r_{cm}(t) - r_{cm}(0))^2 \rangle \tag{9}$$

of the chain and inner 24 methyl groups (4, 6, 8, or 12 beads)

$$g_1(t) = \langle (r_i(t) - r_i(0))^2 \rangle \tag{10}$$

for the CG models and the inner 24 carbon atoms for atomistic simulations for $n = 96$ and 480 could be mapped onto each other by scaling the time for each CG model by a scale factor α. The same dynamic scaling factor, shown in the inset of Fig. 5 also collapsed the MSD data for $\lambda = 3$, 4 and 6 for $n = 960$ and 1920 onto a single curve for each chain length as shown in Fig. 5 for $n = 1920$. We estimate the uncertainty in α to be ∼10% for the different CG models.

The MSD of inner monomers shows a distinct crossover from the early time $t^{1/2}$ Rouse regime to $t^{1/4}$ intermediate scaling predicted by the tube model [54,55] at an entanglement time $\tau_e \simeq 10$ ns. This value of τ_e agrees with the CG simulations of Padding and Briels [21] who used $\lambda = 20$ with a non-crossing constraint to model systems with $n \leq 1000$. Neutron spin-echo experiments by Richter et al. [56] and Schleger et al. [57] estimate $\tau_e \simeq 5$ ns. The MSD data in Fig. 5 as well as the MSD data of Padding and Briels [21] give a tube diameter $d_T = \sqrt{g_1(\tau_e)} \simeq 1.7$ nm. This result differs from that obtained from fitting spin echo scattering data for $S(q,t)$ which give $d_T \simeq 4.35$ nm [56,57]. The difference may be related to the fact that chains of this length are not Gaussian, as shown above in Fig. 4. For late times, as shown in Fig. 5, the MSD of the center of mass and inner monomers converge at a diffusive time $\tau_d \sim 10^5$ ns with a diffusion coefficient $D = 1.2 \times 10^{-12}$ m^2/s for $n = 1920$. These results for the intermediate $t^{1/4}$ power law are in good agreement with previous long time simulations using the bead-spring model [1,58,59]. However, unlike the bead-spring model this result demonstrates that one can capture long time and length scales while accounting for atomistic details.

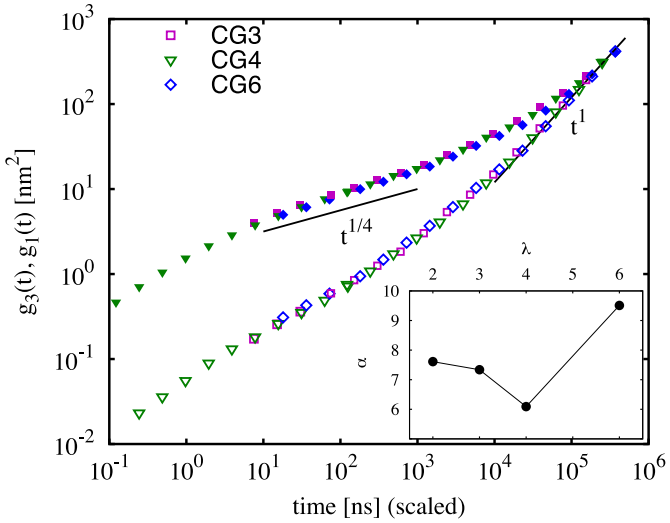

Fig. 5. Mean-squared displacement for inner monomers $g_1(t)$ (upper curve) and center of mass $g_3(t)$ (lower curve) for $n = 1920$ at $T = 500\,\mathrm{K}$. Inset shows the scale factor α as a function of λ.

Strong frictional and stochastic forces can be used to slow down the dynamics of the CG model to match those of the atomistic. Figure 6 shows the MSD of the inner 6 beads for $\lambda = 4$ for five values of the Langevin damping time t_v and the MSD of the inner 24 carbon atoms for the $n = 480$ atomistic system. For weak damping, large t_v, the results are independent of damping. However for $t_v < 1$ ps there is a clear reduction in the chain mobility. For the strongest damping, $t_v = 0.01$ ps, the reduction in the MSD is almost two orders of magnitude after only 100 ps. However in spite of this large reduction in the MSD, the data for all five damping times collapse onto a single master curve by scaling the time for each of the CG models by α as shown in Fig. 6b. The time scaling factor α is shown as a function of damping time t_v in the inset to Fig. 6(b). From this data we estimate that the time scaling factor $\alpha = 1$ for $t_v \approx 0.3$ ps for $\lambda = 4$ at 500 K.

3.2 Viscoelastic properties

The stress response function after a small perturbation $G(t)$ can be expressed by the stress autocorrelation function according to the fluctuation-dissipation theorem. In the Rouse regime, $t < \tau_e$, $G(t) \sim t^{-1/2}$, while for longer times, $G(t)$ plateaus at $G_0^N = \rho RT/M_e$, where M_e is the entanglement molecular weight, for $M/M_e \gg 1$. The plateau region in $G(t)$ occurs for $\tau_e \ll t \ll \tau_d$ where the chains are assumed to move in a tube due to entanglements from the other chains. Only after the chains have reached the diffusive regime, $t > \tau_d$ does $G(t)$ relax to zero. For polyethylene, the experimental values for $G_0^N = 1.6$–2.5 MPa, corresponding to M_e of 1300–2000 g/mol [60–63].

The relaxation modulus for each of our CG models was measured for different chain lengths via equilibrium stress autocorrelations using the Green-Kubo relation $G(t) = (V/k_BT)\langle\sigma_{\alpha\beta}(t)\sigma_{\alpha\beta}(0)\rangle$ where $\sigma_{\alpha\beta}$ are the off-diagonal components xy, xz and yz of the stress. Figure 7 shows $G(t)$ for $n = 96$, 480 and 1920. The times for each model have been scaled by the corresponding value of α. As clearly seen, the

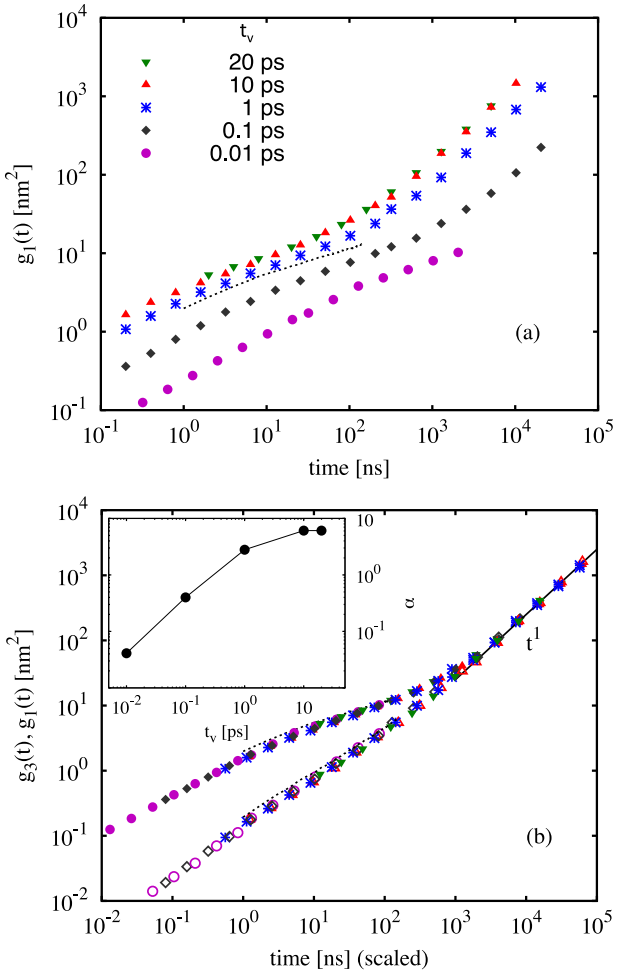

Fig. 6. (a) MSD for inner monomers $g_1(t)$ as a function of time for the CG4 $n = 480$ system for different t_v. (b) Scaled MSD for inner monomers (upper curve) and center of mass $g_3(t)$ (lower curve) for different t_v. (Inset) Time scaling constant α as a function of t_v.

curves collapse for the short-time regime, with longer, more entangled chains forming a more distinct plateau region, though even longer chains are needed to reach a complete plateau [59]. We estimated the plateau modulus G_0^N between 20 and 600 ns for the longest chain length, $n = 1920$. $G_0^N = 2.2 \pm 0.3$ for CG6, 2.1 ± 0.3 MPa for CG4 and 2.1 ± 0.7 MPa for CG3, all within the experimental range. Uncertainties are measured by dividing the data sets in two and measuring the variation in the plateau value. A similar plateau modulus value was found by Padding and Briels [21] for $n = 1000$ with $\lambda = 20$ with their non-crossing constraint.

Non-equilibrium MD simulations were carried out to measure the shear viscosity η as a function of shear rate. Results for η versus scaled shear rate $\dot{\gamma}$ for $n = 96$ to 1920 are shown in Fig. 8 for different values of λ. Here we have assumed that the scaling factor α is independent of shear rate. This assumption was shown to break down for coarse-grained polystyrene chains of ten repeat units at higher shear rates than studied here [64]. For comparison, results for the fully-atomistic model are shown for $n = 96$ and 480. Since the viscosity is the ratio of the stress to shear rate, $\eta = \sigma_{xz}/\dot{\gamma}$,

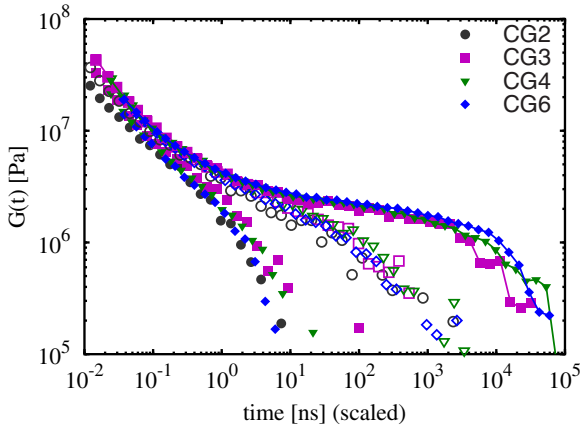

Fig. 7. Stress relaxation modulus $G(t)$ for each of the CG polymer models at 500 K. Filled and open symbols represent chain lengths n = 96 and n = 480, respectively. Solid lines represent $n = 1920$.

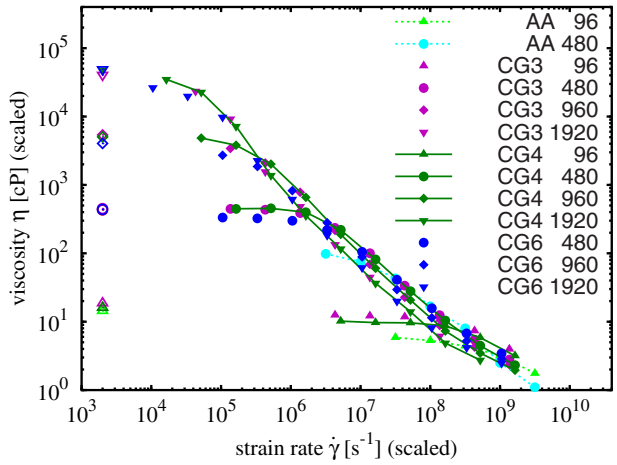

Fig. 8. Shear viscosity η as a function of strain rate $\dot{\gamma}$ for chains of length $n = 96$, 480, 960, and 1920 for $\lambda = 3$, 4, and 6. Values for the zero-rate viscosity, calculated from the integral of G(t) in Fig. 8 are shown as open symbols at the lowest shear rate.

including the scaling factor α increases the effective viscosity and decreases the effective shear rate compared to the unscaled values. The scale factor α significantly increases the range of viscosities and shear rates that can be explored numerically. For high shear rates, all systems show a shear thinning regime in which the viscosity $\eta \sim t^{-n}$ with $n \approx -1.0 \pm 0.1$ independent of molecular weight. This scaling exponent is larger than the earlier result $n \approx 0.6$ of Kröeger and Hess for the fully flexible bead-spring model [65]. As the shear rate is decreased, η reaches a plateau for $\dot{\gamma} \propto \tau_d^{-1}$. The zero shear rate limit of η is in good agreement with that obtained from the using the Green-Kubo formula $\eta = \int_0^\infty G(t)\mathrm{d}t$, shown in Fig. 8 at the lowest shear rate.

Experimentally the viscosity has been found to increase inversely with the molecular weight for unentangled chains, crossing over to $\eta \sim M^{3.4}$ for entangled chains [66,67]. The $M^{3.4}$ dependence on molecular weight is faster than the prediction of reptation theory $\eta \sim M^3$ and is understood to arise from the relaxation of the stress by processes such as contour-length fluctuations, which are faster than

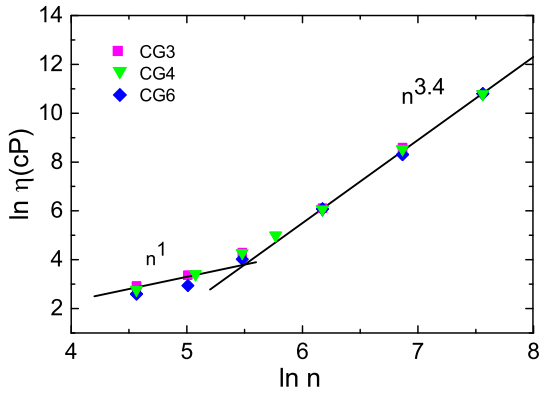

Fig. 9. Zero shear viscosity η as a function of chain length n for $\lambda = 3$, 4, and 6.

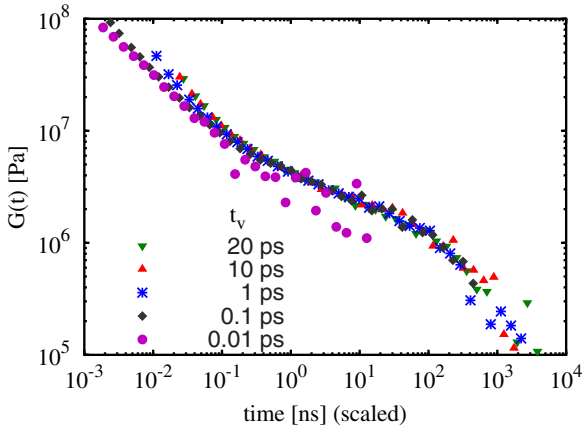

Fig. 10. Stress relaxation modulus $G(t)$ for CG4 for chain length $n = 480$ for damping time t_v from 0.01 ps to 10 ps.

reptation for intermediate chain lengths [68]. As these processes becomes less important as M increases, the viscosity increases faster than the reptation prediction. Our results for viscosity versus chain length are shown in Fig. 9. For the 3 longest chain lengths, a least square fit gives a power law n^a with $a = 3.40$. As shown in Fig. 9, the crossover from the n^1 power law for small n to $n^{3.4}$ for large n occurs at $n_c \sim 250$ or $M_c \sim 3500$ g/mol in excellent agreement with the experimental result $M_c \sim 3800$ g/mol [67,69] and 3000 g/mol from the CG simulation of Padding and Briels [21] for $\lambda = 20$ with a non-crossing constraint.

The relaxation modulus for different t_v was measured for the CG4 model $n = 480$ chains via equilibrium stress autocorrelations as above. Figure 10 shows $G(t)$ for different values of t_v. For each value of t_v the time axis has been scaled by the corresponding value of α, as in Fig. 6(b). Given the good collapse of the MSD data in Fig. 6(b), the collapse of the $G(t)$ data for $t > 0.1$ ns is not surprising. The differences in $G(t)$ at shorter times can be attributed to the different short time dynamics due to the damping time scale. The variation in the short time $G(t)$ behavior is observable in the value of $G(0)$, which increases as the damping time constant is decreased.

4 Conclusions

Here we probed the dynamics of polymers as the number of atoms included in a CG bead is varied from $\lambda = 2$ to 6. We have shown that independent of the degree of coarse graining, all static and dynamic properties are essentially the same once the dynamic scaling factor α and non-crossing constraint for $\lambda = 6$ are included. Using this coarse grained model we were able to reach times of over 500 μs, allowing us to measure a number of quantities which can be compared directly to experiments, including the stress relaxation function, plateau modulus and shear viscosity.

The dynamics of our coarse grained model for PE is 6–10 times faster than the atomistic model at $T = 500\,K$ for the four values of λ studied. This difference in time scales can be eliminated by adjusting the strength of the damping constant t_v to slow down the CG dynamics to match that of the atomistic model. However for entangled polymers which inherently have very slow dynamics, using this additional speed up to reach longer times provides an immense computational advantage. This additional speed up in the dynamics is particularly useful in determining the shear rate dependence of the viscosity η since the dynamic scaling factor α reduces the effective shear rate $\dot{\gamma}$ and increases the effective viscosity η.

Of the four models studied here, CG4 model offers the optimal speedup of more than four orders of magnitude over atomistic simulations, after taking into account the increase in the time step δt, scale factor α, and λ^2 reduction in the number of pairwise interactions. The speedup of the CG4 model is about 3 times in comparison with CG3 model and is comparable the CG6 model. However, because the CG4 model does not require a crossing constraint, it is the preferable model for polyethylene as it captures the atomistic details needed for correct dynamics from monomer to polymer scale. With this speedup, one can readily extend the present study to longer chains as well as include short and long chain branching.

DP acknowledge financial support from Grant No. DE-SC007908 and an allotment of time on the Clemson University Palmetto cluster. This research used resources at the National Energy Research Scientific Computing Center, which is supported by the Office of Science of the U.S. Department of Energy under Contract DE-AC02-05CH11231. This work was supported by the Sandia Laboratory Directed Research and Development Program. Research was carried out in part, at the Center for Integrated Nanotechnologies, a U.S. Department of Energy, Office of Basic Energy Sciences user facility. Sandia National Laboratories is a multi-program laboratory managed and operated by Sandia Corporation, a wholly owned subsidiary of Lockheed Martin Corporation, for the U.S. Department of Energy's National Nuclear Security Administration under contract DE-AC04-94AL85000.

Appendix

A modified segmental repulsive potential (SRP) was added between CG beads in the $\lambda = 6$ model to inhibit chain crossing [37]. The method introduces a potential

$$U^{\mathrm{SRP}} = \frac{b}{2} d_c \left(1 - \frac{d}{d_c}\right)^2 \tag{A.1}$$

between pairs of bonds that are within d_c of one another, but not between adjacent bonds along a chain. This potential gives a force

$$\mathbf{F}_{jk}^{\mathrm{SRP}} = b \left(1 - \frac{d_{jk}}{d_c}\right) \hat{\mathbf{d}}_{jk} \tag{A.2}$$

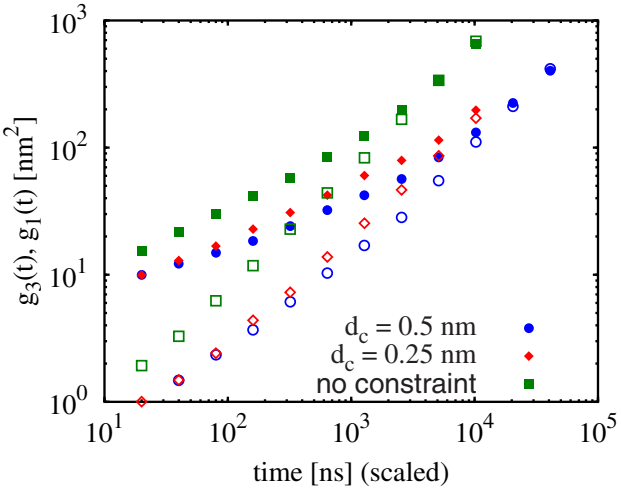

Fig. 11. Unscaled MSD of center monomers $g_1(t)$ (filled) and center of mass $g_3(t)$ (open) for $\lambda = 6$, $n = 1920$ chains with no crossing constraint and with extra bead diameter of $\sigma_B = 0.25$ and 0.5 nm between each CG bead.

between bonds j and k. The distance d_{jk} is calculated as the minimum distance between the two lines formed by the bonds. The force on bond k is transmitted to the CG beads k_L and k_R connected by bond k according to the rule

$$\mathbf{F}_{k_L} = \mathbf{F}_{jk}^{\mathrm{SRP}} L \tag{A.3}$$

$$\mathbf{F}_{k_R} = \mathbf{F}_{jk}^{\mathrm{SRP}} (1 - L), \tag{A.4}$$

where L is the location of the closest approach between the two bonds along bond k, with $L = 0$ corresponding to the right side (at k_R) of the bond and $L = 1$ corresponding to the left side (at k_L) of the bond. The SRP reduces, but does not entirely eliminate chain crossings [37]. The SRP approach to simulating entangled chains with large CG beads is similar to that of Padding and Briels, who used minimization of a chain contour length that includes "entanglements" to enforce non-crossing for a $\lambda = 20$ model.[21] The "TWENTANGLEMENT" algorithm is slower than simulating extra bond beads as in the SRP protocol, however it allows for simulating very large CG beads, thus is faster overall.

As the CG6 model has a large equilibrium bond distance relative to its bead diameter, bond crossing was likely. One indication that chains cut each other was that the dynamic scaling factor α was found to be chain-length dependent for $\lambda = 6$. As the motion of the longer chains is governed by entanglements, the effect of chain crossing increases with increasing chain length. We carried out a series of simulation with different values of d_c and ultimately chose a segmental bead diameter $d_c = 0.5$ nm. For smaller d_c the effect of chains crossing was reduced but not eliminated as seen by the fact that α was still dependent on n. Figure 11 shows the MSD of the center monomers and center of mass for $n = 1920$ with no constraint on chain crossing and with $d_c = 0.25$ nm and 0.5 nm. The chains are significantly more mobile with no constraint and with $d_c = 0.25$ nm. Only for bead diameter $d_c \geq 0.5$ nm is chain crossing reduced to a level that the dynamic scaling factor α is independent of chain length for all n studied here. In the development of the SRP, Sirk et al. studied the effects of the bond constraints on many measures including the system wide pressure and

potential energy [37]. As shown in the supplement [32] in our previous work, the effect of the SRP protocol on $g(r)$ is not discernable, and the effect on the system pressure is small.

References

1. K. Kremer, G.S. Grest, J. Chem. Phys. **92**, 5057 (1990)
2. F. Müller-Plathe, Chem. Phys. Chem. **3**, 754 (2002)
3. S.O. Nielsen, C.F. Lopez, G. Srinivas, M.L. Klein, J. Phys. Condens. Mat. **16**, R481 (2004)
4. C. Peter, K. Kremer, Soft Matter **5**, 4357 (2009)
5. Y. Li, B.C. Abberton, M. Kröger, W.K. Liu, Polymers **5**, 751 (2013)
6. W. Paul, D.Y. Yoon, G.D. Smith, J. Chem. Phys. **103**, 1702 (1995)
7. S.K. Nath, F.A. Escobedo, J.J. de Pablo, J. Chem. Phys. **108**, 9905 (1998)
8. M.G. Martin, J.I. Siepmann, J. Phys. Chem. B **102**, 2569 (1998)
9. M. Mondello, G.S. Grest, J. Chem. Phys. **103**, 7156 (1995)
10. S.J. Marrink, H.J. Risselada, S. Yefimov, D.P. Tieleman, A.H. de Vries, J. Phys. Chem. B **111**, 7812 (2007)
11. S. Izvekov, G.A. Voth, J. Phys. Chem. B **109**, 2469 (2005)
12. M.S. Shell, J. Chem. Phys. **129**, 144108 (2008)
13. V. Rühle, C. Junghans, Macromol. Theor. Simul. **20** (2011)
14. J.T. Padding, W.J. Briels, J.-Phys. Condens. Matt. **23**, 233101 (2011)
15. H. Fukunaga, J.i. Takimoto, M. Doi, J. Chem. Phys. **116**, 8183 (2002)
16. J.T. Padding, W.J. Briels, J. Chem. Phys. **115**, 2846 (2001)
17. H.S. Ashbaugh, H.A. Patel, S.K. Kumar, S. Garde, J. Chem. Phys. **122**, 104908 (2005)
18. X. Guerrault, B. Rousseau, J. Farago, J. Chem. Phys. **121**, 6538 (2004)
19. L.J. Chen, H.J. Qian, Z.Y. Lu, Z.S. Li, C.C. Sun, J. Phys. Chem. B **110**, 24093 (2006)
20. D. Curcó, C. Alemán, Chem. Phys. Lett. **436**, 189 (2007)
21. J.T. Padding, W.J. Briels, J. Chem. Phys. **117**, 925 (2002)
22. J.T. Padding, W.J. Briels, J. Chem. Phys. **118**, 10276 (2003)
23. L. Liu, J.T. Padding, W.K. den Otter, W.J. Briels, J. Chem. Phys. **138**, 244912 (2013)
24. W.L. Jorgensen, J.D. Madura, C.J. Swenson, J. Am. Chem. Soc. **106**, 6638 (1984)
25. W.L. Jorgensen, D.S. Maxwell, J. Tirado-Rives, J. Am. Chem. Soc. **118**, 11225 (1996)
26. S.W.I. Siu, K. Pluhackova, R.A. Böckmann, J. Chem. Theory Comput. **8**, 1459 (2012)
27. T. Schneider, E. Stoll, Phys. Rev. B **17**, 1302 (1978)
28. G.S. Grest, K. Kremer, Phys. Rev. A **33**, 3628 (1986)
29. R.E. Isele-Holder, W. Mitchell, A.E. Ismail, J. Chem. Phys. **137**, 174107 (2012)
30. S. Plimpton, J. Comput. Phys. **117**, 1 (1995)
31. M. Tuckerman, B.J. Berne, G.J. Martyna, J. Chem. Phys. **97**, 1990 (1992)
32. K.M. Salerno, A. Agrawal, D. Perahia, G.S. Grest, Phys. Rev. Lett. **116**, 058302 (2016)
33. J. Mei, J.W. Davenport, G.W. Fernando, Phys. Rev. B **43**, 4653 (1991)
34. G. Milano, F. Müller-Plathe, J. Phys. Chem. B **109**, 18609 (2005)
35. Q. Sun, R. Faller, Comput. Chem. Eng. **29**, 2380 (2005)
36. H. Wang, C. Junghans, K. Kremer, Eur. Phys. J. E **28**, 221 (2009)
37. T.W. Sirk, Y.R. Slizoberg, J.K. Brennan, M. Lisal, J.W. Andzelm, J. Chem. Phys. **136**, 134903 (2012)
38. M. Mondello, G.S. Grest, E.B. Webb III, P. Peczak, J. Chem. Phys. **109**, 798 (1998)
39. L.J. Fetters, D.J. Lohse, D. Richter, T.A. Witten, A. Zirkel, Macromolecules **27**, 4639 (1994)
40. T.A. Witten, S. Milner, Z.G. Wang, Multiphase Macromolecular Syst. (1989)
41. P. Depa, C. Chen, J.K. Maranas, J. Chem. Phys. **134**, 014903 (2011)
42. P.K. Depa, J.K. Maranas, J. Chem. Phys. **123**, 094901 (2005)
43. I.Y. Lyubimov, M.G. Guenza, J. Chem. Phys. **138**, 12A546 (2013)
44. I.Y. Lyubimov, J. McCarty, A. Clark, M.G. Guenza, J. Chem. Phys. **132**, 224903 (2010)
45. V.A. Harmandaris, K. Kremer, Soft Matter **5**, 3920 (2009)

46. V.A. Harmandaris, K. Kremer, Macromolecules **42**, 791 (2009)
47. D. Fritz, K. Koschke, V.A. Harmandaris, N.F.A. van der Vegt, K. Kremer, Phys. Chem. Chem. Phys. **13**, 10412 (2011)
48. S. Izvekov, G.A. Voth, J. Chem. Phys. **125**, 151101 (2006)
49. J.T. Padding, W.J. Briels, J.-Phys. Condens. Matt. **23**, 233101 (2011)
50. P. Espanol, I. Zuniga, Phys. Chem. Chem. Phys. **13**, 10538 (2011)
51. C.C. Fu, P.M. Kulkarni, M.S. Shell, L.G. Leal, J. Chem. Phys. **139**, 094107 (2013)
52. A. Davtyan, J.F. Dama, G.A. Voth, H.C. Andersen, J. Chem. Phys. **142**, 154104 (2015)
53. C. Hijon, P. Espanol, E. Vanden-Eijnden, R. Delgado-Buscalioni, Faraday Discuss. **144**, 301 (2010)
54. M. Doi, S.F. Edwards, The Theory of Polymer Dynamics. International series of monographs on physics (Clarendon Press, 1988)
55. R.S. Hoy, N.C. Karayiannis, Phys. Rev. E **88**, 012601 (2013)
56. D. Richter, R. Butera, L. Fetters, J. Huang, B. Farago, B. Ewen, Macromolecules **25**, 6156 (1992)
57. P. Schleger, B. Farago, C. Lartigue, A. Kollmar, D. Richter, Phys. Rev. Lett. **81**, 124 (1998)
58. K. Kremer, G.S. Grest, in *Monte Carlo and molecular dynamics simulations in polymer science*, edited by K. Binder (Oxford University Press, New York, 1995), pp. 194
59. H.P. Hsu, K. Kremer, J. Chem. Phys. **144**, 154907 (2016)
60. J.F. Vega, S. Rastogi, G.W.M. Peters, H.E.H. Meijer, J. Rheol. **48**, 663 (2004)
61. V.R. Raju, G.G. Smith, G. Marin, J.R. Knox, W.W. Graessley, J. Polym. Sci. Pol. Phys. **17**, 1183 (1979)
62. L.J. Fetters, D.J. Lohse, S.T. Milner, W.W. Graessley, Macromolecules **32**, 6847 (1999)
63. L.J. Fetters, D.J. Lohse, W.W. Graessley, J. Polym. Sci. Pol. Phys. **37**, 1023 (1999)
64. C. Baig, V.A. Harmandaris, Macromolecules **43**, 3156 (2010)
65. M. Kröger, S. Hess, Phys. Rev. Lett. **85**, 1128 (2000)
66. G.C. Berry, T.G. Fox, *The Viscosity of Polymers and Their Concentrated Solutions* (Springer, 1968)
67. J.D. Ferry, *Viscoelastic Properties of Polymers* (John Wiley & Sons, 1980)
68. S.T. Milner, T.C.B. McLeish, Phys. Rev. Lett. **81**, 725 (1998)
69. W.W. Graessley, S.F. Edwards, Polymer **22**, 1329 (1981)

Nanoscale

COMMUNICATION

View Article Online
View Journal

Cite this: DOI: 10.1039/c6nr09206c

Received 26th November 2016,
Accepted 7th December 2016

DOI: 10.1039/c6nr09206c

www.rsc.org/nanoscale

Soft nanoparticles: nano ionic networks of associated ionic polymers†

Dipak Aryal,[a] Gary S. Grest[b] and Dvora Perahia*[a]

Directing the formation of nanostructures that serve as building blocks of membranes presents an immense step towards engineering controlled polymeric ion transport systems. Using the exquisite atomic detail captured by molecular dynamics simulations, we follow the assembly of a co-polymer that consists of polystyrene sulfonate tethered symmetrically to hydrophobic blocks, realizing a new type of long lived solvent-responsive soft nanoparticle.

With an immense advantage of their light weight and versatility, polymers have been integrated into a large variety of technologies. Among these macromolecules are ionic polymers that are imbedded in the core of numerous applications where selective transport is required, including clean energy[1–3] and biotechnologies.[4,5] Notwithstanding their promise, their uses fall short of their potential. A close inspection of these polymeric membranes in-operando shows that at optimal performance, structural changes take place on the nanometer length scale, impacting their macroscopic mechanical stability. These changes arise from the inherent structure of polymer melt where the ionic/ionizable segments segregate into ionic nanodomains, forming physical crosslinks that often control macroscopic mechanical properties. Concurrently, the ionic domains facilitate transport resulting in disruption of these domains leading to destabilization of the overall structures. These opposing effects present a significant challenge to the longevity and efficiency of ionic polymers based devices.

One promising approach to integrating ionic polymers into effective stable devices has been designing structured macromolecules incorporating ionic blocks into co-polymers, taking advantage of the formidable ability of block co-polymers to associate into well-defined structures.[6–9] Similar to van der Waals copolymers, these macromolecules form a rich variety of structures driven by the high segregation between the blocks where the ionic segments segregating into clusters.[10–12] Here we probe the formation of the basic building blocks of such multiple functional ion-containing polymers with molecular dynamics (MD) simulations, the tool of choice to attain molecular insight that can be transposed to device length scales. We find that in contrast to micelles formed by van der Waals block co-polymers, long lived assemblies, or soft nanoparticles are formed, whose structures are tuneable. Their behaviour is controlled by the ionic segment.

The solutions of these ionomers often consist of assemblies[13,14] where the ionic segments form long lived clusters that are retained when cast into membranes. These polymers often exhibit high glass transition temperatures,[12] making solution casting one major route to membrane formation. Therefore, controlling the assembly of structured ionic block co-polymers in solution becomes a critical step in forming membranes with desired properties. While micellization of van der Waals block copolymers have been thoroughly studied,[15,16] the assembly process in highly segregated ionic block co-polymers, where electrostatic interactions drive instantaneous, though strong ionically bound clusters remains one important process that needs to be controlled. Rich varieties of micellar structures have been observed in van der Waals copolymers solutions depending on the nature of the blocks and the solvent environment.[15–21] Incorporating ionic segments affects the structure and the kinetics of their assembly.[22,23]

Structures polymers have been designed with the rational of tailoring transport facilitating domains by the ionic blocks with the rest of the macromolecule providing the much needed mechanical stability. One such a polymer is a pentablock that consists of a centre block decorated with randomly sulfonated polystyrene tethered to ethylene-*r*-propylene as the flexible block and terminated on both sides by *tert*-butyl polystyrene.[24–34] In contrast to lower dimensionality copolymers, the five-block structure, centred on an ionic block would offer complexity to enhance stability, while allowing controlled assembly. In solution these polymers, that serve as casting media for these membranes, consist of assemblies[25,26,28]

[a]*Department of Chemistry, Clemson University, Clemson, South Carolina 29634, USA. E-mail: dperahi@g.clemson.edu*
[b]*Sandia National Laboratories, Albuquerque, New Mexico 87185, USA*
† Electronic supplementary information (ESI) available: Details of simulation methodology and equilibration. See DOI: 10.1039/c6nr09206c

whose symmetry and structure depend on the nature of the solvent, the polymer concentration and the degree of sulfonation. While scattering studies have revealed the overall symmetry of assemblies of this pentablock co-polymer in hydrophobic solvents, their detailed structure needs to be resolved in order to facilitate controlled assembly into well-defined membranes.

Here, using fully atomistic MD simulations, building on our single molecules studies,[35,36] we probe the assembly of this pentablock copolymer as a function of sulfonation fraction f = 0.30 and 0.55 and temperature in a 1 : 1 mixture of cyclohexane/heptane and in water with the goal of understanding the characteristics of these nano structures in comparison with micelles formed by van der Waals polymers. Fully atomistic simulations probe detailed internal structure and coupled dynamics within the assembly that for this type of polymer is on the order of magnitude of 0.1 to *ca*. 150 nanosecond. This specific hydrophobic solvent is used in industrial casting processing. The rational of its choice is to use as good as possible solvent which is volatile enough to be used as a casting solvent. Water is a highly prevalent substance present in the environment and is a by-product of many electrochemical reactions. Water penetrates the pentablock membranes and over long time dissolves the polymer to form colloidal solutions.

Molecular parameters for this study, including sulfonation levels and molecular weights were chosen to be able to correlate with our experimental studies.[28] The number of macromolecules per assembly was chosen to match the aggregation numbers extracted from neutron studies[28] that have shown that each assembly consists of 25–70 polymer molecules, for solution of concentrations ranging between 0.5 to 6 wt% with sulfonation levels that transcends the ionomer–polyelectrolyte range. Here we were able to resolve for the first time the detailed internal structure of these micelles revealing a nano network of ionic segments.

Molecular dynamics simulations of multi-chains of ionic pentablock were carried out using the Large-Scale Atomic/Molecular Massively Parallel Simulator (LAMMPS).[37] The pentablock chains and solvent molecules are modelled using recently updated[38] Optimized Potentials for Liquid Simulations-All Atoms (OPLS-AA) framework of Jorgensen *et al.*[39,40] validated against experimental densities of polystyrene and polyethylene. Additional simulation details are described in our studies of single pentablock chains in dilute solution[35,36] and the attached supplement.

The pentablock molecules and the 1 : 1 mixture of cyclohexane/heptane molecules were constructed using Polymer Builder and Amorphous Cell modules of Accelrys Materials Studio©.[41] Separately we equilibrated a 1 : 1 mixture of 86 400 cyclohexane and 86 400 heptane molecules, and a system of 768 000 water molecules at 300 K in a cubic simulation cell with periodic boundary conditions. The TIP4P/2005 model was used to model the water molecules.[42]

Following the association of macromolecules in solvents computationally amounts to following a large number of atoms for extended times to allow the polymers to aggregate, requiring considerable computational resources. Here an alternative route was developed, collapsing the chains to their experimental density, followed by exposure of the aggregate to solvents and allowing the micelles to evolve. The evolution of the aggregated to micelles are described in details in the ESI Fig. S1† captures visually the transformation of the aggregate into a well define assembly. Fig. S2 and S3† show the evolution of the radius of gyration of the micelle and radial density distribution of the micelle, the ionic block and the solvent in cyclohexane/heptane respectively. While R_g provides the average dimensions of the assembly, the time evolution of the density profiles clearly demonstrate that the polymer molecules are able to rearrange within the time frame of the simulation.

The association of chains in cyclohexane/heptane and in water will be discussed starting from qualitative observation of the assemblies and quantitative structural studies, followed by the internal dynamics of the assemblies. Lastly the response of the aggregates to changes in their environment as they are moved from water to cyclohexane/heptane will be presented.

Representative assemblies formed by the pentablock at different sulfonation fractions within the polyelectrolyte regime in hydrophobic and hydrophilic solvents at 300 K are captured in Fig. 1 in cyclohexane/heptane (Fig. 1a and b) and in water (Fig. 1c and d). For both f values aggregates that appear overall spherical are observed. In cyclohexane/heptane the hydrophobic blocks dominate the interface with the solvent, and the ionic blocks segregate to the centre. The flexible blocks are highly swollen. Surprisingly, most of the end blocks collapse into individual blobs which are segregated from each other. In water, the polymers are collapsed as shown in Fig. 1c and d, where the interface consists of both hydrophilic and hydrophobic groups. The solvent interface is rather broad for cyclohexane/heptane and is well defined in water.

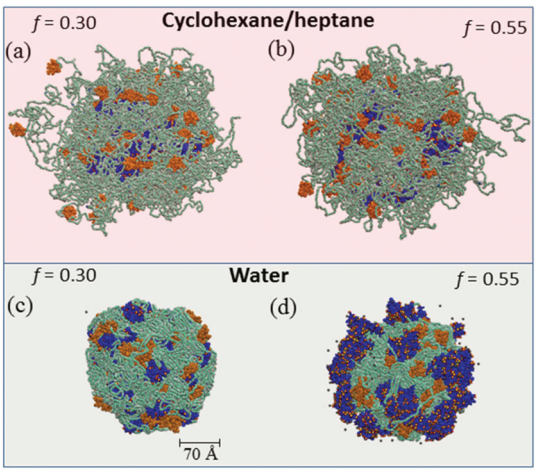

Fig. 1 Snapshots of pentablock assemblies at 300 K in cyclohexane/heptane for (a) f = 0.30 and (b) f = 0.55, and in water for (c) f = 0.30 and (d) f = 0.55. The end block is shown in orange, flexible block in green, centre block in blue. Oxygen atoms are shown in red, sulphur atoms in yellow and sodium atoms in purple.

The overall dimensions and distribution of the blocks as expressed in the radial density profiles as a function of the distance from the centre of mass of the assembly are shown in Fig. 2. These mass density profiles support the initial visual observation however they reveal further structural details. In cyclohexane/heptane the density of the micelle decreases from the centre of mass towards the surface as shown in Fig. 2a. Further, the radius of the micelle extracted from the density profile for both f is ~150 Å, which is in good agreement with range of micelle sizes observed by Choi *et al.*[25]

In cyclohexane/heptane the assembly's interface is dominated by the flexible and end blocks, whose distribution is similar for both f. The sulfonated styrene blocks are more tightly packed in the centre of the micelle for f = 0.55 compared with f = 0.30 as indicated by the higher density of the centre block described by open circles in Fig. 2a. While the hydrophobic blocks are distributed across the micelle, no styrene sulfonate resides at the solvent interface. Further, the multiple maxima are observed in the density distribution plots for centre blocks which capture an ionic network formed across the micelle rather than a homogenous core, commonly observed in van der Waals co-polymer micelles. This network is visualized in the cross-section of the micelle presented as an insert in Fig. 2a. The connectivity of the ionic network is reflected in cluster analysis of the assembly in cyclohexane shown in Fig. S4.† For both sulfonation fractions, most of the ionic groups are assembled into one structure that propagate across the assembly. While the distribution of the hydrophobic blocks is consistent with minimization of the contact area of the hydrophilic block with the overall hydrophobic environment that consists of both the polymer and the solvent, the formation of an internal ionic network is rather surprising. This ionic framework distinguished these assemblies from van der Waals micelles and affects internal dynamics as will be discussed. It forms a stable soft nanoparticle with the non-ionic segments residing within and around the skeleton.

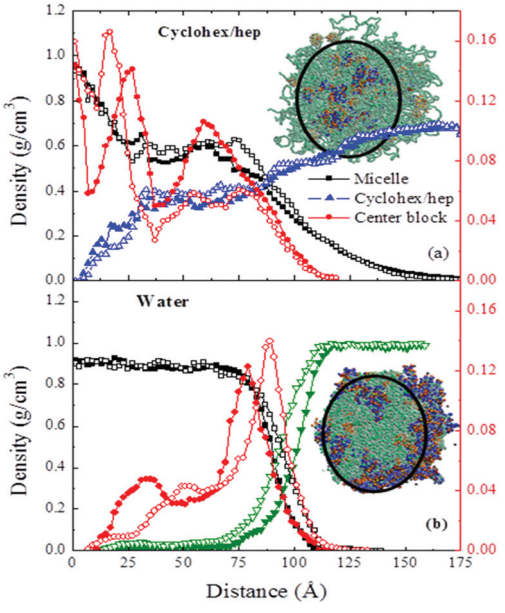

Fig. 2 Radial mass density at 300 K for the aggregate [■], cyclohexane/heptane [▲], water [▼], and centre block of pentablock [●] (a) in cyclohexane/heptane and (b) in water for f = 0.30 (solid) and f = 0.55 (open). Left axis is for both assembly and solvent, and right for centre block.

The solvents are an integral part of these soft assemblies as shown in the density distribution of cyclohexane/heptane Fig. 2a. The hydrophobic solvent contributes about 35% of the mass density of the aggregate. They reside across the assembly with their density decaying towards the centre. In water the polymers are tightly packed resulting in a homogenous overall density as seen in Fig. 2b (squares).

This compact assembly is nearly spherical with the sulfonated styrene blocks residing predominantly towards the outer surface of assembly for both f values with a higher density of the centre block at the surface for f = 0.55 compared to f = 0.30. This result is further manifested in the images of a slice through the micelle in the insert of Fig. 2b for f = 0.55. The radial density distributions of the flexible and end blocks for both f values are rather uniform. While the interface is rich with the ionic block, only a limited amount of water penetrates the micelle as shown in the density profile of the water in Fig. 2b.

Though all the assemblies appear spherical, a closer look shows that both their shape and size as expressed in the root mean square radius of gyration $\langle R_g^2 \rangle^{1/2}$ and the eigenvalues of the moment of inertia are affected by the sulfonation fraction. These values are given in Table S1.† Unexpectedly in cyclohexane/heptane, $\langle R_g^2 \rangle^{1/2}$ is lower for f = 0.55 compared to f = 0.30 for both temperatures. This reduction is attributed to a decrease of the size of the ionic cluster presumably as a mechanism to reduce unfavourable interactions of the sulfonated centre block with the hydrophobic solvent. In water, however, the aggregate dimensions slightly increase with f. With increasing f a larger fraction of sulfonated styrene migrate to the water interface, while the hydrophobic blocks are hardly affected. The shape of the micelles affects their assembly and as such small changes are expected to have a significant impact.

The three eigenvalues of the moment of inertia tensor $\lambda_1 < \lambda_2 < \lambda_3$ at 300 and 500 K are also given in Table S1.† The eigenvalues of the moment of inertia of the micelle are highly sensitive to small divergence from spherical symmetry where the ratios of the two largest eigenvalues to the smallest (λ_2/λ_1 and λ_3/λ_1). These ratios offer an effective measure of degree of sphericity of assemblies whose interface with the solvent is not smooth.[43] In cyclohexane/heptane the eigenvalue ratios are greater than 1.0 which signifies that the symmetry of micelles diverges from spherical. In both solvents these rations are larger than 1 and increase with increasing temperature. The asymmetry is significantly more pronounced in cyclohexane/heptane. These results are in very good agreements with experimental findings of Etampawala *et al.*[28] who observed ellipsoidal core–shell micelles with the centre blocks in the core and Gaussian decaying chains of swollen flexible and end blocks in the corona.

The distribution and dynamics of the ionic species including tethered ionizable groups and the corresponding counterions being among the critical factors, determining structure, mechanical characteristics and transport ability of macromolecules.[44–49] Forming the building blocks of membranes, controlling the ionic distribution in the micelles is one path to impact membrane structure. Here we determined the density distributions of the sulfonated groups as well as the Na^+ counterions as shown in Fig. 3 for micelles in cyclohexane/heptane and in water. In cyclohexane/heptane for f = 0.30, a sparse network of sulfonated groups is observed where for the f = 0.55, a nearly continuous ionic region is manifested in the density profiles. The sodium ions appear condensed for both f. This network is further demonstrated through the cluster analysis presented in Fig. S4.†

In water, the sulfonated groups reside predominantly at the interface with the water and the majority of Na^+ atoms are away from the surface of the micelle for both f values, though some are retained as a network across the micelles. While in cyclohexane/heptane all Na^+ ions are condensed on the sulfonated groups only 10% reside at the SO_3^- groups in water for both sulfonation fractions.

The dynamics within the assemblies of structured ionic polymers defines the path to formation of transport pathways as in membranes are formed. This dynamics has been probed by calculating the dynamic structure factor $S(q,t)$ for representative q values where q in the momentum transfer vector and t is time, shown in Fig. 4a and b for the entire nanoparticle and for each of the blocks separately. The details of the calculations are given in the ESI.† At q = 0.86 Å^{-1} (Fig. 4a), on the scale of 7 Å, the intensity has fully decayed for all components including the ionic region, namely, the ionic groups remain dynamic within the clusters. With increasing dimensions (Fig. 4b) the dynamics of the cluster is highly constrained. This is consistent with macroscopic experimental measurements that have demonstrated that even low amounts of ionic decoration hinder chain dynamics where the ionic clusters remain largely locked.[48,49] The decay of the lower sulfonation levels is slightly faster that the higher one.

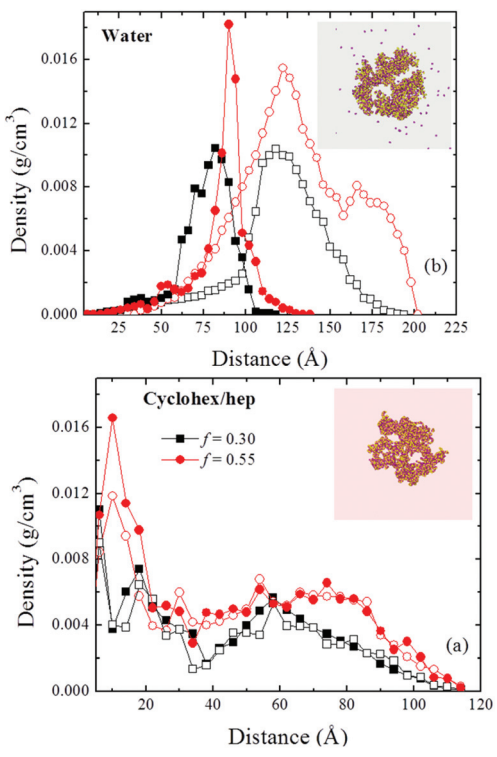

Fig. 3 Radial mass density for sulphur and sodium atoms (a) in cyclohexane/heptane, and (b) water at 300 K for f = 0.30 [■] and f = 0.55 [●]. Solid symbols correspond to sulphur and open for sodium. Images inset are for sulphur in yellow and sodium in purple in both solvents.

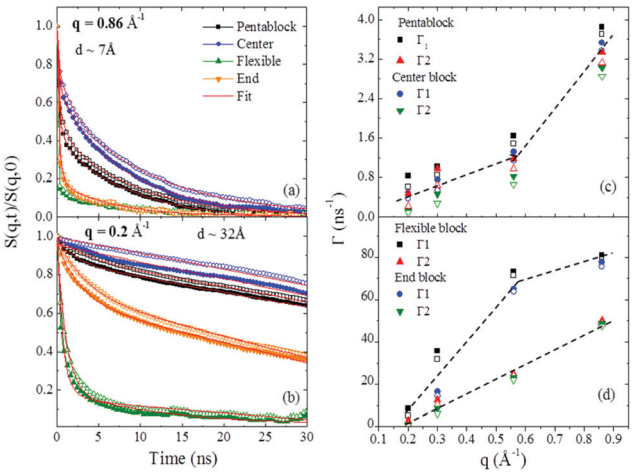

Fig. 4 Dynamic structure function $S(q, t)$ as a function of time and the corresponding effective diffusion constants Γs. $S(q, t)$ for (a) q = 0.86 Å^{-1} and (b) q = 0.2 Å^{-1} in cyclohexane/heptane at 500 K. Γ_1 and Γ_2 for (c) pentablock and center block and (d) flexible block and end block as function of q for f = 0.30 (closed) and 0.55 (open). The values of Γ_1 are multiplied by factor of 30. The distance in real space that corresponds to the q values are marked by d. The dotted lines are for guidance only.

Two time constants, fast and slow were essential to capture the dynamics. The values for Γ_1 and Γ_2 are given as a function of q in Fig. 4c and d. With Γ being inversely proportional to the diffusion, with increasing dimensions the dynamics is constrained. A crossover is observed around the dimensions of the ionic clusters. These values are similar to those previously obtained for ionic assemblies in polystyrene sulfonate melts.[47]

With the understanding of the structure and dynamic of the assemblies we set to explore their response to changing environment. Since ionic polymers are cast into films from one type of solvent, and then exposed to multiple environments, probing the response of the aggregates is a first critical step to understand the effects of the surroundings on membranes. Here aggregates formed in water, a polar solvent were transferred to cyclohexane/heptane, a non-polar solvent and followed as a function of time. The time evolution of the density profiles is shown in Fig. 5a. Initially, at t = 0, the time of the transfer, all blocks are collapsed with well-defined sulfo-

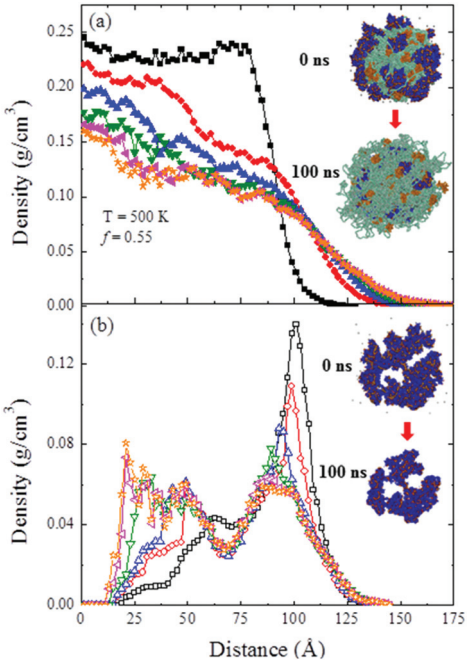

Fig. 5 Radial mass density at 500 K at 0 ns [■], 20 ns [●], 40 ns [▲], 60 ns [▼], 80 ns [◀], and 100 ns [★] for (a) flexible blocks (solid) and (b) centre blocks (open) of pentablock for f = 0.55 in cyclohexane/heptane.

nated blocks at the interface. With increasing time, the flexible blocks migrate to the interface and after 80 ns, the radial density no longer changes. The snapshot of the assembly after 100 ns is shown in the insert of Fig. 5a. Though this micelle is formed in water, it is similar in structure to those assembled directly in cyclohexane/heptane shown in Fig. 1b, as reflected in their density profiles (Fig. S5†).

A close look at the response of the ionic blocks shown in Fig. 5b reveals that while the overall dimensions of the micelle grow, the ionic nano network remains rather stable. The majority of centre blocks that reside at outer surface in water migrate only slightly inward, where the hydrophobic blocks swell and expand into the solvent. Revealing this network stability as the environment is changed demonstrates the role of ionizable segments as physical crosslinks. Further, computationally, these results elucidate that formation of the assemblies in a selective solvent is path independent.

Here we were able to resolve new types of well-defined nanometre scale soft, long lived nanoparticle in selective solvents such as mixture of cyclohexane/heptane and water. In nonpolar solvents, the particle exhibit core–shell structure for both f where the centre consists with an ionic blocks framework. The hydrophobic blocks reside within and around this skeleton. However, in contrast to van der Waals polymers, the core is not homogenous and the ionic blocks form a long lived ionic network across the assembly. In water the nanoparticle interface is dominated by ionic groups while the ionic network is retained and the hydrophobic groups are collapsed. In a hydrophobic environment, the Na^+ counter ions are condensed at the SO_3^- groups. However, in water, the majority of Na^+ atoms are solvated, away from the surface of the micelle. Increasing the degree of sulfonation affects the packing of the ionic groups where in cyclohexane/heptane a more tightly packed network is formed and in water, the interface becomes significantly richer in the ionic block. Overall we find that the ionic network serves as a long lived skeleton of the assembled nanoparticle where the hydrophobic blocks are able to migrate in and out of this structure depending on the nature of the solvent.

Acknowledgements

We thank Carl L. Willis and Marc Charendoff for helpful discussions. The authors gratefully acknowledge financial support from DOE Grant No. DE-FG02-12ER46843. This research used resources at the National Energy Research Scientific Computing Center, which is supported by the Office of Science of the United States Department of Energy under Contract No. DE-AC02-05CH11231. This work was made possible by advanced computational resources deployed and maintained by Clemson Computing and Information Technology. This work was performed, in part, at the Center for Integrated Nanotechnologies, a U.S. Department of Energy and Office of Basic Energy Sciences user facility. Sandia National Laboratories is a multi-program laboratory managed and operated by Sandia Corporation, a wholly owned subsidiary of Lockheed Martin Corporation, for the U.S. Department of Energy's National Nuclear Security Administration under Contract No. DE-AC04-94AL85000.

Notes and references

1 N. P. Balsara and J. Newman, *J. Chem. Educ.*, 2013, **90**, 446.
2 D. S. Kim, M. Guiver, J. E. McGrath, B. S. Pivovar and Y. S. Kim, *Polym. Electrolyte Fuel Cells*, 2010, **33**, 711, 10, Pts 1 and 2.
3 Y. A. Elabd and M. A. Hickner, *Macromolecules*, 2011, **44**, 1.
4 A. Roesler, G. W. M. Vandermeulen and H. Klok, *Adv. Drug Delivery Rev.*, 2012, **64**, 270.
5 A. J. Duncan, B. J. Akle, T. E. Long and D. J. Leo, *Smart Mater. Struct.*, 2009, **18**, 104005.
6 A. M. Castagna, W. Wang, K. I. Winey and J. Runt, *Macromolecules*, 2010, **43**, 10498.
7 Y. A. Elabd, E. Napadensky, C. W. Walker and K. I. Winey, *Macromolecules*, 2006, **39**, 399.
8 R. A. Weiss, A. Sen, C. L. Willis and L. A. Pottick, *Polymer*, 1991, **32**, 1867.
9 Y. S. Kim, F. Wang, M. Hickner, S. McCartney, Y. T. Hong, W. Harrison, T. A. Zawodzinski and J. E. McGrath, *J. Polym. Sci., Part B: Polym. Phys.*, 2003, **41**, 2816.
10 R. A. Weiss, A. Sen, L. A. Pottick and C. L. Willis, *Polymer*, 1991, **32**, 2785.
11 M. J. Park and N. P. Balsara, *Macromolecules*, 2008, **41**, 3678.

12 X. Lu, W. P. Steckle Jr. and R. A. Weiss, *Macromolecules*, 1993, **26**, 6525.
13 D. Nguyen, C. Williams and A. Eisenberg, *Macromolecules*, 1994, **27**, 5090.
14 M. Moffitt, K. Khougaz and A. Eisenberg, *Acc. Chem. Res.*, 1996, **29**, 95.
15 C. J. Huang, B. R. Chapman, T. P. Lodge and N. Balsara, *Macromolecules*, 1998, **31**, 9384.
16 J. Bang, K. Viswanathan, T. P. Lodge, M. J. Park and K. Char, *J. Chem. Phys.*, 2004, **121**, 11489.
17 M. L. Hoarfrost and T. P. Lodge, *Macromolecules*, 2014, **47**, 1455.
18 X. Wang, K. Hong, D. Baskaran, M. Goswami, B. Sumpter and J. Mays, *Soft Matter*, 2011, **7**, 7960.
19 T. P. Lodge, B. Pudil and K. J. Hanley, *Macromolecules*, 2002, **35**, 4707.
20 P. Bhargava, J. Zheng, P. Li, R. Quirk, F. Harris and S. Cheng, *Macromolecules*, 2006, **39**, 4880.
21 C. Dyer, P. Driva, S. W. Sides, B. G. Sumpter, J. W. Mays, J. Chen, R. Kumar, M. Goswami and M. D. Dadmun, *Macromolecules*, 2013, **46**, 2023.
22 Z. Zhou, B. Chu, G. Wu and D. G. Peiffer, *Macromolecules*, 1993, **26**, 2968.
23 P. Guenoun, H. T. Davis, M. Tirrell and J. W. Mays, *Macromolecules*, 1996, **29**, 3965.
24 G. M. Geise, B. D. Freeman and D. R. Paul, *Polymer*, 2010, **51**, 5815.
25 J. Choi, A. Kota and K. I. Winey, *Ind. Eng. Chem. Res.*, 2010, **49**, 12093.
26 P. J. Griffin, G. B. Salmon, J. Ford and K. I. Winey, *J. Polym. Sci., Part B: Polym. Phys.*, 2016, **54**, 254.
27 W. Zheng and C. J. Cornelius, *Polymer*, 2016, **103**, 104.
28 T. Etampawala, D. Aryal, N. Osti, L. He, W. Heller, C. L. Willis, G. S. Grest and D. Perahia, *J. Chem. Phys.*, 2016, **145**, 184903.
29 Y. Fan and C. J. Cornelius, *J. Mater. Sci.*, 2013, **48**, 1153.
30 K. P. Mineart, X. Jiang, H. Jinnai, A. Takahara and R. J. Spontak, *Macromol. Rapid Commun.*, 2015, **36**, 432.
31 G. M. Geise, C. M. Doherty, A. J. Hill, B. D. Freeman and D. R. Paul, *J. Membr. Sci.*, 2014, **453**, 425.
32 J. Choi, C. L. Willis and K. I. Winey, *J. Membr. Sci.*, 2013, **428**, 516.
33 G. M. Geise, C. L. Willis, C. M. Doherty, A. J. Hill, T. J. Bastow, J. Ford, K. I. Winey, B. D. Freeman and D. R. Paul, *Ind. Eng. Chem. Res.*, 2013, **52**, 1056.
34 J. Choi, C. L. Willis and K. I. Winey, *J. Membr. Sci.*, 2012, **394**, 169.
35 D. Aryal, T. Etampawala, D. Perahia and G. S. Grest, *Macromol. Theory Simul.*, 2014, **23**, 543.
36 D. Aryal, D. Perahia and G. S. Grest, *J. Chem. Phys.*, 2015, **143**, 124905.
37 S. Plimpton, *J. Comput. Phys.*, 1995, **117**, 1.
38 K. Murzyn, M. Bratek and M. Pasenkiewicz-Gierula, *J. Phys. Chem. B*, 2013, **117**, 16388.
39 W. L. Jorgensen, J. D. Madura and C. J. Swenson, *J. Am. Chem. Soc.*, 1984, **106**, 6638.
40 W. L. Jorgensen, D. S. Maxwell and J. Tirado Rives, *J. Am. Chem. Soc.*, 1996, **118**, 11225.
41 "Materials Studio", Accelrys. © 2001–2007 Accelrys Software Inc.
42 J. F. L. Abascal and C. Vega, *J. Chem. Phys.*, 2005, **123**, 234505.
43 E. J. Rawdon, J. C. Kern, M. Piatek, P. Plunkett, A. Stasiak and K. C. Millett, *Macromolecules*, 2008, **41**, 8281.
44 A. Eisenberg, B. Hird and R. B. Moore, *Macromolecules*, 1990, **23**, 4098.
45 L. Zhang, B. C. Katzenmeyer, K. A. Cavicchi, R. A. Weiss and C. Wesdemiotis, *ACS Macro Lett.*, 2013, **2**, 217.
46 A. Agrawal, D. Perahia and G. S. Grest, *Phys. Rev. E: Stat. Phys., Plasmas, Fluids, Relat. Interdiscip. Top.*, 2015, **92**, 022601.
47 A. Agrawal, D. Perahia and G. S. Grest, *Phys. Rev. Lett.*, 2016, **116**, 158001.
48 X. Qiao and R. Weiss, *Macromolecules*, 2013, **46**, 2417.
49 R. A. Weiss, J. J. Fitzgerald and D. Kim, *Macromolecules*, 1991, **24**, 1071.

Neutron Reflectivity Study of the Interfacial Region between Ionomers and van der Waals Polymers

Thusitha N. Etampawala[1], Naresh. C. Osti[1], Candice Halbert[2], Jim Browning[2], Jaroslaw Majewski[3], Dvora Perahia[1*],

[1,1*] Department of Chemistry, Clemson University, Clemson, SC 29634

[2] SNS, Oak Ridge National Laboratory, Oak Ridge, TN 37831

[2] Lujan Neutron Scattering Center, Los Alamos National Laboratory, Los Alamos, NM 87545

Abstract

Interdiffusion of polymers across interfaces controls many current and potential applications from alternative energy devices to selective drug delivery systems. The interdiffusion is determined by numerous factors including the chemical and phase structure of polymer coupled with interfacial effects. The interfacial structure is particularly important since in numerous applications the polymer molecules resided at an interface with other polymers. The current work reveals the effects of ionic groups on interdiffusion of a model system that consist of polystyrene and polystyrene sulfonate as resolved from neutron reflectometry measurements. Similar to previous studies we found that at the onset of diffusion the polymer chains interdiffuse at the interface between non-ionic polystyrenes with $t^{½}$ dependence independent of molecular weights and transforms to $t^{1/4}$ as time progresses. In contrast, in presence of ionic groups dynamics at the interface is hindered significantly. For low sulfonation levels the initial rates scale with approximately $t^{½}$, but transitions to a much slower exponent. The fast regime is attributed predominantly to chain end crossing the interface where at later stage effects of confinement either by entanglements of ionic groups becomes dominant. At higher sulfonation levels, the spatial dynamics is very limited.

Introduction

Interdiffusion of polymer chains across interfaces plays a critical role in applications that require controlled motion of polymer chains in thin films. Examples include polymer coatings in dielectric actuators[1], microelectronics[2], composite lamination[3], self-healing[4], and fracture-strength development[5]. The interfacial region is often a key to the use of polymers. In lamination for example, the most desired characteristics are mechanically stable interfaces, where for coating of optical devices, the interfacial regions much be smooth to maintain transparency. Similar challenges exist when response to external perturbation and in polymeric self-healing processes. Interfacial behavior of polymers is controlled by a set of coupled factors that affect the miscibility of two polymers. Among them, are the difference in molecular weight[6], chemical compatibility[7], tacticity[8] and isotope labeling[9]. These factors were elegantly studied experimentally[10-15] and theoretically[6, 16] over the past few decades. One important interface is that formed between ionic and non-ionic polymers. In contrast to interface between Van der Walls polymers, the interfacial regions of ionic polymers are often structured[17]. The current paper presents a first insight into dynamics at the interfaces between polystyrene (PS) and its sulfonated analog, polystyrene sulfonated (sPS). The presence of ionic groups results in diverse polymer morphologies where the shape and the stability of the assemblies depend on the relative ionic strengths of the polymers, the interactions between the ionic as well as the interaction between the ionic groups with the matrix. We found that both ionic clusters and entanglements slow down interdiffusion. Surprisingly though the ionic clarets are slow to rearrange and therefore slow down significantly the dynamics at the interface.

The diffusion of simple liquids into polymers follows Fickian diffusion in which the liquid propagated within the polymer matrix with $t^{1/2}$ dynamics[18]. The dynamics of polymer

melts are an intricate process in which dynamics depend on the interaction of the polymers and topological constraints[19, 20]. Flexible and semi flexible polymers in the low interaction regime, (i.e. $\chi N \leq 10$) often follow a Fickian process with $t^{1/2}$ average displacements of chains segment. In this range the dynamics are explained by the Rouse model[19]. However above the entanglement length, the diffusion slows down and dynamics in melts are described by the Reptation model[20, 21]. In this model, the motion of the polymer chains is confined to a hypothetical tube formed by the neighboring chains in the matrix[20, 21]. In presence of ionic groups, additional constraints imposed by ionic clusters where the degree of association and the ability of the clusters to rearrange impact the dynamics.

Furthermore, in thin films of thicknesses within the several radii of gyration of the polymers, interfacial forces become significant. Specifically interfacial forces between substrate-polymer and polymer-polymer would determine the arrangement of polymer segments in thin films. Along the same lines, entropy often drives chain ends to the interface, impacting both the structure and the dynamics. With decreasing film thicknesses, thermal fluctuations are reduced as well. For example, Lin *et al.*[22] using neutron reflectometry have shown reduced mobility of deuterated and hydrogenated poly(methyl methacrylate) near a solid interface. Along the same lines, Stamm *et al.*[23] showed that conformation of polymers consists of alternating layers of hydrogenated and deuterated polystyrene and the interfacial effects have to be accounted on the interdiffusion of polymers in thin films. Similar observations were made by Brulet *et al.*[24] and Russell *et al.*[25] in which they found that polymer chains retain their unperturbed Gaussian conformations parallel to the surface, where as normal to the interface confinement effects perturbed. In addition to the chain confinement effects that impact the dynamics across an interface, small changes, erasing from chemical diversity becomes significant. Doyle *et al.*[26]

have shown that protonated PS (HPS) and deuterated PS (DPS) are not fully miscible with a slightly positive χ at room temperature, which turned negative with increasing temperature.

There is very little known on the effects of ionic groups[17]. Herein the interdiffusion of PS and sPS are studied in comparison with that of HPS, DPS using neutron reflectometry. This technique probes buried interfaces in sub nm-scale, using the inherent contrast of neutrons between protonated and deuterated polymers. Resolution of 5-10 Å coupled with selective isotope labeling is able to follow the changes of the order of 1 nm at normal to the interface, which is approximately one order of magnitude less compare to the radius of gyration of the PS studied. We found that at early stage of annealing, a fast interfacial broadening which crossovers to a slow process at prolong annealing times. The widths of the interface between two polymers capture the degree of spatial interpenetration and are correlated to their mean square displacement. The evolution of the interfacial widths with time captures the diffusion process. At the both interfaces, ionic PS/PS and that between non-ionic PS/PS, an early fast diffusion stage is observed. In contrast to van der Waals polymers the presence of ions and constraints the extent of interdiffusion is significantly hindered.

Experimental

Materials. Highly monodispersed linear HPS and DPS (The molecular characteristics are presented in Table 1) were used to prepare thin films. Linear DPS were purchased from Pressure Chemicals Co. USA, and linear HPS were purchased from Polymer Source Inc. USA. All non-sulfonated PS samples were used as received. The sPS was prepared by dissolving the HPS in dichloromethane followed by addition of freshly prepared acetyl sulfate at 50 $^{\circ}$C as discussed elsewhere[27]. This reaction produce randomly substituted $-SO_4H$ groups primarily at the *para*-position of the phenyl group along the polymer chain[27]. The sulfonation levels were

determined by titration of sPS in a mixture of 9:1 toluene and methanol with 0.01 M sodium hydroxide dissolved in methanol. The sulfonation levels are presented as the mol%, which is defined as the number of -SO_4H groups-substituted styrene repeat units per 100 of styrene units. The glass transition temperature was determined by differential scanning calorimetric measurements on PerkinElmer DSC-4000, calibrated with Indium standards. The heating rate was 10 $^{\circ}$C/min. Multiple scans were used.

Sample	M_n (kgmol^{-1})	$M_w/M_n \pm 0.01$	$T_g \pm 0.5$°C	Sulfonation Level (mol %)
HPS-160k	160.3	1.06	107.2	0.0
DPS-15k	15.0	1.04	98.5	0.0
DPS-132k	132.0	1.06	106.5	0.0
sPS160k-2 mol% sulfo	162.8	1.06	110.8	2.1
sPS160k-8 mol% sulfo	170.2	1.06	113.2	7.9

Table 1. Characteristics of the polystyrene samples used in reflectivity measurements.

Preparation of Polymer Solutions. Polymer solutions of HPS and DPS were prepared by dissolving 1 wt% of the polymers in toluene. The 1 wt% of sPS solution was prepared by dissolving sPS in mixture of 9:1 toluene and methanol. The solutions were filtered using 2.0 μm Millipore filters prior to spin coating.

Preparation of Composite Layers. A series of two layers were prepared. A DPS layer was cast on silicon oxide surface and either HPS or sPS layer was transferred on top. The composite layer preparation is detailed elsewhere[28] and only briefly reviewed. First, a 1 wt% DPS solution was cast on silicon oxide wafers at 1800 rpm for 2 minutes. The samples were vacuum dried for 16 hours at 28 psi and at 55 $^{\circ}$C to remove residual solvent. Then, the HPS and

the sPS films were spin cast on silicon oxide wafers and subsequently floated off onto deionized water. The HPS and sPS films were then transferred on top of the DPS films. These DPS/HPS and DPS/sPS composite films were allowed to dry at room temperature under vacuum at 28 psi for about 60 hours to remove residual solvent. The film thicknesses of each layer were measured by ellipsometry. Thicknesses reported are the average of measurements made from at least five spots on the dry thin films. The dimension of the each layers and the composite films are given in Table 2.

Composite Layers Top/Bottom	**Layer Thickness (nm)**	
	HPS **layer**	DPS **layer**
HPS160k/DPS15k	69.1 ± 0.2	38.2 ± 0.4
HPS160k/DPS132k	55.3 ± 0.2	39.8 ± 0.4
HPS160k-2 mol% Sulfo/DPS15k	50.9 ± 0.2	43.1 ± 0.4
HPS160k-2 mol% Sulfo/DPS132k	57.4 ± 0.2	37.8 ± 0.3
HPS160k-8 mol% Sulfo/DPS15k	26.6 ± 0.3	49.4 ± 0.4
HPS160k-8 mol% Sulfo/DPS132k	23.6 ± 0.1	46.8 ± 0.3

Table 2. Thicknesses of the layers determined from ellipsometry prior to make composites.

Silicon Wafer Treatment. One-side-polished, 50mm-wide and 5mm-thick silicon oxide wafers were used as substrates. The silicon oxide wafers were purchased from Virginia Semiconductor Inc. USA. The substrates were oxidized by Piranha etching, a solution of 7:3 v/v concentrated sulfuric acid and hydrogen peroxide, at 80 °C for 2 hours. The surface-oxidized

wafers were then rinsed thoroughly with deionized water and blown dry with nitrogen. Concentrated H_2SO_4 and H_2O_2 were used as received from Aldrich Chemicals Co. USA.

Neutron Reflectivity Experiment. Specular neutron reflectivity measurements were carried out on the Surface Profile Analysis Reflectometer[29] (SPEAR) at the Lujan Neutron Scattering Center at Los Alamos National Laboratory, USA and the Liquid Reflectometer[30, 31] (LR) at the Spallation Neutron Source, Oak Ridge National Laboratory, USA. Both spectrometers operated in the time-of-flight mode with a non-polarized pulsed neutron beam with a range of neutron wavelengths from 4.5 to 16 Å and from 2.5 to 17.5 Å respectively. Measurements were carried out over a momentum transfer vector, q range from 0.008 $Å^{-1}$ to 0.2 $Å^{-1}$ on SPEAR and from 0.006 $Å^{-1}$ to 0.18 $Å^{-1}$ on LR. The momentum transfer vector is given by $q = 4\pi \sin\theta/\lambda$, where λ is the neutron wavelength, and θ is the incident angle normal to the sample surface. The background was subtracted from the raw data and reflected intensities were normalized with respect to Fresnel reflectivity of a silicon wafer. The error bars on the reflectivity profiles correspond to the statistical errors of the measurements.

Interdiffusion studies were carried out on the composite samples described in Table 2 as a function of annealing time at 120 $^{\circ}$C. The reflectivity profiles of "as-prepared" composite films were measured as a base line. The reflectivity profiles of "as-prepared" are defined as the reflectivity patterns acquired immediately after drying the composite in a vacuum oven. For time dependent interdiffusion measurements, samples were annealed for varying times under vacuum at temperatures above the T_g (120 $^{\circ}$C). The samples were then quenched to room temperature which is significantly below Tg of the system.

Data Analysis. Scattering length density (SLD) of each polymer was calculated using their corresponding bulk densities. MOTOFIT, a fitting analysis package running on the IGOR

Pro 6.21 platform was used to analyze the reflectivity data[32]. A multilayer recursive Parratt formalism was used to analyze the data by simulating the reflectivity profiles using genetic optimization to obtain the best least square fit[33]. The quality of a fit was determined by the χ^2 where the acceptable $\chi^2 < 2.0$. The profiles of SLD as a function of the distance from the solid substrate were generated using a multilayer model where each layer was described as a box with a given thickness and SLD. The roughness between two adjacent layers was described by the Gaussian function.

Calculations of Interfacial Widths. The SLD profiles obtained from the data analysis in terms of scattering length density as a function of distance from the solid substrate were shifted such that the polymer/polymer interface is located at the origin. The interfacial widths were extracted as shown in Figure 1. The interfaces of composites layers prior to annealing are not smooth, the experimentally determined interfacial widths σ_t, were corrected to the initial roughness σ_0, as shown in Equation 1.

$$\Delta\sigma = \sqrt{\sigma_t^2 - \sigma_0^2} \tag{1}$$

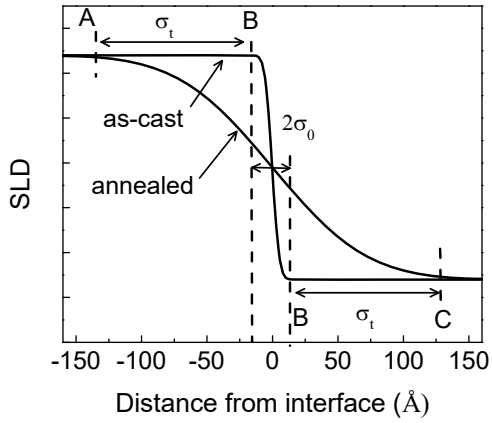

Figure 1. Schematic representation of the definitions of the interfacial widths (σ_t) and the initial roughness (σ_0).

Results and Discussion

Using neutron reflectometry we have studied the dynamics at the interface between ionic polystyrene and polystyrene, in comparison that of two poly styrene films. Two factors were probed: the effects of molecular weights and those of degree of sulfonation with the rational that both entanglements and ionic clusters would constraint the dynamics. The neutron reflectivity profiles together with the corresponding fits as a function of annealing time are presented in Figure 2. For each sulfonation level 0, 2 and 8 mol %, the study probed the interface with low, 15 kg/mol, and high, 132 kg/mol, molecular weight polystyrene.

The reflectivity patterns are characterized by the position of critical edge, q_c, the distance between consecutive minima, Δq, and often the intensity of fringes. A clear critical edge was observed for all as-prepared samples. We found that q_c hardly changes with annealing time. This is a strong indication that the air and solid interfaces remain unperturbed as the samples are annealed. The sample thicknesses were extracted from $2\pi/\Delta q$, where Δq is the distance between two successive minima. Note that the thicknesses are sensitive to reflection of substrate/DPS and DPS/HPS interfaces. The thicknesses calculated from Δq are in agreement with those measured by ellipsometry and are shown in Table 3. With annealing the reflectometry patterns become more complex and structured.

Composite Layers Top/Bottom	**Layer Thickness (nm)**	
	Composite$_{(NR)}$	**Composite $_{(SLD)}$**
HPS160k/DPS15k	38.7	107.4
HPS160k/DPS132k	41.4	95.3
HPS160k-2 mol% Sulfo/DPS15k	44.2	93.1

HPS160k-2 mol% Sulfo/DPS132k	38.1	96.2
HPS160k-8 mol% Sulfo/DPS15k	51.1	73.7.
HPS160k-8 mol% Sulfo/DPS132k	47.0	67.8

Table 3. Thicknesses of the composite layers determined from neutron reflectometry and from scattering length density profiles obtained from data fitting. The subscript represents the corresponding method used to measure the thickness.

The reflectometry profiles were analyzed in terms of a two layer model, a HPS layer on top of a DPS layer. The SLD of the each layers were not allowed to vary while allowing the film thickness and the interfacial roughness to change. The values of SLD determined from the fitting of non-annealed samples are comparable to that of the SLD values calculated using molecular parameters and the density of bulk PS. We attribute slight deviation of SLD differences from theoretical values either to trapped solvent during the sample preparation or to different interfacial densities due to confinement of polymer chains on thin films. The total film thicknesses are hardly changed as annealing progressed. However the roughness at polymer/polymer interface evolves with annealing time as a result of interdiffusion of polymer chains across the polymer/polymer interface. The roughness is described by a Gaussian function[34, 35], *G(z)*, given in Equation 2.

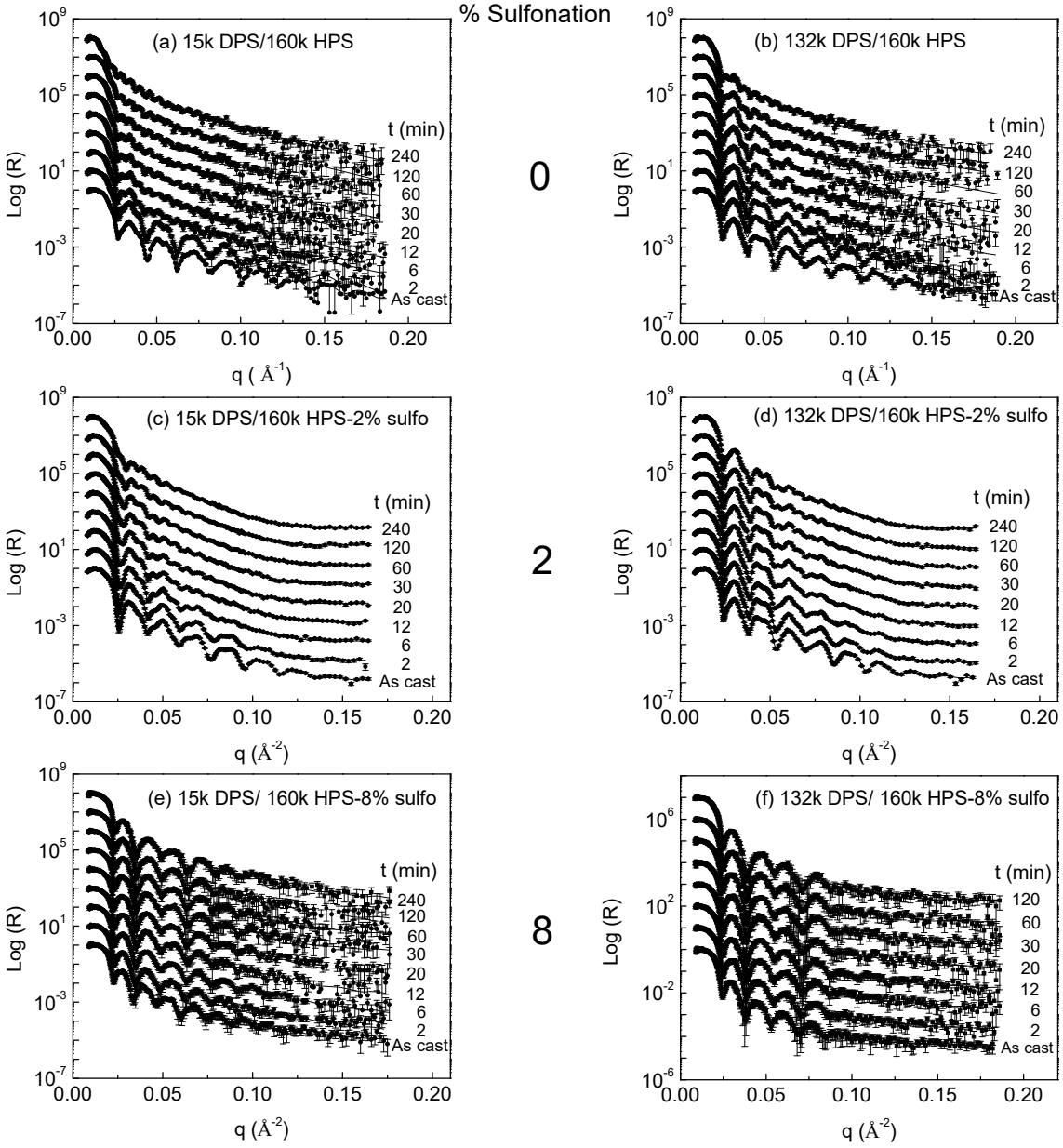

Figure 2. NR profiles and the corresponding fits at the indicated annealing times and sulfonation levels. Left column corresponds to low molecular weight DPS and right column corresponds to

high molecular weight DPS. Symbols are the experimental reflectivities and solid lines are the best fits. The profiles are vertically shifted for clarity.

$$G(z) = \frac{\Delta(b/V)}{(2\pi)^{1/2} z_0} \exp\left(-\frac{z^2}{2z_0^2}\right) \quad (2)$$

where, $\Delta(b/V)$ is the scattering length density difference between the two layers across the interface, Z_0 is standard deviation of the Gaussian function that reflects the interfacial width and Z is the depth of the film. The evolution of interfacial widths with annealing time is used to extract the interdiffusion of HPS and DPS. The polymer profiles in terms of scattering length densities (b/V) as a function of distance (Z) from the polymer/polymer interface derived from the best fits are shown in Figure 3. All non-annealed profiles are characterized by an inherited interfacial roughness approximately 10 to 15 Å. The roughness may originated from trapped solvent introduced during the sample preparation or partially crystalized polymer domains[36].

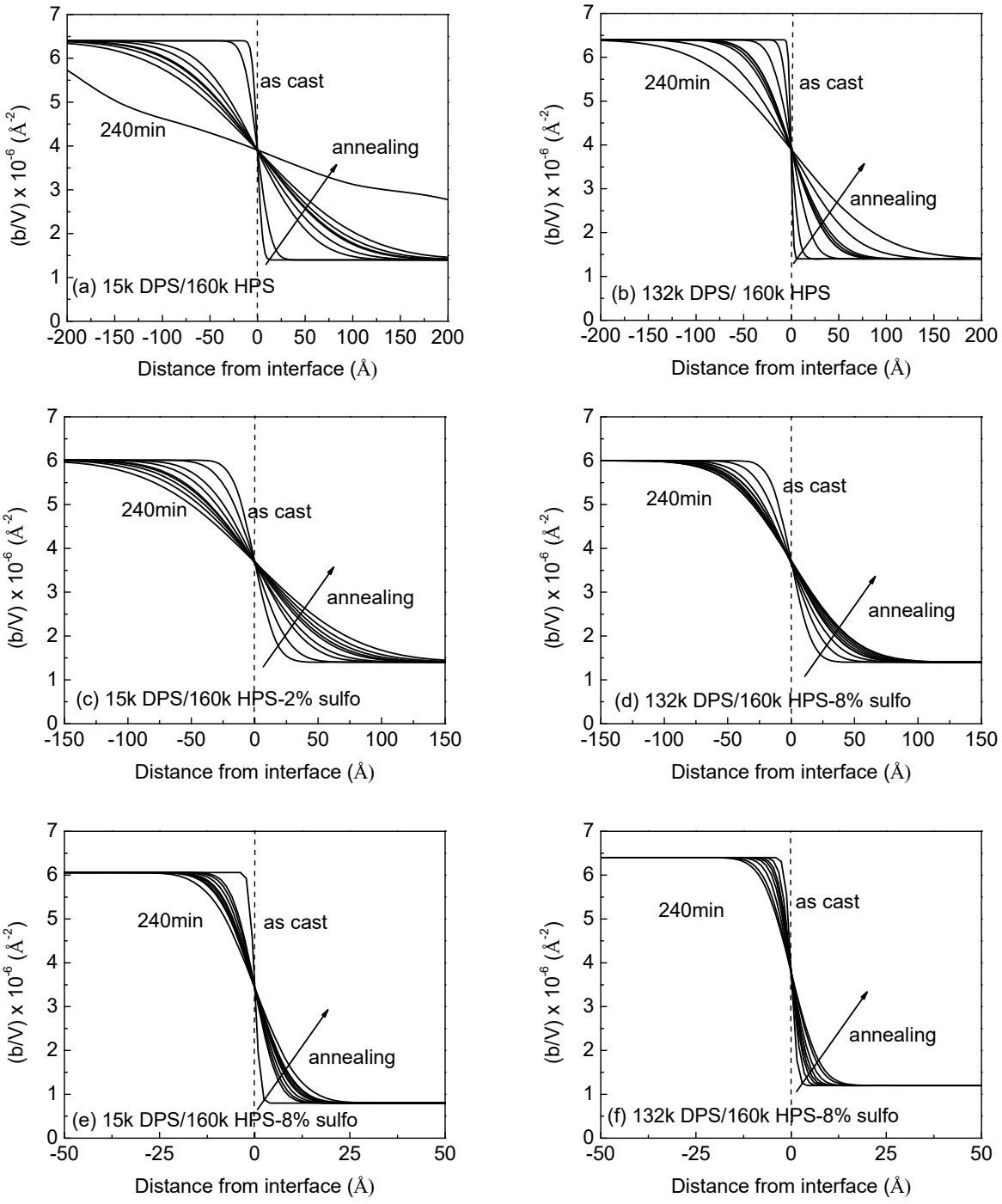

Figure 3. Polymer profiles in terms of scattering length density (b/V) as a function of distance from the composite interface as a function of annealing times for indicated composites. Left

column corresponds to low molecular weights and right column corresponds to high molecular weights. For clarity of the interface region the x-axis varies.

The interfacial width increases with annealing. However in presence of ionic groups the degree of interfacial broadening is significantly lower. For nonionic PS the degree of migration of the polymers across interfaces is primarily determined by the molecular weight. The symmetry is impacted by the choice of a Gaussian function to characterize the roughness between the polymer/polymer interfaces. Although the dynamics of individual polymers cannot be extracted from the interfacial broadness, the characteristics of the mutual diffusion of both polymers across the interface were resolved.

As expected, in absence of sulfonation Figure 3 a and b, show that the interfacial width increases significantly faster for polystyrene below the entanglement length than that for high molecular weight analog, above the entanglement length. For both polymers however the initial broadening is rather fast followed by slow changes. Similar observation of fast dynamics in low molecular weight PS than that of high molecular weight PS was observed by Karim et al.[36, 37] for series of HPS/DPS melt having molecular weights above 200 kg/mol.

Introducing even small number of ionic groups onto the PS backbone significantly reduces the degree of inter-penetration. The evolution of interfaces in presence of 2and 8 mol% sulfonation on HPS is shown in Figure 3 c-d and e-f respectively. While the interdiffusion is significantly hampered, the origin of the effects of ionic groups is not obvious. The ionic groups may simply enhance T_g, of the PS or when clustering they add further constraints for rearrangements. Our T_g measurements at thin films show that T_g is only slightly enhanced. Therefore we attributed the limited interdiffusion to the constraints exerted by ionic groups.

The evolution of interfacial widths with annealing times were quantified and compared with Rouse and Reptation characteristics. The $\Delta\sigma(t)$ with annealing time are presented in Figure 5. We assume that the mean square displacements of the polymer across the interfaces are reflected in the interfacial broadening, $\Delta\sigma(t)$. The broadening strongly depends on the sulfonation level. In absence of sulfonation interfacial widths increase rather fast at early stages of annealing and then crossed over to slow changes after approximately 20-30 minutes.

In analogous with diffusion of solvents in bulk polymers, the diffusion process or mass transport, is characterized by t^{α} where t is time and α is a scaling exponent. The α = ½ is characterized for a diffusive process[38]. As $\Delta\sigma(t)$ is a result of chain diffusion it follows a similar scaling behavior. The scaling exponents for each of the composites are extracted from a log-log plot of the data shown in Figure 4.

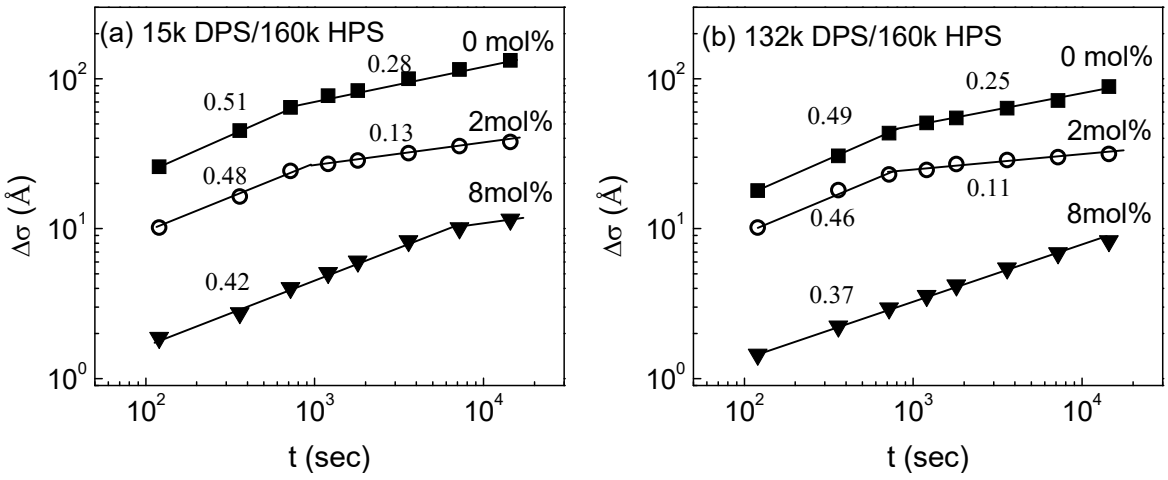

Figure 4. Log-log plots of interfacial width, $\Delta\sigma(t)$, and annealing time for indicated samples as a function of sulfonation level as indicated. The symbol corresponds to the experimental data and the solid lines are the best linear fits.

At zero degree sulfonation both the short 15k DPS and the 132 k DPS exhibit a $t^{1/2}$ behavior with extended time. It transitions to0.28 for 15k DPS and 0.25 to 132k DPS.

These findings are agreement with recent results of Pierce et al. who determined that the chain ends are the first to cross an interface. At this stage the entanglements do not affect the interdiffusion. As sulfonation is slightly increase to 2 mol% the initial stage scaling remains close to 0.5 however the scaling exponent at later times decreases significantly. These low values of 0.13 for 15kg/mol and 0.11 for 132kg/mol DPS are a result of the additional constraints by the ionic groups. Increasing the sulfonation level to 8 mol% $\Delta\sigma(t)$ becomes order of magnitude smaller and α at onset decrease.

In order to compare the mutual inter-diffusivities of HPS and sPS with DPS, we have plotted the interfacial widths with $t^{1/2}$. Figure 6 are the changes of interfacial widths with time. Mutual diffusion coefficients were determined using $(\Delta\sigma)^2 = 2Dt$ [37]. The results are given in Table 4. As expected interdiffusion of low molecular weight HPS/DPS is higher than that of high molecular weight HPS/DPS regardless of the sulfonation level. However, in presence of sulfonation groups, diffusion constant becomes one to two orders of magnitude slower. This large impact must be correlated with a significant constraint. As the glass transition temperature is only slightly affected in these ionic constraints, it becomes apparent that the ionic groups pin down the polymer.

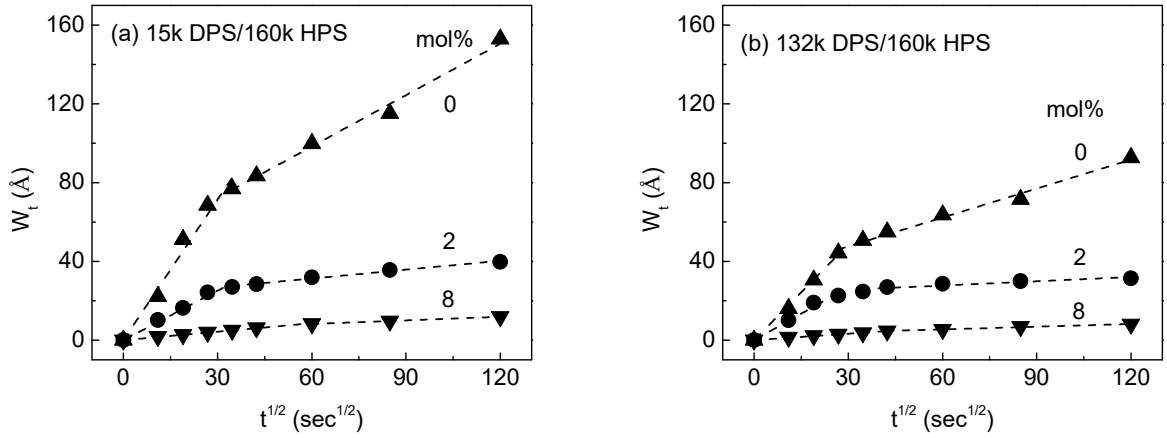

Figure 5. Interfacial widths as a function of $t^{1/2}$ and sulfonation level of HPS for indicated samples. The symbol corresponds to the experimental data and the dash lines are guide to the eye.

The order of magnitude we observed for the interdiffusion of HPS/DPS composites on silicon oxide substrates is comparable with the previously observed values of the interdiffusion of polymers across interfaces using neutron reflectometry[37, 39]. However, it is significantly slow compared to the bulk diffusivities[40, 41]. The mutual diffusion constants in presence of ionic groups are significantly small. To the best of our knowledge no mutual diffusion constant are available for the interdiffusion of polystyrene sulfonate at interfaces to compare.

HPS**(sulfo) (mol %)**	**$D_{(15k\ DPS\ /\ 160k\ HPS)}$ x 10^{-17} (cm^2s^{-1})**	**$D_{(132k\ DPS\ /\ 160k\ HPS)}$ x 10^{-17} (cm^2s^{-1})**
0	28.37	13.15
2	3.51	3.19
8	0.10	0.06

Table 4. Diffusivities of the composites annealed at 120 °C.

Summary

The effects of constrains imposed by ionic groups on the evolution of interfacial broadening at polymer/polymer interface of ionic and nonionic PS bilayers at temperature above the T_g of the PS were presented for the first time. The polymer composites of thin PS and sulfonated PS with different sulfonation levels were annealed at 120 $^{\circ}$C and the reflectivity patterns of quenched samples were measured as a function of annealing time. In order to quantify the process, interfacial widths were extracted and interpreted in terms of the diffusion of the polymers. At early stage of the annealing a fast interfacial broadening was observed which transit into a slow process at prolong annealing times. The transition time increased with increasing the sulfonation level. At early stages of annealing, the interfacial broadening was linearly changed with $t^{1/2}$ and deviated at extended annealing times. Surprisingly, even in presence of small amount of ionic groups hindered the motion of polymer chains across the interface.

Acknowledgment

This work was supported by the US Department of Energy under the contract DE-FG02-12ER46843. The neutron reflectivity measurements were conducted at the liquid reflectometry at ORNL's Spallation Neutron Source was sponsored by the Scientific User Facilities Division, Office of Basic Energy Sciences, US Department of Energy. The other part of the work has been conducted at the SPEAR at the Lujan Center at Los Alamos Neutron Science Center, funded by DOE Office of Basic Energy Sciences. Los Alamos National Laboratory is operated by Los Alamos National Security LLC under DOE Contract DE-AC52-06NA25396.

Reference

1. P. Dubois, S. Rosset, S. Koster, J. Stauffer, S. Mikhailov, M. Dadras, N. F. de Rooij and H. Shea, *Sensors and Actuators a-Physical*, 2006, **130**, 147-154.

2. M. L. Chabinyc, W. S. Wong, A. Salleo, K. E. Paul and R. A. Street, *Applied Physics Letters*, 2002, **81**, 4260-4262.

3. T. Bahners and J. S. Gutmann, *Journal of Adhesion Science and Technology*, 2011, **26**, 121-130.

4. K. Pingkarawat, C. H. Wang, R. J. Varley and A. P. Mouritz, *Composites Part a-Applied Science and Manufacturing*, 2012, **43**, 1301-1307.

5. L. Fasce, G. Chiaverano, R. Lach and P. Frontini, *Macromolecular Symposia*, 2007, **247**, 271-281.

6. H. Z. Zhang and R. P. Wool, *Macromolecules*, 1989, **22**, 3018-3021.

7. S. Sakurai, H. Jinnai, H. Hasegawa, T. Hashimoto and C. C. Han, *Macromolecules*, 1991, **24**, 4839-4843.

8. G. Beaucage, R. S. Stein, T. Hashimoto and H. Hasegawa, *Macromolecules*, 1991, **24**, 3443-3448.

9. W. W. Graessley, R. Krishnamoorti, N. P. Balsara, L. J. Fetters, D. J. Lohse, D. N. Schulz and J. A. Sissano, *Macromolecules*, 1993, **26**, 1137-1143.

10. E. J. Kramer, P. Green and C. J. Palmstrom, *Polymer*, 1984, **25**, 473-480.

11. H. H. Kausch and M. Tirrell, *Annual Review of Materials Science*, 1989, **19**, 341-377.

12. G. Reiter, S. Huttenbach, M. Foster and M. Stamm, *Macromolecules*, 1991, **24**, 1179-1184.

13. K. A. Welp, R. P. Wool, S. K. Satija, S. Pispas and J. Mays, *Macromolecules*, 1998, **31**, 4915-4925.

14. D. G. Bucknall, J. S. Higgins and S. A. Butler, *Chemical Engineering Science*, 2001, **56**, 5473-5483.

15. U. Steiner, K. Chaturvedi, O. Zak, G. Krausch, G. Schatz and J. Klein, *Nuclear Reaction Analysis Studies on the Formation in Polymer Mixtures* 1990.

16. K. R. Haire, T. J. Carver and A. H. Windle, *Computational and Theoretical Polymer Science*, 2001, **11**, 17-28.

17. L. L. He, C. H. Fujimoto, C. J. Cornelius and D. Perahia, *Macromolecules*, 2009, **42**, 7084-7090.

18. J. Crank and G. S. Park, *Diffusion in Polymers*, Oxford Academic Press, UK., 1986.

19. P. E. Rouse, *Journal of Chemical Physics*, 1953, **21**.

20. P. G. De Gennes, *Journal of Chemical Physics*, 1971, **55**.

21. M. Doi and S. F. Edwards, *The Theory of Polymer dynamics*, Oxford University, U.K., 1986.

22. E. K. Lin, R. Kolb, S. K. Satija and W. L. Wu, *Macromolecules*, 1999, **32**, 3753-3757.

23. T. Kuhlmann, J. Kraus, P. Muller-Buschbaum, D. W. Schubert and M. Stamm, *Journal of Non-Crystalline Solids*, 1998, **235**, 457-463.

24. A. Brulet, F. Boue, A. Menelle and J. P. Cotton, *Macromolecules*, 2000, **33**, 997-1001.

25. R. L. Jones, S. K. Kumar, D. L. Ho, R. M. Briber and T. P. Russell, *Macromolecules*, 2001, **34**, 559-567.

26. P. F. Green and B. L. Doyle, *Macromolecules*, 1987, **20**, 2471-2474.

27. H. S. Makowski, R. D. Lundberg and G. S. Singhal, *US patent*, 1975, **3870841**.

28. D. Kawaguchi, K. Tanaka, A. Takahara and T. Kajiyama, *Macromolecules*, 2001, **34**, 6164-6166.

29. M. Dubey, M. S. Jablin, P. Wang, M. Mocko and J. Majewski, *European Physical Journal Plus*, 2011, **126**.

30. *LR: the Liquids Reflectometer at SNS - ORNL Neutron Sciences*, http://neutrons.ornl.gov/lr/.

31. V. V. Nagarkar, D. Penumadu, I. Shestakova, S. C. Thacker, S. R. Miller, J. F. Ankner, H. Z. Bilheux and C. E. Halbert, *Ieee Transactions on Nuclear Science*, 2009, **56**, 2493-2498.

32. A. Nelson, *Journal of Applied Crystallography*, 2006, **39**, 273-276.

33. L. G. Parratt, *Physical Review*, 1954, **95**, 359-369

34. Y. Feng, R. A. Weiss, A. Karim, C. C. Han, J. F. Ankner, H. Kaiser and D. G. Peiffer, *Macromolecules*, 1996, **29**, 3918-3924.

35. B. J. Gabrys, A. A. Bhutto, D. G. Bucknall, R. Braiewa, D. Vesely and R. A. Weiss, *Applied Physics a-Materials Science & Processing*, 2002, **74**, S336-S338.

36. A. Karim, A. Mansour, G. P. Felcher and T. P. Russell, *Physical Review B*, 1990, **42**, 6846-6849.

37. A. Karim, G. P. Felcher and T. P. Russell, *Macromolecules*, 1994, **27**, 6973-6979.

38. J. Crank, Clarendon Press, Oxford, Editon edn., 1975, pp. 44-49.

39. D. Kawaguchi, A. Nelson, Y. Masubuchi, J. P. Majewski, N. Torikai, N. L. Yamada, A. R. S. Sarah, A. Takano and Y. Matsushita, *Macromolecules*, 2011, **44**, 9424-9433.

40. P. T. Callaghan and D. N. Pinder, *Macromolecules*, 1981, **14**, 1334-1340.

41. R. Bachus and R. Kimmich, *Polymer*, 1983, **24**, 964-970.